The University of Nottingham

UNITED KINGDOM • CHINA • MALAYSIA

Two-phase flow in open-cell metal foams with application to aero-engine separators

Thiago Piazera de Carvalho

B.Eng (FURB), MSc. (UNott)

Thesis submitted to the University of Nottingham

for the degree of Doctor of Philosophy

April 2016

Abstract

Oil-air separation is a key function in aero engines with closed-loop oil systems. Aero-engine separators are employed to separate oil from air before being released overboard. Typically, these devices make use of a porous medium such as an open-cell metal foam, in order to enhance oil separation. Although quite scarce, there has been some research aimed at developing a suitable modelling framework for aero-engine separators. However, numerical modelling of the air/oil flow through the open-cell metal foams employed in aero-engine separators has never been properly addressed.

This thesis presents the development of a pore-scale numerical modelling approach to determine the transport properties of fluid flow through open-cell metal foams. Micro-computer tomography scans were used to generate 3D digital representations of several commercial open-cell metal foams. A code was developed in Matlab to render the CT images into 3D volumes and perform morphological measurements on the samples. Subsequently, conventional finite volume simulations are carried out in order to obtain the airflow and compute the pressure gradient across the investigated samples. Simulations were performed for a wide range of Reynolds numbers and the feasibility of using Reynolds-averaged Navier-Stokes (RANS) turbulence models is investigated. Validation was done by comparing the pore-scale pressure gradient results against experimental measurements. Further simulations were carried out to isolate and analyse particular effects in more detail, such as wall and entrance effects, fluid compressibility, time-dependent flow features, anisotropy of the foam structure and the impact of porosity and surface area on the pressure gradient.

The oil phase within aero-engine separators has the form of disperse droplets. Thus, the oil phase in the pore-scale simulations was modelled using a Lagrangian particle tracking approach. Lagrangian simulations were run in steady state and one-way coupled, due to the low mass

fraction of oil normally present within aero-engine separators Converged airflow pore-scale solutions were employed as the base flow for the Lagrangian tracking approach. A simplified oil capture criterion assumed the droplet trajectory to be terminated upon collision against the foam solid ligaments. The focus of the present work was on separation of small droplets with a diameter smaller than 10 µm. Hence, a series of calculations were performed using a representative droplet diameter range, and multiple flow velocities. The outcome of such approach was a qualitative evaluation of the oil separation effectiveness for several commercial open-cell metal foams under a representative range of flow regimes. Furthermore, rotational effects which are experienced by the metal foams within aero-engine separators were modelled using a moving frame of reference (MRF) approach. Finally, a methodology for upscaling the results obtained by the detailed pore-scale simulations into a simple macroscopic porous medium model is described, showing promising results.

One of the aims of this work was to develop a numerical modelling framework able to provide an accurate representation of the airflow and a qualitative assessment of the oil capture within aero-engine separators. The feasibility of using the current state-of-the-art modelling framework is assessed. The separator design and geometry are based on the oil separation test rig located at the Karlsruhe Institute of Technology (KIT). Experimental measurements of the overall pressure drop and oil capture performed at KIT are used to validate the simulations. The methodology presented here overcomes some limitations and simplifications present in previous similar studies. The upscaled macroscopic porous medium model was applied to full aero-engine separator CFD simulations. Experiments and simulations were conducted for three different separator configurations, one without a metal foam, and two with metal foams of different pore sizes. For each configuration, a variation of air flow, shaft rotational speed and droplet size was conducted. The focus was on the separation of droplets with a diameter smaller than 10 µm. Single-phase air flow simulation results showed that overall pressure drop increases with both increased shaft speed and air flow, largely in agreement with the experi-

ments. Oil capture results proved to be more difficult to be captured by the numerical model and indicate that droplet re-atomization might play a significant role in the oil separation phenomena. Re-atomization, droplet-droplet collisions and droplet breakup were not considered at the present stage, but could be subject of future work. The modelling framework described here should not be seen as a definite answer but as an improvement upon the current state-of-the-art methodology, providing important lessons and recommendations for future work on aero-engine separators.

List Of Publications

Published

[1] de Carvalho, Thiago P., et al. Limitations of a state-of-the-art numerical modelling framework for two-phase flow in aero-engine air/oil separators. *ASME Turbo Expo 2016: Turbine Technical Conference and Exposition. American Society of Mechanical Engineers*, 2016.

[2] de Carvalho, Thiago P., et al. Experimental and Tomography-Based CFD Investigations of the Flow in Open Cell Metal Foams With Application to Aero Engine Separators. *ASME Turbo Expo 2015: Turbine Technical Conference and Exposition. American Society of Mechanical Engineers*, 2015.

[3] de Carvalho, Thiago Piazera, Hervé P. Morvan, and David Hargreaves. Pore-level numerical simulation of open-cell metal foams with application to aero engine separators. *ASME Turbo Expo 2014: Turbine Technical Conference and Exposition. American Society of Mechanical Engineers*, 2014.

Pending/In review

[1] de Carvalho, Thiago P., et al. Pore-scale numerical investigation of pressure drop behaviour across open-cell metal foams, *Transport in Porous Media*, XXXX.

Acknowledgements

I am extremely thankful for the support of my supervisors, Dr Hervé P. Morvan and Dr David Hargreaves, and their dedication, commitment and trust throughout the course of this research. It has been an unique and fulfilling experience to learn from and with you.

I am specially grateful to Hatem Oun and Dr Andrew Kennedy, who were kind enough to share their experimental data regarding metal foams, which turned out to be an essential part of the work described here. Without their input this thesis would not have been possible. Special thanks to the team at the Karlsruhe Institute of Technology, Laura Cordes, Tim Pychynski and Corina Hofler, for collaborating with the breather research and for sharing their experimental data, which was employed to validate the breather simulations.

I also acknowledge the funding received from the European Union Seventh Framework Programme under grant agreement no. 314366, in the Engine Breakthrough Components and Subsystems project, for enabling this research.

I'd like to acknowledge my colleagues at the Gas Turbine and Transmissions Research Centre, Al Baydu, Thomas Yue, Alexandre Crouchez, Andrea Bristot, Gervasio Salerno, Bruce Kakimpa, Akinola Adeniyi, Natarajan Arun Prakash, Peduto Davide (KIT), Roberto Ovando Martinez, Arno Kruisbrink, Graham Johnson. Your friendship and support have been essential during the course of this research.

I want to thank the people close to me. Special thanks go to my grandmother Gildete, and my mother Silvia, who have enabled all of this to happen. I'm also very grateful for the support given by the other members of my family. Finally, I want to express my gratitude to my partner, Mariana, who has given me her unconditional love, support and encouragement.

Contents

List of Figures

List of Tables

Nomenclature

Acronyms

BCC	Body-centred cubic
BET	Brunauer Emmett Teller method
CAD	Computer aided design
CFD	Computational fluid dynamics
CT	Computer tomography
DEM	Discrete element method
DNS	Direct numerical simulation
DPD	Dissipative particle dynamics
DPM	Discrete phase model
DRW	Discrete random walk
EDM	Electric discharge machining
HPC	High performance computing
KIT	Karlsruhe Institute of Technology
LAMMPS	Large-scale atomic/molecular massively parallel simulator
LES	Large eddy simulation
LMB	Lattice Boltzmann method
MC	Monte Carlo method
MD	Molecular dynamics
MGRV	Minimum geometrical representative volume
MIP	Mercury intrusion porosimetry
MRF	Moving reference frame
MRI	Magnetic resonance imaging

NRMS	Normalized root mean square
PPI	Pores per inch
RANS	Reynolds-averaged Navier Stokes
REV	Representative elementary volume
RMS	Root mean square
RNG	Re-normalisation group
RPM	Rotations per minute
RSM	Reynolds stress model
SE	Structuring element
SEM	Scanning electron microscopy
SG	Spray generator
SPH	Smoothed particle hydrodynamics
SST	Shear stress transport
stl	Standard tessellation language
UDF	User-defined function
VOF	Volume of fluid

Characteristic numbers

Kn	Knudsen number
Ma	Mach number
Re	Reynolds number
Stk	Stokes number

Greek letters

β	Curve fitting coefficient
χ	Pore indicator function
δ	Band size

Δ_e	Triangle edge length
Δ_k	Convolution kernel size
δ_{bl}	Boundary layer thickness
δ_{ij}	Kronecker delta
ε	Turbulent dissipation rate
η_{fd}	Fraction of non-captured droplets
γ	Gamma image correction factor
λ	Mean free path of molecules
μ	Dynamic viscosity
ν	Kinematic viscosity
Ω	Vector acting along the axis of rotation
ω	Angular velocity
ϕ	Porosity
Π	Non-dimensional pressure gradient
Ψ	Set of grey values
ψ,φ	Scalar quantity
Ψ_0	Grey value threshold level
ρ	Density
τ	Stress tensor
ξ	Oil capture efficiency
ζ	Normally distributed random number

Subscripts/Superscripts

0,ref	Reference value
air	Oil phase
avg	Average value
bin	Binary values

c	Critical
CFD	Simulated using computational fluid dynamics
cyl	Cylindrical
D	Darcian
d	Droplet
e	Equivalent spherical diameter
eff	Effective
exp	Experimental
f	Foam
fd	Free (non-captured) droplets
g	Gas phase
I	Interface
i,j,k	Indices
in	Inlet
l	Liquid film
m	Solid matrix
max	Maximum
min	Minimum
mp	Effective pore space
n	New value
oil	Air phase
out	Outlet
p	Pore space/particle
pg	Pressure gradient
r	Relaxation/relative
s	Streamwise

T	Transpose
tot	Total
w	Wall
x,y,z	Spatial coordinates

Variables

$\dot{m}$	Mass flow rate
$\mathbf{F}$	Additional forces
$\mathbf{f}$	External force term
$\mathbf{g}$	Gravitational acceleration vector
$\mathbf{n}$	Unit normal vector
$\mathbf{q}$	Heat flux
$\mathbf{u}$/u,v,w	Velocity vector/components
$\mathbf{x}$	Spatial position vector
A	Interface/cross-sectional area
a	Constants/coefficients values
B	Boundary of compact set
b	Cell width
C_2	Inertial resistance factor
C_Δ	Convergence of pressure drop
C_D	Drag coefficient
C_f	Courant number
C_L	Convergence of pressure gradient
C_m	Moment coefficient
d	Diameter
D_p	Diameter of the largest sphere within the pore space
E	Dimensionless impact energy

e	Internal energy/Relative deviation
F	Forchheimer coefficient
f	Darcy-Weisbach friction factor
h	Tomography scan resolution
h_0	Liquid film height
I	Unit tensor/2-D image matrix
K	Permeability
k	Turbulent kinetic energy
L	Characteristic length scale
l	Length scale
L_e	Eddy length scale
P	Centroid of representative elementary volume
p	Static pressure
Q_m	Heat source term
r	Radius
s	Specific surface
S_m	Source term
t	Time
T_L	Integral time
U	Porous medium domain
U_I	Solid-pore interface
U_{mp}	Effective pore space domain
U_m	Solid matrix domain
U_p	Pore space domain
V	Volume
v	Cell volume

v_t	Tangential velocity component
v_z	Axial velocity component
w_i	Volume fraction of phase i
y	Distance to the wall
y^+	Dimensionless distance to the wall
z	Streamwise spatial position

Chapter 1

Introduction

1.1 Background

A closed-loop recirculating oil system is commonly employed in aero engines. The oil is responsible for lubricating and cooling many engine components including gears, bearings and splines. As the oil is injected into the bearing chambers, a complex two-phase flow is created due to the interaction with air. The majority of oil leaves the chamber via the scavenge pipes, where it eventually flows towards a de-aerator for removal of entrained air and goes back into the oil tank. The remainder of oil exits the chamber through the air vent, where the air-oil mixture flows towards an aero-engine separator before being ejected overboard. Since the oil system is a closed-loop, and releasing oil overboard must be kept to a minimum, air-oil separation is essential. A simplified diagram of the oil system is shown in Figure 1.1.

Aero-engine air-oil separators are commonly referred to as *breathers* or *de-oilers*, having two distinct designs: one internal to the bearing chamber, and another external. The focus here is on the external design, which is essentially a mechanical separator. Figure 1.2 shows a schematic of a typical air-oil separator. The inlet mixture is composed of air and oil mostly in the form of dispersed droplets. The mixture enters the separator tangentially and oil separation occurs by means of two physical processes. Primary separation occurs due to the swirling flow generated by the tangential inlets and rotating shaft, which drives the largest droplets towards the static chamber walls, where they collide and generally form a thin film of oil, which flows under gravity, towards the scavenge ports. Smaller droplets tend to follow the air flow into the secondary separation device. It is common in the literature to use the word *breather* to refer

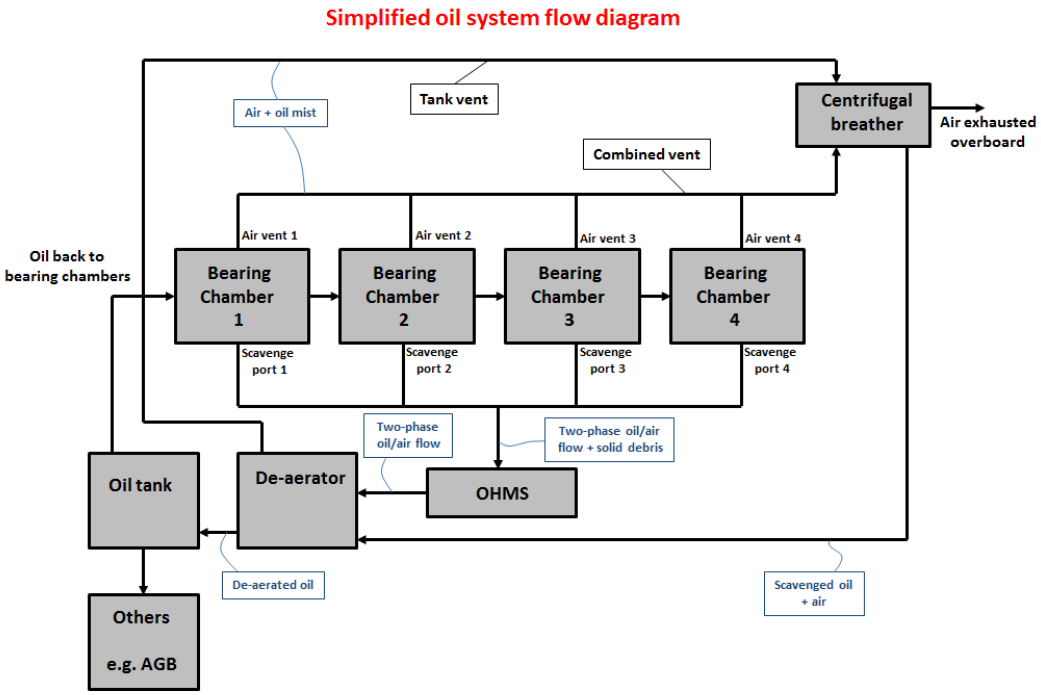

Figure 1.1: Simplified oil system diagram for a typical aero-engine.

to the secondary separation device and its casing instead of the entire separator. This is the terminology employed hereafter.

The breather is attached to the rotating hollow shaft and its components include a metal casing, which houses either a set of solid vanes or a porous medium, used to trap the remaining oil droplets. This research is concerned with the use of a porous medium, more specifically open-cell metal foams for secondary separation. Droplets flowing through the metal foam are expected to collide and coalesce onto the foam struts. Open-cell metal foams have interesting properties such as a high-porosity web-like solid matrix that provides a large surface area per unit volume, thus maximizing the likelihood of capturing oil whilst maintaining a low pressure drop. As the breather rotates with the shaft, accumulated oil is directed radially outwards by centripetal forces, where peripheral drain holes on the breather casing allow the oil back into the main chamber. Any oil which is not captured within the breather is ejected overboard. Therefore to summarize, primary separation occurs by centrifuging large droplets against the outer walls, and secondary separation occurs by trapping and coalescing smaller droplets using

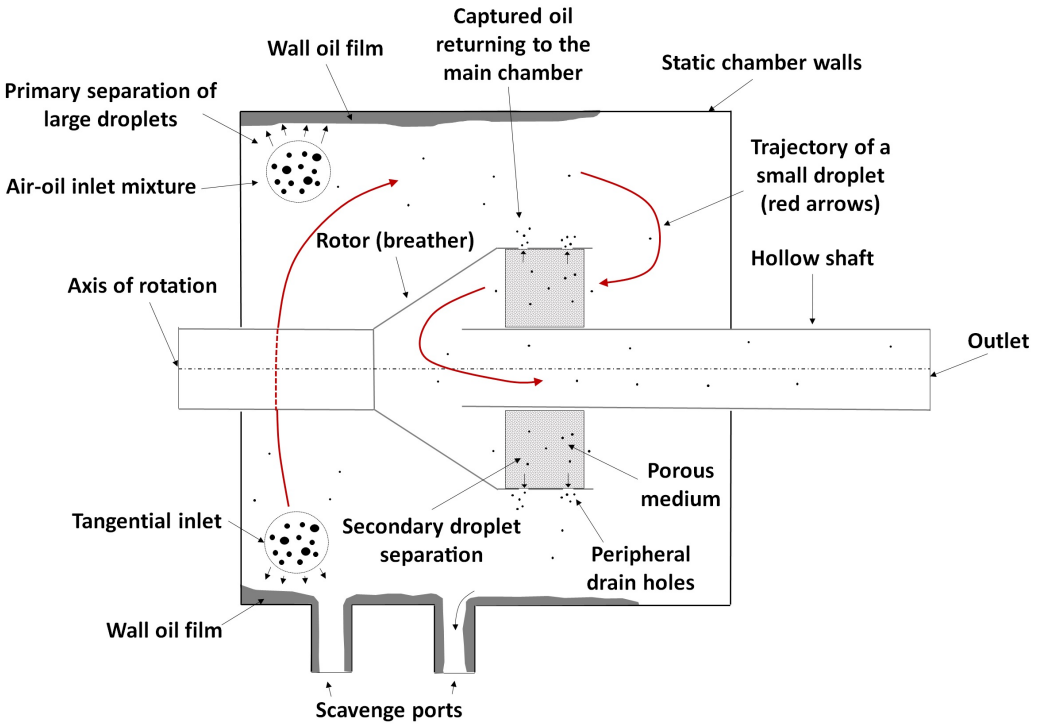

Figure 1.2: Schematic of a typical aero-engine separator.

a porous medium.

Aero-engine air-oil separators have normally very high separation efficiencies, over 99.8 % at real engine conditions (Klingsporn, 2004). Highest efficiencies are achieved when operating at cruise (∼10,000 RPM) or maximum take off (∼15,000 RPM) engine regimes. Efficiency worsens at the ground idle regime (∼5,000 RPM) but is still over 99 %. However, a common problem known as *breather smoke* happens at such low engine rotations (ground idle) and seems to be independent of the type of breather (metal foam or solid vanes) employed. It is described as a visible smoke that comes out from the aero-engine separator outlet pipe. Although not fully characterized, it has been argued that the breather smoke is formed by sub-micron droplets that are not captured during secondary separation inside the breather. Even though the separation efficiency is still very high and emissions are environmentally compliant, formation of smoke at the ground idle regime is highly undesirable and a source of concern for engine manufacturers.

The design and optimization of aero-engine separators is a challenging task, where a com-

promise between size, efficiency and pressure drop must be made. The use of computational fluid dynamics (CFD) can offer excellent insights on the underlying two-phase flow phenomena, especially in areas which are very difficult to measure or reproduce experimentally. The two-phase flow inside aero-engine air-oil separators can be characterized as being three-dimensional, turbulent, highly swirling, shear driven and having oil present as droplets, film or mist (sub-micron droplets). From the numerical modelling point of view, these phenomena are very complex and difficult to model and simulate, very often requiring the use of empirical correlations derived from simple experiments. This type of approach can be highly case dependent, which becomes a problem, not to mention the difficulty of devising experiments for cases of practical importance. Nevertheless, the development of an appropriate CFD methodology is highly desirable and must be pursued. The next section gives a survey of previous related studies, with emphasis on the numerical modelling of the two-phase flow within aero-engine separators, identifying the numerical framework state-of-the-art.

1.2 Previous related studies

Although of great interest for the aerospace industry, there are still very few studies investigating the flow inside aero-engine separators published in the open literature. Experimental data concerning the two-phase flow in aero-engine separators is also very scarce due to inherent difficulties in undertaking relevant measurements. The flow phenomena in air-oil separators has many similarities with the gas-liquid flow within aero-engine bearing chambers, where there is a flow of air and oil taking place between a stationary outer casing and a rotating shaft. A significant amount of research into the droplet and oil film flow in bearing chambers has been undertaken at the Gas Turbine and Transmissions Research Centre (G2TRC) at the University of Nottingham and at the Institute of Thermal Turbo-machinery at the Karlsruhe Institute of Technology (KIT). Some of the work described in this section comes from internal reports and projects carried out at these two institutions.

The earliest investigations on several aspects of the flow phenomena occurring in aero-engine bearing chambers were focused on obtaining experimental measurements to characterize the air and oil flow within the chamber (Wittig et al., 1993; Chew, 1996; Glahn et al., 1995; Glahn and Wittig, 1996, 1999). Results from the these studies indicate that a thin film of oil is formed on the outer casing of the chamber and that the oil is present predominantly as droplets in the core flow. The data gathered by these experimental studies have helped the development of a modelling approach for the flow within bearing chambers. Wang et al. (2001) have carried out CFD simulations using an Eulerian-Lagrangian treatment for the flow, to investigate the initial droplet impact locations in the outer chamber. The air is modelled as a continuous phase whereas the droplets are tracked using a Lagrangian approach. This modelling framework was further expanded by Farrall et al. (2001), where an oil film model was developed based on simplified film models as the one described by Chew (1996).

A preliminary research concerning the numerical modelling of the flow in aero-engine separators has been carried out by Hossain et al. (2000), using an Eulerian-Lagrangian approach. One of the main differences between a bearing chamber and an air-oil separator is the presence of a breather in the latter. A simplified separator geometry was investigated as shown in Figure 1.3. Oil droplets in the range of 1-100 μm were modelled using a Lagrangian discrete phase model (DPM) and the trajectories were stopped at the entrance of the breather. The metal foam was modelled using a macroscopic porous medium approach, i.e. the metal foam geometry is not explicitly represented, instead the porous zone is treated as a momentum sink using a volume-averaging method (Whitaker, 1998), and its parameters are determined empirically. The porous zone is assumed to be isotropic, stationary and the pressure gradient to follow Darcy's law (Darcy, 1856). Rotating parts were accounted for by a *moving wall approach*, i.e., a specified tangential velocity at the walls. The effects of turbulence on the flow were accounted by the $k-\varepsilon$ model (Launder and Spalding, 1974). Results showed the separator pressure drop to be weakly affected by shaft speed. The critical droplet diameter, which is defined in this context

as the size of the largest droplet at the metal foam entrance, was found to be in the range of 3-4 µm, independent of shaft speed.

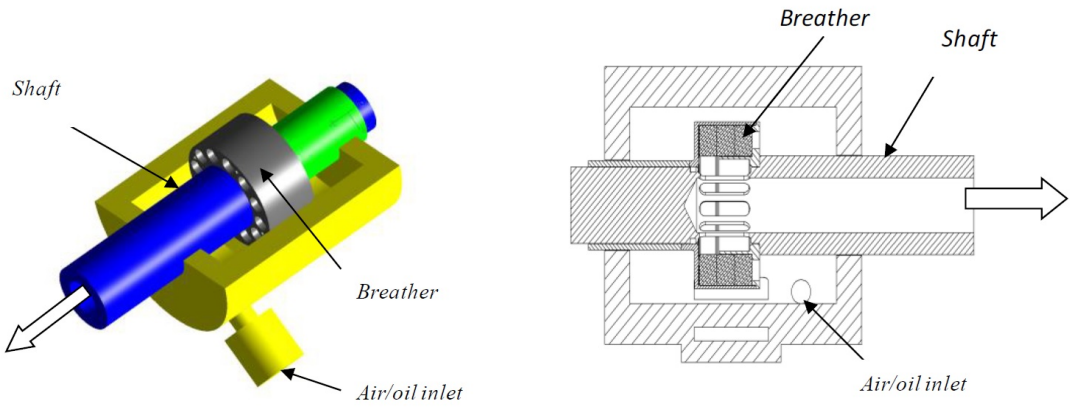

(a) (b)

Figure 1.3: (a) 3-D rendering of the aero-engine separator geometry (b) Schematic of the separator (Hossain et al., 2000).

Eastwick et al. (2006) simulated two distinct separator designs using the same modelling framework as in (Hossain et al., 2000), comparing the oil separation prior to the breather entrance. The first separator design was internal to the bearing chamber (Figure 1.4), and the second, external (Figure 1.3). Validation data for the air flow was available for the internal design only, but a number of difficulties were found during the experimental tests and uncertainty bars of ± 30 % were assigned. Shaft speeds of 0 to 10,000 RPM were investigated. Both designs embody a form of cyclonic separation with simulation results suggesting that the external design is more efficient for aero-engine applications. The choice is justified by a more effective primary separation, for which a smaller droplet critical diameter was obtained (3 µm). Separation performance was found to be independent of shaft speed.

Dems et al. (2009) further improved the modelling framework, giving more attention to the numerical part, where the effects of mesh density, turbulence model, flow compressibility, time-dependency of the flow and spatial discretization scheme where considered. The separator

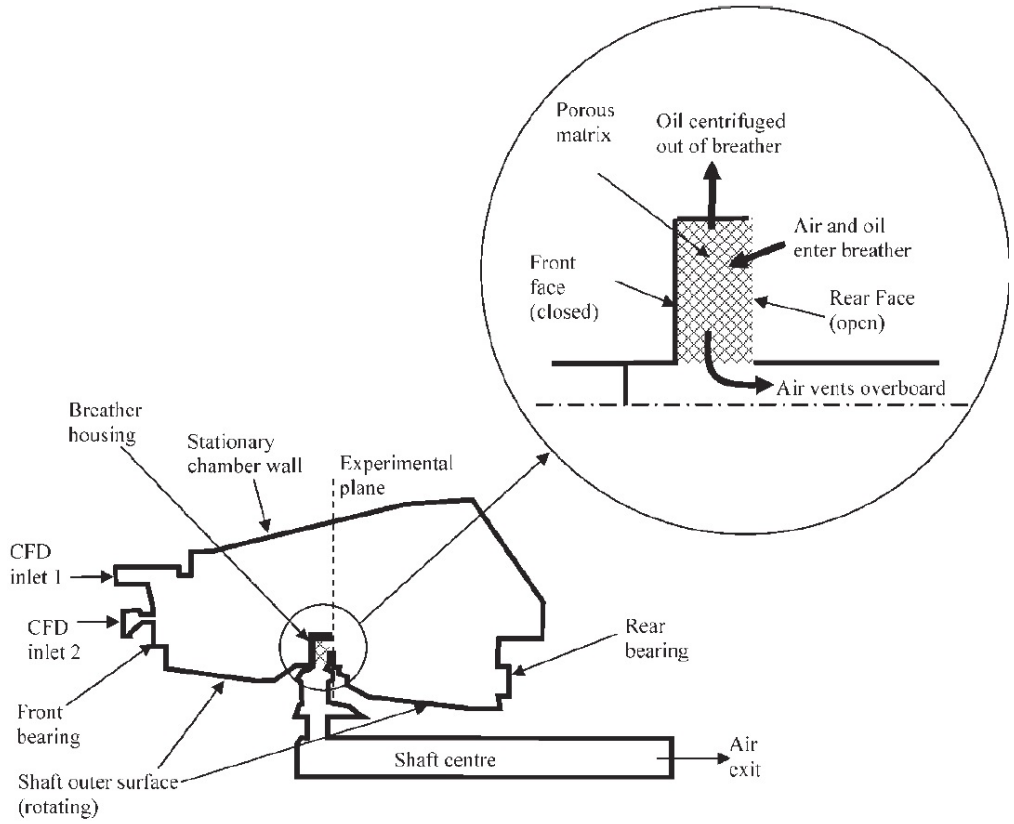

Figure 1.4: Schematic of an internal aero-engine separator design (Eastwick et al., 2006).

geometry was a simplification of a real industrial exterior design, as shown in Figure 1.5. The porous medium model parameters were determined from experimental pressure drop tests on a commercial open-cell metal foam sample, namely the Retimet 45 pores-per-inch (PPI), suggesting that the pressure gradient is better described by quadratic equation instead of Darcy's law. The porous zone was modelled as stationary. It has been argued that this simplification affects the pressure drop across the breather due to the increased relative velocity between the fluid and solid structure. When the circumferential velocity within the separator chamber is close to the shaft speed, the relative velocity has low axial and radial components compared to the tangential one. With a stationary porous medium, the circumferential velocity component is added and the air flows through the breather with unrealistic high velocities causing an over prediction of the pressure drop. As in the previous studies, droplet tracking calculations were stopped at the breather entrance. Three shaft speeds were studied based on the real engine regimes (ground

idle, cruise and take off). The air flow simulations showed that flow compressibility must be accounted for, and that the Reynolds Stress Model (RSM) (Versteeg and Malalasekera, 2007), gives a better representation of the flow within the separator when compared to the $k-\varepsilon$ turbulence model. The droplet tracking calculations found the critical diameter to be 4 μm (cruise regime) and 12 μm (ground idle and take off regimes).

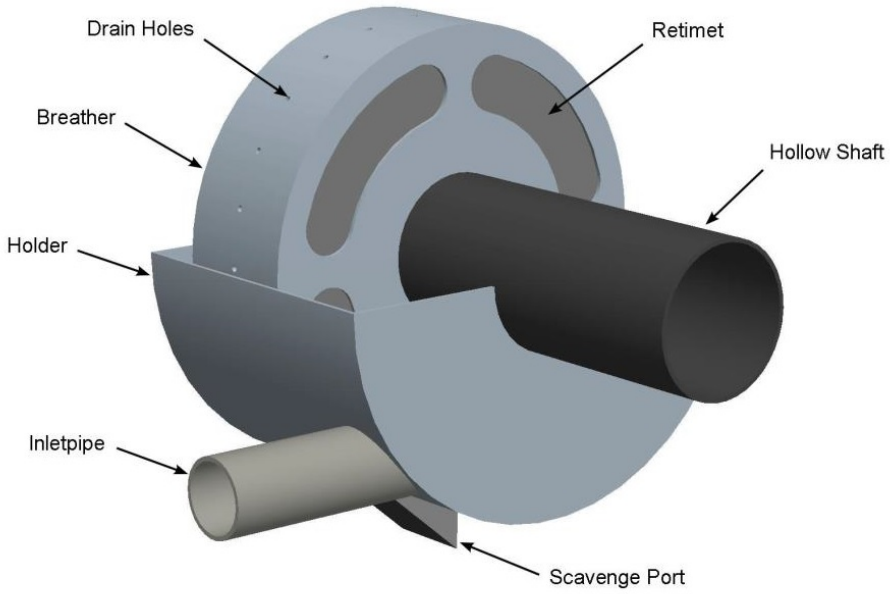

Figure 1.5: Simplified geometry of an industrial separator design (Dems et al., 2009).

More recently, a thin-film modelling approach was employed by Verger and Morvan (2011) to investigate the two-phase flow in an industrial separator design. The work is described in an internal report at the G2TRC. The modelling approach was similar to the one in (Dems et al., 2009), with the addition of the thin-film modelling on the separator outer walls. Three shaft speeds were investigated in the same way as in (Dems et al., 2009). The film model was employed to qualitatively visualise the oil film flow on the outer wall. Results showed the tendency of oil pooling at lower shaft speeds, together with a higher risk of droplet stripping and re-entrainment. Particle tracking calculations showed the critical droplet diameter to be 17 μm (ground idle regime) and 7 μm (cruise and take off regimes). Figure 1.6 depicts the 3-D model of the separator investigated and a film thickness contour plot on the outer walls.

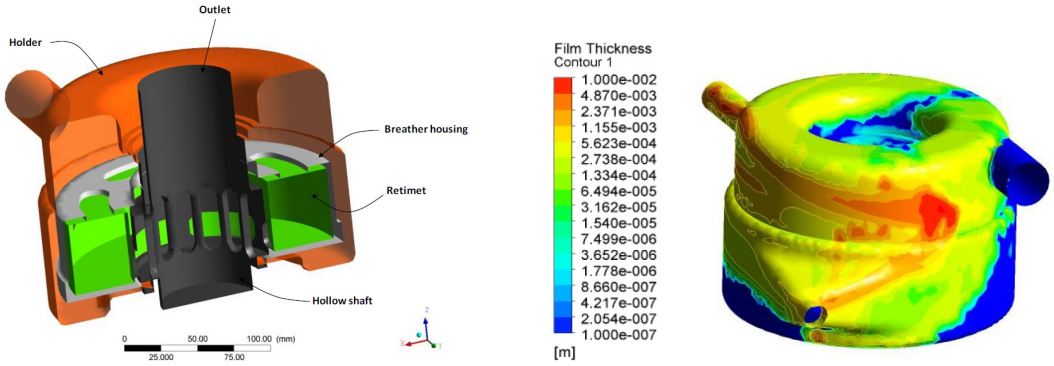

(a) (b)

Figure 1.6: (a) 3-D model of an industrial separator geometry and (b) film thickness contour plot (logarithmic scale) (Verger and Morvan, 2011).

On the experimental side, Willenborg et al. (2008) employed non-intrusive optical measurement techniques to investigate the separation efficiency and identify potential optimization parameters of a commercial separator design (see Figure 1.7), emphasising separation of small droplets ($<$10 µm). Results showed separation efficiency to increase with both increasing shaft speed and mean inlet droplet diameter, and decreasing air flow. Pressure drop increased with both increasing shaft speed and air flow. Additionally, it was observed that sub-micron ($\approx$ 0.5 µm) droplets were able to pass through the breather and leave the separator.

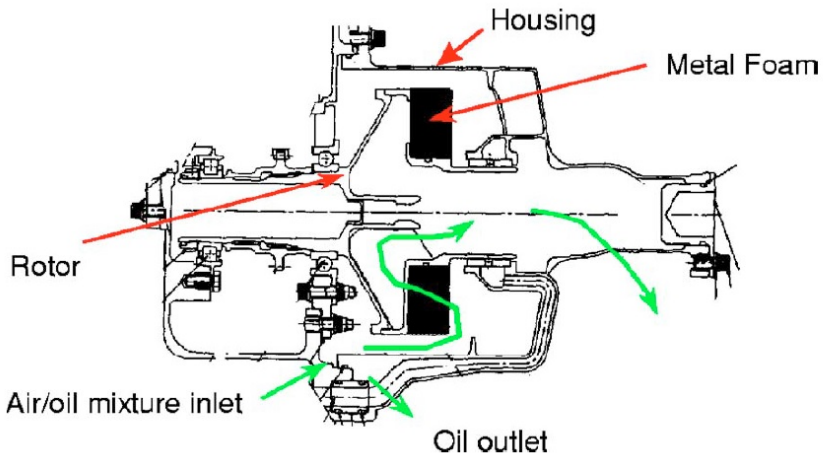

Figure 1.7: Schematic of the separator design investigated by Willenborg et al. (2008).

None of the studies described above have considered the numerical modelling of the sec-

ondary separation that takes place inside the metal foam in the breather. Phillips (2003) attempted to model a breather design by means of a macroscopic porous media approach using an idealized two-dimensional annular geometry and including rotational effects by means of a moving reference frame (MRF). The porous medium parameters were empirically determined from the Retimet 45 PPI metal foam. Air flow results showed that a quadratic equation is better suited to describe the pressure gradient in metal foams. The two-phase calculations on the 2-D annular geometry involved several assumptions and simplifications and the results were not very conclusive.

The challenge of modelling the secondary separation inside the breather remains one of the largest gaps yet to be filled in the current modelling framework of aero-engine separators. From the experimental point of view the task is quite challenging, since the intricate metal foam geometry prevents one from evaluating the air-oil behaviour within the pore space with a reasonable degree of accuracy. The macroscopic porous media approaches commonly employed are ill-suited for this particular application due to the nature of the underlying separation phenomena. As the oil droplets enter the metal foam, they are expected to collide against the foam struts, where several outcomes are possible after a collision, e.g. stick, splash or rebound. Therefore, if a macroscopic porous media approach is to be used, it would require experimental input in order to determine the parameters of the governing flow, and the oil separation effectiveness. Clearly, such an approach is highly case-dependent, since each type of metal foam would have different parameters and coefficient values. In summary, it is not possible to model the oil separation within metal foams without having at least some information regarding the foam geometry, since separation is dependent on the interaction between oil droplets and the porous structure.

There exists however, another way of tackling the problem of flow through porous media that is not case-dependent and is more firmly based on first principles. Direct pore-scale modelling considers the geometry of a small representative elementary volume (REV) of the porous material explicitly. Therefore, no experimental input is required to determine the flow

coefficients and even multiphase flow can be considered (Meakin and Tartakovsky, 2009). The main difficulty lies in obtaining an accurate description of the porous geometry. If a small REV of a metal foam sample has its geometry explicitly represented, it may be possible to use an Eulerian-Lagrangian treatment for the gas-liquid flow and obtain some insight on the separation phenomena, thus offering a solution to the numerical modelling of secondary separation within aero-engine separators.

1.3 Aims and objectives

The aim of this research is to develop a numerical framework for the simulation of gas-liquid flow through open-cell metal foams with application to aero-engine separators. Specific objectives include:

- Develop and validate a model for single-phase air flow within open-cell metal foams.
- Run pore-scale Lagrangian tracking simulations to obtain a qualitative assessment of the oil separation within open-cell metal foams.
- Investigate the feasibility of including rotational effects in the pore-scale simulations.
- Transfer the pore-scale results into an enhanced macroscopic model of the porous medium.
- Application of the enhanced macroscopic porous medium model to realistic aero-engine separator simulations.

1.3.1 Proposed methodology

The proposed methodology is illustrated in Figure 1.8, where the intention is to work from right to left. Firstly, a detailed pore-scale representation for a small REV of an open-cell metal foam is generated and used to simulate the air flow through a static sample. Validation of this procedure is carried out by comparing the overall pressure drop against experimental data. Using

the air flow results obtained from the single-phase simulations, a series of Lagrangian tracking calculations are performed in order to obtain qualitative oil separation results. Rotational effects are added to the pore-scale simulation framework by using a moving reference frame (MRF) approach, in order to simulate the conditions present within real aero-engine separators.

The results obtained from the pore-scale simulations are then volume-averaged and applied to a macroscopic description of the porous medium, which becomes an integral part of a full separator simulation.

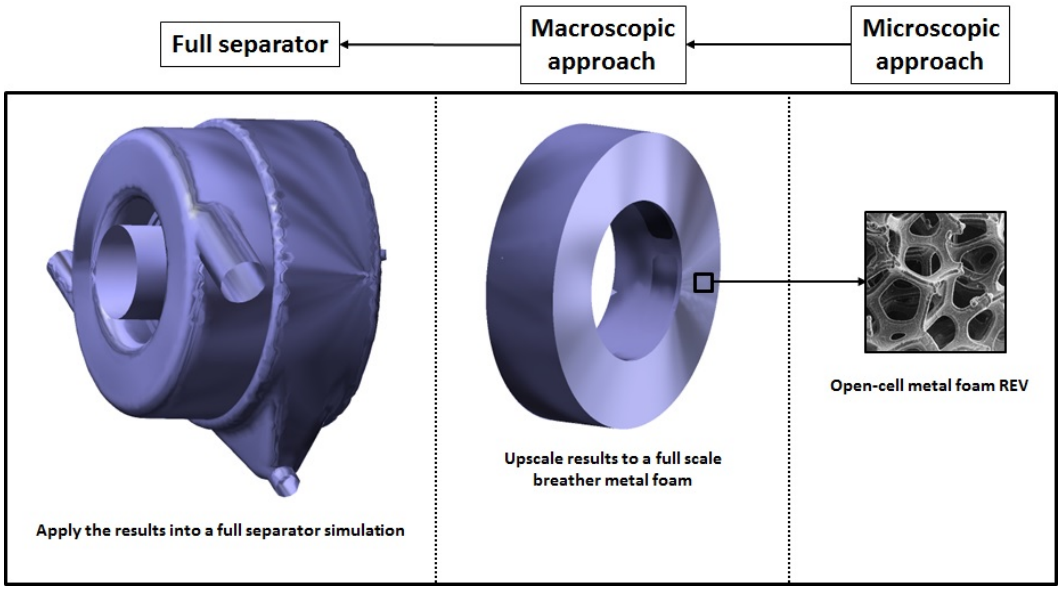

Figure 1.8: Numerical modelling proposal illustrating the different scales employed in order to characterize the two-phase flow through open-cell metal foams used in aero-engine separators.

1.4 Thesis structure

Chapter 2 covers the theory related to the fluid flow through porous media, more specifically through open-cell metal foams. Basic porous media definitions are given, followed by a description of the governing equations and the fundamentals of the volume-averaging technique. Several porous media flow regimes and pressure gradient relationships are described. This is followed by background information on metal foams, including production methods, applica-

tions and their main characteristics. Finally, an overview of the most relevant pore-scale metal foam numerical studies is provided.

The basic methodology employed for the development of a pore-scale modelling framework for open-cell metal foams is covered in Chapter 3. The pore-scale geometry is represented from micro-computer tomography (μCT) scans, requiring a significant amount of experimental input. A full set of pressure drop measurements on seven different open-cell metal foam samples are used as validation data for the air flow simulations. The μCT scans and pressure drop measurements were conducted by a separate research team inside the University of Nottingham and their work is described elsewhere (Oun and Kennedy, 2014). A brief description of the experimental methods is given, followed by the development of an image processing technique used to characterize the samples and generate the three-dimensional geometries employed in the simulations. A series of sensitivity studies are performed on the computational samples in order to analyse any source of uncertainty arising from the numerical approach.

Chapter 4 describes all the pore-scale simulation results, including single-phase airflow simulations and Lagragian tracking calculations for the oil flow. Airflow results for all samples are validated against experimental pressure gradient measurements. Additional simulations are carried out in order to investigate the influence of additional effects, such as flow compressibility, porosity variation, wall effects, thickness effects, among others. The converged airflow solutions are employed for the Lagrangian tracking calculations, which investigate the effects of droplet diameter and flow velocity on the separation effectiveness. Finally, a method to transfer pore-scale results to a macroscopic formulation is described.

Chapter 5 concerns the application of an enhanced porous medium model to a realistic aero-engine separator design. The geometry simulated is a representation of the oil separation test rig at the KIT. The airflow simulations are validated by comparing the overall pressure drop against experimental values. The feasibility of obtaining qualitative oil separation results is evaluated by performing Lagrangian tracking calculations using the enhanced macroscopic porous medium

approach.

Lastly, Chapter 6 gives an overall conclusion to the research carried out, covering what can be drawn from this work and the main limitations associated with the current modelling framework. Suggestion are made for the paths that may be taken in future similar studies.

Chapter 2

Flow modelling in porous media

This chapter provides an overview of fundamental concepts regarding porous media flow modelling. The fluid flow governing equations are described and basic flow models for porous media are introduced. Background information regarding metal foams is given, highlighting their basic properties, types and applications. Statements are made concerning the applicability of classic porous media approaches to open-cell metal foams. A survey of the most relevant numerical studies concerning the characterization and simulations of fluid flow in open-cell metal foams is presented.

2.1 Porous media fundamentals

2.1.1 Porous medium concept

A porous medium is defined as a portion of space that is partly occupied by a solid phase (or *solid matrix*) and partly by *void space* (or *pore space*), with the latter being occupied by one or more fluid phases and being distributed throughout the porous medium domain (Bear and Corapcioglu, 2012). In addition to that, it is required that at least some of pores in the void space to be interconnected, and these will be part of the *effective pore space*. The effective pore space should contain at least one or more continuous paths from one side of the domain to the other. Unconnected pores contained inside the solid matrix not relevant to fluid flow may even be considered as part of the solid matrix (Bear, 2013). In some specific cases, the solid matrix may suffer deformation due to the action of external stresses. However, for the purpose of work described here, the solid matrix is assumed to be completely rigid without being subjected to

any kind of deformation.

2.1.2 Basic definitions

Let U be a compact set in $\mathbb{R}^3$ comprised of two closed sets: U_m and U_p such that $U_\mathrm{m} \cup U_\mathrm{p} = U$, where U denotes the porous medium domain, U_m and U_p represent the solid matrix and pore (void) space respectively. The solid-pore interface is defined as $U_\mathrm{m} \cap U_\mathrm{p} = U_\mathrm{I}$, having finite area, $A(U_\mathrm{I})$ and zero volume, $V(U_\mathrm{I}) = 0$. The total porosity ϕ, and specific surface s, are defined as respectively

$$\phi(U) = \frac{V(U_\mathrm{p})}{V(U)} \tag{2.1}$$

$$s(U) = \frac{A(U_\mathrm{I})}{V(U)} \tag{2.2}$$

If B is defined as the boundary of U, let B_1 and B_2 be defined as two disjoint subsets of B with a non-empty intersection with U_p. Subsets B_1 and B_2 are equivalent to two disjoint domain boundaries. The effective pore space U_mp is defined as the largest subset of U_p that connects B_1 and B_2. Therefore, the effective porosity, ϕ_eff and effective specific surface, s_eff are defined as

$$\phi_\mathrm{eff}(U) = \frac{V(U_\mathrm{mp})}{V(U)} \tag{2.3}$$

$$s_\mathrm{eff}(U) = \frac{A(U_\mathrm{mp} \cap U_\mathrm{I})}{V(U)} \tag{2.4}$$

The pore indicator function, χ, at a given position vector $\mathbf{x}$ is defined as

$$\chi(\mathbf{x}) := \begin{cases} 1 & \text{if } \mathbf{x} \in U_\mathrm{p} \\ 0 & \text{if } \mathbf{x} \in U_\mathrm{m} \end{cases} \tag{2.5}$$

The pore space of consolidated media such as the ones that will be covered here can be characterized by means of a pore size distribution. The pore diameter at a given position vector $\mathbf{x}$ in U, is defined as the diameter of the largest sphere D_p that contains $\mathbf{x}$ and remains entirely within the pore space, U_p, without overlapping the solid matrix, U_m, (Bear, 2013),

$$d_p(\mathbf{x}) = \max\{d_p | D_\mathrm{p} \cap U_\mathrm{p} = D_\mathrm{p} \wedge \mathbf{x} \in D_\mathrm{p}\} \tag{2.6}$$

where d_p is the pore diameter. Thus, by attaching a pore diameter to each point of the pore space, a pore-size distribution can be defined.

2.1.3 The continuum hypothesis and the representative elementary volume

Fluids are composed of a large number of molecules with intermolecular space in between, which are in constant movement and colliding with each other. According to the theories of classical mechanics, their behaviour could be fully described by knowing their current positions in space and their momenta. However, the number of molecules in any relevant portion of matter is extremely high, which makes computation of their motion impractical, without mentioning the difficulty in knowing all their initial positions and velocities. On the other hand, if the typical length scales being investigated are much larger than the mean free path of the molecules, i.e. the average distance travelled by a moving molecule, it makes sense to consider the matter as being a continuum.

The concept of a representative elementary volume, or REV hereafter, is essential to the continuum approach. A REV is an ensemble of many molecules with a characteristic size much larger than the mean free path of molecules, but much smaller than the dimensions of the physical domain being investigated. By averaging the properties over the molecules contained in the REV, it is possible to obtain meaningful values about the bulk properties of the material, such as density or viscosity for example.

Before elaborating how these concepts fit in the context of a porous medium, it is neces-

sary to define the relevant length scales associated with porous media flow. First, there is the molecular scale, where effects arising from the motion of the molecules are dominant. Above the molecular scale comes the microscopic scale (or pore scale), where the characteristic length scale is given by the average size of the pores or channels. Any fluid present in the interstitial space can be regarded as being a continuum, as long it satisfies the conditions described previously. One way of evaluating these conditions are satisfied is by calculating the dimensionless Knudsen number (Knudsen, 1950), K_n, which is defined as

$$K_\mathrm{n} = \frac{\lambda}{L} \tag{2.7}$$

where λ is the mean free path of the molecules and L is a characteristic physical length scale, which in the case of porous media can be taken as the mean pore size for example. According to Bear (2013), the continuum hypothesis is applicable to flow in porous media when $K_\mathrm{n} < 0.01$. If $K_\mathrm{n} \sim 1$, the flow is in the slip-flow regime and when $K_\mathrm{n} > 1$, it is in the Knudsen flow or free molecular flow. If $K_\mathrm{n} \sim 1$, it means that the mean free path of the molecules is comparable to the length scale of the underlying physical phenomena, meaning that the continuum assumption is not a good approximation. Finally, the macroscopic scale is reached by zooming out of the microscopic scale. The macroscopic porous medium properties should remain similar for a homogeneous medium, e.g. a packing of uniform spheres, or could change gradually for inhomogeneous media. e.g. layers of soil.

The REV in the context of porous media is a step necessary to pass from a microscopic to a macroscopic level of description of the porous domain. In that sense, the REV volume, U_0, with its centroid located in P, can be defined as the smallest subset of the porous domain, U, for which averaged quantities within U_0 are representative of U and the continuum assumption is valid. Figure 2.1 gives an illustration of the REV determination. There should be a range $U_\mathrm{min} < U_0 < U_\mathrm{max}$, where U_min and U_max represent the minimum and maximum REV size respectively. If the total porosity, ϕ, is chosen as the averaged quantity of interest, U_min is the minimum

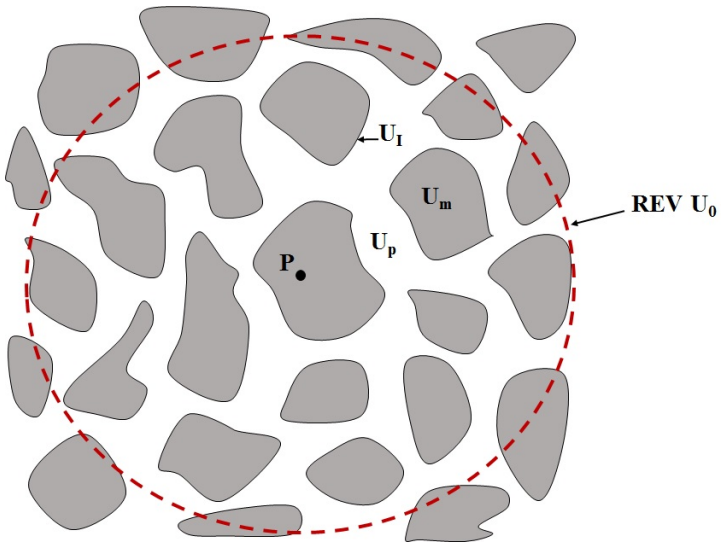

Figure 2.1: Illustration of the REV U_0, with centroid in P, showing the solid matrix, U_m, the pore space, U_p and the solid-void interface U_I.

volume where fluctuations in ϕ have a small amplitude due to the random distribution of pores. If $U_0 < U_{\min}$, the characteristic length of U_0 starts to approach the size of a single pore, and large amplitude fluctuations in ϕ suddenly begin to take place. Similarly, when $U_0 > U_{\max}$, the total porosity may undergo gradual changes related to large scale heterogeneities if the porous medium is inhomogeneous. Figure 2.2 depicts the conceptual selection of the REV size based on the total porosity of the medium. The concept of REV forms the basis of all volume-averaging porous medium approaches.

2.1.4 Volume averaging basics

Let V be an averaging volume of a multi-component medium (such as porous media), with M components. Each component $i = 1, ..., M$ has a volume fraction w_i and its corresponding partial volume V_i, such that $V = \sum_{i=1}^{M} V_\mathrm{i}$ and $V_\mathrm{i} = w_\mathrm{i} V$. The scalar quantity ψ_i for component i can be defined as the sum of its superficial average and fluctuating component, such as

$$\psi_\mathrm{i} = \langle \psi_\mathrm{i} \rangle + \psi_\mathrm{i}' \tag{2.8}$$

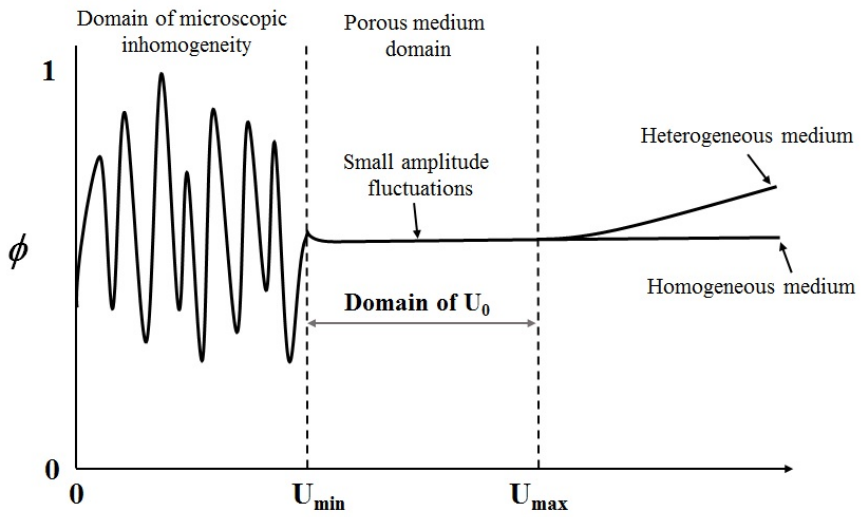

Figure 2.2: Conceptual determination of the REV size for a porous medium showing the total porosity,ϕ, as a function of the REV size.

where the superficial average, $\langle \psi_i \rangle$, is defined as

$$\langle \psi_i \rangle = \frac{1}{V} \int_V \psi_i dV \tag{2.9}$$

The intrinsic average, $\langle \psi_i \rangle^i$ is given as

$$\langle \psi_i \rangle^i = \frac{1}{V_i} \int_{V_i} \psi_i dV \tag{2.10}$$

A scalar quantity associated with a particular component can be written as

$$\psi_i = w_i \langle \psi_i \rangle \tag{2.11}$$

According to Whitaker (1998), the spatial averaging theorem defines the relation between the superficial average of the discrete-scale gradient of ψ_i and the continuum-scale of $\langle \psi_i \rangle$ as

$$\langle \nabla \psi_i \rangle = \nabla \langle \psi_i \rangle - \frac{1}{V} \sum_{j=1}^{N_i} \int_{A_{ij}} \psi_i \mathbf{n}_{ji} dA \tag{2.12}$$

where A_{ij} is the interface surface area between components i and j, N_i is the total number of components adjacent to i, and $\mathbf{n}_{ij}$ is the unit normal vector at the interface A_{ij} pointing to

component i. The relation of a time derivative to the time derivative of the average is given by the transport theorem, written as

$$\left\langle \frac{\partial \psi_{\mathrm{i}}}{\partial t} \right\rangle = \frac{\partial \psi_{\mathrm{i}}}{\partial t} + \frac{1}{V} \sum_{j=1}^{N_{\mathrm{i}}} \int_{A_{\mathrm{ij}}} \psi_{\mathrm{i}} \mathbf{u}_{\mathrm{ji}} \cdot \mathbf{n}_{\mathrm{ji}} \mathrm{dA} \tag{2.13}$$

where $\mathbf{u}_{\mathrm{ji}}$ is the velocity vector at the interface A_{ij}. However, for stationary, rigid interfaces, $\mathbf{u}_{\mathrm{ji}} = 0$, which is always the case in the present work.

The volume averaging technique is directly linked with the REV concept. In this context, the averaging volume can be thought of being the REV itself such that, $V = U_0$. It is necessary that the averaging volume (or REV) be sufficiently large such that it includes all the relevant morphological properties of the porous medium, and sufficiently small compared to the total size of the porous domain such that $\langle \psi_{\mathrm{i}} \rangle$ and $\langle \nabla \psi_{\mathrm{i}} \rangle$ can be assumed to be continuous scalar and vector fields respectively. This imposes one requirement in the length scales chosen for the REV:

$$l \gg d \tag{2.14}$$

where l stands for the characteristic length scale of the REV and d is the diameter of an individual pore. This leads to a macroscopic formulation where only measurable statistical properties of the porous medium and the fluids are required.

2.2 Fluid flow governing equations

This section presents the governing equations for the flow of a single-phase fluid in clear space (i.e. void space). Under the continuum hypothesis, the fluid flow of a Newtonian fluid in the void space can be described by the Navier-Stokes equations along with the mass and energy conservation equations. The continuity allows the properties of the fluid to be described by (piecewise) continuous functions in space and time, thus ruling out the creation or destruction

of mass, momentum or energy within the fluid's domain.

The conservation equations are derived in an Eulerian frame of reference, for an infinitesimal control volume with all the fluxes across the its boundaries set in balance. The conservation of mass is given as

$$\frac{\partial \rho}{\partial t} + \nabla(\rho \mathbf{u}) = S_{\mathrm{m}} \tag{2.15}$$

where ρ is the fluid density, $\mathbf{u}$ is the velocity vector and S_{m} is a source term which accounts for added mass to the continuous phase. Eq. (2.15) is the general form of the mass conservation equation and is valid for both compressible and incompressible flows.

The conservation of momentum in a static reference frame is given by

$$\frac{\partial \rho \mathbf{u}}{\partial t} + \nabla(\rho \mathbf{u}\mathbf{u}) = -\nabla p + \nabla(\overline{\tau}) + \rho \mathbf{g} + \mathbf{F} \tag{2.16}$$

where p is the static pressure, τ is the stress tensor, $\rho \mathbf{g}$ and $\mathbf{F}$ are the gravitational and body force and external body forces terms respectively. For Newtonian fluid, the stress tensor is defined as

$$\overline{\tau} = \mu \left[(\nabla \mathbf{u} + \nabla(\mathbf{u})^T) - \frac{2}{3} \nabla \mathbf{u} I \right] \tag{2.17}$$

where μ is the fluid dynamic viscosity, I is the unit tensor and the second term on the right hand side accounts for the effect of volume dilation.

The conservation of energy is defined as

$$\frac{\partial \rho (e + \frac{1}{2}u^2)}{\partial t} + \nabla(\rho \mathbf{u}(e + \frac{1}{2}u^2)) = -\nabla(p\mathbf{u}) + \nabla(\overline{\tau}\mathbf{u}) + \rho \mathbf{f}\mathbf{u} - \nabla \mathbf{q} + Q_s \tag{2.18}$$

where e is the fluid's internal energy, $\mathbf{f}$ is an external force term, $\mathbf{q}$ is the heat flux term and Q_s is a heat source term.

2.2.1 Flow regimes in porous media

Not every flow through porous media is laminar. High speed flow (high Reynolds number) through porous media can occur and lead to the onset of turbulence within the pore space. This is even more likely if the interstitial fluid is a gas and if the porous medium is coarse (high porosity). Since this project is concerned with airflow through highly porous open-cell metal foams, the onset of turbulence within the pore space is very likely, given the wide range of flow velocities investigated. The Reynolds number based on the mean pore diameter, Re_p, is commonly employed to characterize flow through highly porous media and is defined as

$$\mathrm{Re}_p = \frac{\rho u_D d_p}{\mu} \tag{2.19}$$

where d_p is the mean pore diameter and u_D is the Darcian velocity, which is defined as the superficial average pore-scale velocity, $\mathbf{u}$, over a representative elementary volume V,

$$u_D = \frac{1}{V}\int_V \mathbf{u}\, dV \tag{2.20}$$

The literature has distinguished essentially four types of flow regimes in porous media (De Lemos, 2012; Pedras and de Lemos, 2001), which based on Re_p, are identified as:

1. Darcy or creeping flow regime $(\mathrm{Re}_p < 1)$;
2. Forchheimer flow regime $(1 < \mathrm{Re}_p < 150)$;
3. Post-Forchheimer flow regime (unsteady laminar flow $150 < \mathrm{Re}_p < 300$);
4. Fully turbulent flow regime $(300 < \mathrm{Re}_p)$;

One extra flow regime referred to as the *pre-Darcy regime* has been identified by Dukhan et al. (2014) at extremely low fluid velocities, but it is not relevant to the work presented here.

2.2.2 Turbulence modelling

Turbulence is characterized by chaotic, three-dimensional, rotational motion within the fluid. having a wide range of characteristic length and time scales. In theory, the time-dependent Navier-Stokes equations fully describe turbulence, but that would require an enormous amount of information, since taking into account all turbulent length and time scales would be extremely computationally expensive for any flow relevant to engineering or industrial applications (Wilcox et al., 1998). However, a turbulence model can be employed instead of trying to solve the whole range of spatial and temporal scales of the turbulence, greatly facilitating the solution to the problem.

Most turbulence models rely on what is referred to as Reynolds averaging technique. As turbulence is characterized by random fluctuations, the instantaneous Navier-Stokes equations can be decomposed into the mean (ensemble-averaged or time-averaged) and fluctuating components. This is similar to the volume-averaging technique described previously, but the quantities are averaged in time (or ensemble) rather than in space. In this way, the velocity components, using Einstein notation, are decomposed as

$$u_i = \overline{u}_i + u_i' \tag{2.21}$$

where $\overline{u}_i$ and u_i^i are the mean and fluctuating velocity components respectively. Likewise, this decomposition can be applied to other scalar quantities

$$\varphi = \overline{\varphi} + \varphi^i \tag{2.22}$$

where φ denotes any scalar such as pressure, energy or species concentration.

Applying this approach to the instantaneous mass and momentum equations and time-averaging them (and dropping the over-bar on the mean velocity, $\overline{u}$) yields the Reynolds-averaged Navier-Stokes (RANS) equations, written in Cartesian tensor form as

$$\frac{\partial \rho}{\partial t} + \frac{\partial}{\partial x_i}(\rho u_i) = 0 \tag{2.23}$$

$$\frac{\partial}{\partial t}(\rho u_i) + \frac{\partial}{\partial x_j}(\rho u_i u_j) = -\frac{\partial p}{\partial x_i} + \frac{\partial}{\partial x_j}\left[\mu\left(\frac{\partial u_i}{\partial x_j} + \frac{\partial u_j}{\partial x_i} - \frac{2}{3}\delta_{ij}\frac{\partial u_i}{\partial x_i}\right)\right] + \frac{\partial}{\partial x_j}(-\rho\overline{u_i' u_j'}) \tag{2.24}$$

Eqs. 2.23 and 2.24 have the same general form of the instantaneous Navier-Stokes equations, with the velocities and other flow variables now representing time-averaged (or ensemble-averaged) values. Eq. 2.24 include additional terms representing the effects of turbulence. The energy equation can be time-averaged (or ensemble-averaged) in the same way.

The Reynolds stresses $-\rho\overline{u_i' u_j'}$ require additional equations to close the problem. Turbulence models arise from the modelling of such terms. A common method is based on the Boussinesq hypothesis, which states that Reynolds stresses might be proportional to mean rates of deformation (Versteeg and Malalasekera, 2007), thus

$$-\rho\overline{u_i' u_j'} = \mu_t\left(\frac{\partial u_i}{\partial x_j} + \frac{\partial u_j}{\partial x_i}\right) - \frac{2}{3}\left(\rho k + \mu_t\frac{\partial u_k}{\partial x_k}\right)\delta_{ij} \tag{2.25}$$

where μ_t is introduced as the eddy or turbulent viscosity and $k = \frac{1}{2}(\overline{u'^2} + \overline{v'^2} + \overline{w'^2})$ is the turbulent kinetic energy per unit mass. The Boussinesq hypothesis is employed in several turbulence models, including the k-ε and k-ω models, for which two additional transport equations are solved (for the turbulent kinetic energy, k, and for either the turbulent dissipation rate, ε, or specific dissipation rate, ω). It should ne noted however, that the Boussinesq hypothesis implies an isotropic assumption for the normal Reynolds stresses, which is not strictly true. Nevertheless, this assumption typically works well for many types of flows.

In the present work, variants of the k-ε and k-ω models are employed as well as the Reynolds Stress Model (RSM), which solves transport equations for each of the terms in the Reynolds stress tensor, thus abandoning the isotropic eddy viscosity assumption. The full formulation of the turbulence models employed here are beyond the scope of the present thesis. However, for

the sake of completeness, a brief description of the standard k-ε model, standard k-ω model and RSM are provided in the following sections.

2.2.2.1 The standard k-ε model

The standard k-ε model is based on the work of Launder and Spalding (1974), introducing two transport equations, one for k and other for ε. The derivation of these transport equations are based on the best understanding of the relevant physical processes affecting these variables with a certain degree of empiricism. The derivation of the k-ε model assumed the flow to be fully turbulent and the effects of molecular viscosity to be negligible. Therefore, k is computed from the following transport equation

$$\frac{\partial}{\partial t}(\rho k)+\frac{\partial}{\partial x_i}(\rho k u_i)=\frac{\partial}{\partial x_j}+\left[\left(\mu+\frac{\mu_t}{\sigma_k}\right)\frac{\partial k}{\partial x_j}\right]+G_k+G_b-\rho\varepsilon-Y_M+S_k \tag{2.26}$$

where σ_k is the turbulent Prandtl number for k, G_k accounts for the generation of turbulence kinetic energy due to the mean velocity gradients, G_b represents the generation of turbulence kinetic energy due to buoyancy, Y_M is the contribution of the fluctuating dilatation in compressible turbulence to the overall dissipation rate and S_k is a source term. Details on the modelling of these extra terms can be found in (Versteeg and Malalasekera, 2007). The turbulent dissipation rate, ε is calculated from the following transport equation

$$\frac{\partial}{\partial t}(\rho\varepsilon)+\frac{\partial}{\partial x_i}(\rho\varepsilon u_i)=\frac{\partial}{\partial x_j}+\left[\left(\mu+\frac{\mu_t}{\sigma_\varepsilon}\right)\frac{\partial\varepsilon}{\partial x_j}\right]+C_{1\varepsilon}\frac{\varepsilon}{k}(G_k+C_{3\varepsilon}G_b)-C_{2\varepsilon}\rho\frac{\varepsilon^2}{k}+S_\varepsilon \tag{2.27}$$

where σ_ε is the turbulent Prandtl number for ε and S_ε is a source term. The constants $C_{1\varepsilon}$, $C_{2\varepsilon}$ and $C_{3\varepsilon}$ along with σ_k and σ_ε are determined from experiments for fundamental turbulent flows. The eddy viscosity can be computed from k and ε as

$$\mu_t=\rho C_\mu\frac{k^2}{\varepsilon} \tag{2.28}$$

where C_μ is a constant determined empirically. Variants of the standard k-ε model include the Re-Normalisation Group (RNG) k-ε model by Yakhot et al. (1992), and the Realizable k-ε model by Shih et al. (1994). Both variants have included refinements over the standard k-ε model, showing substantial improvements where the flow features include strong streamline curvature, vortices and rotation.

2.2.2.2 The standard k-ω model

The standard k-ω model by Wilcox et al. (1998) is a two-equation model that introduces transport equations for the turbulent kinetic energy, k, and the specific dissipation, ω, which can be thought of the ration of ε to k. Compared to the k-ε model, the k-ω formulation provides a better treatment in regions of low turbulence such as wall boundary layers, when both k and ε tend to zero. However, one of the weak points of the k-ω model is the sensitivity of solution values outside the shear layer (free-stream). The transport equation for turbulent kinetic energy, k, is written as

$$\frac{\partial}{\partial t}(\rho k) + \frac{\partial}{\partial x_i}(\rho k u_i) = \frac{\partial}{\partial x_j}\left(\Gamma_k \frac{\partial k}{\partial x_j}\right) + G_k - Y_k + S_k \tag{2.29}$$

where the newly introduced Γ_k represents the effective diffusivity of k, G_k is the generation of turbulence kinetic energy due to mean velocity gradients, Y_k accounts for the dissipation of k due to turbulence and S_k is a source term. The transport equation for the specific dissipation, ω is given as

$$\frac{\partial}{\partial t}(\rho \omega) + \frac{\partial}{\partial x_i}(\rho \omega u_i) = \frac{\partial}{\partial x_j}\left(\Gamma_\omega \frac{\partial \omega}{\partial x_j}\right) + G_\omega - Y_\omega + S_\omega \tag{2.30}$$

where Γ_ω represents the effective diffusivity of ω, G_ω is the generation of ω, Y_ω accounts for the dissipation of ω due to turbulence and S_ω is a source term. The terms Γ_k and Γ_ω are calculated as

$$\Gamma_k = \mu + \frac{\mu_t}{\sigma_k} \tag{2.31}$$

$$\Gamma_\omega = \mu + \frac{\mu_t}{\sigma_\omega} \tag{2.32}$$

where σ_k and σ_ω are the turbulent Prandtl numbers for k and ω, respectively. The eddy viscosity is then computed as

$$\mu_t = \rho \frac{k}{\omega} \tag{2.33}$$

Details on the derivation of the other terms can be found in (Wilcox et al., 1998). Variants of the standard k-ω model include the baseline (BSL) and shear stress transport (SST) k-ω models by Menter (1994), both of which blend the robust k-ω formulation for flow near the wall region with the k-ε formulation for the far field flow.

2.2.2.3 The Reynolds Stress model

The RSM closes the RANS equations by solving additional transport equations for each of the Reynolds stresses, along with an equation for the turbulent dissipation rate. Thus, for 3-D cases, seven additional transport equations are solved. However, the RSM is more elaborate than two-equation models such as the k-ε, and is not limited by the assumption of isotropic turbulence and can account for the effects of streamline curvature, swirl and rapid changes in strain rate in a more rigorous manner. The RSM transport equations can be derived by taking moments of the exact momentum equation, however, several terms in the equations still require modelling assumptions to close the problem. The exact RSM transport equations can be written as

$$\overbrace{\frac{\partial}{\partial t}(\rho\overline{u_i'u_j'})}^{\text{Local time derivative}} + \overbrace{\frac{\partial}{\partial x_k}(\rho u_k\overline{u_i'u_j'})}^{C_{ij}\equiv\text{Convection}} = -\overbrace{\frac{\partial}{\partial x_k}\left[\rho\overline{u_i'u_j'u_k'} + \overline{p'\left(\delta_{kj}u_i' + \delta_{ik}u_j'\right)}\right]}^{D_{T,ij}\equiv\text{Turbulent diffusion}}$$
$$+\overbrace{\frac{\partial}{\partial x_k}\left[\mu\frac{\partial}{\partial x_k}\left(\overline{u_i'u_j'}\right)\right]}^{D_{I,ij}\equiv\text{Molecular diffusion}} - \overbrace{\rho\left(\overline{u_i'u_j'}\frac{\partial u_j}{\partial x_k} + \overline{u_j'u_k'}\frac{\partial u_i}{\partial x_k}\right)}^{P_{ij}\equiv\text{Stress production}}$$
$$-\overbrace{\rho\beta\left(g_i\overline{u_j'\theta} + g_j\overline{u_i'\theta}\right)}^{G_{ij}\equiv\text{Buoyancy production}} + \overbrace{\overline{p'\left(\frac{\partial u_i'}{\partial x_j} + \frac{\partial u_j'}{\partial x_i}\right)}}^{\Phi_{ij}\equiv\text{Pressure Strain}} - \overbrace{2\mu\overline{\frac{\partial u_i'}{\partial x_k}\frac{\partial u_j'}{\partial x_k}}}^{\varepsilon_{ij}\equiv\text{Dissipation}}$$
$$-\overbrace{-2\rho\Omega_k\left(\overline{u_j'u_m'}\varepsilon_{ikm} + \overline{u_i'u_m'}\varepsilon_{jkm}\right)}^{F_{ij}\equiv\text{Production by system rotation}} + \overbrace{S_{RSM}}^{\text{Source term}} \tag{2.34}$$

The terms C_{ij}, $D_{I,ij}$, P_{ij} and F_{ij} do not require any additional modelling, however $D_{T,ij}$, G_{ij}, Φ_{ij} and ε_{ij} still need to be modelled in order to close the equations. The description of the additional modelling assumptions required to close the equation set is beyond the scope here, but can be found in (Speziale, 1990). The eddy viscosity is computed in the same manner as for the k-ε model, using Eq. 2.28.

2.2.2.4 Near-wall treatment

The no-slip condition associated with solid boundaries greatly affects the turbulent flow in the region next to them. Very close to a solid boundary, the flow is dominated by viscous effects, not depending on free-stream parameters, resulting in a thin layer with a linear velocity profile, commonly known as *viscous sub-layer*. A *buffer region* is present right above the viscous sub-layer, for which the viscous and turbulent (inertial) effects are of similar magnitude. The layer right above the buffer region is dominated by the turbulent stresses and is commonly known as the *log-law layer* (Versteeg and Malalasekera, 2007). The extent of each of these layers is defined in terms of a dimensionless distance to the wall, y^+, given by

$$y^+ = \frac{u_* y}{\nu} \tag{2.35}$$

where u_* is the frictional velocity, y is the distance to the wall and ν is the kinematic viscosity of

the fluid. The viscous sub-layer is in practice very thin $(y^+ < 5)$, and the log-law layer normally is valid for $(30 < y^+ < 500)$, with the upper limit dependent on the Reynolds number. The buffer region lies between these two regions $(5 < y^+ < 30)$.

Correct modelling of the near-wall flow can significantly impact the overall flow solution. The straightforward approach would be to have a sufficiently fine numerical grid able to fully resolve the phenomena in the boundary layer. However, in many cases this level of grid refinement would impose very high computational costs, rendering the problem not feasible.

Another approach consists in not resolving the viscosity-dominated inner region. Instead, semi-empirical formulas referred to as *wall functions*, are employed to account for this region and bridge the viscosity-dominated and fully turbulent regions. There exists several different wall functions available, however, the simulations carried out in the present thesis employed the use of an enhanced near wall treatment (ANSYS, 2013), which is briefly described here.

The enhanced wall treatment (EWT) is a near-wall modelling approach which formulates the law-of-the-wall as a single law valid for the entire wall region (viscous sub-layer, buffer region and logarithmic layer). This is achieved by the use of a blending function as proposed by Kader (1981), enabling a smooth transition between the linear viscous sub-layer and the logarithmic layer. The extent of each region is defined by a wall-distance-based turbulent Reynolds number, Re_k, given as

$$Re_y \equiv \frac{\rho y \sqrt{k}}{\mu} \tag{2.36}$$

where y is the wall-normal distance. Therefore, meshes with varying y^+ values can be employed with EWT. If the mesh y^+ value is within the viscous sub-layer, it will resolve the entire velocity profile next to the wall. Instead, if the mesh y^+ value is within the logarithmic layer, it will make use of standard wall functions. Finally, if the mesh y^+ value is within the buffer layer, it will use a blending function to have a smooth transition between the viscous sub-layer and logarithmic region.

In the viscous sub-layer, the one-equation model of Wolfshtein (1969) is employed to solve the turbulent quantities and a two-equation turbulence modelling approach is employed for the logarithmic layer, with a blending function enabling the transition between both. For a complete description of the EWT formulation the reader should refer to (ANSYS, 2013).

In the context of flow through porous media, the turbulence modelling approaches described above are applicable for turbulent flow within the interstitial pore space for a given porous material. Moreover, there have been attempts of employing volume-averaging techniques on the RANS equations to derive a bulk (macroscopic) turbulence model for porous media, which will be commented on the following sections.

2.3 Basic flow models for porous media

Fluid flow through porous media is associated with energy dissipation due to the interaction between the solid and fluid phase. When applied to porous media, the flow governing equations must account for the porosity of the medium. Thus, the continuity equation can be modified and written as

$$\frac{\partial(\phi\rho)}{\partial t} + \nabla(\rho u_D) = S_m \tag{2.37}$$

By using a volume-averaging technique (Whitaker, 1986), it can be shown that at very low fluid velocities, the viscous drag dominates the energy dissipation and the Navier-Stokes equation is reduced to the Darcy's law (Darcy, 1856) on a macroscopic level, given by

$$u_D = -\frac{K}{\mu}(\nabla p - \rho \mathbf{g}) \tag{2.38}$$

where the quantity K is referred to as the medium permeability, and it is related to the geometry of the solid matrix only. The linear relationship between velocity and pressure gradient depicted in Eq. (2.38) becomes no longer valid at higher flow velocities. Dupuit (Dupuit, 1863) and

Forchheimer (Forchheimer, 1901) suggested the inclusion of a quadratic term to account for energy dissipation due to inertial effects at higher flow velocities, resulting in the non-linear Forchheimer equation

$$u_D = -\frac{K}{\mu}(\nabla p - \rho \mathbf{g}) - F\rho |u_D|\, u_D \tag{2.39}$$

where F is the Forchheimer coefficient, which is believed to be fixed for a given class of porous media (Dukhan et al., 2014). The derivation of F is cumbersome and it is usually obtained from best-fit to experimental data. Another modification of Eq. 2.38 is given by Brinkman (1949), adding a diffusion term to account for the effects of confining walls

$$u_D = -\frac{K}{\mu}(\nabla p - \rho \mathbf{g}) + K\nabla^2 u_D \tag{2.40}$$

There have been numerous attempts to derive analytical expressions for K and F as a function of the medium geometry. Ergun (1952) gives one of the most well-known analysis of this type, where expressions for K and F are obtained from the solution of a laminar flow through a bed of packed spheres,

$$K = \frac{d^2\phi^3}{a(1-\phi)^2} \tag{2.41}$$

$$F = \frac{b(1-\phi)}{\phi^3 d} \tag{2.42}$$

where d is the particle diameter in a packed bed and a and b are parameters that depend on the medium morphology. Usual values of a and b for laminar flow through packed beds with a porosity range between 0.35 to 0.5 are 150 and 1.75 respectively.

2.3.1 Pressure drop relationships

The pressure drop is one of the mostly easily measurable parameters in applications involving flow through porous media. Since in most cases, the pressure drop can be assumed to be unidirectional, it makes sense to rewrite the flow model equations aforementioned in terms of pressure drop. Assuming unidirectional pressure gradient for Eq. 2.38 gives,

$$\frac{\Delta p}{L} = -\frac{\mu}{K} u_D \tag{2.43}$$

where L is the foam sample streamwise length. Applying the same assumption to Eq. 2.39 gives

$$\frac{\Delta p}{L} = -\frac{\mu}{K} u_D - F \rho {u_D}^2 \tag{2.44}$$

Eq. 2.44 can be written in its non-dimensional form as

$$\frac{\Delta p d_p^2}{L \mu u_D} = \Pi_{pg} = -\frac{d_p^2}{K} - F d_p \mathrm{Re}_p \tag{2.45}$$

where Π_{pg} is the dimensionless pressure gradient.

According to Dukhan and Ali (2012a), when gas is forced to flow through metal foam at high flow speeds the pressure-drop across the foam can become large enough to induce compressibility effects leading to a gas density change. In those cases, the pressure drop should be computed using the following correction

$$\Delta p = \frac{p_{\mathrm{in}}^2 - p_{\mathrm{out}}^2}{2 p_{\mathrm{ref}}} \tag{2.46}$$

where p_{in} and p_{out} are the absolute pressure values at the sample inlet and outlet respectively. p_{ref} is the reference pressure at which the fluid properties are calculated (usually p_{in} or p_{out}). Eq. 2.46 is obtained by integrating a compressible version of Darcy's law as a relationship between the mass flow rate and pressure drop, assuming the fluid as an ideal gas (Bear, 2013).

2.3.2 Extended models for porous media and their applicability

Various studies have taken the aforementioned porous media flow models in consideration and extended their applicability. As a full review of these models is beyond the scope of the present work, only a few of them will be mentioned. Vafai and Tien (1981) used a volume-averaging approach in order to include inertial and boundary effects in their porous media flow model. The model was further extended in the work of Vafai (1984) to account for media with variable porosity. Amiri and Vafai (1994) published an analysis of dispersion effects of a non-Darcian incompressible flow through porous media. An investigation on the variants related with several volume-averaged porous media flow models was carried out by Alazmi and Vafai (2000).

All the studies mentioned so far have dealt with laminar flow, however, some authors have derived volume-averaged flow models that account for turbulence within porous media. In the study by Antohe and Lage (1997), a two-equation $k-\varepsilon$ model for incompressible flow within a fluid saturated rigid porous medium was developed starting from the space-averaged Navier-Stokes equations. The turbulent quantities are defined by time-averaging of space-averaged quantities. Results of the analysis have shown that the effect the presence of the porous matrix damps the turbulence. An alternative $k-\varepsilon$ turbulence model was developed by Nakayama and Kuwahara (1999) by spatially averaging the RANS equations. New constants were introduced by calibrating the model from 2D numerical experiments using a periodic array of squares. A two-equation turbulence model was derived by Pedras and de Lemos (2001), which showed that the order of averaging (spatial or in time) of the Navier-Stokes equations is immaterial in regard to the final expression obtained. Finally, Teruel et al. (2009) derived a $k-\varepsilon$ turbulence model validated by means of pore-scale simulations using a staggered arrangement of square cylinders.

The applicability of these volume-averaged flow models depend strongly on the flow regime for which they have been developed, and on the morphology of the porous medium for which they were calibrated. As a general remark, these models are suitable for traditional types of porous media (e.g., packed bed of spheres, granular media). Open-cell metal foams have signif-

icant morphological discrepancies when compared to traditional porous media. Firstly, the very high porosity (often over 80 %) normally associated with open-cell metal foams tends to allow for much higher fluid velocities compared to traditional media, which might cause the onset of turbulence within the pore space. Secondly, the peculiar web-like solid structure greatly affects the local flow field by forming and destroying boundary layers (Dukhan et al., 2014). Even the volume-averaged turbulence models aforementioned were calibrated for idealized porous media (e.g array of squares or cylinders), therefore limiting their application to flows within open-cell metal foams.

2.3.3 Pore-scale flow modelling

Pore-scale modelling constitutes a different branch of porous media flow modelling. A representative elementary volume that captures the intricate details of the porous medium is defined and the pore geometry is explicitly considered and resolved. The level of detail needed for accurately describing the porous geometry is one the main constraints of pore-scale approaches due to the associated high computational cost. In the last decade, the feasibility of such approaches has been greatly improved due to the sustained improvement in computational power. Pore-scale flow modelling can be divided in basically two distinct categories: network models that use rule-based approaches and direct pore-scale simulations based on first principles.

Network models represent the pore space of a given porous material by a lattice of large pores connected by narrower throats. The flow phenomena is then represented by incorporating adequate physics on top of the pore network structure. Fatt et al. (1956) were the first to introduce such a method, and since then there has been a continued development of such network models to incorporate a varied of processes in porous media. A thorough review of such models is outside the scope of the present study, however the for a detailed review regarding network models the reader is referred to Blunt (2001); Blunt et al. (2002); Mukherjee et al. (2011). While pore network models have been primarily developed to deal with low-porosity

and low-permeability geological porous media, more recently this approach has been applied to high-porosity fibrous media (Thompson, 2002; Gostick, 2013). In addition to that, imaging techniques such as magnetic resonance imaging (MRI) and computer-tomography (CT) scans have been used to extract realistic networks from the actual pore geometry (Bakke et al., 1997; Øren and Bakke, 2003; Al-Raoush and Willson, 2005; Al-Kharusi and Blunt, 2007; Blunt et al., 2013). Figure 2.3 illustrates three different pore networks generated from 3-D images taken of actual porous rocks. Nevertheless, pore network models still rely on a simplified representation of the actual porous geometry, which can be problematic when the physics of the process being investigated strongly depends on the morphology of the medium, e.g. impact of dispersed droplets.

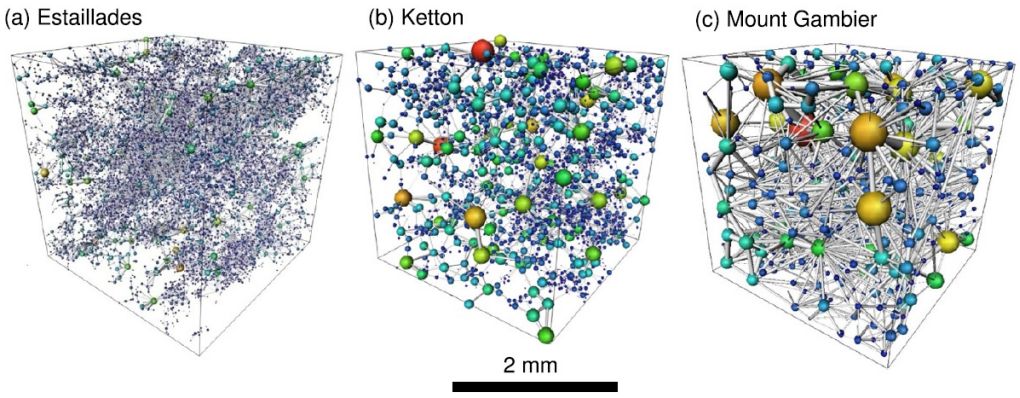

Figure 2.3: Pore networks extracted from the images of real geological porous rocks: (a) Estaillades; (b) Ketton; (c) Mount Gambier. The lattice of wide pores (shown as spheres) represent the pore space which are connected by narrower throats (shown as cylinders) (Blunt et al., 2013).

Direct pore-scale simulations normally resolve the underlying transport processes by numerically solving the governing flow equations. Thus, the problem of fluid flow can be approached by the use of methods more firmly based on first principles. Theoretically, the flow of a Newtonian fluid in the pore space of a porous medium can be accurately described by the continuity and Navier-Stokes equations using the appropriate boundary conditions. Additionally, if the flow within the pore space becomes turbulent, there are several turbulence models available

that can be employed. Although much more computationally expensive than the pore network models, direct pore-scale have attracted a growing interest from the scientific community in the last decade. Quite often researchers have been drawn to the use of particle-based numerical models such as such as molecular dynamics (MD), dissipative particle dynamics (DPD), Monte Carlo (MC) method, smoothed particle hydrodynamics (SPH) and the Lattice Boltzman method (LBM) due to their inherent ability of handling complex geometries (Pomeau and Frisch, 1986; Koplik et al., 1988; Hoogerbrugge and Koelman, 1992; Malevanets and Kapral, 1999; Liu and Liu, 2010; Boek and Venturoli, 2010). Figure 2.4 shows a simulation of fluid-fluid displacement carried out using an X-ray image of a Benthheimer sandstone using LBM. Multiphase simulations at the pore-scale are much more challenging than single-phase flow simulations due to the difficulty to track the complex dynamics of fluid-fluid interfaces, the presence of large density, viscosity and/or compressibility ratios and the complexity of fluid-fluid-solid contact lines behaviour. Thus, most direct pore-scale studies have mainly dealt with idealized cases (Meakin and Tartakovsky, 2009; Raeini et al., 2012).

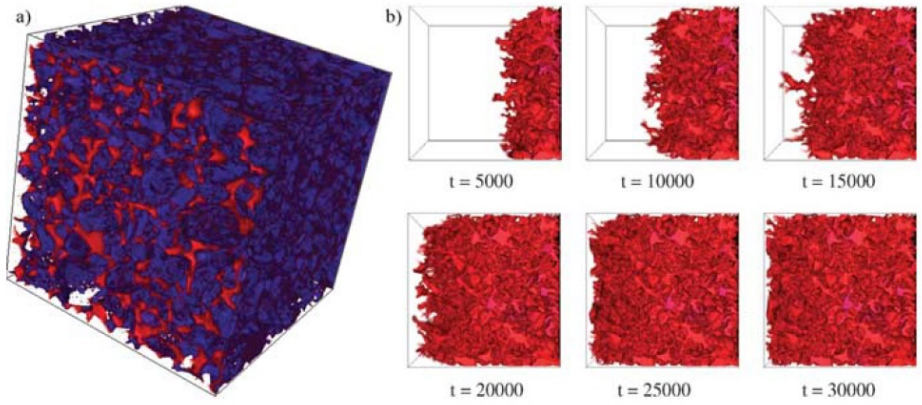

Figure 2.4: Lattice Boltzmann simulation of fluid-fluid displacement in a Bentheimer sandstone: (a) visualization of the X-ray tomography image with the mineral phase in blue and the pore space in red; (b) six stages in a lattice Boltzmann simulation of gravity-driven fluid-fluid displacement in the pore space with only the displacing fluid shown in red (Harting et al., 2005).

The focus of the present work is in using traditional grid-based methods due to their supe-

rior numerical efficiency and their longer heritage in engineering. With respect to the current application of airflow with oil in the form of dispersed droplets, due to the small oil volume fraction normally present in aero-engine separators ($< 1\%$), it may make more sense to track the oil droplets by using a Lagrangian approach. In that way, the oil droplets are represented as points within the computational domain, and their interaction with the surrounding airflow takes place via momentum exchange terms in the governing equations. This overcomes many of the problems commonly associated with multi-phase modelling in porous media. Therefore, with a given set of suitable boundary conditions, the governing flow equations can be discretized on a computational grid using standard CFD approaches such as finite difference, finite element or finite volume methods.

2.4 Foams

According to Banhart (2001), a *foam* is defined as an uniform dispersion of a gaseous phase in either a liquid or a solid, without completely dissolving the gas. The gas phase is generally arranged in cells, which are separated from each other by portions of liquid or solid. Foams have a well-defined morphology that results from the minimization of the liquid surface energy. Solid foams can be obtained by letting the liquid phase solidify, which is normally the case with metallic foams. Solid foams are a subset of what is commonly referred to as *cellular solids*, which are not necessarily made from the liquid state, and can therefore have a very different morphology.

2.4.1 Foam structure

The basic constituents of a foam are cells, windows, struts and nodes. Cells are where the gas bubbles were formed. The faces shared between distinct cells are referred to as *windows*. The place where the cell walls intersect are called Plateau's borders or *struts*. Finally, the location where the Plateau borders intersect are denoted as *nodes*. The final morphology of a foam

is determined by its internal energy, i.e the internal surface area should be minimal, and the resulting arrangement of cells should be space filling. Figure 2.5 illustrates the basic foam constituents for an idealized regular cell shape.

Generally, foams can be divided into two categories, dry and wet foams, each with its own distinguished characteristics. Wet foams have a high liquid fraction, which enables the bubbles to be easily rearranged, making the entire foam behave like a liquid, easily deforming under the action of shear forces. By successive reduction of the liquid fraction, a wet foam can be transformed into a dry foam, which has long straight cell walls, and liquid fractions of typically $< 1\%$. If the liquid fraction tends to zero, the Plateau borders collapse into cell edges. The individual cells have their mobility restricted in the case of dry foams, so they are prone to suffer elastic cell deformation (Kraynik and Reinelt, 1999).

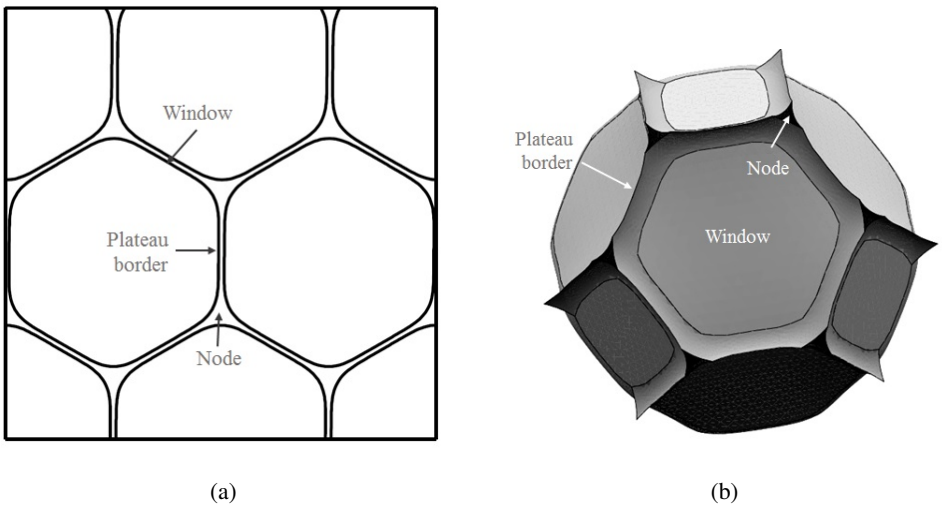

(a) (b)

Figure 2.5: Illustration of the basic constituents of a foam using an idealized cell shape. (a) Two-dimensional cut-plane and (b) 3-D representation of a single cell (Kraynik and Reinelt, 1999).

The search for the optimum cell geometric model has been a long standing problem in physics, having received many different approaches. For almost 100 years the best solution was the one given by Lord Kelvin, described in Thomson (1887). The objective was to partition a three-dimensional space into cells of equal volume with the smallest possible surface area. This

represents a minimum-surface-energy geometry, which would be thermodynamically preferred for equilibrium closed-cell foams of vanishing liquid content. Thomson (1887) postulated in that the ideal cell shape was the so-called tetrakaidecahedron (Figure 2.6a), which is a polyhedron consisting of six planar quadrilateral faces and eight non-planar hexagons of zero net curvature. This shape satisfies Plateau's conditions for a network of foam films, which states that surfaces which bound the cells meet at 120° and the intersecting lines meet at $\cos^{-1}(1/3)$, which is the tetrahedral angle.

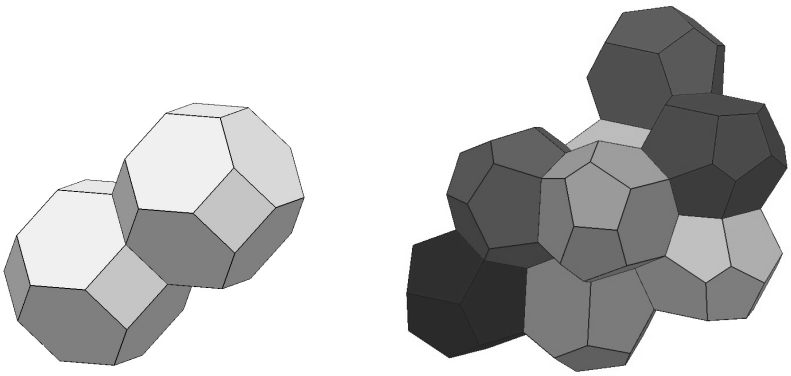

(a) (b)

Figure 2.6: (a) Two Kelvin unit cells; (b) Weaire-Phelan structure.

A counterexample to Kelvin's cell was proposed by Weaire and Phelan (1994), which reduced the surface energy of the packing cells by 0.3 % when compared to Kelvins approach while still holding Plateaus rules for a periodic cellular matrix. It is known was the Weaire-Phelan structure (Figure 2.6b), and it differs from Kelvins approach in that it uses two kinds of polyhedrons, though they both have the same volume. One is an irregular dodecahedron with pentagonal faces and the second is a tetrakaidecahedron with two hexagonal and twelve pentagonal faces. Nevertheless, the cell shape of real foams is seldom similar to those of theoretical space-filling polyhedrons, since foam forming processes generally do not end up with optimum cell structures.

2.5 Metal foams

Using metal as the base material of the foam often results in a structure with very interesting properties such as high surface area per unit volume, low density, high stiffness and good energy absorption. Metal foams can be manufactured from a wide of raw materials, e.g. aluminium, nickel, copper or Inconel alloys. Metal foams are classified as a wet foam, and depending on their manufacture process and final intended application, their structure can be further sub-categorized into two major types, namely closed or open-cell.

Both types share the same base structural unit, which is a gas-filled cell. The main difference as the name suggests, is that in the case of the closed-cell, the thin windows which separate each cell are present, and the cells are segregated from each other. Since this type of foam has a relatively high liquid volume fraction ($\sim 20\%$), it presents almost exclusively spherical-shaped cells. This particular morphology grants them a good mass to stiffness ratio, low density and good energy absorption properties. An example of a closed-cell foam is given in Figure 2.7a.

Open-cell foams on the other hand, have their inter-cellular windows removed during their manufacturing process as illustrate in Figure 2.7b, therefore presenting an interconnected porous space, with a high surface area and low density, resulting in a contiguous web-like solid matrix.

It is important to notice that there is some controversy in the naming convention employed for metal foams. Some researchers prefer to use the term *porous metals* to define such type of materials (Hargather and Thole, 2013), whereas others prefer to use the term *metal sponge* (Habisreuther et al., 2009). Nevertheless, in the current work, the metal foam terminology, with closed-cell or open-cell types is employed.

2.5.1 Production processes

There are many different ways of producing cellular solids, and a complete description of those is beyond the scope of the present work. For a detailed review on many production processes the reader should refer to Banhart (2001). However, a brief description of the manufacturing

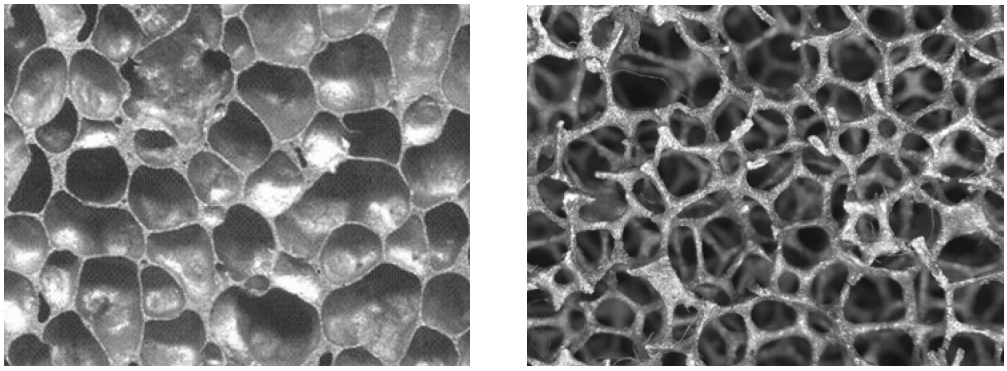

(a) (b)

Figure 2.7: Examples of (a) closed-cell and (b) open-cell metal foams (Ettrich, 2014).

process of open-cell metal foams which are relevant within the context of the present study is provided below.

2.5.1.1 Electro-deposition

Electro-deposition techniques make use of the ionic state of metals, so that the metal is electrically deposited onto a polymeric preform, which is later removed, therefore the actual foaming does not occur in the metallic state. The preform is normally a polymeric open-cell foam which is electro-plated into a electrically conductive slurry. After the metal is deposited, the polymeric preform is removed by using a thermal treatment and the resulting metallic foam has hollow struts. The process is illustrated in Figure 2.8. The preferred metals used in this technique are nickel or nickel-chromium. Retimet (Dunlop, GB) and Recemat (SEAC, The Netherlands) are two examples of commercial foams that make use of this technique. A wide range of grades (pore size) is offered and the porosity is often independent of the pore size.

2.5.1.2 Vapour-deposition

Vapour-deposition technique makes use of a solid preform, similarly to the electro-deposition methods, and a gaseous metal or metallic compounds. The solid preform can be a polymeric open-cell foam or a lattice-block polymer. A vacuum chamber can be used to generated metal

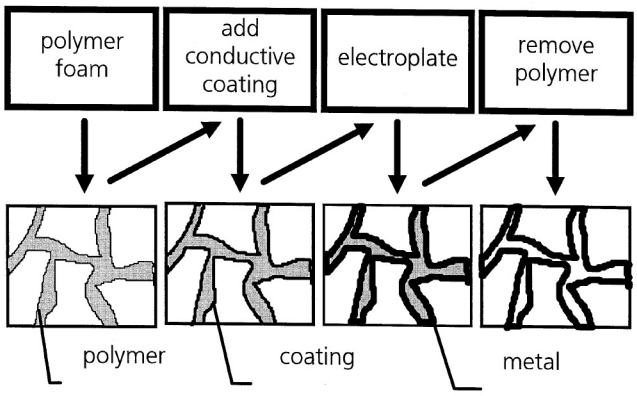

Figure 2.8: Illustration of the electro-deposition manufacturing process (Banhart, 2001).

vapour, which is later condensed onto the solid preform, forming a coating film of a certain thickness. Nickel carbonyl gas can be used to coat the polymeric preform with nickel at relatively low temperatures. After the preform is fully coated, the polymer can be removed by thermal or chemical treatment. The resulting metal foam is very similar to the ones obtained via electro-deposition, and also present hollow struts. Commercial nickel foams manufactured using vapour-deposition are available under the name Incofoam (Canada).

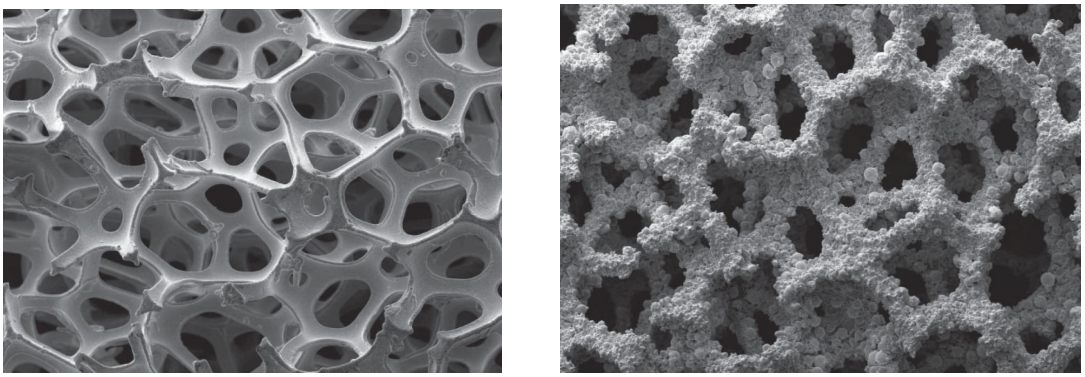

(a) (b)

Figure 2.9: SEM images of (a) nickel foam produced by vapour-deposition; (b) transformed alloyed foam (Walther et al., 2008).

The foam resulting from this process have been transformed into alloyed foams, as described in the work by Walther et al. (2008). The transformation process starts with the coating of a nickel foam with a binder followed by a specified metal powder using a spraying technique.

A heat treatment is applied subsequently, which ensures a homogeneous distribution of the metal alloy onto the foam surface. Figure 2.9 shows a comparison between scanning electron microscope (SEM) images of an original nickel foam produced by vapour-deposition and the transformed alloyed foam. The higher surface roughness resulting from the alloy transformation process offers a number of advantages for certain applications, e.g. higher surface area and good adhesion of catalytic coatings. Commercial alloyed foams have been manufactured by Alantum (Korea).

2.5.2 Applications

Metal foams can be used in a vast number of distinct applications, and the suitability of a given metal foam for any particular application will depend essentially on the foam morphology, base material and the production process. Figure shows a schematic of common applications of metal foams according to their porosity. Typically, closed-cell foams are used in structural applications, since their morphology does not allow for a fluid to pass through. Common applications are as energy absorbers, light-weight construction materials, noise control, and load-bearing components to mention a few.

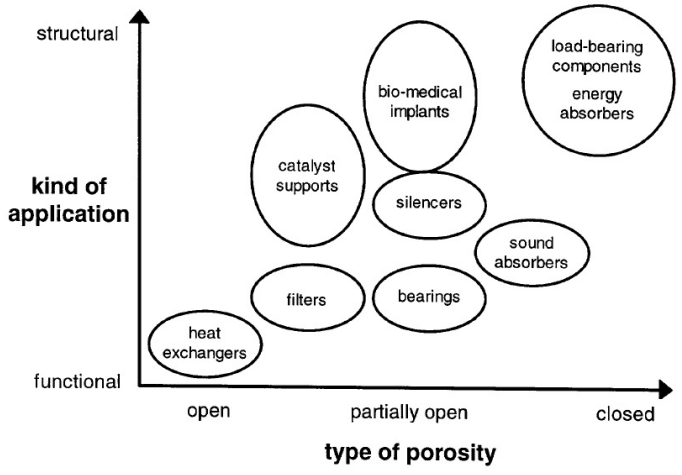

Figure 2.10: Typical applications of metal foams according to their porosity. The terms *open* and *closed* have the meaning of high and low porosity respectively (Banhart, 2001).

Open-cell foams are used in what are often referred to as functional applications (Banhart, 2001), such as heat exchangers, filters, separation devices, catalyst supports, flow distributors and biological implants. The high surface are per unit volume and low density make them especially attractive for use in heat enhancement applications, with a considerable amount of research being undertaken in this particular area (Boomsma et al., 2003). Since fluid flow through open-cell metal foams is of great interest for many applications, obtaining a reasonable understanding of their transport properties is essential but far from trivial. The foam's intricate geometry makes experimental acquisition of detailed flow data troublesome, and normally only macroscopic quantities such as pressure drop can be easily extracted, drawing many researchers to employ numerical simulations in order to overcome such limitations.

2.5.3 Previous studies concerning fluid flow

The problem of fluid flow through open-cell metal foams has often eluded the use of typical porous media modelling approaches. As argued by Boomsma et al. (2003), volume-averaging approaches are suitable for low pore-based Reynolds numbers ($\mathrm{Re}_p < 100$) and intermediate porosity values ($0.3 < \phi < 0.5$), and the morphology of the solid matrix is quite different than that of a packing of spheres or granulated media. Many researches have since then resorted to the use of pore-scale modelling approaches in order to overcome these issues. Figure 2.11 illustrates some of the geometries discussed in this section.

The accurate geometrical description of the pore-scale structure of metal foams is far from a trivial task. There are usually two approaches to this problem. The first makes use of idealized geometries which have similar characteristics to real foams, such as the Kelvin cell or Weaire-Phelan structure previously mentioned. The use of such approaches offers a relatively easy way of representing the porous geometry and have the advantage of being periodic in space. On the other hand, these idealized structures do not possess the random disorder of real foams. The second way is to use imaging techniques such as X-ray μ-CT or MRI scans of real samples. Non-

destructive imaging allied with advances made in 3-D image processing techniques have made it possible to obtain very realistic digital representations of real porous samples and directly characterize them. However, X-ray μCT and MRI scans are often very time consuming.

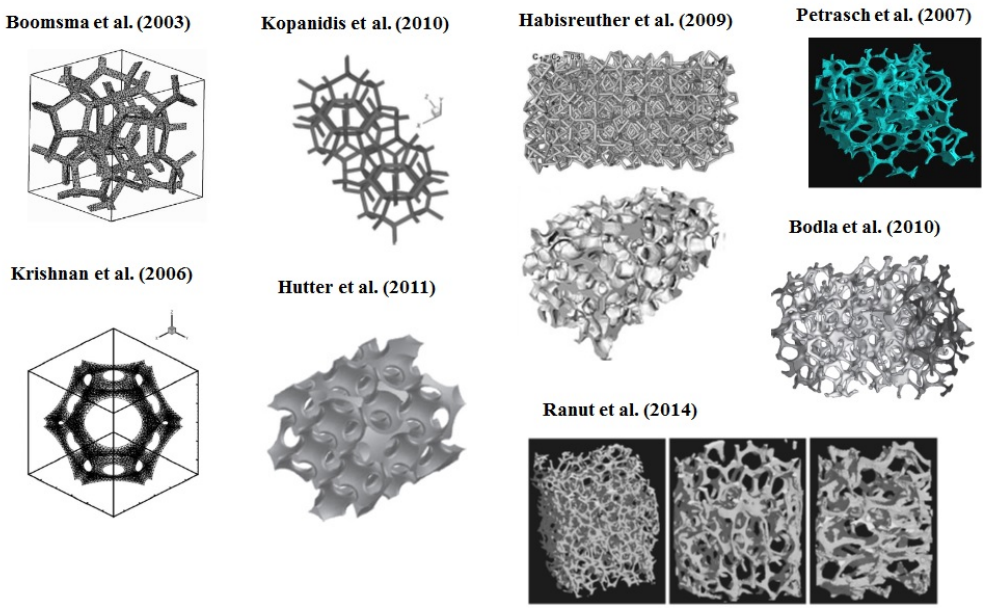

Figure 2.11: Illustration of some of the pore-scale REVs employed in various studies.

The earliest pore-scale numerical studies concerning the flow in open-cell metal foams are the ones by Du Plessis et al. (1994) and further extended by Du Plessis and Diedericks (1997). These made use of a REV consisting of a set of rectangular prisms to model the open-cell metal foam structure. An analytical flow analysis was applied to this REV yielding relatively good qualitative results. A comprehensive investigation of several transport properties of high porosity open-cell metal foams was carried out by Bhattacharya et al. (2002) by means of both analytical flow solutions and experiments. A two-dimensional array of hexagonal cells was employed as the idealized foam structure for the analytical flow calculations.The results showed that the permeability increases with both porosity and pore size, whilst the inertial coefficient seems to be a function of only the porosity.

An idealized geometry based on the Weaire-Phelan structure was employed by Boomsma et al. (2003) to investigate laminar water flow through open-cell metal foams. The computa-

tional domain consisted of a single Weaire-Phelan unit cell with periodic boundary conditions. Simulation results under predicted pressure drop by 25% when compared to experimental data, a fact that was attributed to the lack of wall effects in the simulated domain. Krishnan et al. (2006) performed a direct numerical simulation (DNS) of single phase laminar flow through an idealized periodic body-centred-cubic (BCC) structure based on the Kelvin cell. Results for permeability and heat transfers parameters were presented, showing relatively good qualitative agreement with literature data.

A simple model based on a cubic lattice of cylinders was employed by Lacroix et al. (2007) to predict the pressure drop in open-cell ceramic foams, showing good agreement with experimental measurements. Edouard et al. (2008) carried out a survey on various open-cell foam flow models and reported that standard deviations of up to 100 % can be found between theoretical values and experiments. Entrance and exit effects were observed in the pressure drop measurements performed by Baril et al. (2008). Results showed the pressure gradient to be dependent on the foam sample thickness in the direction of the flow. Smaller foams showed a higher pressure gradient, which decreased with increasing the sample size up until a critical thickness was achieved. Similar results were found by experiments realized by Dukhan and Patel (2010). Transverse size effects were reported by Dukhan and Ali (2012b), though it was argued that these have a smaller magnitude than entrance and exit effects. More recently, Dukhan et al. (2014) investigated water flow through open-cell metal foams under virtually all flow regimes (pre-Darcy to fully turbulent), where transition regions were identified from one to another.

Kopanidis et al. (2010) employed the Weaire-Phelan structure to study conjugate heat transfer in open-cell metal foams. Good agreement with literature data was reported, however the idealized geometry was compared against real foams with different porosities and pore sizes. Turbulent flow at the pore-scale was investigated by Hutter et al. (2011), where a large eddy simulation (LES) was carried out in a streamwise-periodic structure akin to a metal foam. Simulation results agreed well with experiments but proved to be very sensitive to small changes in

geometrical features of the computational model.

The use of non-destructive imagining techniques such as X-ray μCT and MRI to characterize and simulate open-cell metal foams has become increasingly popular over the last decade. A CT-based image processing technique was developed by Montminy et al. (2004), to generate accurate 3-D digital representation of real polyurethane foam samples. Additionally, measurements on the computer generated models were able to determine several morphological features such as strut length distribution, number of pore windows, cell volume distribution and pore size distribution. Maire et al. (2007) employed X-ray tomography scans to characterize several samples of cellular solids. Various morphology analysis tools were employed by Vicente et al. (2006) to investigate the transport characteristics of open-cell metal foams. Characterization of the pore space was done by the watershed transform, which can identify individual cells in the interconnected pore space.

In a series of papers, Petrasch et al. (2007, 2008a,b) developed a CT-based method to characterize and simulate reticulate ceramic foams. The porosity, surface-to-volume ratio, minimum REV size were directly computed from the CT scans using robust approaches. Morphological measurements performed directly on the tomographic datasets were validated against experimental measurements of porosity and mean pore diameter. The finite volume method was employed to solve the incompressible Navier-Stokes equations under laminar flow at the pore-scale for a ceramic foam. Simulations results were used to determine permeability, Forchheimer coefficient and the interface heat transfer coefficient. The pore-scale simulation results were used as a reference for comparison against several analytical porous media flow models. It was shown that the analytical models were mostly incapable of achieving agreement with values determined by the pore-scale simulations.

Magnico (2009) presented an analysis of hydrodynamic properties of open-cell metal foams using microcomputer tomography and used the lattice Boltzman method to solve laminar flow through the samples. Results showed that the optimum REV size to be between 2.5 to 4.5

pore diameters. Habisreuther et al. (2009) analysed pressure drop and tortuosity in open-cell foams using the finite volume method. A comparison between a stochastic structure based on the Kelvin unit cell and a MRI-generated foam sample was made. Simulations were run under laminar regime and pressure drop results were compared against experimental data from literature showing good agreement for the MRI-generated geometry. Significant modifications in the idealized structure were necessary in order achieve the same degree of agreement obtained with the MRI-generated sample. Additionally, a Lagrangian particle tracking approach was employed in order to measure the sample's tortuosity. Bodla et al. (2010) investigated several heat transfer parameters of open-cell aluminium foams using μCT data. Finite volume simulations were performed in the laminar regime but were not validated against experimental data.

CT scans were used to characterize and simulate reticulate porous ceramic foams by Haussener et al. (2010). Finite volume techniques were used for heat transfer and flow characterization. Direct numerical simulations of incompressible laminar flow were carried out by Akolkar and Petrasch (2012) on X-ray CT-generated ceramic foam samples. Results from the simulations were compared against several permeability and Forchheimer flow models from literature, all of which presented some degree of deviation. No experimental measurement of the transport properties was performed. More recently, Ranut et al. (2014) performed μCT-based finite volume simulations on open-cell aluminium foams with three different pore sizes in order to determine pressure drop and heat transfer parameters. Results showed the foams to be slightly anisotropic when the direction of the flow was varied, but no comparison against experiments was made.

2.6 Summary

The peculiar morphology of open-cell metal foams do not allow for the use of macroscopic volume-averaging porous media flow models in order to compute their transport properties. In addition to that, the nature of the flow of dispersed oil droplets within an open-cell metal foam requires geometrical input for a model to give a qualitative assessment of the oil separation

effectiveness.

There have been many pore-scale studies concerning fluid flow through open-cell metal foams. It has been shown by many studies that a correct and accurate representation of the foam geometry is essential in order to obtain good agreement between simulation and experimental measurements. The use of non-destructive imaging technique has proven to be fundamental in the development of more robust pore-scale approaches. Most studies however, are concerned with laminar flow only, whereas turbulent flow is certainly present in the conditions found within aero-engine separators. Some authors have investigated multi-phase flow through open-cell metal foams (Topin et al., 2006; Płaczek et al., 2012), however with flow configurations that are not relevant to the present work.

The present work is aimed at using a pore-scale simulation approach in order to characterize the two-phase flow within open-cell metal foam samples, under conditions relevant to aero-engine separators.

Chapter 3

Methodology

This chapter describes the methodology employed for the characterization, pore-scale geometry generation and simulation of open-cell metal foam samples. Seven distinct commercial foam samples of different base materials and pore sizes were investigated. Significant experimental input was used in the form of μCT scans, which have been employed to generate accurate digital representations of the real foam samples. An in-house Matlab code was developed and used to perform the three-dimensional volume rendering of the samples. Additional routines for calculating morphological quantities such as porosity, specific surface area, pore-size distribution and REV size directly from the tomographic datasets are described. Pressure drop measurements were performed on all samples, under a wide range of air flow velocities, and is used as validation data for the pore-scale simulations. It is important to emphasize that all the experiments (μCT scans and pressure drop measurements) were performed by a separate research group within the University of Nottingham and are only briefly explained here for clarity. For a detailed description of the experimental methods the reader should refer to (Oun and Kennedy, 2014, 2015).

3.1 Samples investigated

Seven different commercial foams were investigated: one Recemat® nickel-chromium foam with 17-23 pores per inch (PPI), three Retimet® nickel foams with 20, 45 and 80 PPI and two Alantum® Inconel 625 alloy foams with nominal pore sizes of 450 μm, 1200 μm and a hybrid sample with two layers of different pore sizes merged together, namely 580 μm and 1200 μm.

Figure 3.1 shows images obtained using a scanning electron microscope (SEM) of the Inconel 625 alloy 450 μm foam and a pure nickel foam, similar to the Recemat foam, which are manufactured via different routes. The web-like solid matrix made up of many struts surrounded by an interconnected pore space, typical of open-cell foams, is clearly seen. The electro deposition process employed in the manufacture of the pure nickel foam, generates a smooth surface. Conversely, the alloy powder spraying process used on the Inconel foams creates a very rough surface with a granular topology.

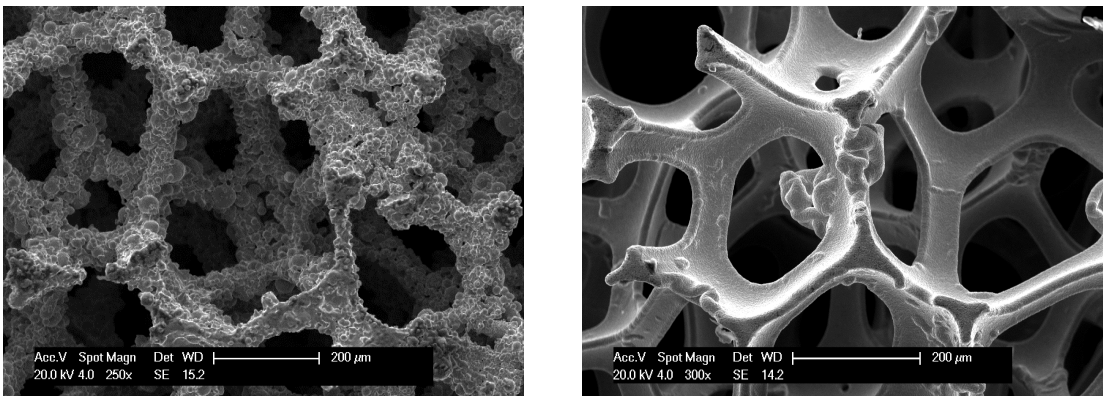

(a) (b)

Figure 3.1: SEM images of: (a) Inconel 625 alloy 450 μm foam (b) Pure nickel 450 μm foam

3.2 Experimental data acquisition

The experimental input was essential for the development of the pore-scale simulation methodology, therefore, it is reasonable to provide a simplified description of the data acquisition methods. High resolution X-ray μ-CT scanning was employed for generating realistic pore-scale representations of real metal foam samples. Electric discharge machining (EDM) was used to cut cylindrical samples from the original foam slabs, ensuring clean cuts and avoiding distortion. A Desktop cone-beam μCT 40 from SCANCO Medical was employed for scanning of the samples. The instrument presents a trade-off between the scanning resolution and size of the samples. The scan resolution, defined as h, is given in voxels, a volumetric pixel which repre-

sents the smallest detectable sub-volume in 3-D Cartesian coordinates. The cylindrical samples were placed inside a 8 mm diameter sample holder, so that the maximum isotropic digital resolution of h = 12 µm could be achieved. This helps minimize the error in exposure and ensures that the foam micro-structure is well represented. With the intent of obtaining a larger sample, a digital resolution of h = 16 µm was employed for the Recemat NC 1723 sample, which enabled the use of a 12 mm diameter sample holder.

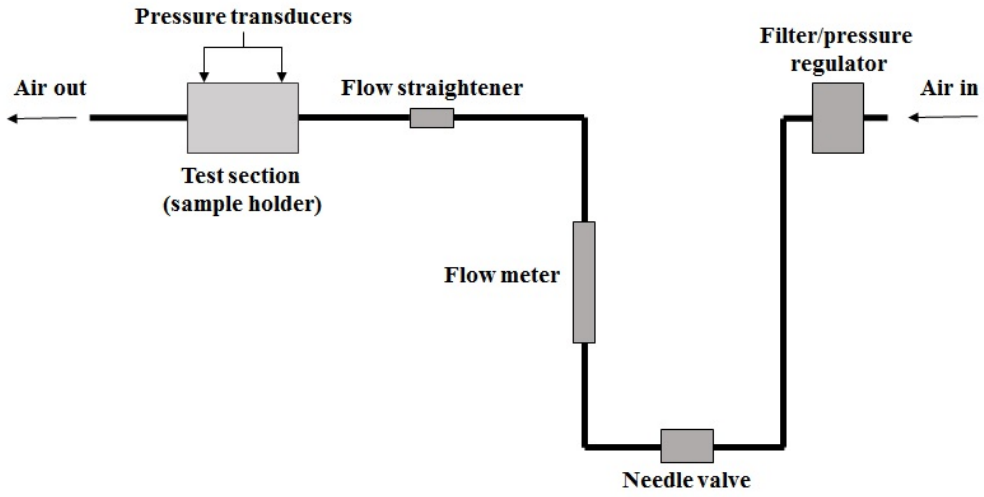

Figure 3.2: Schematic of the pressure drop experimental apparatus.

Pressure drop measurements were performed on all the samples investigated under a wide range of air flow velocities, from laminar to turbulent flow regimes. Basically, the test rig consisted of a manual control valve, pressure regulator and filter, a needle valve, a flow meter and the test section (sample holder), as illustrated in Figure 3.2. The detailed specifications of the parts are found in (Oun and Kennedy, 2014). The sample holder was designed to hold samples with a diameter of up to 25±0.2 mm (actual flow diameter of 21.183 mm), and a maximum streamwise thickness of 30 mm. The pressure transducers were positioned approximately 25 mm away from the sample. The input pressure was regulated and the air flow velocity was varied according to the desired conditions. Pressure readings were taken after a stabilization period to avoid any fluctuations and recorded using a Labview software connected to a computer. Repeatability tests showed a maximum standard deviation of 5 % in the measurements. The

cylindrical samples were cut from the foam slabs by EDM, similarly to the samples employed in the μ-CT scans. Note that the samples used for the pressure drop measurements were considerably larger than the ones scanned. Table 3.1 gives the general characteristics of the analysed samples, including the CT dataset size, scan resolution, and the streamwise length, defined as L_f, of the samples employed in the pressure drop measurements.

Table 3.1: Characteristics of the analysed samples

Sample	Dataset size (voxels)	h (μm)	L_f (mm)
Recemat NC 1723	$1024 \times 1024 \times 292$	16	10.01
Inconel 450 μm	$1024 \times 1024 \times 835$	12	10
Inconel 1200μm	$1024 \times 1024 \times 835$	12	10
Inconel 580 + 1200 μm	$1024 \times 1024 \times 547$	12	6.94
Retimet 20 PPI	$1024 \times 1024 \times 262$	12	17.53
Retimet 45 PPI	$1024 \times 1024 \times 262$	12	13.93
Retimet 80 PPI	$1024 \times 1024 \times 262$	12	13.03

3.3 Image processing

Various image processing routines were written in Matlab using some of its built-in toolboxes, along with a few community contributed functions (available in the Mathworks website) for rendering 3-D volumes, performing morphological measurements and computing the minimum geometrical representative volume (MGRV) size for each sample.

Tomographic datasets are defined as sets of grey values Ψ_{ijk} uniformly distributed in a Cartesian grid with spacing h. The scanning process generates stacks of N_z 8-bit grey-scale images of $N_x \times N_y$ pixels each, corresponding to $N_x \times N_y \times N_z$ voxels[1]. The 3-D matrix of grey values

[1] voxel as the digital volume unit

can be regarded as a smoothed representation of the pore and solid space respectively, with a smoothing kernel of size h, corresponding to the scan resolution.

The pore and solid spaces of porous media have distinct optical densities, which are associated with local X-ray absorption coefficients, reflecting different phases (solid or fluid) within the material. The process of digitally identifying these phases and partitioning them into disjoint segments is referred to as segmentation. However, it is often necessary to perform image enhancement operations before segmentation. The resulting images obtained from the CT scanning process are not sharp enough and can present significant light scattering and noise. These issues are corrected prior to segmentation by applying image intensity adjustments (to enhance contrast), unsharp masking (sharpens the edges) (Sheppard et al., 2004), and 2-D median filtering (to reduce noise). Due to the nature of the images, it has been noticed that careful selection of the image adjustment parameters is necessary, since it can greatly affect the final outcome of the volume rendering procedure. The image intensity adjustment is done by applying a gamma correction filter defined as

$$I_\gamma = 255 \times (I/255)^{\frac{1}{\gamma}} \tag{3.1}$$

where I and I_γ represent the original and adjusted intensity values respectively and γ is the correction factor.

The image enhancement is followed by segmentation. The solid-pore interface is determined by defining a grey-value threshold level, Ψ_0. All pixels in the input image with a value greater or equal than the threshold are replaced with the value 1 for the solid space and value 0 for the pore space, yielding a set of binary values $\Psi_{(\mathrm{bin})\mathrm{ijk}}$. The global grey-value threshold level Ψ_0 is determined using Otsu's method (Otsu, 1975). This process yields a continuous representation of the solid-pore interface, represented as an iso-surface, $\Psi(\mathbf{x}) = \Psi_0$. Therefore, the pore indicator function can be rewritten as

$$\chi(\mathbf{x}) := \begin{cases} 1 & \text{if } \Psi_{ijk}(\mathbf{x}) < \Psi_0 \\ 0 & \text{if } \Psi_{ijk}(\mathbf{x}) \geq \Psi_0 \end{cases} \tag{3.2}$$

and is used to convert the grey-scale matrix into a $0/1$ binary matrix.

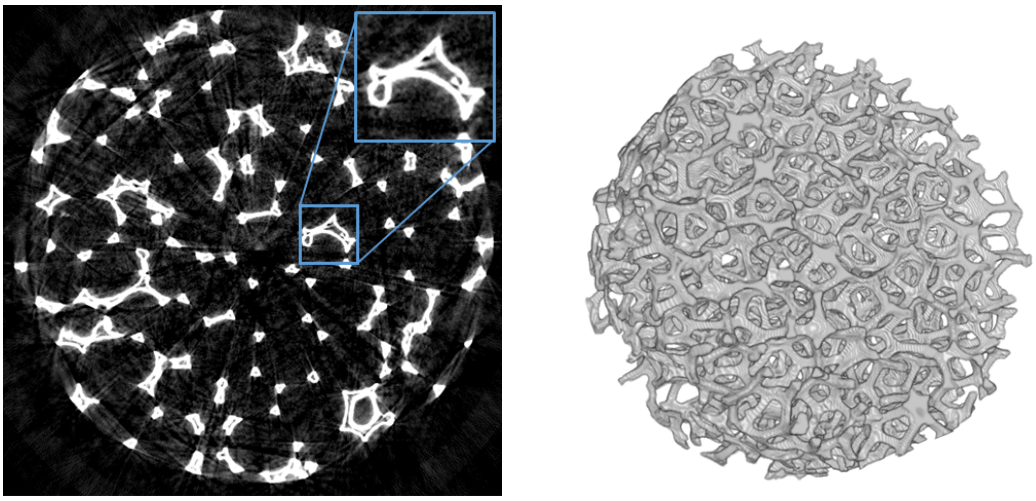

(a) (b)

Figure 3.3: (a) 2-D cross-sectional reconstruction of the Recemat foam geometry, highlighting a hollow strut; (b) 3-D rendering of the a 12 mm diameter cylindrical Recemat sample

It is common for open-cell metal foam samples to have hollow struts due to their manufacturing process, constituting a number of disjoint pore regions not relevant to fluid flow. Therefore, the largest subset of the pore space is computed by the use of a flood fill operation. A starting voxel is selected from the pore space and added to a labelled subset. All adjacent voxels in the six-neighbourhood which are within the pore space are subsequently added to the subset, and the operation is repeated until no connected voxels are left. The largest subset constitutes the main pore space. The remaining smaller disjoint pores within the struts are artificially closed by converting their voxels to 1 (solid), since they are irrelevant for the flow simulations. A second flood fill approach is applied on the solid space, ensuring that no disjoint solid regions remain. Subsequently, a 3D Gaussian smoothing operation is performed on the volume using a convolution kernel of size $\Delta_k = 5h \times 5h \times 5h$, which prevents a stair-stepped solid-pore in-

terface to be generated. Finally, the marching cubes algorithm (Lorensen and Cline, 1987), is applied to generate a triangulated representation of the solid-pore interface, which is converted to a stereo-lithography (.stl) format. A 2-D cross-sectional reconstruction of the metal foam geometry is depicted in Figure 3.3a, with the highlighted part showing a hollow strut. The final 3-D rendering of a cylindrical sample with a diameter of 12 mm is shown in Figure 3.3b. Since the CT scanning resolution and sample holder size were fixed, the sizes of the rendered tomographic datasets were proportionally (in terms of pore size) different, as shown in Figure 3.4. The Inconel samples were considerably longer in the axial direction compared to the others.

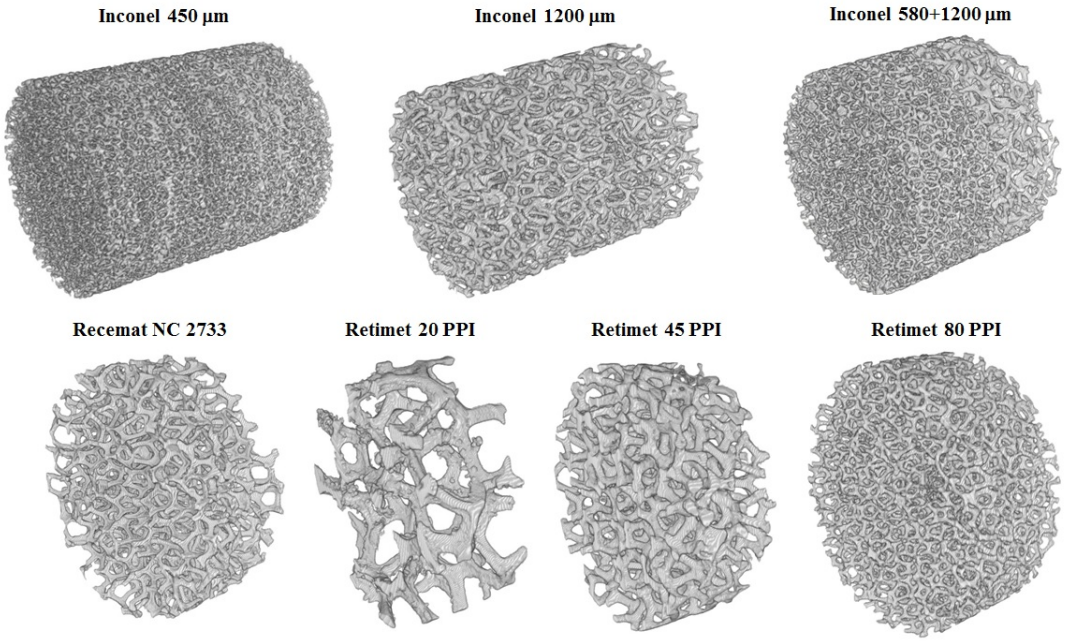

Figure 3.4: 3-D volume rendering of the tomographic dataset of all the foam samples investigated.

3.4 Morphological characterization

Transport properties of open-cell metal foams strongly depend on the local morphology of the pore and solid space. The tomographic datasets can be used for direct computation of morphological parameters such as porosity, specific surface, pore size distribution and REV size.

Additionally, the pore space can be segmented into individual cells, for further characterization of the samples. Results of all morphological parameters performed in this section are summarized in Tables 3.2, 3.3 and 3.4.

3.4.1 Porosity

The porosity ϕ is determined from the tomographic datasets by counting the number of voxels in the solid phase and dividing by the total number of voxels from the binarized datasets, namely

$$\phi = 1 - \frac{\sum_{k=1}^{N_x} \sum_{k=1}^{N_y} \sum_{k=1}^{N_z} \Psi_{(bin)ijk}}{N_x \times N_y \times N_z} \tag{3.3}$$

The results of the porosity measurements depicted in Table 3.2 show that the foam samples investigated are highly porous, with values of total porosity ranging from 0.82 to 0.89. In the work of Oun and Kennedy (2014), mercury intrusion porosimetry (MIP) was used to determine the total porosity of the Inconel 1200 μm sample, which showed a value of 0.8870, presenting a relative error of less than 1% when compared to the tomographic datasets. These results are also in line with data from Lee et al. (2010), which analysed CT scans of the Inconel 450 and 1200 μm foams and reported total porosity values of 0.8214 and 0.8770 respectively. The total porosity value of 0.8899 for the Recemat NC 1723 computed from the tomographic dataset compares well against total porosity values in the range of 0.89 - 0.90 reported by Medraj et al. (2007), where several samples of the Recemat NC 1723 were analysed. The fraction of unconnected pore space was shown to be generally quite small ($< 1\%$) for all foam samples. No porosimetry tests were performed on the other foams. However, since the structure of these foams is similar to the others and the exact same volume rendering approach was employed, it seems reasonable to assume that results reported in Table 3.2 are within the same level of accuracy as the other foam samples.

Table 3.2: Morphological measurements results for porosity and specific surface area.

Sample	ϕ_{tot}	ϕ_{eff}	s_{tot} (m^{-1})	s_{eff} (m^{-1})
Recemat NC 1723	0.8899	0.8872	2584.84	2405.01
Inconel 450 µm	0.8208	0.8199	7182.13	7144.25
Inconel 1200 µm	0.8800	0.8767	3761.84	3482.66
Inconel 580+1200 µm	0.8542	0.8522	5736.50	5531.48
Retimet 20 PPI	0.8972	0.8960	1586.43	1467.14
Retimet 45 PPI	0.8232	0.8184	3807.97	3455.22
Retimet 80 PPI	0.8593	0.8549	5467.86	5020.86

3.4.2 Specific surface

The specific surface is defined as the solid-pore interface surface area per unit volume and is determined by applying the Cauchy-Crofton theorem (do Carmo, 1976), using a Matlab routine. Results showed the specific surface to increase with decreasing pore diameter. Differently from the porosity, the foam samples analysed here showed a large range of specific surface values, as Table 3.2 shows. The discrepancy between total and effective specific surface values is especially noticed in samples with larger pore size, where the unconnected pore space inside the struts is better captured by the tomography scans.

It is important to notice that values of specific surface are highly dependent on the tomography resolution. The surface roughness associated with the Inconel foams, as depicted in Figure 3.1a, is not fully captured with the tomography resolution employed here, hence the generated tomographic datasets have considerably smoother surfaces. Experimental techniques such as the BrunauerEmmettTeller (BET) method (Brunauer et al., 1938) for example, generally can measure the surface area with a resolution in the scale of nanometres. Oun and Kennedy (2014) reported a specific surface value of 87.203×10^3 m^{-1} for the Inconel 450 µm foam using BET. In contrast, Lee et al. (2010) reported a specific surface value of 7088.8 m^{-1} for the Inconel

450 μm foam, computed from CT scans, which is relatively good agreement with the values computed here, though the CT scan resolution was not specified in their work.

Regarding the feasibility of the tomography generated domains being used for CFD simulations, Petrasch et al. (2008a) argued that while features smaller than the tomographic scan resolution (30 μm in their work) might be relevant for chemical/adsorption processes, they tend to not influence the fluid flow significantly, since these small features are usually smaller than the boundary layer thickness. However, it is important to notice that their work concerned laminar flow through ceramic samples akin to the ones investigated here. Since the boundary layer thickness generally decreases with increased Reynolds number, the statement made by (Petrasch et al., 2008a) might not hold under all flow conditions.

About half the samples investigated here have a smooth surface, so the features not captured with the current scan resolution are indeed extremely small and should not affect the fluid flow in any significant way. On the other hand, the Inconel samples have a granular rough surface, and these features are not fully captured by the tomographic scan with the current resolution. The effect of not capturing these features is not addressed here, due to the lack of data regarding the actual size of the granules, however one could in theory use a surface roughness model in order to investigate this effect.

3.4.3 Pore and strut size distribution

The pore size distribution defined by Eq. 2.6 is determined from the tomographic samples by computing the opening size distribution. *Opening* is an operation of mathematical morphology, consisting of an *erosion* followed by a *dilation* using the same structuring element (SE), thus eliminating all geometrical features smaller than the current SE. Morphological opening was carried out by sequentially inscribing spherical SEs of increasing diameter in the pore space of the tomographic datasets and counting the remaining number of (pore) voxels, until no more voxels are left. The opening size distribution is obtained by relating the number of remaining

voxels with each increase in the SE diameter. Cubical subsets of the original tomographic datasets were used for determination of the pore size distribution due to heavy computational costs associated with such operations. A detailed description of the application of this technique on consolidated porous media can be found in (Maire et al., 2007; Petrasch et al., 2008b). The mean pore diameter, d_p, is calculated as

$$d_p = \frac{\int_0^\infty d_{\mathrm{SE}} f(d_{\mathrm{SE}}) d d_{\mathrm{SE}}}{\int_0^\infty f(d_{\mathrm{SE}}) d d_{\mathrm{SE}}} \tag{3.4}$$

where d_{SE} is the SE diameter and $f(d_{\mathrm{SE}})$ is the opening size distribution. The mean pore size and the coefficient of variance (CV_p), defined as the standard deviation normalized by the mean pore size, are listed in Table 3.3.

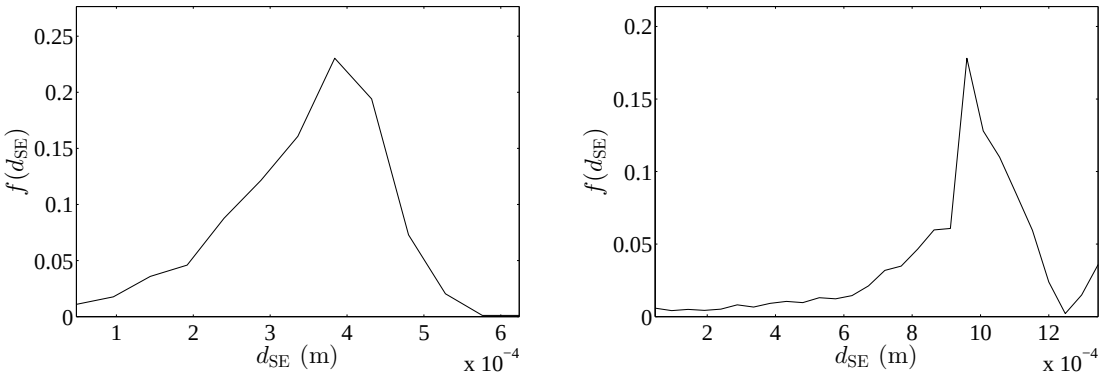

(a) (b)

Figure 3.5: Pore size distributions computed as opening size distributions for the Alantum Inconel 450 µm (a) and Inconel 1200 µm (b) respectively.

Figure 3.5 depicts the pore size distributions obtained for the Inconel 450 and 1200 µm foams, where it can be seen that the maxima of both distributions approaches the nominal pore diameter. Generally, the mean pore diameter computed by opening size distribution was lower than the nominal pore diameter of the foams. This is expected since the sub-volumes employed for the calculations included ”incomplete” pores next to the boundaries, and is an inherent limitation of this method. Pore size distributions obtained of the other foams are depicted in the

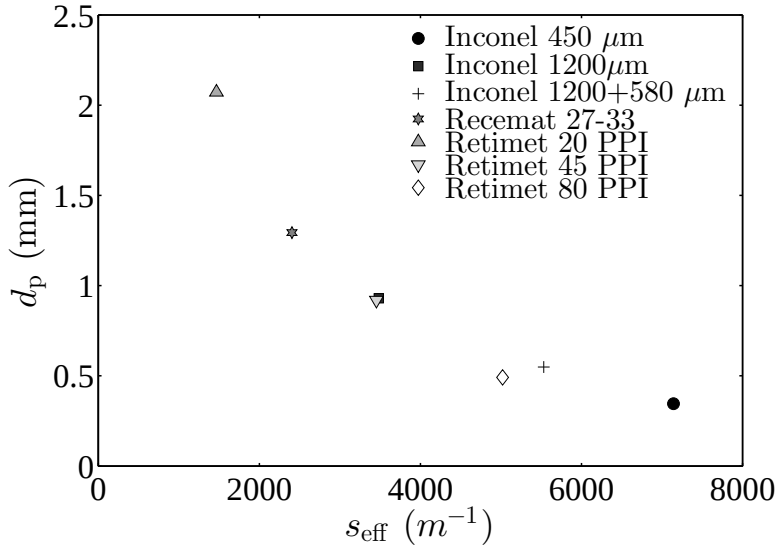

Figure 3.6: Mean pore diameter as a function of the effective specific surface for all foams.

Appendix A, Section A.1.

The mean pore size is inversely proportional to the specific surface of the foams. Figure 3.6 depicts the mean pore diameter as a function of the effective specific surface for all foam samples investigated. The pore size increases with decreasing values of specific surface and decreases with increasing specific surface area. The only foam sample that deviates from this trend is the hybrid Inconel 580+1200 µm, due to the fact that it has a slightly different morphology since it is composed of two foams with different pore sizes merged together.

The strut size distribution is computed in exactly the same way as the pore size, but instead of performing the morphological opening operations in the void space, they are performed in the solid matrix using spherical SEs of increasing diameter. It should be noted that the strut cross-section is not always cylindrical, instead it can be convex or concave triangular depending on the foam type. The mean strut size, d_s, is computed in the same way as the mean pore diameter, and represents the equivalent strut diameter. Results for d_s and its coefficient of variance (CV_s), are listed in Table 3.3. The mean strut diameter is on average, roughly five times smaller than the mean pore size. Figure 3.7 shows the strut size distributions computed for the Inconel 450 and 1200 µm foams, as a function of the opening SE diameter. The strut size distributions are

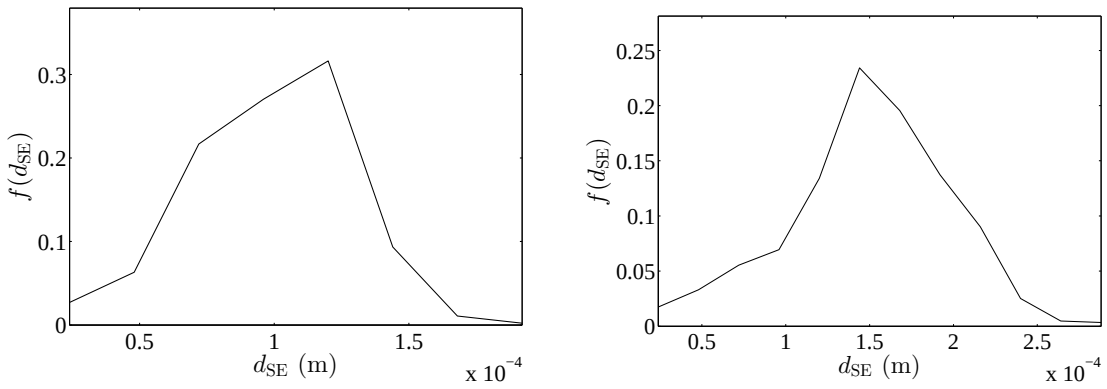

(a) (b)

Figure 3.7: Strut size distributions computed as opening size distributions for the Alantum Inconel 450 µm (a) and Inconel 1200 µm (b) respectively.

generally wider than the pore size distributions, for all samples. Results obtained for the other foams are depicted in the Appendix A, Section A.2.

3.4.4 Determination of the minimum geometrical representative volume

The REV is defined here in as the smallest sub-volume of the open-cell metal foam for which statistically meaningful local average quantities can be obtained. At this stage, the REV is defined in terms of geometric properties, however one must note that the size of REV based on transport properties may be different. Therefore, the minimum geometrical representative volume (MGRV) is defined as smallest subset of the porous medium, U, for which a morphological quantity, such as the porosity ϕ, is computed for subsequent larger subsets of U, until it asymptotically reaches a constant value within a band of $\pm\delta$. In that sense, the edge length of a cubic sub-volume of the porous medium is defined as,

$$L_{\mathrm{MGRV},\delta} = \min\{L \leq L^* | \phi - \delta < \phi(U_{L^*}) < \phi + \delta\}, \delta \ll 1 \tag{3.5}$$

where U_{L^*} is a cubic subset of U with edge length L^* (Petrasch et al., 2008b). This method is based on the work of Petrasch et al. (2007), where a large subset of the tomographic data is

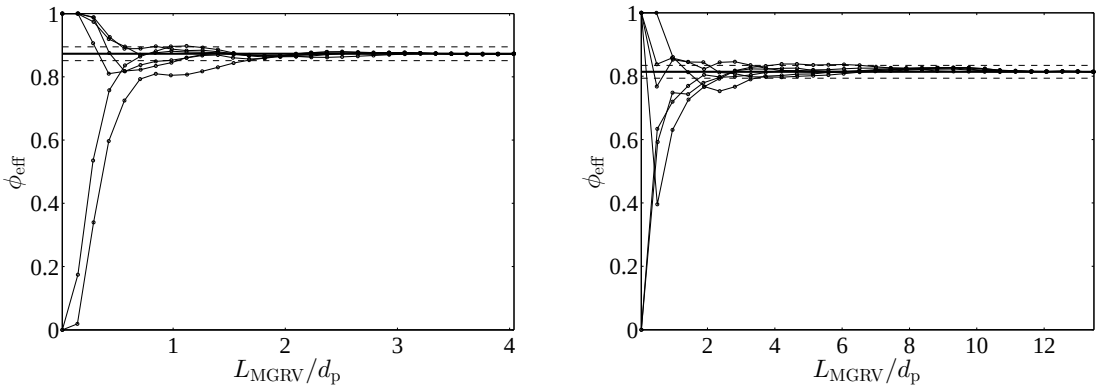

(a) (b)

Figure 3.8: Effective porosity as function of the normalized sampling cubic edge L_{MGRV}/d_p for the (a) Recemat and (b) Inconel 450 µm foams. The dashed horizontal lines denote the ± 2.5 % bands.

initially generated, and the porosity ϕ is subsequently calculated in sub-volumes of increasing size until ϕ converges around an average value ϕ_∞, satisfying the condition stated by Eq. 3.5. The MGRV defines a lower bound for the computational domain size, since a second REV calculation must still be carried out taking a transport property into account.

The effective porosity is analysed here. For the limiting case where the sub-volume cubic edge L_{MGRV} is zero, ϕ_{eff} is either 0 or 1, since the sampling sub-volume is only a point, which can be located either in the solid or fluid phase. As L_{MGRV} increases, ϕ_{eff} converges around a mean value within a band of $\pm\phi_{\text{eff}}$. Figure 3.8a shows ϕ_{eff}, as function of the sub-volume cubic edge length normalized by the mean pore size, L_{MGRV}/d_p, around six different starting locations for the Recemat sample. ϕ_{eff} converges for $L_{\text{MGRV}}/d_p \approx 2$. The same analysis is shown in Figure 3.8b for the Inconel 450 µm foam, where ϕ_{eff} converges at $L_{\text{MGRV}}/d_p \approx 4$. Results for the minimum MGRV normalized cubic edge length, L_{MGRV}/d_p, are listed in Table 3.3 for all samples. Results for other samples are shown in the Appendices, Section A.3.

Table 3.3: Morphological measurements results for the mean pore and strut diameters along with their coefficient of variance, and the minimum MGRV normalized cubic edge length.

Sample	d_p (mm)	CV_p $(\%)$	d_s (mm)	CV_s $(\%)$	L_{MGRV}/d_p
Recemat NC 1723	1.172	25.5	0.191	28.71	2.03
Inconel 450 µm	0.399	28.8	0.098	29.92	2.32
Inconel 1200 µm	1.044	25.4	0.149	32.21	1.88
Inconel 580+1200 µm	0.549	34.7	0.104	36.08	2.55
Retimet 20 PPI	2.252	28.4	0.300	31.93	1.39
Retimet 45 PPI	1.033	26.1	0.2151	33.87	1.84
Retimet 80 PPI	0.557	27.6	0.113	29.97	1.95

3.4.5 Watershed segmentation

The pore space of the foams can be segmented into individual cells by using a combination of Euclidean distance and watershed transforms (Schladitz et al., 2008). This approach allows the measurement of several cell morphological parameters such as volume, width in each direction and equivalent sphere diameter. Anisotropy in the pore space and foam structure can be investigated by using this technique.

The cell segmentation starts by applying the Euclidean distance transform on the 3-D binary datasets, $\Psi_{(\mathrm{bin})\mathrm{ijk}}$, generated during the volume rendering process using the algorithm by Maurer Jr et al. (2003). The distance transform assigns to each pore space voxel a distance to the solid struts. Subsequently, the generated distance map is inverted and smoothed. The watershed transform (Meyer, 1994), is analogous to the flooding of a topological surface where all local minima are water sources. Watershed ridge lines are erected when water from different sources meet. Hence, each *catchment basin* represents a distinct cell in the pore space. In practice, watershed transform is hampered by over-segmentation due to noise and discretization effects (Lautensack et al., 2008). The h-minima transform (Pierre, 1999), is applied to the dis-

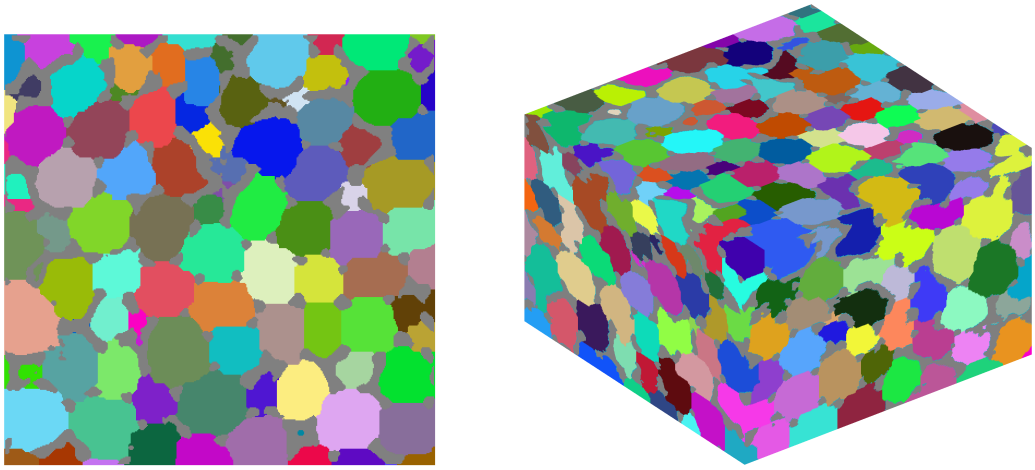

(a) (b)

Figure 3.9: (a) 2-D cut plane and (b) 3-D visualization of the segmented cells in the sub-volume for the Retimet 80 PPI foam with each colour representing a different pore cell.

tance map prior to watershed transform, removing local minima if their relative value is below a certain threshold when compared to the neighbouring values. Finally, the watershed transform is masked with the solid matrix, yielding the individual porous cells. All watershed pore segmentation calculations were performed on the largest possible rectangular sub-volumes of the original tomographic datasets.

The concept of cell in the context of foams has been described in Section 2.4.1. Figure 3.9 shows a 2-D cut plane and the 3-D visualization of the segmented cells for a sub-volume of the Retimet 80 PPI foam. Each cell consists of a convex polyhedron, and mean values for the cell volume $\bar{v}$, width in each orthogonal direction ($\bar{b}_{\text{avg}}, \bar{b}_x, \bar{b}_y, \bar{b}_z$) and equivalent sphere diameter $\bar{d}_e$, are computed. The cell volume is calculated by counting the number of voxels belonging to a given cell and multiplying by the (cubed) voxel resolution. The cell width is computed by taking the distance between the maximum and minimum voxel position in each orthogonal (X,Y,Z) direction. The average cell width, $\bar{b}_{\text{avg}}$, computes the mean value of the cell width in the three orthogonal directions. Finally, the equivalent sphere diameter is determined by calculating the cell volume and computing the diameter of an equivalent spherical volume. Since the

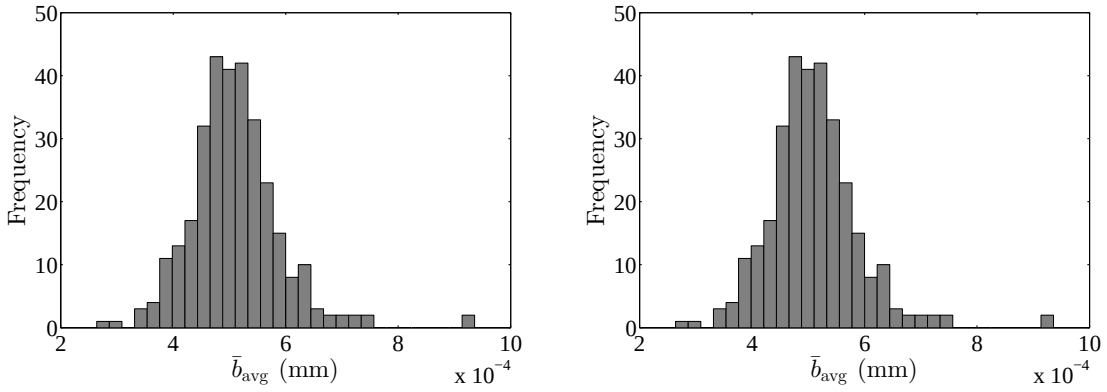

Figure 3.10: Examples of the computed cell width distributions for the (a) Inconel 450 µm and (b) Retimet 80 PPI foams.

boundaries of the rectangular sub-volumes employed for calculation have incomplete cells, with ligaments that were chopped due to sub-volume cropping, only interior cells were considered for computation of cell morphological parameters. Figure 3.10 illustrates the computed average cell width distribution for the Inconel 450 µm and Retimet 80 PPI foams. Table 3.4 shows the computed mean cell morphological parameters for all samples.

Table 3.4: Mean cell morphological parameters

Sample	$\bar{v}(mm^3)$	$\bar{b}_{\text{avg}}(mm)$	$[\bar{b}_x, \bar{b}_y, \bar{b}_z](mm)$	$\bar{d_e}$ (mm)
Recemat NC 1723	2.185	1.807	1.768, 2.024, 1.629	1.592
Inconel 450 µm	0.057	0.510	0.493, 0.511, 0.527	0.469
Inconel 1200 µm	0.588	1.183	1.183, 1.011, 1.120	0.975
Inconel 580 + 1200 µm	0.108	0.611	0.610, 0.601, 0.641	0.559
Retimet 20 PPI	4.756	2.221	2.223, 2.475, 1.934	1.950
Retimet 45 PPI	0.494	0.845	0.836, 0.891, 0.808	0.756
Retimet 80 PPI	0.161	0.729	0.734, 0.757, 0.694	0.665

It is interesting to note that measurements of cell width in each spatial direction showed some anisotropic features, with the cells being slightly elongated along one direction. This small anisotropy in the cell shape has been previously reported by other studies (Ranut et al., 2014; Vicente et al., 2006), and it shows that the cell shape is not exactly spherical, instead, it resembles an ellipsoid. The equivalent sphere diameter is systematically larger than the mean pore size computed by the opening distribution. This can be attributed to the fact that computation of d_e did not take into account cells next to the domain boundaries, which are significantly smaller than interior ones because of the sub-volume domain cropping. Nevertheless, in order to be consistent with similar studies in the literature, the mean pore size, d_p, is chosen as the main characteristic length of the pore space.

3.5 Meshing and computational domain generation

The outcome of the 3-D volume rendering process is a triangulated surface of a foam sample with triangular edge length $\Delta_e = h$, exported as a stereo-lithography file to a commercial meshing software, namely Ansys Fluent 15 (ANSYS, 2013). The complexity of the foam structures required the use of an unstructured grid generation algorithm. A tetrahedral mesh was firstly created and used as a template for creation of a polyhedral mesh. Curvature-based grid-refinement was employed, i.e., the cell mesh size was refined based on the curvature of the foam surface, where a high level of refinement was achieved due to the intricate features of the geometry. Away from the foam surface the mesh size increases at a rate of 1.3 until a pre-set maximum value, to ensure a good resolution of the flow boundary layer. Accurate computation of the boundary layer is dependent on the mesh resolution next to the foam surface. The numerical meshes were refined to the point where the first cell next to the surface is within the viscous sub-layer ($y^+ < 5$, although it is worth mentioning that Fluent considers the cell to be within the linear velocity profile until $y^+ = 11.225$). An illustration of the foam surface mesh and a 2-D cut plane of the pore space mesh are depicted in Figure 3.11.

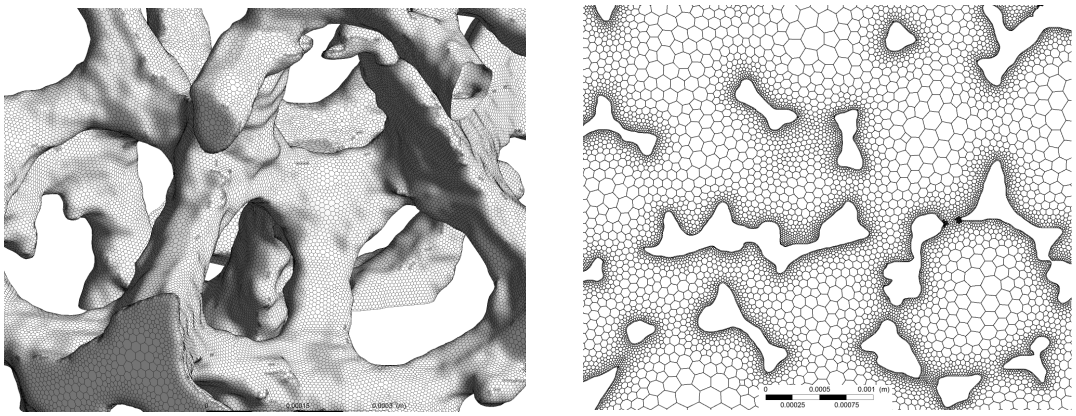

(a) (b)

Figure 3.11: View of the (a) surface polyhedral mesh and (b) sectional view of the pore space mesh. The grid size is minimum next to the foam surface and increases towards a pre-set maximum at a growth rate of 1.3

Mesh independence was investigated by performing simulations on grids of increasing levels of refinement at $\mathrm{Re}_p = 100$ (laminar flow) and $\mathrm{Re}_p = 1000$ (turbulent flow), computing the pressure drop at each level. Additionally, it is important for the computational domain to have a cross-sectional size perpendicular to the flow direction such that it does not affect the numerical solution. The minimum domain cross-sectional size orthogonal to the flow was determined through convergence studies on cubic sub-volumes of increasing size, similarly to the MGRV calculations described in Section 3.4.4. Computational samples with volumes ranging from $2d_p \times 2d_p \times 2d_p$ to $5d_p \times 5d_p \times 5d_p$ were simulated at $\mathrm{Re}_p = 100$ and $\mathrm{Re}_p = 1000$, and the pressure gradient was computed for each sub-volume. All turbulent flow calculations ($\mathrm{Re}_p = 1000$) employed the RNG k-ε turbulence model using the enhanced wall treatment.

Both grid independence and cross-sectional size studies were performed on two samples which were representative of the entire sample range, namely the Retimet 80 PPI (small pore size) and the Recemat NC 1723 (large pore size). This seems to be a sensible choice, since all samples have similar geometrical features, with the main difference being the mean pore size. The relative convergence of pressure drop (C_Δ) for the mesh independence study and pressure

gradient (C_L) of the cubic sub-volumes of increasing size are defined respectively as

$$C_\Delta = \frac{\|\Delta p_i - \Delta p_{\text{ref1}}\|}{\Delta p_{\text{ref1}}} \tag{3.6}$$

$$C_L = \frac{\|(\Delta p_i/L_i) - (\Delta p_{\text{ref2}}/L_{\text{ref2}})\|}{(\Delta p_{\text{ref2}}/L_{\text{ref2}})} \tag{3.7}$$

where the subscripts ref1 and ref2 refer to the finest grid and largest cubic domain evaluated respectively. The grid convergence plots are shown in Figure 3.12 for both the Retimet 80 PPI and Recemat samples. Grid independence is achieved when employing a mean pore size to average mesh length scale ratio (d_p/Δ_m) of approximately 40 or more. However, using this ratio on all samples would lead to prohibitively large meshes. Therefore a ratio in the range of 30 to 35 was employed for all meshes. The convergence plots showed an error of approximately 1 % or less compared to the reference solution (d_p/Δ_m = 50) when a ratio in the range of 30 to 35 was used. This level of error was considered acceptable for the current application.

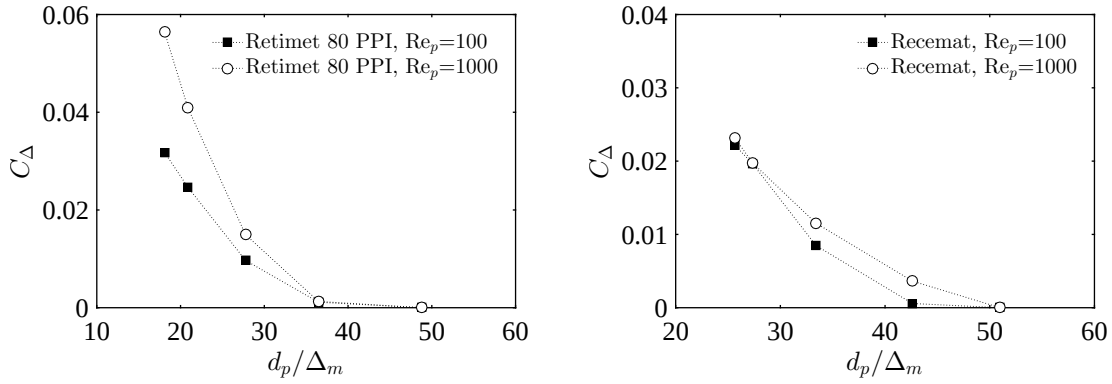

Figure 3.12: Convergence of pressure drop versus grid refinement for the (a) Retimet 80 PPI and (b) Recemat samples (Δ_m as the average mesh length).

Analysis of the minimum domain cross-sectional size showed convergence of the pressure gradient values when a volume of with a cubic edge length, L_{REV}, of $4d_p$ was used (domain size of $4d_p \times 4d_p \times 4d_p$). Convergence plots are depicted in Figure 3.13 for both the Retimet 80 PPI

and Recemat samples. Therefore, the domain used for the CFD simulations must ideally have a cross-sectional size perpendicular to the flow direction of at least $4d_p \times 4d_p$. However, this criterion could not be reached for all samples, due to the tomographic datasets limited size. This is especially significant for the Retimet 20 PPI sample, because of its large pore size relative to the tomographic sample size. Nevertheless, all other samples were built with a cross-sectional size perpendicular to the flow direction larger than $3.25d_p \times 3.25d_p$ at least.

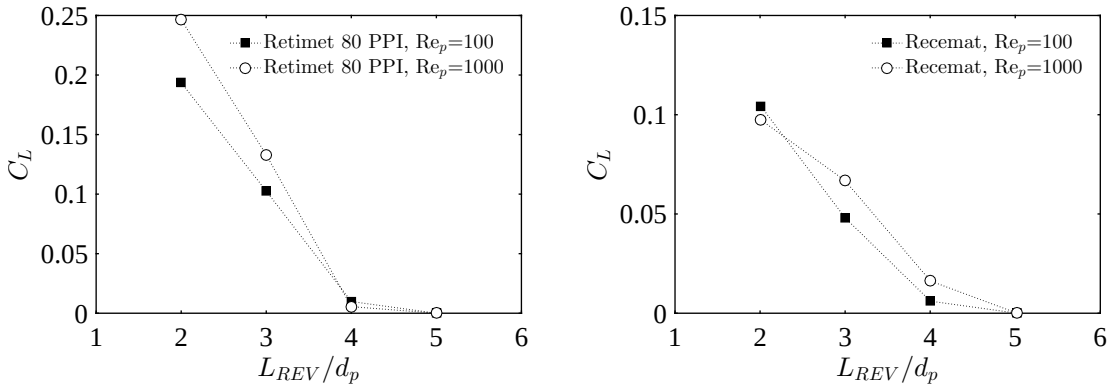

Figure 3.13: Convergence of pressure gradient versus domain size for the (a) Retimet 80 PPI and (b) Recemat samples (L_{REV} as the domain cubic edge length).

Figure 3.14 shows a plot of the average y^+ values calculated at the first cell next to the foam surface for different levels of mesh refinement, computed from a flow solution at Re$_p$=1000 for both Retimet 80 PPI and Recemat samples. Even at the smallest d_p/Δ_m ratios investigated, y^+ values are still equal or less than unity, therefore well within the viscous sub-layer. Since the y^+ scales linearly with the Reynolds number, and the maximum Re$_p$ values are not expected to exceed 7,500 in the current work, it is reasonable to assume that the first cell next to the foam surface will be always within the linear velocity profile region.

The rationale behind the computational domain configuration was that it has to be representative of the conditions present in the pressure drop measurements. For that reason, two different configurations were employed. The first one is defined as a rectangular channel consisting of

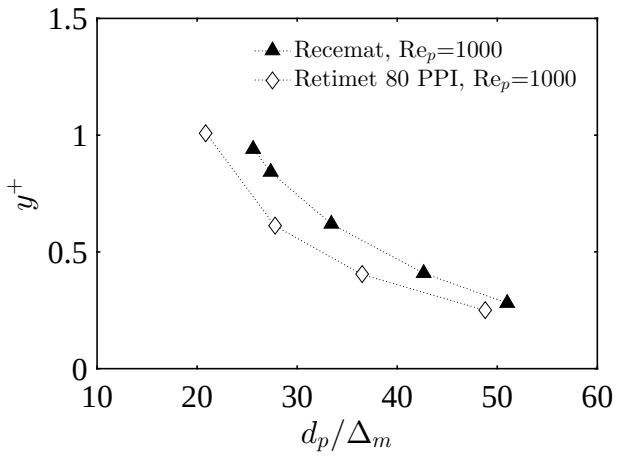

Figure 3.14: Average y^+ values at the first cell next to the foam surface for different levels of mesh refinement computed from a flow solution at Re$_p$=1000 for the Retimet 80 PPI and Recemat samples.

an undisturbed inlet and exit regions and an intermediate section containing the foam mesh. Dirichlet and Neumann boundary conditions were specified at the inlet and outlet respectively. A uniform velocity profile, u_0, was defined at the inlet and a gauge pressure, $p_0 = 0$, was defined at the outlet. The walls of the duct have free-slip conditions, and the foam surface is assumed to be perfectly smooth with a no-slip condition. This computational domain configuration is representative of the central part of the experimental samples (away from the walls).

The second configuration is defined as sector of a cylindrical channel, with walls on one of the sides, which is representative of the foam region next to the sample holder walls in the experiments. This configuration was built with the intent of investigating possible wall effects on the flow. Figure 3.15 shows a schematic of the computational domain configuration and its boundaries. The inlet and outlet region were positioned away from the foam at a distance of one foam streamwise length. Both domain configurations are depicted in Figure 3.16, showing that the main difference between both configurations if the presence of an additional no-slip wall condition in the cylindrical channel domain.

The computational domains have been built in order to resemble the conditions of the experimental measurements. The work of Dukhan and Patel (2010) has shown experimental evidence

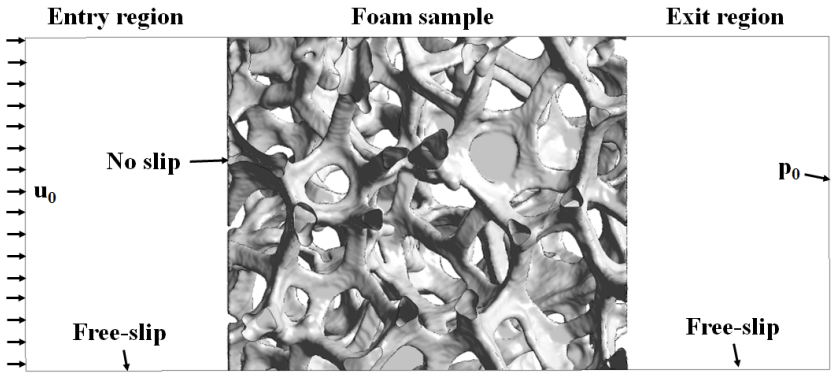

Figure 3.15: Schematic of the computational domain and its boundary conditions.

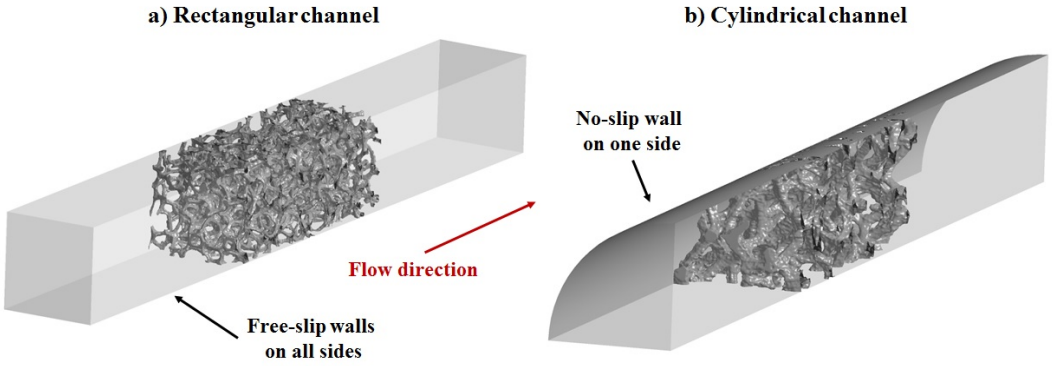

Figure 3.16: Illustration of the two different computational domain configurations showing a rectangular (a) and a cylindrical (b) channel. The main difference between both is that one of the walls of the cylindrical channel has a no-slip boundary condition.

of the presence of entrance and exit effects on pressure drop measurements of flow through open-cell metal foams. The authors have argued that the streamwise thickness of the sample might strongly affect the unit-length normalized pressure drop of the foam samples. Therefore, the streamwise thickness of the computational samples was kept as close as possible to the experimental ones. Unfortunately, the limited size of the tomographic datasets (as shown in Figure 3.4) have not made it possible to closely match the streamwise thickness of all samples. The discrepancy between the computational and experimental streamwise thickness of the samples was more pronounced for the Retimet foams, where the computational samples had a smaller thickness than the experimental ones.

Table 3.5: Dimensions and polyhedral mesh count of the computational domains

Sample	Domain size (mm)	Domain size (d_p)	Mesh count ($\times 10^6$)
Recemat NC 1723	$4.7 \times 4.7 \times 10$	$3.63 \times 3.63 \times 7.72$	7.713
Inconel 450 µm	$2 \times 2 \times 10$	$5.79 \times 5.79 \times 28.95$	9.868
Inconel 1200 µm	$3.6 \times 3.6 \times 10$	$3.87 \times 3.87 \times 10.76$	6.217
Inconel 580+1200 µm	$2.4 \times 2.4 \times 6.54$	$4.37 \times 4.37 \times 11.92$	14.235
Retimet 20 PPI	$3.1 \times 4.4 \times 8$	$1.50 \times 2.12 \times 3.86$	2.157
Retimet 45 PPI	$3 \times 3 \times 7.45$	$3.26 \times 3.26 \times 8.11$	4.720
Retimet 80 PPI	$2.4 \times 2.4 \times 7.7$	$4.88 \times 4.88 \times 15.68$	5.431

The total mesh count of the computational domains used for comparison against experiments ranged from $0.2 - 1.5 \times 10^7$ polyhedral cells depending on the metal foam type. Larger cell counts were obtained for foams with smaller pore size, due to a greater surface area and thus requiring a larger number of refined mesh cells next to the foam surface. Table 3.5 summarizes the total mesh count and dimensions of the computational domains used for comparison against the experiments, where the sample streamwise thickness is given by the largest dimension. Domain size is also shown in terms of numbers of mean pore sizes in each dimension. Additional smaller computational domains have also been generated and employed in some numerical studies which will be presented in the next chapter, having the same boundary conditions as the rectangular channel domain.

3.6 Summary

A tomography-based methodology for characterization procedure of morphological parameters and pore-scale geometry generation of open-cell metal foams has been described. A total of seven distinct commercial open-cell metal foams have been scanned by means of computer

tomography and had their pressure drop experimentally measured under a wide range of air flow velocities. In-house Matlab routines have been devised for the 3-D volume rendering and morphological characterization routines performed on all samples.

Morphological measurements performed directly from the tomographic datasets have shown that all foam samples are highly porous, with a porosity values above 0.82. Comparison of porosity and specific surface area results against experiments and literature data have shown good agreement. The pore and strut size distribution was measured using a series of morphological image operations. Results have shown that the mean pore diameter to vary from approximately 0.4 to 2.25 mm across all the investigated foams. The equivalent strut diameter is on average more than five times smaller than the mean pore size.

Segmentation of the pore space within the foams was performed by using a combination of Euclidean and watershed transforms. The outcome of this approach is a segmented pore space composed of pore cells. Measurement of the cell widths in each Cartesian direction have shown a certain level of anisotropy, with some cells being elongated along one or more spatial directions. Moreover, the equivalent sphere diameter was computed and shown to be always larger than the mean pore size. This is explained by the fact that cells which are next to the sub-volume were not included in the pore segmentation analysis. On the other hand, mean pore size computations have to take into account ”incomplete” pores which are located right next to the domain boundaries.

The computer generated representation of the foam geometry is meshed using a commercial CFD package. Mesh and domain size sensitivity analysis have been carried out to minimize error arising from the numerical procedure and proper mesh refinement settings have been defined. Two distinct domains configurations representative of the experimental conditions have been created for comparison and validation against the pressure drop measurements.

Chapter 4

Pore-scale simulations

This chapter describes the pore-scale simulation results for single and two-phase flow across open-cell metal foams. The aim of the single phase flow simulations is to obtain reasonably accurate solutions of the airflow field under a wide range of flow velocities for all samples. Validation of the airflow simulation results is done by comparing numerical and experimental values for the pressure gradient across the samples. Furthermore, the pore-scale simulations are employed in order to gain a better understanding of the pressure gradient behaviour across the investigated foam samples. For that purpose, several additional features are analysed numerically, such as wall and entrance/exit effects, fluid compressibility, time-dependent flow features, porosity variation and foam anisotropy.

The qualitative assessment of the oil capture effectiveness within the foam samples is carried out by means of Lagrangian tracking calculations. Various droplet tracking simulations are carried out within the steady state airflow solutions computed for all samples. A simplified oil capture criterion is employed, neglecting the droplet dynamics phenomena. The effects of the flow velocity, droplet diameter and foam pore size in the oil capture effectiveness are evaluated. Rotational effects, which are experienced by metal foams within aero-engine separators, are accounted for by the use of a moving reference frame (MRF) approach. Finally, a methodology for transferring the pore-scale simulation results to a macroscopic porous medium model is proposed.

4.1 Validation procedure

The flow field in the interstitial pore space is expected to be complex with inhomogeneous distributions of velocity magnitude and direction. The pressure gradient, defined as the pressure drop normalized by the foam streamwise (flow direction) length, $\Delta p/L_f$, is the parameter chosen for validation of the simulation results, since it is accessible experimentally. Therefore, the pressure gradient in the simulations was calculated by computing the area-averaged static pressure at the domain inlet and outlet as

$$\frac{\Delta p}{L_f} = \frac{1}{L_f}\left[\frac{1}{A_{\text{out}}}\int_{A_{\text{out}}} p\,dA - \frac{1}{A_{\text{in}}}\int_{A_{\text{in}}} p\,dA\right] \tag{4.1}$$

where L_f is the foam thickness, A_{out} is the outlet cross-sectional area and A_{in} is the inlet cross-sectional area. In the experiments, inlet and outlet pressure are computed from pressure transducers positioned 25 mm away from the metal foam sample. For flow in porous media applications, the pressure gradient is normally plotted versus the Darcian velocity, u_D, a procedure which is also adopted here. The experimental values for Darcian velocity where computed by measuring the volumetric airflow rates upstream the foam samples and dividing by the cross-sectional flow area. In order to be consistent with the experiments, the Darcian velocity is computed at the domain inlet in the CFD simulations. Because the flow is considered to be incompressible, and the inlet section upstream the foam sample is a clear channel, the Darcian velocity will have the same magnitude as the prescribed inlet velocity for the simulations.

4.2 Airflow solving procedure

The flow governing equations described in Section 2.2 are solved by the finite volume method using the commercial solver Ansys Fluent 15 (ANSYS, 2013). Airflow is simulated through static and completely rigid foam samples. The fluid is assumed to be incompressible unless explicitly stated otherwise. Furthermore, simulations are performed in steady state unless ex-

plicitly stated otherwise. The Knudsen number (Eq. 2.7) is estimated to be lower than approximately $< 10^{-4}$ for the flow conditions investigated here, therefore showing that the continuum hypothesis still holds. The SIMPLE algorithm by Patankar and Spalding (1972) is employed for pressure-velocity coupling. Some cases more difficult to converge employed a fully coupled approach. A second-order upwind scheme was used for the spatial discretization and the linearised equations were solved using algebraic multi-grid acceleration. A detailed description of the equations and numerical methods employed here is beyond the scope of the present thesis, and can be found in Versteeg and Malalasekera (2007). A dimensionless convergence criterion of 10^{-6} was set for the equation scaled residuals together with the monitoring of the convergence of field-variables in order to ensure the solution has converged.

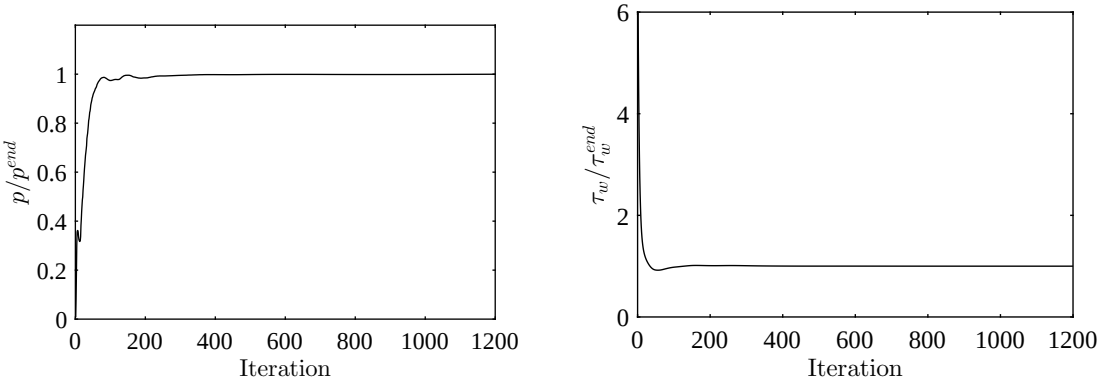

Figure 4.1: Convergence of the (a) average static pressure at the domain inlet and (b) average wall shear stress at the foam surface. Both variables are normalized by the their value at the last iteration.

Figure 4.1 depicts typical convergence plots for field-variables computed from a steady-state simulation. It shows the convergence of average static pressure at the domain inlet and average wall shear stress at the foam surface. Both variables are normalized by their values computed at the last iteration, which is the converged solution. The variables seem to stabilize around a mean value after approximately 300 to 400 iterations. Apart from the convergence of field-variables,

the overall mass and forces balances were checked at the end of simulations to verify for any imbalances in those quantities.

4.2.1 Turbulence modelling

As the Re_p is expected to range from approximately 120 - 7100, quite above the Darcy regime and far exceeding the fully turbulent threshold value for many cases, as defined in section 2.2.2, two Reynolds-averaged Navier-Stokes (RANS) turbulence models were evaluated, namely the RNG k-ε model used in conjunction with an enhanced near wall treatment and the SST $k-\omega$ model. The detailed formulation of the near wall treatment employed for the RNG k-ε and SST $k-\omega$ can be found in (ANSYS, 2013). For the cases where $\mathrm{Re}_p < 300$, the flow was considered to be laminar.

It is important to note that if the flow turbulence were to be fully resolved by means of direct numerical simulation (DNS), an estimation of the Kolmogorov micro-scales (Tennekes and Lumley, 1972), shows that the mesh refinement would have to increase by a factor of roughly 10, without mentioning the obvious necessity of time discretization, in order to account for the turbulent time scales. The computational resources available to the present study do not allow one to solve DNS-type simulations within a reasonable time.

4.3 Comparison to experiments

The square channel domain configuration (Figure 3.16a) was employed for comparison of the pore-scale simulation results against the experimental measurements. The reason for not employing the cylindrical domains is that due to the limited size of the tomographic scans, they had a considerably smaller diameter perpendicular to the flow when compared to the actual diameter of the experimental samples. A smaller diameter perpendicular to the flow implies (possibly) greater wall effects. Therefore, the square channel configuration is expected to be more representative of the conditions found in the experiments.

Table 4.1: Simulated Re_p range, minimum and maximum average y^+ values at the foam surface for each sample.

Sample	Re_p range	$\min y^+$	$\max y^+$
Recemat	440 - 2650	0.397	1.563
Inconel 450 µm	120 - 1200	0.401	2.112
Inconel 1200 µm	320 - 3200	0.270	1.613
Inconel 580+1200 µm	190 - 1880	0.321	1.801
Retimet 20 PPI	710 - 7100	0.119	0.857
Retimet 45 PPI	315 - 3150	0.282	1.685
Retimet 80 PPI	170 - 1680	0.255	1.477

The pore-scale simulation results reported in this section concern steady state incompressible airflow. Table 4.1 depicts the pore-based Reynolds number range simulated for each sample, the minimum and maximum values of the average non-dimensional wall distance, y^+, at the foam surface. The y^+ values are computed at the minimum and maximum pore-based Reynolds numbers within the turbulent regime ($\mathrm{Re}_p > 300$) respectively. The choice of Re_p range was based on the available experimental data for each sample.

A comparison between the experiments and numerical solutions obtained with the RNG k-ε and SST $k-\omega$ turbulence models was made using the Recemat foam sample. Note that the computational domain had a streamwise length $L_f = 10$ mm, identical to the experimental sample. Pressure measurements were taken under a range of $u_D = 2.3$ to 26 m/s and simulations were performed for $u_D = 5$ to 25 m/s. Pressure gradient results for the Recemat foam are plotted in Figure 4.2a as a function of u_D. Flow streamlines are shown in Figure 4.2b, for a flow velocity, $u_D = 25$ m/s ($\mathrm{Re}_p \approx 2250$).

The Recemat pressure gradient simulation results agreed relatively well with the measure-

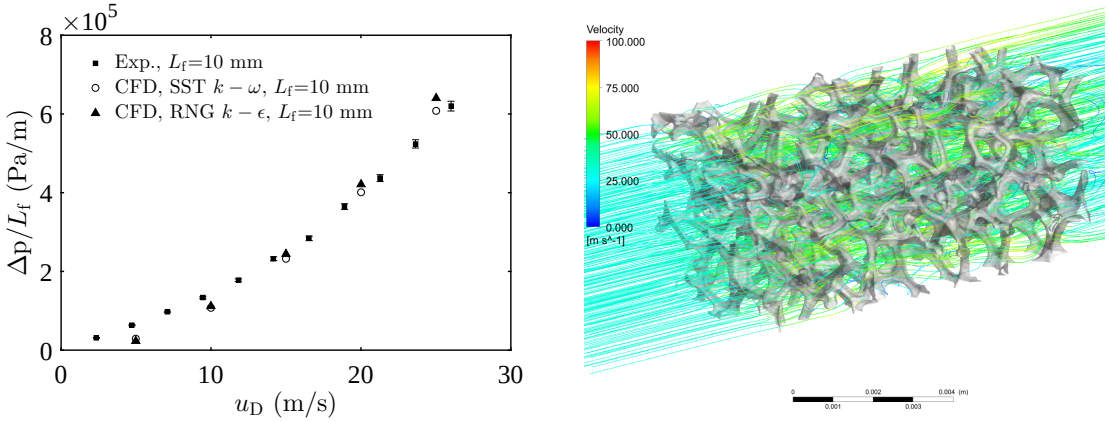

(a) (b)

Figure 4.2: (a) Simulated pressure gradient for the Recemat sample and (b) simulated flow streamlines for the Recemat sample for $u_D = 25$ m/s ($\mathrm{Re}_p \approx 2250$).

ments, showing larger deviations at lower Darcian velocities values, $u_D < 10$ m/s ($\mathrm{Re}_p \approx 800$). Results obtained using the RNG k-ε and SST $k-\omega$ turbulence models were similar. The permeability, K, and Forchheimer coefficient , F, values can be obtained by least squares fitting a second-order polynomial to the pressure gradient curves, using the Forchheimer equation (Eq. 2.39). Values of permeability and Forchheimer coefficient computed this way can be sensible to the velocity range employed for the curve fitting procedure. Here, the curve fitting procedure only considered flow data within the turbulent flow regime ($\mathrm{Re}_p > 300$), since most of the data lies within that regime for all samples.

For the Recemat sample, values of K and F obtained using the RNG k-ε model presented a better agreement than values obtained using the SST $k-\omega$ when compared against experimental data, as shown in Table 4.2. Furthermore, cases which employed the RNG k-ε model were more stable numerically, and converged faster. For these reasons, all subsequent pore-scale simulations reported in this thesis employed the RNG k-ε model. The square of correlation factor, R^2, was greater than 0.99 for all the curve fitting results reported here.

Pressure gradient measurements for the Inconel and Retimet foams were carried out for $u_D = 2.3$ to 49.6 m/s, except for the hybrid Inconel 580 + 1200 µm, where the range $u_D = 2.3$

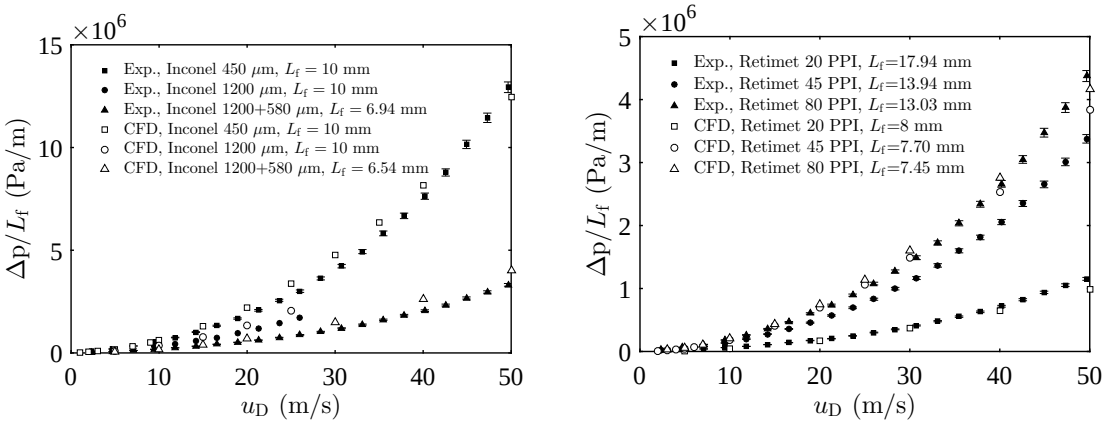

Figure 4.3: Simulated pressure gradient for the (a) Alantum Inconel samples; (b) for the Retimet samples

to 26 m/s was considered. All the simulations were performed for $u_D = 5$ to 50 m/s, except for the hybrid Inconel 580+1200 µm, which was limited to the maximum value of $u_D = 25$ m/s, since no pressure gradient measurements were carried out above that. The streamwise length of the Inconel computational samples was identical to the experimental ones, except for the hybrid Inconel 580+1200 µm, which presented a small discrepancy of 0.40 mm, due to the limited size of the tomographic scan.

The Retimet foams computational domains were smaller than ones evaluated experimentally due to the limited size of the tomographic datasets. Figures 4.3a and 4.3b depict the simulated pressure gradient as a function of u_D for all the Inconel and Retimet foams respectively. The pore-scale simulations have been able to reproduce the pressure gradient curves up to a satisfactory level of agreement. Table 4.2 summarizes both the experimental and simulated permeability and Forchheimer coefficient values obtained for all samples, along with the root-mean-square (RMS) deviation for each variable (using experimental data as a reference). Generally, permeability showed a greater RMS deviation than the Forchheimer coefficient.

As the flow conditions investigated here are well beyond the Darcy's regime, and data is mostly within the turbulent regime, it is reasonable to assume that the pressure losses are mainly

Table 4.2: Computed values for permeability (m^2) and Forchheimer coefficient (m^{-1}) along with the RMS error for each quantity.

Sample	$K_{CFD} \times 10^{-9}$	$K_{exp} \times 10^{-9}$	RMS error (%)	F_{CFD}	F_{exp}	RMS error (%)
Recemat, RNG k-ε	9.46	2.21	76.6	736	485	34.0
Recemat, SST $k-\omega$	13.0	2.21	82.9	795	485	38.8
Inconel 450 µm	0.88	0.54	63.1	3745	4677	19.9
Inconel 1200 µm	2.96	1.48	100.8	1150	1049	45.2
Inconel 580+1200 µm	4.82	17.6	72.6	1254	1050	19.3
Retimet 20 PPI	13.7	43.3	68.3	302	382	20.9
Retimet 45 PPI	2.67	4.24	37.0	1149	1150	0.5
Retimet 80 PPI	2.50	2.78	10.2	1248	1510	17.4

due to inertial effects. Larger pressure gradients are observed in samples with smaller pore sizes, which present a greater flow restriction due to their larger surface area. Permeability generally decreases with decreasing pore size whereas the Forchheimer coefficient values normally increase with decreasing the pore size. This same trend was observed in a similar study by Ranut et al. (2014). Simulation results obtained with the Retimet foams did not show the pressure gradient to be very sensitive to their smaller streamwise length compared to the experimental samples.

The reasonably large discrepancies between experimental and simulated permeability and Forchheimer coefficient values indicate a high sensitivity of these parameters to relatively small deviations on the pressure gradient. Such large discrepancies have been noted previously in similar studies (Bhattacharya et al., 2002; Ranut et al., 2014), showing that two separate experimental measurements carried out for a similar type of metal foam can show large discrepancies for permeability and Forchheimer coefficient values. There are several possible sources of errors, given that each experiment employs a specific sample streamwise thickness, diameter and velocity range. Dukhan and Patel (2010) noted that there are no standards specifying the

metal foam test sample size in experiments. Nevertheless, geometrical differences between the samples employed for the tomographic scans and the ones employed for pressure gradient measurements are the most likely cause for these discrepancies in the present work. Unfortunately, the level of discrepancy between the two sample sets could not be evaluated in the present work.

It was interesting to note that permeability values showed a greater deviation between experiments and simulations. Since the flow regime investigated here is mostly in the turbulent regime, it is reasonable to assume that the viscous losses (related to the permeability) are negligible compared to the inertial losses (related to the Forchcheimer coefficient) within the metal foam. Therefore, assuming that is the case (fixing the permeability term to zero), the pressure gradient of the foam samples analysed here can be written as a function of the quadratic term in the Forchheimer equation (Eq. 2.44), such as

$$\frac{\Delta p}{L_f} = -F\rho {u_D}^2 \tag{4.2}$$

Therefore, the pressure gradient curves obtained by both experiments and CFD simulations can be fitted using Eq. 4.2 in order to compute the Forchheimer coefficient values. Table 4.3 depicts the results of this procedure, also showing the normalized RMS deviation between experimental and simulated data (using the experiments as reference). The square of correlation factor, R^2, was higher than 0.99 for all cases. The agreement between experiments and simulations is better using Eq. 4.2. A possible explanation is that, when assuming the pressure gradient to be governed by Eq. 2.44 (which includes both permeability and Forchheimer coefficient), the curve fitting procedure is basically searching a 2-D parameter space, which might have an infinite number of permeability and Forchheimer coefficient pairs as solutions. Additionally, it is reasonable to say that for the flow conditions investigated here, the Forchheimer coefficient is a more representative parameter than permeability.

Generally, the pore-scale simulations were able to satisfactorily reproduce the pressure gradient results measured in the experiments. For the purposes of this project, an approximated

Table 4.3: Forchheimer coefficient (m^{-1}) curve fitting results for the experimental and CFD data using Eq. 4.2 and the normalized RMS deviation.

Sample	F_{exp}	F_{CFD}	RMS error (%)
Recemat NC 1723	789.62	806.63	2.15
Inconel 450 µm	4019.33	4146.50	3.16
Inconel 1200 µm	2157.15	2697.02	25.03
Inconel 580+1200 µm	1070.99	1324.16	23.64
Retimet 20 PPI	373.49	326.27	12.64
Retimet 45 PPI	1069.73	1279.59	19.62
Retimet 80 PPI	1382.38	1387.97	0.40

steady state flow field within the pore space is a satisfactory solution. All simulations were carried out using the university's high performance computing (HPC) facility, employing normally 24 to 32 Intel Harpertown 3 GHz cores, depending on the availability. Moreover, a typical steady state pore-scale simulation takes between 30 minutes to 2 hours of computing time depending on the mesh size. It is beyond the scope of the present study to capture the transient effects associated with complex phenomena such as flow separation, vortex shedding and boundary layer detachment. A scale-resolving approach such as LES or DNS would be necessary to capture these phenomena, which would increase the computational costs by several orders of magnitude.

4.3.1 Details of the flow field

Figure 4.4a depicts a pressure contour plot on a 2-D cut plane for the Recemat foam, at a flow velocity, u_D, of 20 m/s. A complex pressure distribution is caused by the intricate foam geometry, with stagnation points seen in front of the foam struts. A velocity contour plot on

a 2-D cut plane for the Recemat foam at $u_D = 20$ m/s is depicted in Figure 4.4b. The flow is separated and accelerated through the pores apertures, showing a preferential flow through large passages, with high velocity streaks seen through the narrowest gaps. The flow behaviour is similar to the flow past multiple bluff bodies in this case, with a low velocity region present on the wake of every solid ligament. Simulation results obtained with the other samples showed similar behaviour.

The pressure gradient behaviour along the streamwise sample length is more clearly shown in Figure 4.5a, where the area-weighted averaged dimensionless pressure profile was computed in multiple cross-sections perpendicular to the flow, and is plotted against the pore size normalized sample streamwise length, z/L_f, with z as the streamwise position inside the foam. The dimensionless pressure is calculated according to Eq. 2.45. For all cases, the profile shows an almost linear pressure gradient behaviour, with local fluctuations caused by the intricate foam morphology. At the exit of the sample, the local pressure falls below the far field pressure, with the drop becoming more pronounced as the inlet flow velocity, u_0, increases. This phenomenon is likely to be caused by vortices generated at the wake of the foam. The linear pressure gradient behaviour observed here has been reported in similar pore-scale studies (Petrasch et al., 2008a; Akolkar and Petrasch, 2012). Figure 4.5b shows the velocity profile normalized by the inlet flow speed. As the incompressible fluid enters the foam, its bulk velocity is immediately increased due to the reduction in the cross-sectional area, and continues to fluctuate above unity, proportionally to the cross-sectional area variation along the foam. At the exit, the normalized velocity gradually goes back to unity, and a small exit effect is present at the wake of the foam.

Simulation results obtained with other foam samples presented similar behaviour, even for different pore sizes. Figure 4.6 depicts the dimensionless pressure gradient profile across the Inconel 450 µm ($d_p = 0.345$ mm) and Retimet 45 PPI ($d_p = 0.918$ mm) foams respectively, for inlet flow velocities varying from 5 to 30 m/s. The slope of the dimensionless pressure gradient is steeper in the case of the Inconel 450 µm. Nevertheless, both foams show an apparent linear

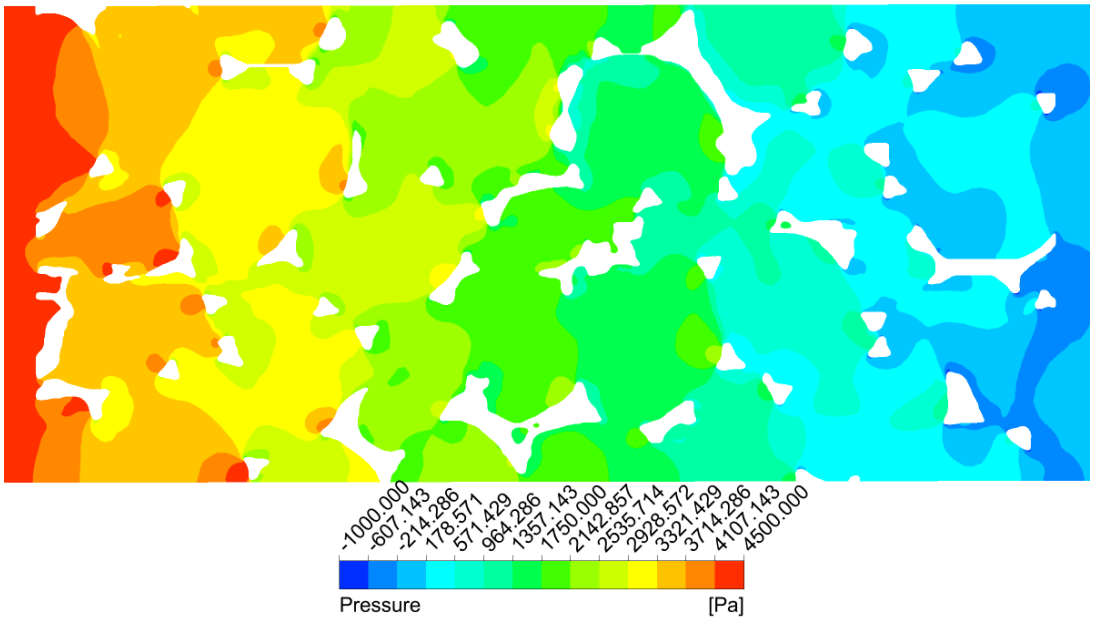

(a)

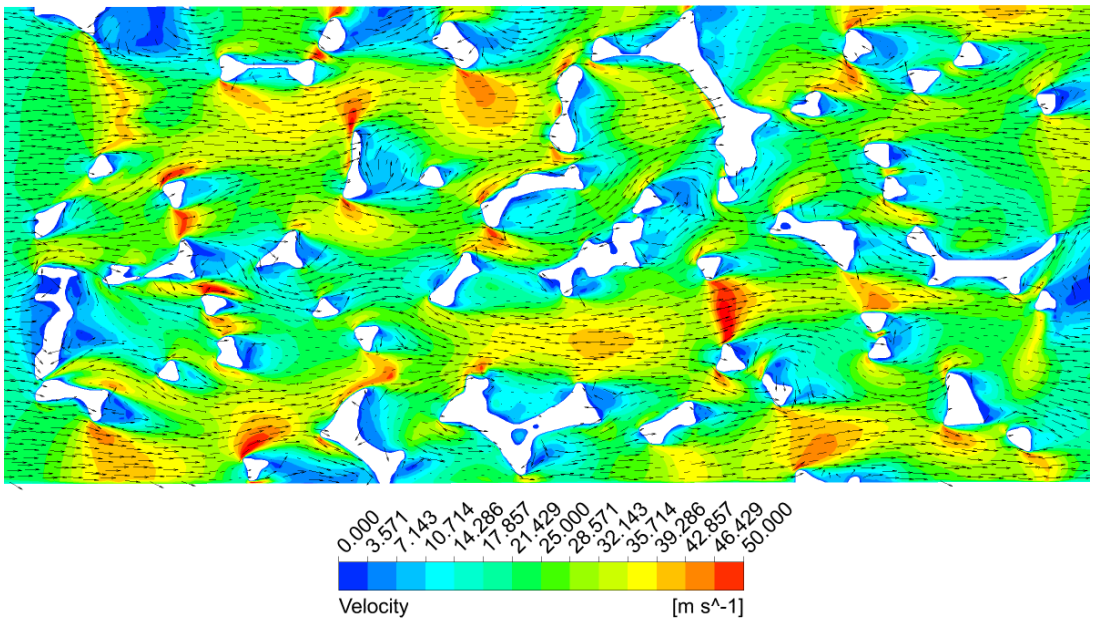

(b)

Figure 4.4: (a) Pressure and (b) velocity vector contour plots on a 2-D cut plane located at the centre of the computational sample for simulation results obtained at $u_D = 20$ m/s.

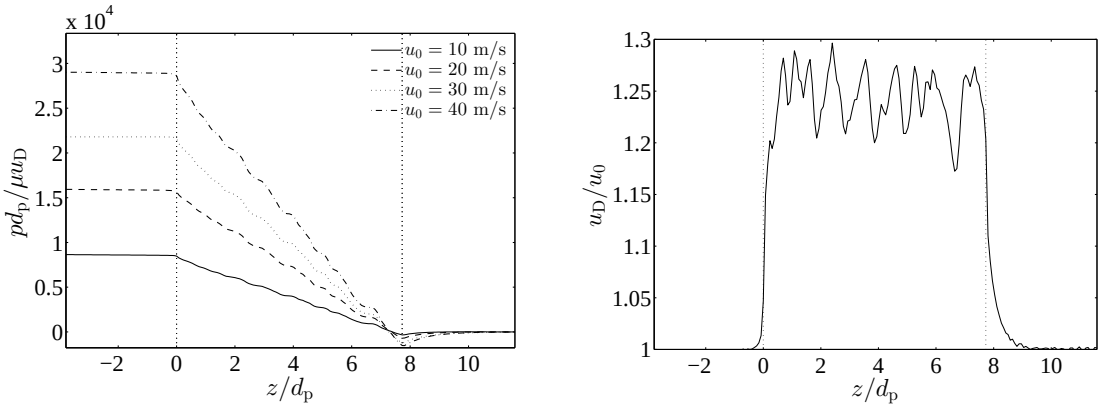

(a) (b)

Figure 4.5: (a) Dimensionless pressure profile across the Recemat foam at varying inlet velocities and (b) normalized velocity profile across the Recemat foam at $u_0 = 20$ m/s. The vertical dashed lines depict the entrance and exit of the foam respectively.

pressure gradient behaviour along their streamwise length. Results for the Retimet 45 PPI foam showed a pronounced fall in the local pressure right next to the foam exit, which is apparently absent in the Inconel 450 µm results. One explanation is that the magnitude of this drop in pressure might be related to exit effects, and that these are proportinal to the pore size. As the Retimet 45 PPI computational sample has a much smaller normalized streamwise length (L_f/d_p) when compared to the Inconel 450 µm, its results are likely more affected by any size-related effects.

A foam sample which was quite unique is the hybrid Inconel foam, which was built by merging a foam with a nominal pore diameter of 580 µm with another one with nominal pore diameter of 1200 µm. Analysis of the tomographic dataset indicate that about 55 % of the foam length is composed of the Inconel 580 µm. The computational sample was built with the larger nominal pore size (1200 µm) constituting the first half of the sample (next to the inlet side) and the smaller nominal pore size (580 µm) the other half (next to the outlet side). Figure 4.7a shows a schematic of the computational foam sample.

The dimensionless pressure gradient profile across the sample for varying air inlet velocities

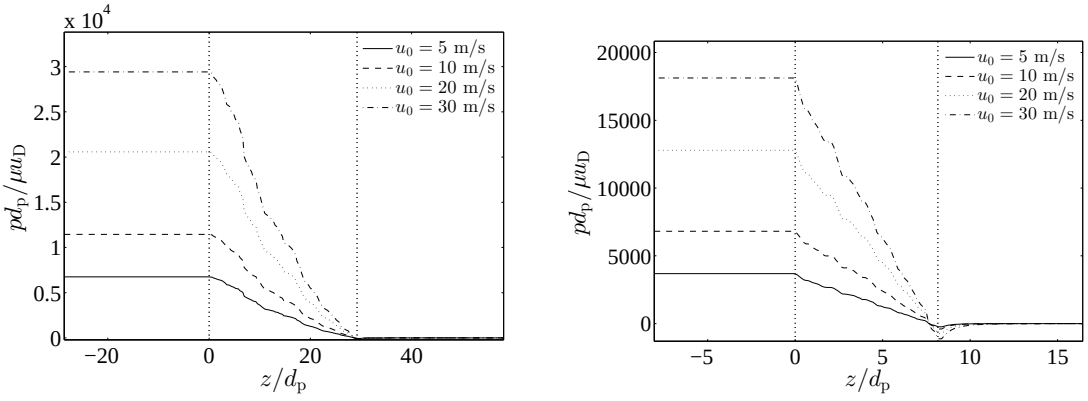

(a) (b)

Figure 4.6: Dimensionless pressure profile at varying inlet velocities across the Inconel 450 µm (a) and Retimet 45 PPI (b) foams respectively. The vertical dashed lines depict the entrance and exit of the foam respectively.

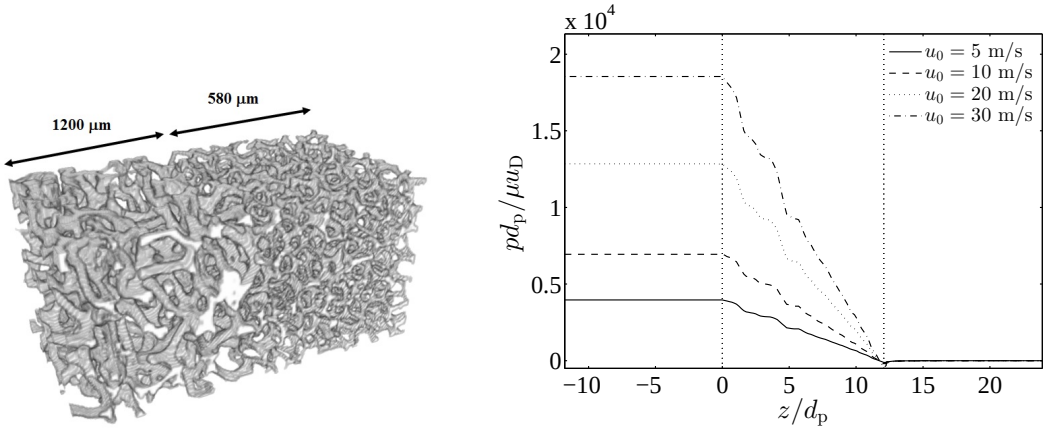

(a) (b)

Figure 4.7: Schematic of the Inconel 1200+580 µm computational sample employed in the simulations (a) and (b) dimensionless pressure gradient profile across the sample for varying air inlet velocities. The vertical dashed lines depict the entrance and exit of the foam respectively.

is plotted in Figure 4.7b. Larger pressure fluctuations are observed across the first half of the foam streamwise thickness, which is occupied by the foam with a nominal pore size of 1200 µm. The fluctuations are significantly smaller in the second half of the sample occupied by the smaller pore size of 580 µm. Experimental measurements showed that the alignment order of

the pore sizes (whether the 580 or 1200 μm is facing the inlet side) has a negligible effect on the overall pressure gradient. Hybrid foams are relatively novel, and could offer a greater flexibility in terms of managing the overall pressure gradient in systems which employ open-cell metal foams.

4.4 Numerical investigations of additional effects

The pressure gradient across open-cell metal foams applied to aero-engine separators should be kept to a minimum, given the tight operational constraints within aero-engines. Therefore, it is important to understand the parameters which might affect the pressure gradient across open-cell metal foams. Even though reasonably accurate results were obtained by the pore-scale simulations, there are still several factors that should be analysed in more detail, such as wall and entrance effects, fluid compressibility, time-dependent flow features, anisotropy of the foam structure and the impact of porosity and surface area on the pressure gradient. These effects are investigated by means of pore-scale simulations. All simulations described in the following sections are performed assuming incompressible flow and in steady state, unless stated otherwise. The RNG k-ε turbulence model was employed when the flow was not laminar.

4.4.1 Wall effects

Wall effects were evaluated by performing simulations using the quarter of a cylinder domain configuration. A total of four different samples were employed for this analysis, namely the Inconel 450 μm, Recemat, Retimet 45 and 80 PPI foams. The streamwise length of the computational samples were identical to the ones employed in the square channel domains as reported in Section 4.3. It is unlikely that the average porosity of the foam changes near the walls, as happens in the case in a bed of packed spheres. The nature of wall effects in open-cell metal foams is mainly viscous, simply due to the additional shear stress next to the wall region. As noted in the experimental work of Dukhan and Ali (2012b), one way of quantifying the magnitude of the

wall effects is by computing the Darcy-Weisbach friction factor, defined as

$$f = \frac{2\Delta p}{\rho u_D^2} \tag{4.3}$$

where Δp is the overall pressure drop through the sample. For the current application, it is interesting to include the pressure gradient ($\Delta p/L_f$) and the Reynolds number characteristic length scale (d_p) in the friction factor as well, such that a modified friction factor, f^*, can be defined as

$$f^* = \frac{2\Delta p}{\rho u_D^2}\frac{d_p}{L_f} \tag{4.4}$$

Therefore, the magnitude of the wall effect can be computed by subtracting the friction factor obtained with the cylindrical domain from the friction factor calculated from the square channel domains, where wall effects are absent, such that

$$\text{Wall effect} = \frac{f^* - f^*_{\text{ref}}}{f^*_{\text{ref}}} \times 100\% \tag{4.5}$$

where f^*_{ref} is the reference friction factor, computed from the square channel domain results. For comparison purposes, f^* and f^*_{ref} are taken at the same pore-based Reynolds number. The magnitude of the wall size effects computed for each of the four foam samples are plotted in Figure 4.8, which also includes the dimensionless cylinder diameter ratio, defined as the diameter of the cylinder divided by the mean pore diameter, d_{cyl}/d_p.

The wall size seems to be a function of both the cylinder diameter and the Reynolds number, however the effect seems different depending on the foam sample. Apparently, for samples with small mean pore sizes (< 0.5 mm), namely the Inconel 450 µm and Retimet 80 PPI, the wall effect magnitude seems to decrease with increasing Reynolds number. Conversely, the opposite seems to take place with the other foams, where wall effect increases with increased Reynolds number. The magnitude of the wall effect is similar to experimental results reported by Dukhan

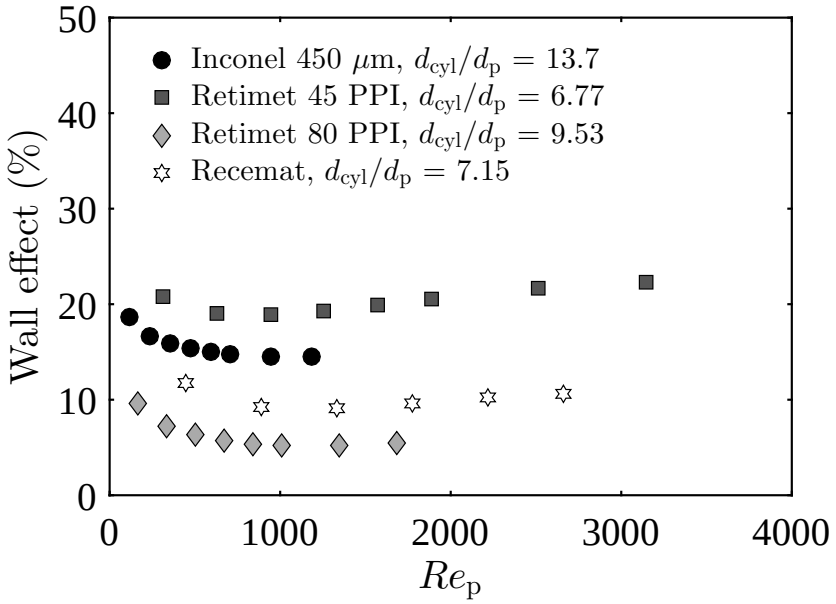

Figure 4.8: Wall effect magnitude as a function of Reynolds number based on the cylinder diameter. The dimensionless cylinder diameter for each foam sample is given, defined as d_{cyl}/d_p.

and Ali (2012b).

The dependence oj friction factor on the Reynolds number can be explained by the fact that the boundary layer thickness decreases as the Reynolds number is increased. Therefore, the velocity gradient in the region close to the wall gets steeper and generates higher shear stresses in that region. Viscous drag becomes less significant as the Reynolds number increases and above a certain critical value, pressure losses become proportional to the square of the average flow velocity. In this region, the friction factor starts to become independent of the Reynolds number. Figure 4.9 shows a contour plot of the pore velocity normalized by the inlet velocity, u/u_0, at a cut plane halfway through the Retimet 45 PPI sample, at two different $\mathrm{Re_p}$. It shows that region of low velocity right next to the cylinder wall (and foam surface) seems to be slightly thicker at a lower Reynolds numbers, although the difference is very subtle.

The ratio of pore size to the cylinder diameter, characterized by the dimensionless cylinder diameter, d_{cyl}/d_p, seems to be important as well. As expected, the foam with the smallest dimensionless diameter, Recemat, presented the highest wall effects. However, the wall effect

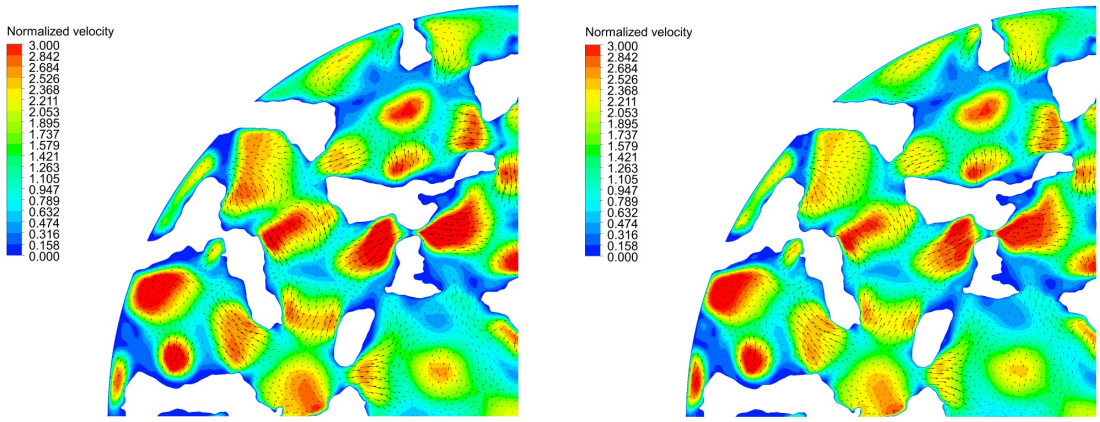

(a) (b)

Figure 4.9: Contour plot of the normalized velocity, u/u_0, for the Retimet 45 PPI at $\mathrm{Re_p}$ values of approximately (a) 315 and (b) 1250 respectively.

magnitude was not always proportional do the dimensionless cylinder diameter, as the results obtained for the Inconel 450 µm and Retimet 80 PPI foams have shown. Interestingly, the experiments of Dukhan and Ali (2012b) showed the magnitude of the wall effect increased from relatively small values with Reynolds number for a foam with large pore size, and decayed with increased Reynolds number for foams with smaller pore size, attributing such behaviour to the different foam morphologies. However, it is important to remember that the samples employed in the experimental measurements had a much larger cylinder diameter ($\sim$ 25 mm) than the ones described in this section. Thus, the magnitude of the wall effect in the experiments was probably quite small. This further adds credibility to the choice of using the square channel domains for comparison against the experiments. The wall shear stress, τ_w, can be normalized as $\frac{\tau_w}{\frac{1}{2}\rho u_d^2}$. Figure 4.10 shows the normalized wall shear stress contour plot at the cylinder wall for Re_d values of approximately 315 and 1250 respectively. These results show that the normalized wall shear decreases with increased Reynolds number.

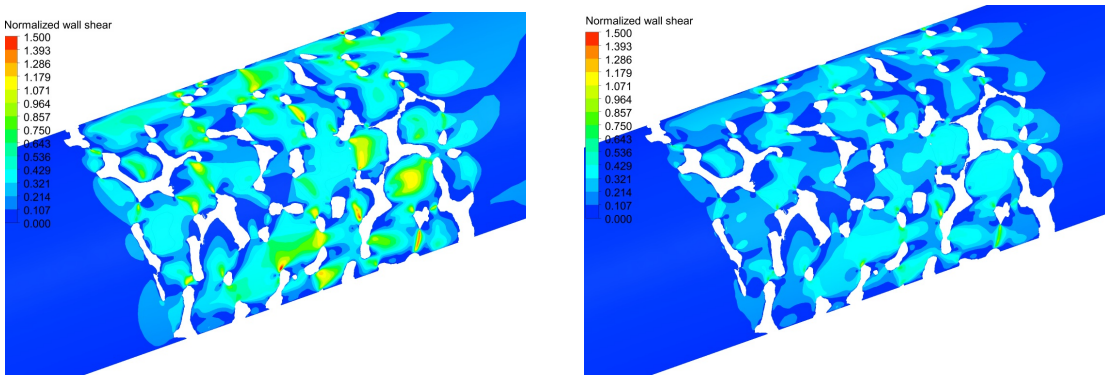

(a) (b)

Figure 4.10: Contour plot of normalized wall shear stress at plotted at the cylindrical no-slip wall for the Retimet 45 PPI at Re_d values of approximately (a) 2200 and (b) 6700 respectively.

4.4.2 Entrance/exit effects

There has been experimental evidence showing the sample streamwise length to affect the normalized pressure gradient in open-cell metal foams due to entrance and exit effects Baril et al. (2008); Dukhan and Patel (2010). At small sample streamwise lengths, the pressure gradient is sensitive to increases in sample length, although any changes decrease as the sample length becomes large. Hence, entrance or exit effects decrease asymptotically with sample length. Although the mechanisms behind entrance and exit effects are not still well understood, it is believed that they are caused by the sudden acceleration and deceleration of the fluid upon entering and exiting the porous sample, due to large changes in the flow cross-section area.

The effect of the foam streamwise length is evaluated numerically for the Inconel 450 µm foam. The 3, 4 and 7 mm samples are subsets of the 10 mm tomographic dataset, whereas the 20 mm is generated by combining two 10 mm computational samples together. Note that this merging procedure will result in small discontinuity in the foam morphology at the merging position. However, no statistically significant change in porosity or specific surface area was observed for the combined 20 mm computational sample. The Inconel 450 µm sample was chosen for this analysis for having the largest streamwise thickness relative to the mean pore

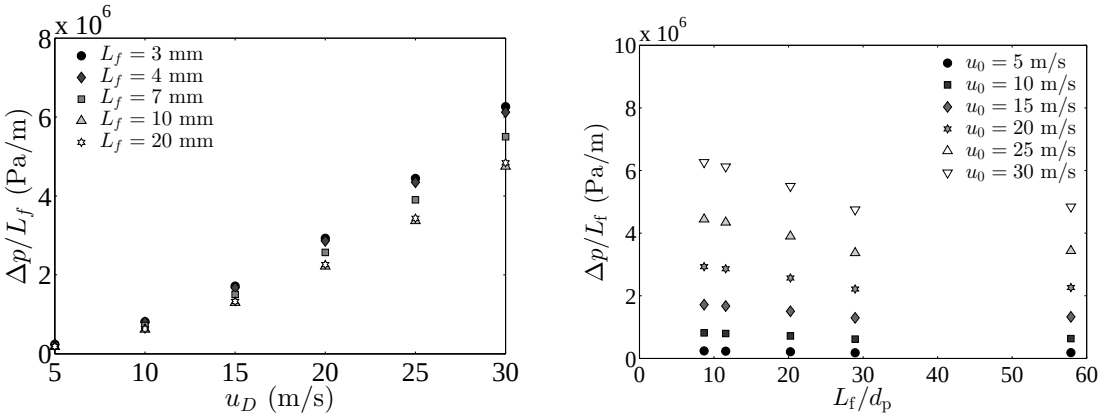

(a) (b)

Figure 4.11: (a) Simulated pressure gradient as a function of u_D for Inconel 450 µm samples with increasing streamwise length and (b) simulated pressure gradient as a function of the normalized sample streamwise length for different air inlet velocities.

size.

It is clear from Figure 4.11a that the normalized pressure gradient decreases with increasing sample streamwise length, a trend which was observed experimentally in other studies (Dukhan and Patel, 2010; Oun and Kennedy, 2014). The pressure gradient for the 10 and 20 mm samples almost collapse into a single curve for the velocity range investigated, indicating that the critical streamwise length is likely to be between these values. A plot of the normalized pressure gradient as a function of the normalized sample streamwise length is shown in Figure 4.11b. The same trend observed in Figure 4.11a extends across the entire velocity range, being more pronounced at higher fluid velocities.

The critical thickness for open-cell metal foams is normally given in terms of number of pore sizes or cells, which makes the comparison between foams with different pore sizes more meaningful, as noted in (Dukhan and Patel, 2010; Oun and Kennedy, 2014). Apparently, the critical streamwise length for the Inconel 450 µm foam lies between roughly 25 d_p and 50 d_p, which is in accordance with experimental work publish in literature, which has found critical thickness values between 30 and 50 d_p.

As mentioned before, the Inconel 450 μm is the largest sample in terms of pore size normalized length. According to the results reported in this section, it is very likely that both the experimental and computational samples of all foams (with exception of the Inconel 450 μm) investigated in the present work have a streamwise thickness smaller than the critical one. Nevertheless, based on the results shown here and on experimental evidence in the literature, it is reasonable to assume that entrance and exit effects are present and captured in both the experiments and the pore-scale simulations.

4.4.3 Time-dependent effects

Steady state RANS calculations often fail to provide accurate predictions of complex flows with separation, due to inherent unsteady flow features. In open-cell metal foams, flow separation takes place next to the foam's solid struts, therefore complex flow patterns such as vortex shedding may take place, giving rise to unsteady flow structures. When the flow is not statistically stationary, Reynolds averaging is not the same as time-averaging Iaccarino et al. (2003), and therefore an unsteady approach is better suited.

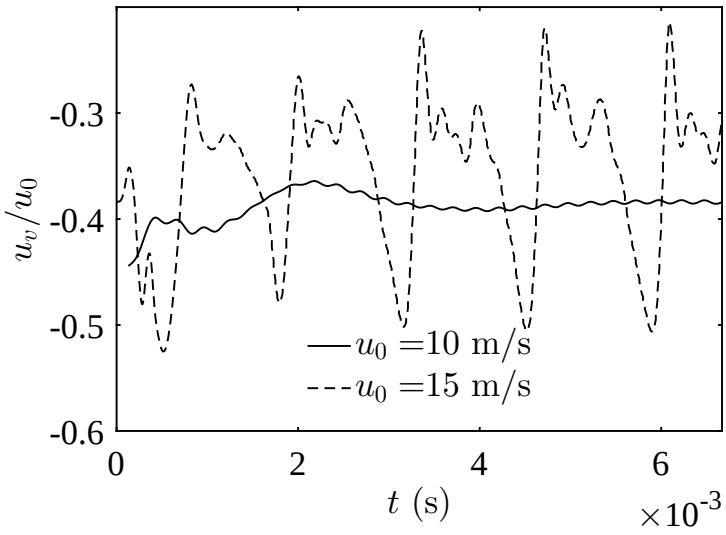

Figure 4.12: Simulations results showing the evolution of a velocity component perpendicular to the flow direction normalized by the inlet velocity at a monitor point positioned in the wake of the Recemat foam sample for inlet velocities of $u_0 = 10$ m/s and $u_0 = 15$ m/s respectively.

A set of unsteady RANS simulations were carried out in the Recemat foam sample with a streamwise thickness of 4.27 mm (intermediary domain size so that computational costs remain reasonable). These simulations are performed with the intent to verify and evaluate time-dependent flow features. Investigation of unsteady flow behaviour was done by monitoring a velocity component perpendicular to the flow (u_v) at predefined monitor points. The monitor points were located in the wake of the sample, at a distance of 0.2 mm from the centre of the foam. Time step of each simulation was adjusted in a way that the flow Courant number remained constant regardless of the time step size. The Courant number is defined as

$$C_f = \frac{u\Delta t}{\Delta l} \leq C_{max} \tag{4.6}$$

where C_f is the flow Courant number, Δt is the time step size, Δl is the characteristic mesh length and C_{max} is the maximum Courant number value allowed. Here, C_{max} value was kept close to unity, even though a higher value could be used since an implicit solver is employed. The time evolution of the streamwise velocity component at a monitor point positioned in the wake of the foam sample is shown in Figure 4.12 for air inlet velocities of 10 and 15 m/s respectively. The amplitude and frequency of the unsteady behaviour of the streamwise velocity component greatly differs depending on the inlet velocity. It also can be seen that the velocity fluctuations becomes periodic after a certain time for both cases.

The simulations were run for a Darcian velocity range of 5 - 20 m/s. Results obtained with the unsteady simulations are time-averaged and compared against steady state simulation results. Note that the time averaging is performed only after the monitored streamwise velocity component started to show a periodic behaviour. Figure 4.13 shows a comparison of the normalized pressure gradient between the time-averaged unsteady cases with steady state ones. The unsteady simulations take at least 10-20 times more CPU time when compared with the stationary ones. Absolute average difference between both approaches is 2.61 %, therefore not justifying the consideration of unsteady flow effects, given the extra computational cost and

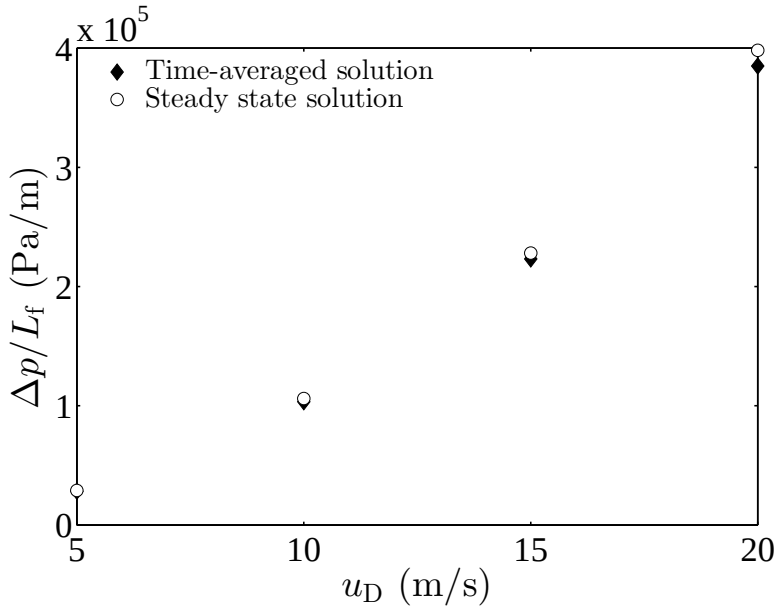

Figure 4.13: Comparison between steady state and time-averaged simulation results for the pressure gradient for the Recemat foam sample with streamwise thickness of 4.27 mm.

marginal difference in the pressure gradient results.

4.4.4 Fluid compressibility effects

Analysis of the pore-scale simulation results for incompressible airflow showed that the Mach number in the pore space can sometimes exceed 0.3, especially at high inlet airflow velocities. Under such conditions, fluid compressibility effects can start to become significant and it is necessary to evaluate their impact when included in the numerical model.

A set of simulations was carried out assuming the air to be a compressible ideal gas. The inlet and outlet were specified as pressure boundary conditions. Therefore, a pressure gradient is specified for the domain and the fluid Darcian velocity is computed afterwards. Compressibility effects were investigated using the Inconel 450 µm and Retimet 80 PPI foams respectively. For comparison purposes, the dimensionless pressure gradient and pore-based Reynolds number was computed from the experimental data by assuming the air density to vary according to an ideal gas. Therefore, for each data point, temperature was fixed as ambient, and air density was

estimated using the inlet pressure and Darcian velocity values. Figure 4.14 shows a comparison of the dimensionless pressure gradient (Eq. 2.45) between the experiments and the pore-scale simulations. The dimensionless pressure gradient varies linearly with the pore-based Reynolds number. A Mach number contour plot is shown in Figure 4.15 for compressible airflow across the Retimet 80 PPI foam at $u_D = 47.04$ m/s, clearly showing several regions where the Mach number is equal or higher than 0.3.

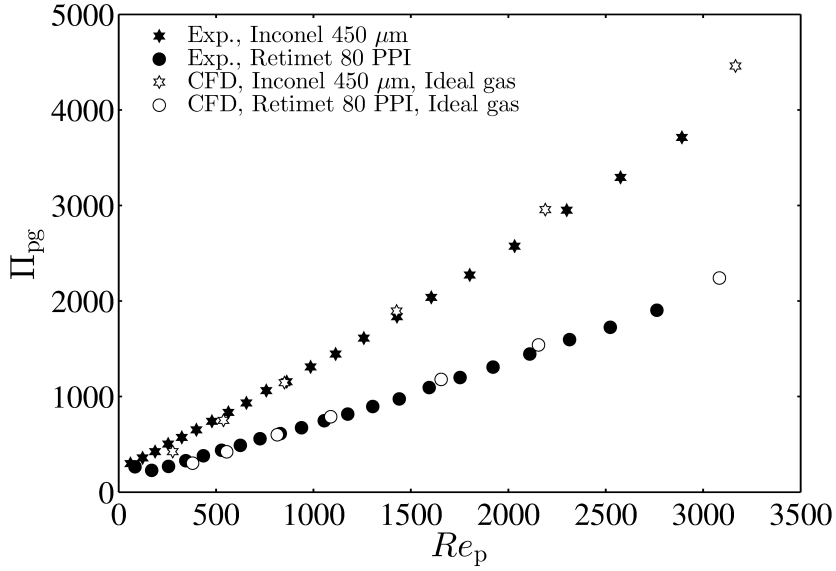

Figure 4.14: Comparison of the dimensionless pressure gradient vs. Re_p between experiments and simulations assuming compressible ideal gas for the Inconel 450 μm and Retimet 80 PPI samples.

The permeability and Forchcheimer coefficient can be computed using Eq. 2.45 by performing a linear fit to the dimensionless pressure gradient data. Table 4.4 summarizes the permeability and Forchheimer coefficient values obtained from both experiments and pore-scale simulations. Note that these values are different from the ones obtained when considering the air to be incompressible, listed in Table 3.2. The discrepancy between experimental and numerical permeability results is much greater when taking into account fluid compressibility, showing deviations of roughly 700 and 490 % for the Inconel 450 μm and Retimet 80 PPI samples respectively. On the other hand, better agreement was found between the experimental and

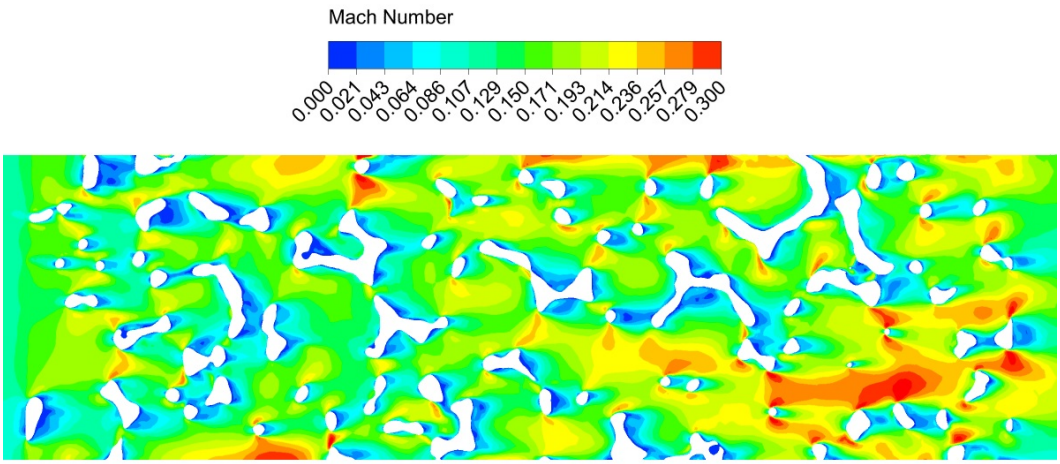

Figure 4.15: Contour plot on a 2-D cut plane at the centre of the Retimet 80 PPI sample showing the Mach number for compressible airflow at $u_D = 47.04$ m/s.

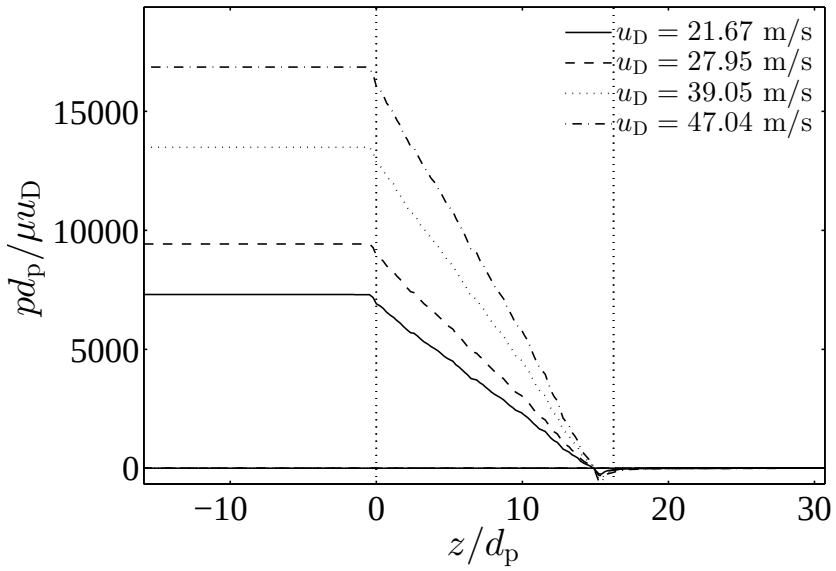

Figure 4.16: Dimensionless pressure profile at varying Darcian velocities across the Retimet 80 PPI foam for compressible airflow. Vertical dashed lines denote the entrance and exit of the foam sample respectively.

numerical Forchheimer coefficient results, showing deviations of approximately 16 and 13 % for the Inconel 450 µm and Retimet 80 PPI foams respectively. At high Reynolds numbers, the pressure losses along the foam length are mainly due to inertial effects, and the viscous losses are comparatively small. Thus, the Forchheimer term is likely more significant under these con-

ditions. For the flow conditions investigated here, the Mach number seems to increase together with Re_p, and compressibility effects becoming stronger at higher Mach numbers.

Table 4.4: Experimental and simulated results for permeability (m^2), and Forchheimer coefficient (m^{-1}) obtained from a linear fit using Eq. 2.45.

Sample	$K_{\mathrm{CFD}} \times 10^{-9}$	$K_{\mathrm{exp}} \times 10^{-9}$	RMS error (%)	F_{CFD}	F_{exp}	RMS error (%)
Inconel 450 µm	5.76	0.69	732.4	4030	4540	11.3
Retimet 80 PPI	13.5	3.07	340.33	1450	1500	3.31

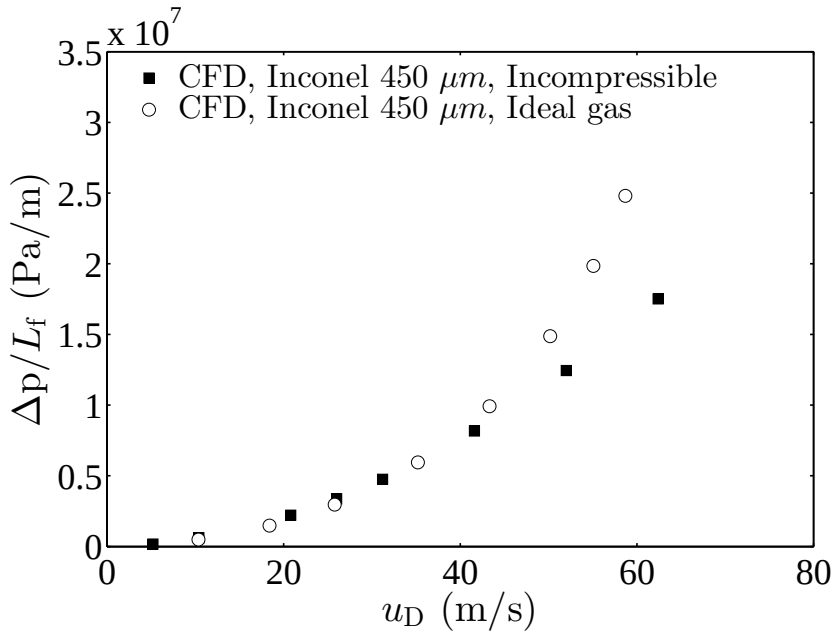

Figure 4.17: Comparison of the pressure gradient across the Inconel µm foam between simulations assuming incompressible and compressible ideal gas flow respectively.

The pressure gradient behaviour remains linear when considering fluid compressibility. Figure 4.16 depicts the dimensionless pressure profile across the Retimet 80 PPI sample at different Darcian velocities. Similarly to results obtained when considering incompressible airflow, the profile is linear, showing almost an absence of fluctuations due to the foam morphology.

Comparison between the normalized pressure gradient for simulations concerning incompressible and compressible ideal gas flow across the Inconel µm foam are depicted in Figure

4.17. It can be seen that the pressure gradient results given by both approaches start to diverge at Darcian velocities of over 40 m/s or approximately $\mathrm{Re}_p \sim 2000$. Therefore, the Mach number increases above 0.3 at high Reynolds numbers, and compressibility effects become significant. It is worth mentioning that the expected velocities next to the metal foam inlet within aero-engine separators are not expected to exceed 30 m/s at the ground idle engine regime, which is the worst in terms of oil separation. This corresponds to a range of approximately $1000 < \mathrm{Re}_p < 1500$ depending on the foam pore size and Mach numbers below 0.3.

4.4.5 Anisotropy analysis

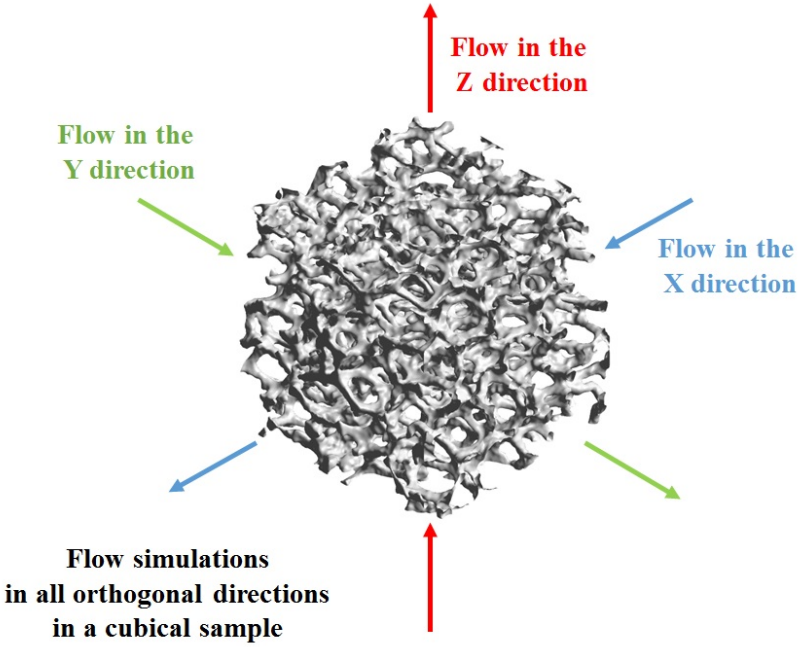

Figure 4.18: Schematic of the anisotropy flow analysis by means of numerical simulations. The Z direction is fixed as the axial direction of the tomographic datasets. Cubical foam samples are simulated with the flow aligned with all orthogonal directions.

The effect of anisotropy in the open-cell foam structure is often neglected in many pore-scale flow studies. As shown by the watershed pore segmentation results in Section 3.4.5 in Chapter 3, the pore cells of the foams seem to be slightly elongated in one Cartesian direction. The slight structural anisotropy is normally caused by the removal of inter-cellular material dur-

ing the manufacturing process. The question of whether the foam anisotropy affects the flow can be answered by means of pore-scale simulations on cubical foam samples varying the flow Cartesian (orthogonal) direction. Figure 4.18 depicts a schematic of the anisotropy numerical analysis. Representative cubical computational samples were generated from the original tomographic datasets. Laminar flow was computed varying the flow orthogonal direction, with $\mathrm{Re}_p = 1 - 200$, where the Z axis is the axial direction in the original tomographic datasets.

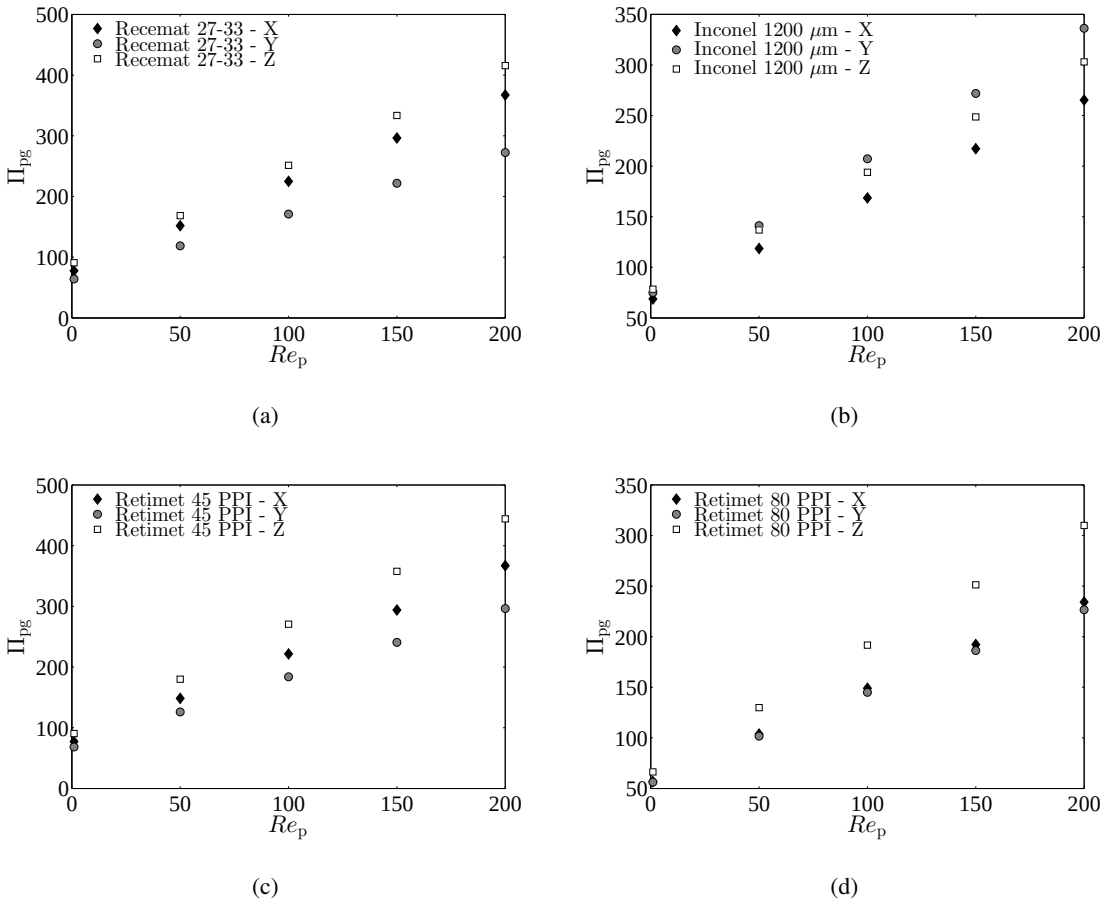

Figure 4.19: Simulations results showing the dimensionless pressure gradient along the three orthogonal directions for the (a) Recemat, (b) Inconel 1200 µm, (c) Retimet 45 PPI and (d) Retimet 80 PPI foams respectively.

Four samples are investigated, namely the Inconel 1200 µm, Recemat, Retimet 45 and 80 PPI. Figure 4.19 shows the variation of dimensionless pressure gradient with Reynolds number for various samples in all three Cartesian directions. Clearly, varying the orthogonal direction

of the incoming flow significantly impacts the dimensionless pressure gradient. This effect can be explained by the different mean pore cell widths in each orthogonal direction found in the investigated foams. A watershed pore segmentation routine is performed on the cubical samples used in the simulations, and the pore width in each orthogonal direction is measured, along with the average XYZ pore width. Table 4.5 shows the results for the average and mean cell width in each orthogonal direction. For comparison purposes, the mean dimensionless pressure gradient at all three orthogonal directions is computed for each sample. Thus, the relative deviation from the mean XYZ and the average dimensionless pressure gradient at each orthogonal direction can be calculated as

$$e(\bar{\Pi}_{\mathrm{XYZ}}, \Pi) = \sum_{i=1}^{n} \left(\frac{\bar{\Pi}_{\mathrm{XYZ}} - \Pi_i}{\bar{\Pi}_{\mathrm{XYZ}}}\right) \times 100\% \tag{4.7}$$

where e stands for the average relative deviation from the mean, $\bar{\Pi}_{\mathrm{XYZ}}$ is the mean dimensionless pressure gradient along the X, Y and Z directions and Π_i is the dimensionless pressure gradient at the i^{th} orthogonal direction.

Table 4.5: Cell width characteristics and the average relative dimensionless pressure gradient deviation from the mean.

Sample	$\bar{b}_{\mathrm{avg}}(mm)$	$[\bar{b}_x, \bar{b}_y, \bar{b}_z](mm)$	$[e_x, e_y, e_z](\%)$
Recemat NC 1723	1.159	[1.102, 1.277, 1.098]	[3.38, -20.26, 16.88]
Inconel 1200 µm	0.854	[0.908, 0.803, 0.850]	[-10.49, 7.87, 2.63]
Retimet 45 PPI	0.921	[0.916, 0.954, 0.893]	[-1.43, -17.45, 18.88]
Retimet 80 PPI	0.623	[0.632, 0.639, 0.597]	[-7.50, -9.68, 17.18]

The dimensionless pressure gradient average relative deviation from the mean is shown in Table 4.5. Results show that the pore width in a given direction is directly related with the pressure gradient in that same direction. Larger pore widths in a given spatial direction imply

in a smaller pressure gradient in that same direction. The opposite is also true, for a small pore width in a given direction implies in a greater pressure gradient in that same direction. For example, the pore width of the Recemat foam in the Y direction is roughly 10 % larger than the mean, whereas the dimensionless pressure gradient is approximately 20 % smaller than the mean. Conversely, the pore width in the Z direction is about 5 % smaller than the mean, whereas the dimensionless pressure gradient is roughly 17 % larger than the mean. Given the fact that the porosity and surface area remained constant for any given foam, the results clearly show a relationship between pore width and pressure gradient.

The spatial alignment of the samples was not taken into account when performing the pressure gradient measurements employed for validation. Therefore, it is not known if the computational samples employed for comparison against experimental data are spatially aligned in the same direction as the ones in the experiments. If the alignment between both was different, this could explain some of the discrepancies found between simulations and experiments. However, the question of whether these anisotropy effects remain significant if larger samples are simulated is left open, since larger tomographic datasets would be necessary.

4.4.6 Porosity variation effect

The effect of porosity variation on the pressure gradient can be explored by artificially varying the porosity of a given tomographic dataset by means of image morphological operations. The effect of addition or removal of solid material can be simulated by using iterative image morphological *dilations* and *erosions*, as described in the work of Akolkar and Petrasch (2012). These operations are performed using a spherical structuring element and are therefore isotropic. Dilations are equivalent to adding solid material at the solid-void interface and erosions are equivalent to removing material. In this case, the interest is in varying the effective porosity only, therefore the hollow struts are completely filled using image processing techniques prior to changing the porosity. In this way, dilations will decrease the effective porosity and erosions

increase it. Note that the specific surface will also change as a direct consequence of the porosity variation.

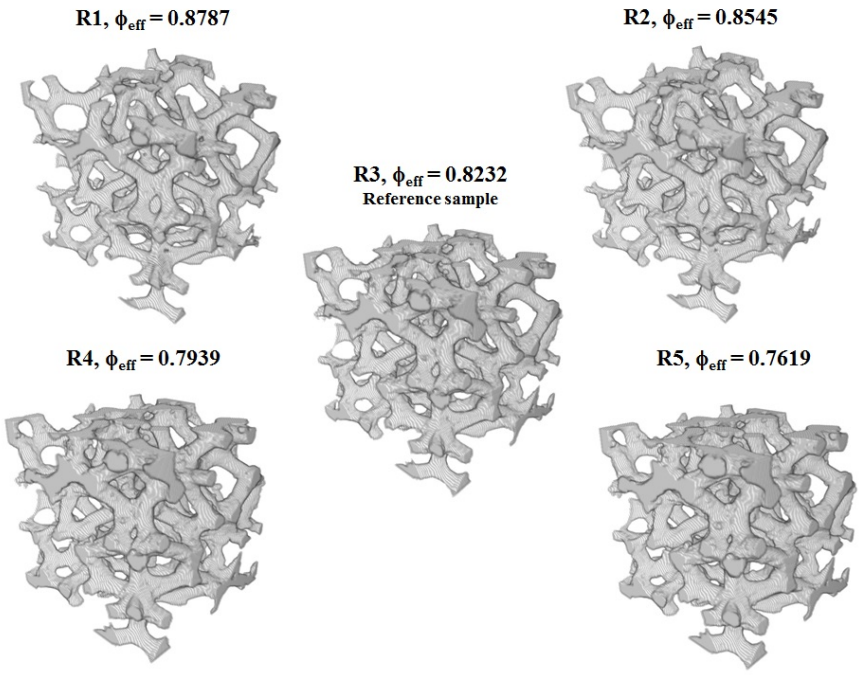

Figure 4.20: Volume rendering of the five Retimet 45 PPI samples investigated and their respective porosity values.

The effective porosity of a Retimet 45 PPI sample is artificially modified in order to investigate the sensitivity of pressure gradient to porosity variations. Five identical Retimet 45 PPI samples with different effective porosities were simulated under laminar flow, with $\mathrm{Re}_p = 1 - 200$. Figure 4.21 shows the plot of dimensionless pressure gradient for the five samples, where sample R3, with $\phi_{\mathrm{eff}} = 0.8232$ is the original unmodified foam.

Results demonstrated that small changes in effective porosity can greatly affect the pressure gradient across the foam. Table 4.6 shows the effective porosity and specific surface of each sample and the average deviation of the dimensionless pressure gradient, using sample R3 as the reference. For example, a decrease of ~ 3 % in ϕ_{eff} caused an increase of approximately 21 % in Π_{pg}. Increasing the effective porosity caused a decrease in the specific surface, whereas smaller porosity values increased specific surface values. It is worth mentioning that values of

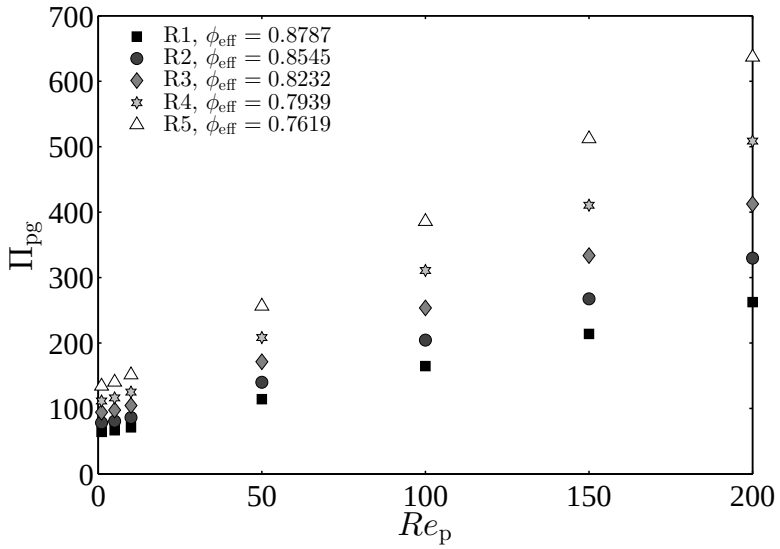

Figure 4.21: Simulated dimensionless pressure gradient for the Retimet 45 PPI foam with varying Re$_p$ and porosity.

permeability and Forchheimer coefficient are consequently affected by the porosity variations as shown in Table 4.6. Permeability increases with increasing porosity whilst Forchheimer coefficient values decrease.

Table 4.6: Characteristics of the Retimet 45 PPI samples with varying porosity and the dimensionless pressure gradient average deviation (Sample R3 is the reference).

Sample	ϕ_{eff}	s_{eff} (m^{-1})	Avg. Π_{pg} deviation (%)	$K_{\text{CFD}} \times 10^{-9}$ (m^2)	F_{CFD} (m^{-1})
R1	0.8787	2475.39	-33.68	13.4	1095.31
R2	0.8545	2777.04	-18.48	11.2	1390.72
R3	0.8232	3105.84	Reference	9.31	1760.04
R4	0.7939	3228.49	21.05	7.89	2193.95
R5	0.7619	3284.32	48.70	6.54	2773.82

4.5 Overview of the airflow pore-scale simulation results

For a more general base of comparison, the pressure loss characteristics of the metal foam samples investigated here can be viewed in terms of non-dimensional flow factors. One of which is the pore-based Reynolds number already mentioned. Another commonly used non-dimensional flow parameter is the Darcy-Weisbach friction factor (modified here to include the sample length and mean pore size), which was defined earlier in Eq. 4.4. Figure 4.22 shows friction factor values versus pore-based Reynolds number computed from the CFD solutions obtained for all samples.

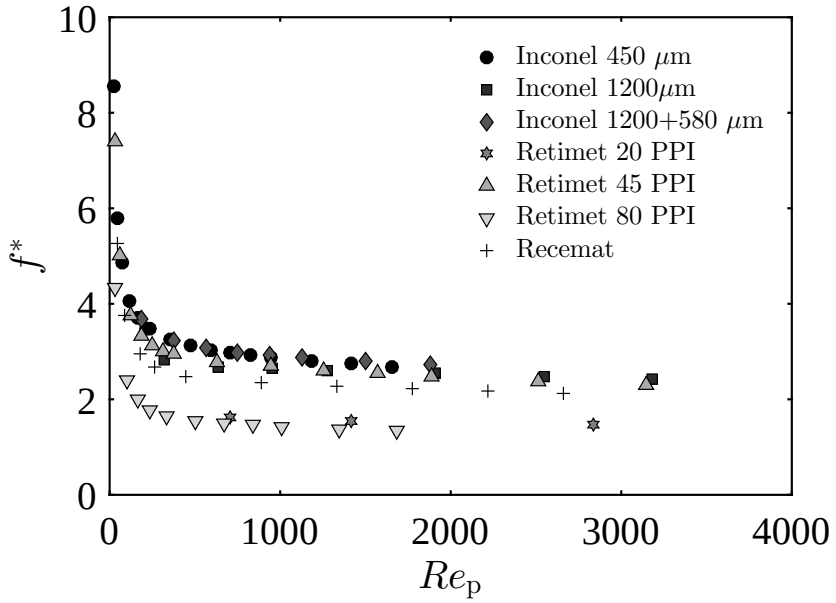

Figure 4.22: Friction factor versus pore-based Reynolds number for all samples investigated.

The Retimet 20 and 80 PPI friction factor behaviour seems to deviate from the other samples. For the Retimet 20 PPI, this is probably due to its large pore size compared to the other foams. On the other hand, the Retimet 80 PPI sample has a very peculiar behaviour, since it has a pressure gradient comparable to the Retimet 45 PPI, which has a mean pore size almost twice the size of Retimet 80 PPI. Nevertheless, the relationship between friction factor and pore-based Reynolds number depicted here follows a similar trend as the results reported in the work of (Liu et al., 2006).

Table 4.7: Permeability (m^2) and Forchheimer coefficient (m^{-1}) values calculated from Eqs. 2.41 and 2.42 (derived from Ergun equation), and deviation from experiments.

Sample	$K_{\text{Ergun}} \times 10^{-9}$	RMS error (%)	F_{Ergun}	RMS error (%)
Recemat	14.20	540.20	1430.50	194.65
Inconel 450 µm	1.48	172.05	4832.89	3.32
Inconel 1200 µm	8.16	453.13	1892.64	11.22
Inconel 580+1200 µm	2.94	83.35	3235.55	207.97
Retimet 20 PPI	53.4	23.30	714.23	87.08
Retimet 45 PPI	6.35	49.81	2359.67	104.39
Retimet 80 PPI	4.00	43.96	2738.72	81.18

Table 4.7 shows the permeability and Forchheimer coefficient values computed from the Ergun equation, using Eqs. 2.41 and 2.42 respectively, along with the RMS error for each parameter (experimental data as reference). The mean strut diameter was employed as the characteristic diameter for Eqs. 2.41 and 2.42. This is because the Ergun equation was developed for a packed bed of spheres, using characteristic length of the solid phase (sphere diameter). Results showed larger deviations between experimental data than the pore-scale simulations.

Section 4.4 attempts to provide a detailed analysis on the pressure gradient behaviour across open-cell metal foams, also uncovering possible sources of discrepancies between the experiments and pore-scale simulations. Wall effects were investigated by performing a set of simulations on a cylindrical channel computational domain. The results have shown that wall effects can become quite significant if the dimensionless diameter of the cylinder, d_{cyl}/d_p, is small. In other words, wall effects are larger if the cylinder diameter is small in relation to the foam pore size, as expected. The test samples measured experimentally had a large dimensionless diameter, thus minimizing wall effects.

Entrance effects have been captured in simulations of a foam with varying streamwise thickness. Results have shown that there is a critical streamwise thickness above which the pressure gradient is no longer affected. The critical thickness is commonly measured in terms of number of pore sizes. Simulation results have shown the critical thickness of the Inconel 450 µm foam to lie between 25 - 50 d_p, which is in agreement with literature data (Baril et al., 2008). However, these results also show that most samples investigated in the present work probably have a streamwise thickness smaller than the critical one, in both the experiments and simulations.

Transient simulations performed on a Recemat sample showed the presence of unsteady flow features. However, time-averaged pressure gradient results showed a negligible difference when compared to a steady state simulation. Transient simulations take from 10-20 times longer to run, therefore their use is not justified in the context of the present work. Simulations assuming air compressibility have shown that the Mach number can increase significantly at higher pore-based Reynolds numbers ($\mathrm{Re}_p > 2000$), and fluid compressibility effects become important. At high inlet airflow velocities, several regions of the interstitial space within the foam can show Mach number values larger than 0.3, and pressure gradient results start to deviate from incompressible simulation results at such conditions.

The watershed pore segmentation results depicted in Chapter 3 have shown a certain level of anisotropy in the pore space of the investigated foams. Simulations on a cubical sample with the incoming flow varying along three orthogonal directions have shown that the spatial alignment of the foam sample may affect the pressure gradient significantly. A direct relation between the pore width and pressure gradient in a specific spatial direction has been shown. Higher pore width in a given spatial direction implies a lower pressure gradient in that same direction. Thus, a certain level of anisotropy in the foam morphology seems to significantly affect the pressure gradient.

Finally, effect of porosity variation on the pressure gradient has been analysed by artificially varying the effective porosity of a Retimet 45 PPI sample. Results have shown that the pressure

gradient is greatly affected by a relatively small ($\sim 3-6\%$) variation in porosity. A decrease in the effective porosity causes a greater increase in the pressure gradient. Although these results were expected, the magnitude of the effect had to be quantified.

Single phase airflow steady state solutions can be employed for performing Lagrangian oil droplet tracking calculations, with the purpose of obtaining a qualitative assessment of the oil capture effectiveness. Since the pressure gradient is extremely important in the context of aero-engine separators, Figure 4.23 depicts the CFD (square channel domain) results of all samples together, comparing the normalized pressure gradient as a function of the Darcian velocity, under a range of 0-50 m/s.

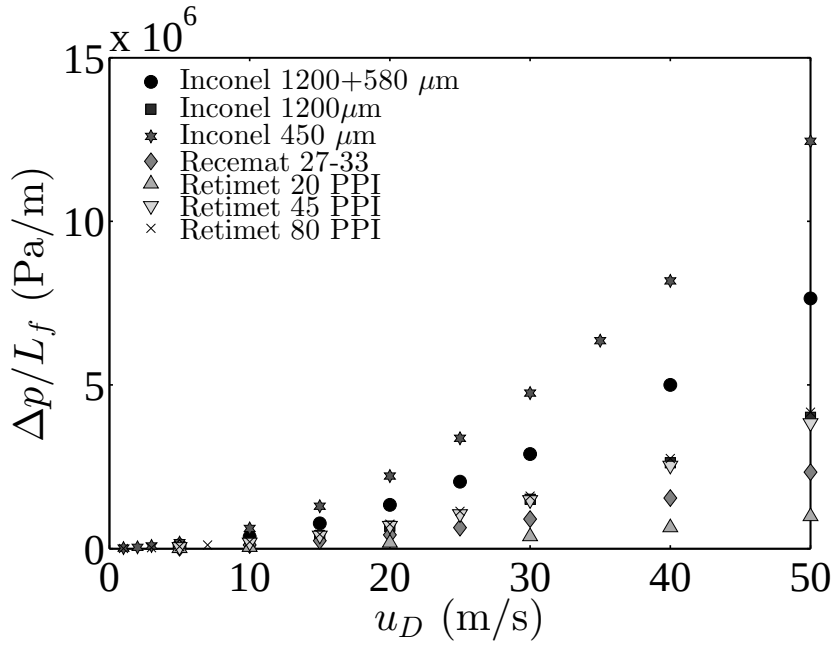

Figure 4.23: Comparison of the simulated pressure gradient gradient of all open-cell metal foam samples investigated.

Generally, foams with smaller pore sizes show a higher normalized pressure gradient, whereas samples with the larger pore sizes presented lower normalized pressure gradient values. Morphological characterization results reported in Chapter 3 have shown that the pore size is inversely proportional to the specific surface area. Similarly, the computed permeability values from pore-scale simulations have been found to be inversely proportional to the surface area

of the foams, with some samples presenting a small deviation from this general trend. Figure 4.24a depicts the CFD permeability values for all foams as a function of the specific surface area. Permeability is also a function of porosity, but since the samples investigated here have a relatively narrow porosity range, 0.82-0.89, the specific surface area seems to be a more representative morphological parameter. It is interesting to compare results for the Inconel 1200 µm and Retimet 45 PPI, since both foams have very similar morphological properties. Even though the Inconel 1200 µm has a larger specific surface than the Retimet 45 PPI, it also presents a higher permeability, which goes against the general trend. This discrepancy is probably caused by the specific arrangement of the solid matrix of the Inconel 1200 µm, since permeability is a property of the porous medium structure.

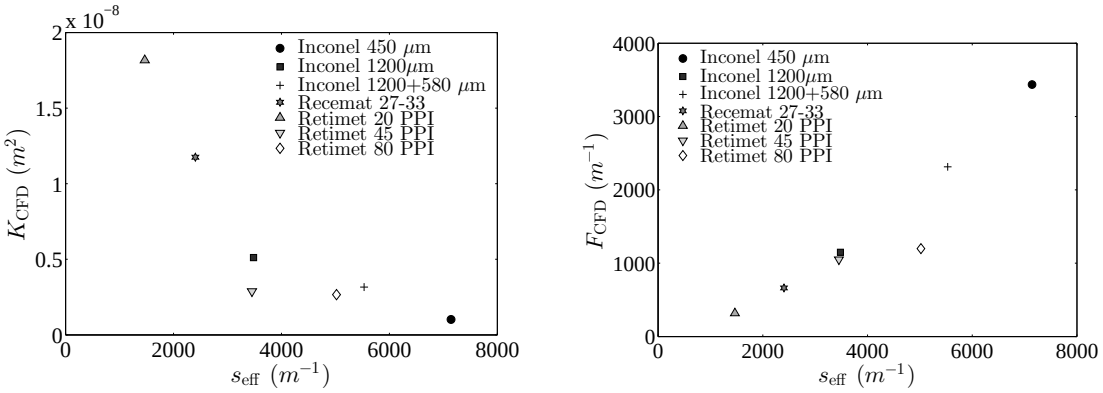

(a) (b)

Figure 4.24: Permeability (a) and Forchheimer coefficient (b) values computed from the pore-scale simulations as a function of the effective specific surface for all foam samples.

Figure 4.24b depicts the computed CFD Forchheimer coefficient values as a function of the effective specific surface area. The Forchheimer coefficient appears to be proportional to the effective specific surface of the foam. Furthermore, higher values of the coefficient have been found to be associated with higher normalized pressure gradient values and vice-versa. Interestingly, the Forchheimer coefficient obtained for the Retimet 80 PPI foam is at the same level of the Forchheimer coefficnet values obtained for the Inconel 1200 µm and Retimet 45 PPI foams,

even though the specific surface of the Retimet 80 PPI is much larger. Like permeability, the Forchheimer coefficient is a property of the porous medium structure. This shows that transport properties are affected by the morphological parameters but also by the specific arrangement of the solid matrix.

As a general trend, it is expected that foams with larger specific surface to be more efficient at oil capture, which assumes that a greater *blockage* of the flow area would cause a larger number of oil droplets to hit the solid structure, thus being captured. If this assumption is true, the oil capture effectiveness would also be a function of the permeability and Forchheimer coefficient, a fact that would likely facilitate the transferring of pore-scale simulation results to a macroscopic model which can be employed in a full aero-engine separator simulation. The following section describes a first attempt at obtaining a qualitative assessment of the oil capture in open-cell metal foams by the use of a series of Lagrangian droplet tracking calculations.

4.6 Oil phase pore-scale simulations

The assessment of the oil capture effectiveness within open-cell metal foams by means of pore-scale simulations should be considered as a feasibility study in the present work. To the knowledge of the author, there are no similar studies published in the open literature. Furthermore, no experimental data to validate the oil separation within open-cell metal foams is available. Therefore, the approach employed in the present work is qualitative. Nevertheless, it is a first step in the development of an aero-engine modelling framework that takes into account oil separation phenomena within metal-foam-based breathers.

The numerical modelling methodology for treating gas-liquid two-phase flow can be basically distinguished between Eulerian-Eulerian and Eulerian-Lagrangian approaches. Eulerian-Eulerian methods solve both phases in the same inertial frame of reference, and some models also require an additional interface tracking algorithm. The volume of fluid (VOF) method by Hirt and Nichols (1981) is one example of such type of approach. VOF is suited to model immiscible fluid phases and has extremely high mesh requirements in order to accurately resolve the gas-liquid interface. The VOF tends to become very computationally intensive if there is a very high number of liquid droplets and/or ligaments in the flow. Other Eulerian-Eulerian methods track the liquid volume fraction instead, and require empirical relationships to account for the effect of the disperse phase on the continuous one.

An alternative is to employ an Eulerian-Lagrangian approach to model low volume loading gas-liquid flows. The gas phase is treated as a continuous phase in an inertial frame, whereas the droplets (or parcels representative of a certain number of droplets) are treated in a Lagrangian framework, with each representative droplet having its own reference frame. In this context, a droplet can be regarded as a spherical liquid volume held together by surface tension forces. The interaction with the gas phase could cause deformation on the droplet shape due to aerodynamic drag for example. Nevertheless, the focus here is on the motion of droplets with small diameters

(< 15 μm), therefore shape deformation can be considered negligible.

In the commercial solver employed here, Ansys Fluent, the Lagrangian model is referred to as the Discrete Phase Model (DPM). Numerically, each representative droplet is essentially a mathematical point that travels along the continuous phase, with an associated diameter and physical properties. A particle tracking algorithm is employed to solve the Lagrangian phase equations. The DPM approach is able to calculate the motion of a large number of representative droplets using relatively low computational resources. One of the drawbacks however, is that droplet-droplet and droplet-solid interaction phenomena often require the use of empirical correlations, which are available only for simple idealized cases.

4.6.1 Lagrangian tracking formulation

Within the DPM modelling framework, the fluid phase is treated as a continuum phase by solving the usual flow governing equations described in Section 2.2, whilst the disperse phase is solved by tracking a large number of particles through the computed flow field. The particles can be either solid or liquid. The trajectory of a particle is computed by integrating the force balance as

$$\frac{\partial \mathbf{u_d}}{\partial t} = \frac{\mathbf{u_g} - \mathbf{u_d}}{\tau_r} + \frac{\mathbf{g}(\rho_d - \rho_g)}{\rho_d} + \mathbf{F} \tag{4.8}$$

with the subscripts g and d referring to the gas and droplet state variables. The term $\mathbf{F}$ is an additional acceleration (force/unit droplet mass) term, and $\frac{\mathbf{u_g}-\mathbf{u_d}}{\tau_r}$ is the drag force per unit droplet mass. τ_r is the droplet relaxation time, defined as

$$\tau_r = \frac{\rho_d d_d^2}{18\mu_g} \frac{24}{C_D \mathrm{Re_d}} \tag{4.9}$$

where Re_d is the droplet Reynolds number, defined as

$$\mathrm{Re}_d = \frac{\rho_g d_d |\mathbf{u_d} - \mathbf{u_g}|}{\mu_g} \tag{4.10}$$

The term **F** incorporates additional forces acting upon the droplet that arise under special circumstances. Examples of additional forces include the virtual mass force, and forces due to a pressure gradient in the fluid. However, these only become significant when the density ratio between the liquid and gas phases approach unity, which is not the case here.

The term C_D denotes the drag coefficient. Here, the droplets are assumed to be perfectly spherical and non-deforming. The drag coefficient is expressed by

$$C_D = a_1 + \frac{a_2}{\mathrm{Re}_d} + \frac{a_3}{\mathrm{Re}_d^2} \tag{4.11}$$

where a_1, a_2 and a_3 are constants that apply over several ranges of the particle Reynolds number, and are given in Morsi and Alexander (1972). The droplets are assumed to be isothermal and inert, therefore without undergoing energy or mass transfer.

If the Lagrangian phase is affected by the Eulerian phase but not the other way around, it is referred to as a *one-way coupling*. However, there might be instances where both phases affect each other, which is referred to as *two-way coupling*. When that is the case, the calculations must be carried out in a transient manner. Thus, the momentum exchange for a droplet passing through a control volume is expressed as a source term in the momentum equations for the continuum as

$$\mathbf{F} = \sum \left(\frac{18\mu_g}{\rho_d d_d^2} \frac{C_D \mathrm{Re}_d}{24} (\mathbf{u}_g - \mathbf{u}_d) \right) \dot{m}_d \Delta t \tag{4.12}$$

where Δt denotes the flow time step, and $\dot{m}_d$ denotes the mass flow rate of the droplet.

The droplet trajectory equation and any auxiliary equations are solved by stepwise integration over discrete time steps. The droplet displacement is computed using a trapezoidal implicit scheme,

$$\mathbf{x}_i^n = \mathbf{x}_i^o + \frac{1}{2} \Delta t (\mathbf{u}_{di}^o + \mathbf{u}_{di}^n) \tag{4.13}$$

where the subscripts o and n refer to old and new values respectively, and $\mathbf{u}_{di}$ is the velocity vector of the i_{th} droplet.

4.6.2 Turbulent dispersion of droplets

The dispersion of droplets due to turbulence in the gas phase is predicted by using a stochastic tracking approach. The random walk model is employed, where the instantaneous velocity fluctuations on droplet trajectories are represented by stochastic methods.

The prediction of turbulent dispersion is achieved by integrating the trajectory equations for individual droplets using the instantaneous fluid velocity, $\overline{u}_d + u'_d(t)$, along the droplet path. The random effects of turbulence are included by computing the trajectories in this manner for a sufficient number of representative droplets.

4.6.2.1 The Discrete Random Walk Model

The discrete random walk (DRW) model simulates the interaction of a droplet with a succession of discrete stylized fluid phase turbulent eddies. The fluctuating velocity components are defined as discrete piecewise functions of time. The interval of time in which their random value is kept constant is defined by the characteristic lifetime of the eddies. Each eddy is characterized by a Gaussian distributed random velocity fluctuation, u', v' and w', and a time scale, τ_e. The values of the random velocity fluctuation components that prevail during the lifetime of a turbulent eddy are sampled assuming they obey a Gaussian probability distribution,

$$u' = \zeta \sqrt{\overline{u'^2}} \tag{4.14}$$

where ζ is normally distributed random number and the remainder of the right-hand side accounts for the local root-mean-square (RMS) velocity fluctuations. Assuming the kinetic energy of turbulence is isotropic in the flow, the values of the RMS fluctuating components can be defined as

$$\sqrt{\overline{u'^2}} = \sqrt{\overline{v'^2}} = \sqrt{\overline{w'^2}} = \sqrt{\frac{2k}{3}} \tag{4.15}$$

where k is the turbulent kinetic energy. This is valid for the k-ε, the k-ω models and their variants. The characteristic lifetime of an eddy is defined as a constant, such as

$$\tau_e = 2T_L \tag{4.16}$$

with $T_L \approx C_L \frac{k}{\varepsilon}$, where T_L is the integral time, k and ε are the turbulent kinetic energy and dissipation rate respectively, and C_L is a constant that depends on the turbulence model. The characteristic lifetime of an eddy can also be defined as a random variation about T_L, such as

$$\tau_e = -T_L \ln(\lambda) \tag{4.17}$$

where λ is a uniform random number greater than zero and less than 1. The droplet eddy crossing time is defined as

$$t_{\text{cross}} = -\tau_r \ln\left[1 - \left(\frac{L_e}{\tau_r \mid \mathbf{u_g} - \mathbf{u_d} \mid}\right)\right] \tag{4.18}$$

where L_e is the eddy length scale, τ_r is the droplet relaxation time and $\mid \mathbf{u_g} - \mathbf{u_d} \mid$ is the magnitude of the relative velocity.

The droplet is assumed to interact with the continuous phase eddy over the smallest of the eddy lifetime and crossing time. After this time is reached, a new value of the instantaneous velocity is computed by applying a new value of ζ. Thus, the only inputs the DRW model require are the value of the constant C_L, and the choice of eddy lifetime prediction method.

4.6.3 Simplifications, assumptions and boundary conditions

Nearly every numerical model involves a certain number of simplifications and assumptions due to unknown physics (lack of information regarding initial or boundary conditions) and time

constraints aimed at reducing the computational costs. Some knowledge concerning the form and behaviour of the oil phase next to the metal foam region is necessary in order to make the right assumptions and develop a suitable CFD approach.

As mentioned previously, there is no experimental data available concerning the oil flow within open-cell metal foams. The scarcity of information regarding the oil phase poses a problem in the development of an appropriate numerical approach. The best information available in order to estimate the boundary conditions around the metal foam region within aero-engine separators come from experiments and in-house CFD simulations performed for an industrial aero-engine separator design.

Willenborg et al. (2008) have measured performed measurements in an aero-engine separator which employed a Retimet 45 PPI foam. Results have shown the presence of sub-micron droplets (~ 0.5 µm) at the separator outlet, thus not being captured by the metal foam. However, it was not possible to measure the droplet diameter distribution at the foam entrance region. CFD simulations conducted by Verger and Morvan (2011) have shown that the maximum droplet size able to reach the metal foam entrance was dependent on the shaft rotational speed. The worst case scenario happened at lower rotational speeds, and droplet diameters up to 12 µm were observed at the porous medium inlet.

As noted in Willenborg et al. (2008), the main concern in terms of separation effectiveness is with small droplets, which normally represent a very small portion of the typical oil flow at real engine conditions. More recently, unpublished experiments conducted at the KIT employed an oil mass fraction of up to 2 % at the inlet of the aero-engine separator test rig. Since not all the oil manages to get to the metal foam entrance, it is safe to assume that the quantity of oil at the metal foam inlet should be less than 2 % mass fraction at that experimental configuration. Here, a conservative oil mass fraction value of 5 % is assumed at the metal foam entrance for all DPM simulations. No droplet diameter distribution is assumed, instead, separate uniform sized droplet calculations are performed for diameters ranging from 0.1 - 15 µm. This way, the

oil separation effectiveness can be evaluated qualitatively for each individual droplet diameter. This choice of diameter range is quite arbitrary, however, the limited literature data points that this diameter range is the most problematic in terms of oil separation.

The modelling of all physical effects related to droplet dynamics can be very computationally intensive even for a single droplet. Droplet deformation and breakup are not taken into account in the present work, which is reasonable given the small droplet sizes being analysed. No dynamic interaction with the metal foam solid structure is considered, such as film formation, splashing, rebounding or stripping. Even though liquid film models are available in Ansys Fluent, they have a limited range of applicability. The complexity of the solid structure of the foams and the small length scales involved here are likely render such models ill-suited for the present study.

A simplified oil capture criterion is employed, assuming the droplet trajectory to be terminated if it hits the solid structure of the foam. It is assumed that the droplet always sticks to the foam surface if it comes in contact with it. Even though this approach might not be realistic in a sense that all the droplet-solid interaction phenomena is being neglected, it offers a simple way to qualitatively evaluate the separation effectiveness. However, it should be noted that in reality, it is likely that the oil accumulates and forms a film on the surface of the foam. Oil extinction curves can be obtained by computing the impact normalized (streamwise) location (z/L_f) of each droplet along the entire metal foam length. In that way, the fraction of captured (or non-captured) droplets can be computed as a function of the normalized metal foam streamwise length. Figure 4.25 shows a schematic of the oil capture approach employed here, illustrating examples of the trajectories of a non-captured and captured droplet respectively.

Gasoil-liquid ($C_{16}H_{29}$) material properties were used for the oil phase. An inlet oil mass fraction of 5 % results in a volume fraction of approximately 0.008 %, which is an important parameter in order to estimate the interaction between the gas and oil phase. According to Eaton (2009), the dispersed phase can have a very strong effect on the gas-phase flow, even at

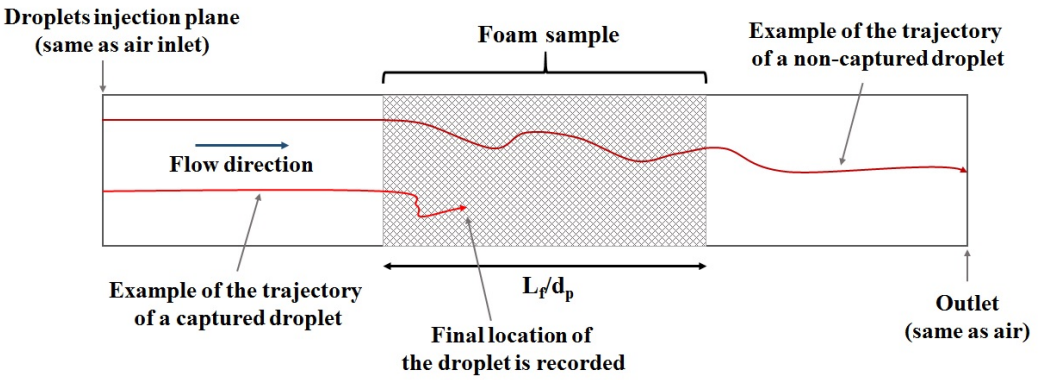

Figure 4.25: Schematic of the oil droplet capture criterion employed. It depicts examples of the trajectories for a non-captured and captured droplet respectively.

particle volume fractions below 0.1 %. Alternatively, Elghobashi (1994) argues that interaction between the gas flow and disperse phase can take place between volume fractions of 0.0001 - 0.1 %, with particle-particle interactions being negligible. The oil volume fractions values considered here are within an intermediate range where interaction with the continuous phase may become important. Taking into account the interaction with the gas phase implies the need of a transient simulation, which could raise the computational costs by more than one order of magnitude, compared to a steady state Lagrangian approach. However, Kulick et al. (1994) showed by means of experiments that the interaction between small dense particles and airflow has mainly attenuated the fluid turbulence, whereas the fluid velocity profiles remained virtually unchanged. In view of these results, and to reduce computational costs, it was decided to not take into account the effect of the droplets on the gas phase. Furthermore, droplet-droplet interactions are neglected.

All Lagrangian calculations are performed one-way coupled and in steady-state, using converged pore-scale solutions of the airflow. The results obtained using the square channel computational domains are employed. The effect of the airflow velocity on the droplet capture is evaluated by performing the Lagrangian simulations under different airflow velocities, ranging from 5 - 50 m/s. The droplets are injected from a plane located next to the air inlet, assuming

the same velocity of the incoming airflow. The droplet dispersion due to turbulence is taken into account by the use of a random walk stochastic model.

Since converting the oil injection mass flow rate into the actual number of droplets often results in a prohibitively high number, the concept of droplet parcel is employed. A parcel can be seen as a representative droplet, with a specified diameter and a relaxation time associated with a single droplet. Therefore, the DPM model actually tracks a number of parcels, each being representative of a certain real number of droplets, and containing a fraction of the total mass flow injected. A sensitivity analysis showed that a total number of 25,000 droplet parcels can produce statistically representative oil capture results that are independent of the number of injected parcels. The gravitational force is neglected due to the small droplet mass and relatively large inertial forces. Table 4.8 provides an overview of the Lagrangian model assumptions and settings.

Table 4.8: Overview of the DPM settings and model assumptions

DPM setting	Model assumption
Droplets, gasoil-liquid ($C_{16}H_{29}$)	inert, spherical
Droplet energy transfer	no
Droplet mass transfer	no
Forces considered	aerodynamic drag
Droplet breakup	no
Droplet-droplet interaction	no
Droplet splashing, rebounding	no
Film formation	no
Turbulent dispersion	yes
Coupling	one-way
Diameters investigated (μm)	0.1, 0.5, 1, 3, 5, 10

Droplet injection velocity	same as air
Airflow velocities considered (m/s)	5, 10, 20, 30, 40, 50
Droplet injection location	distributed over the air inlet
Number of droplet parcels injected	25,000

4.6.4 Oil capture results

The oil capture criterion assumes the termination of the droplet parcel trajectory if it intercepts the foam surface. Therefore, the main separation mechanism here is the droplet's inertia and the only force acting on the droplets is the aerodynamic drag. The flow streamlines diverge as they approach the metal foam ligaments, since the air passes around the foam solid ligaments. In the case of droplets, if they have sufficient inertia, they tend to follow different trajectories from the fluid streamlines. Typically, the more inertia the droplet has, the larger the deviation from the fluid streamlines, therefore, if the amount of deviation from the fluid streamlines is large enough, the droplet may end up intersecting the solid ligaments and get captured. It is worth mentioning that the size of the foam solid ligaments here is roughly more than 10 times the size of the largest droplet diameter investigated. Figure 4.26 illustrates the oil droplet trajectories across the Retimet 45 PPI foam for an inlet velocity of 20 m/s and three different droplet diameters: 0.5, 1 and 3 μm. Clearly, as the droplet diameter increases, so does the number of droplets captured as they pass through the metal foam, since larger droplets have more inertia.

The fraction of escaped or free droplets, η_{fd}, is defined as the number of non-captured droplets divided by the total number of droplets injected. In order to determine when a droplet has hit the foam, the full trajectory data is exported from Ansys Fluent and read by a Matlab script, which computes the final streamwise position, z, of all droplet trajectories, and then normalizes it by the mean pore size of the given foam sample, such that z/d_p. Thus, the fraction

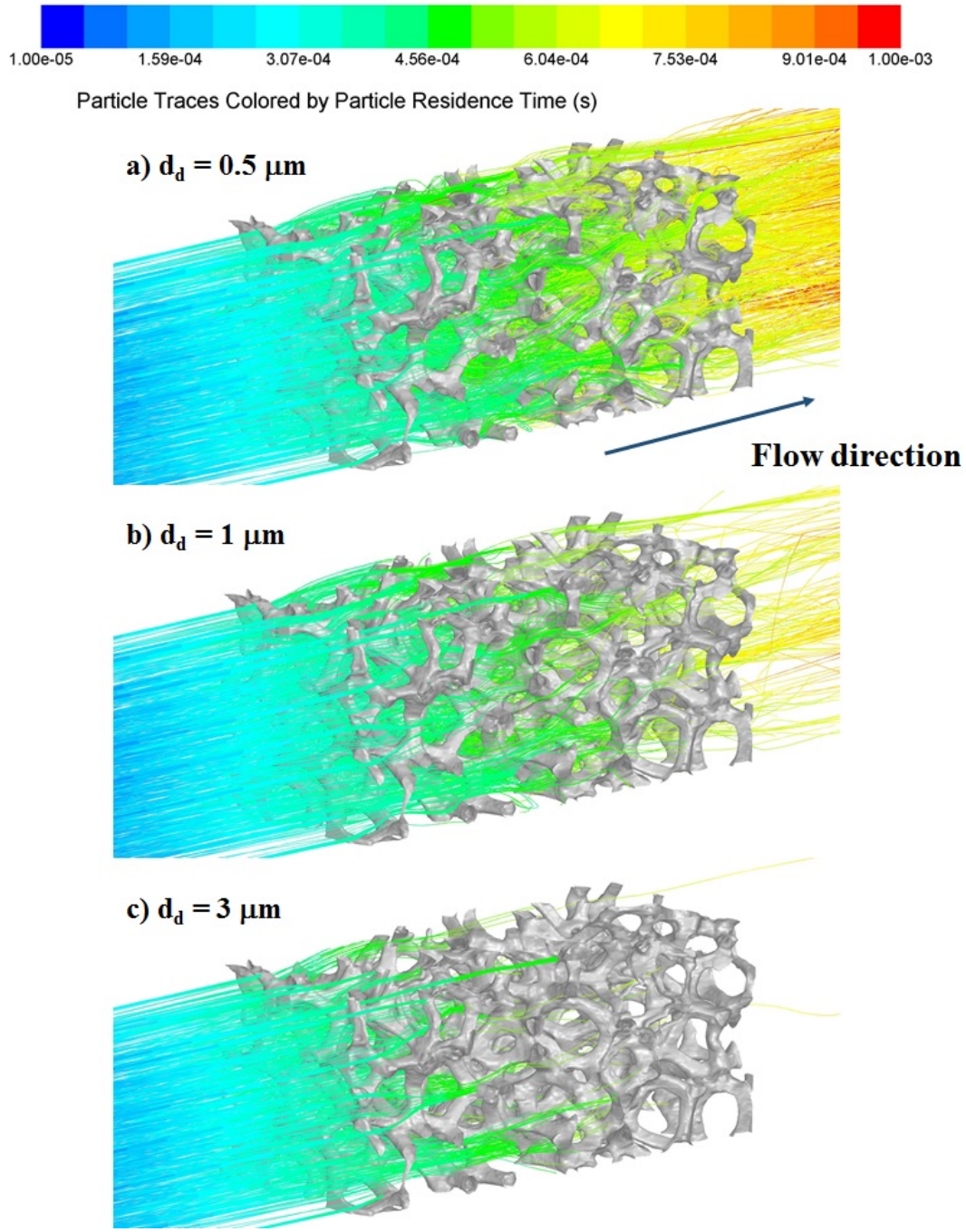

Figure 4.26: Droplet trajectories through the Retimet 45 PPI foam for an inlet velocity of 20 m/s and three uniform droplet diameters: 0.5, 1 and 3 µm. The number of trajectories was reduced for illustration purposes.

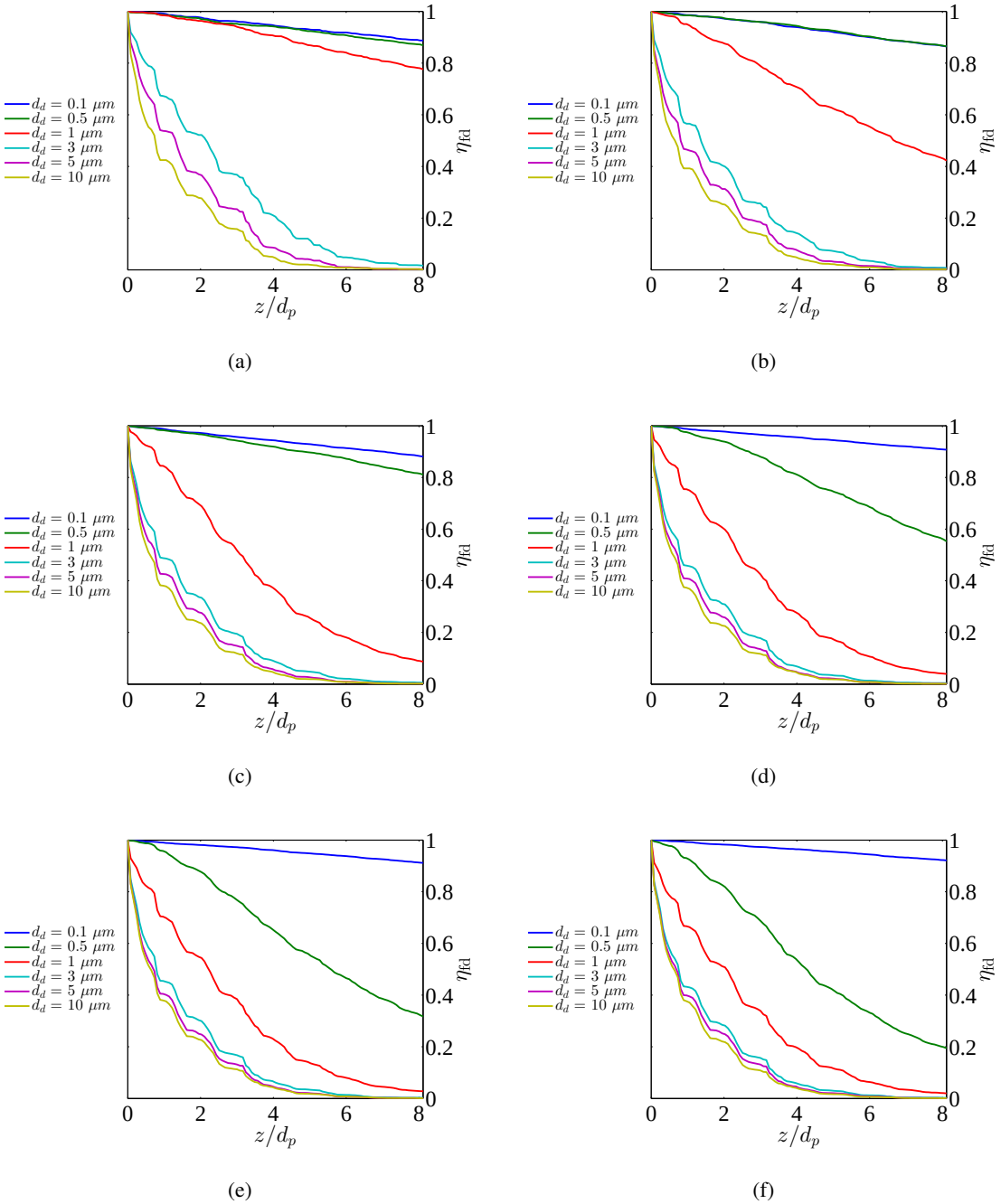

Figure 4.27: Lagrangian simulations results showing oil capture curves for the Retimet 45 PPI for different droplet diameters. Results are shown for six Darcian velocities: (a) 5, (b) 10, (c) 20, (d) 30, (e) 40 and (f) 50 m/s.

of non-captured droplets is computed along the entire length of the foam, generating distinct oil capture curves for each droplet diameter and flow velocity. Figure 4.27 shows the oil capture curves obtained with the DPM simulations performed on the Retimet 45 PPI foam at Darcian velocities of 5, 10, 20, 30, 40 and 50 m/s and six different droplet diameters. Oil capture curves obtained for other foam samples are depicted in Appendix B.

These results show that the flow velocity has a significant impact on the oil capture for intermediate diameters of 0.5 to 3 μm. Higher droplet inertia implies in a greater deviation from the flow streamlines, thus leading to a higher probability of collision against the foam ligaments. A marginal increase in the oil capture is observed for larger droplet diameters (5 and 10 μm) when the flow velocity is increased, since the oil capture is already very high even at low flow velocities. Conversely, for the smallest diameter of 0.1 μm, no clear pattern seems to emerge, and the majority of droplets tend to pass unnoticed through the foam, with the fraction of free droplets seeming to be independent of the flow velocity.

Oil capture results obtained for the other foams showed a very similar pattern, but with different values of oil capture depending on the foam. Perhaps unsurprisingly, foams with a smaller pore size and larger specific surface area showed an increased oil capture when compared with foams with larger pore sizes and smaller specific surface area. In order to perform a meaningful comparison between the oil capture results obtained for different foam samples, values of the fraction of free droplets computed at the normalized position of $z/d_p = 5$, are plotted together in Figure 4.28 for four different droplet diameters, 0.5, 1, 3 and 5 μm. The Retimet 20 PPI was left out of this analysis due to the fact that it had a total normalized streamwise length smaller than 5 pore sizes. Results clearly show the fraction of free droplets at $z/d_p = 5$ decreases with an increase in the flow velocity for all samples, with this effect being more significant for smaller droplet diameters.

A closer inspection in the results displayed in Figure 4.28 show some interesting insights. The Inconel 450 μm sample yielded the highest oil capture, as expected. However, it does so at

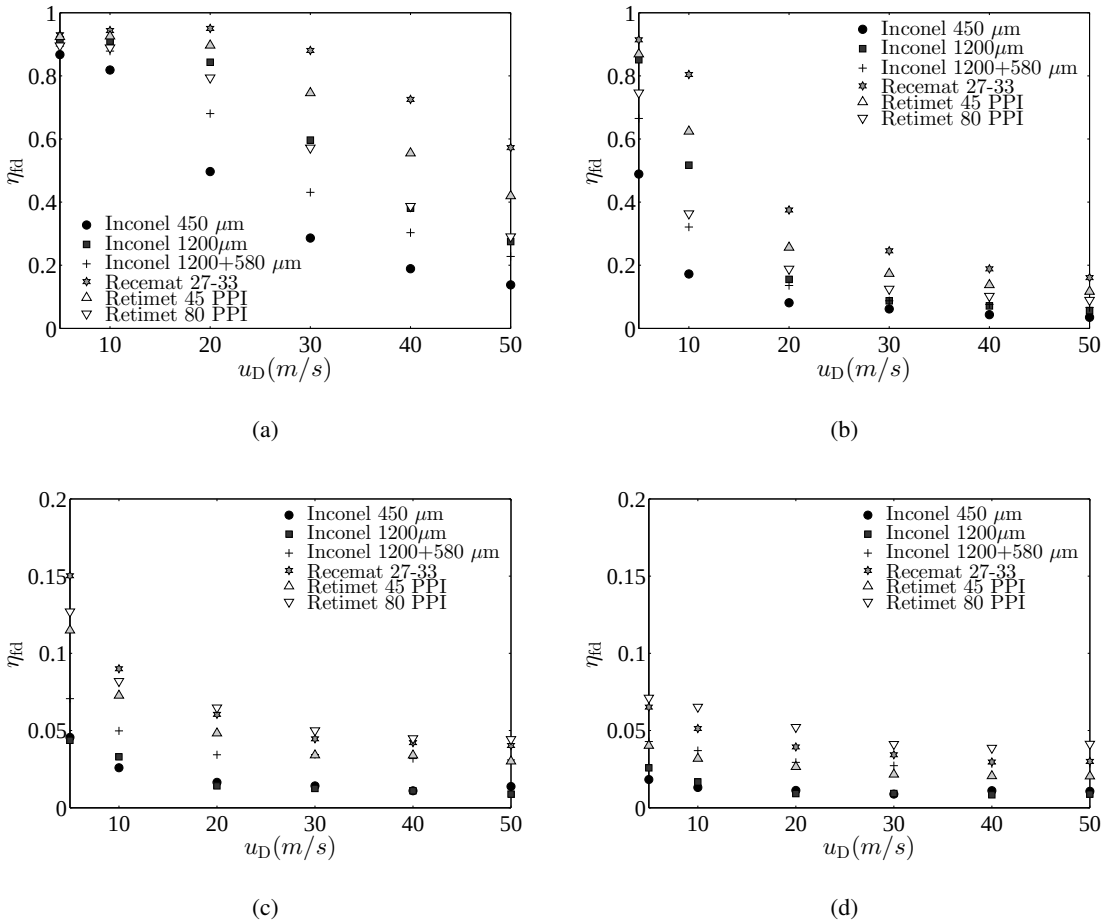

Figure 4.28: Fraction of non-captured droplets computed at the normalized position $z/d_p = 5$ versus the Darcian velocity for four different droplet diameters, (a) 0.5, (b) 1, (c) 3 and (d) 5 µm.

the expense of having a higher pressure gradient, as shown in Figure 4.23. The hybrid Inconel 1200+580 µm, which has the second highest pressure gradient, showed also the second highest oil capture results for droplet diameters of 0.5 and 1 µm. Interestingly, this trend is not observed for droplet diameters of 3 and 5 µm. For these two larger diameters, the Inconel 1200 µm sample showed a better oil capture than the Inconel 1200+580 µm foam. This is a largely unexpected result, since the Inconel 1200 µm sample has a smaller specific surface area. The results depicted in Figure 4.23 show that the Retimet 45 PPI, 80 PPI and the Inconel 1200 µm presented very similar pressure gradients. However, very distinct oil captured results were obtained for these

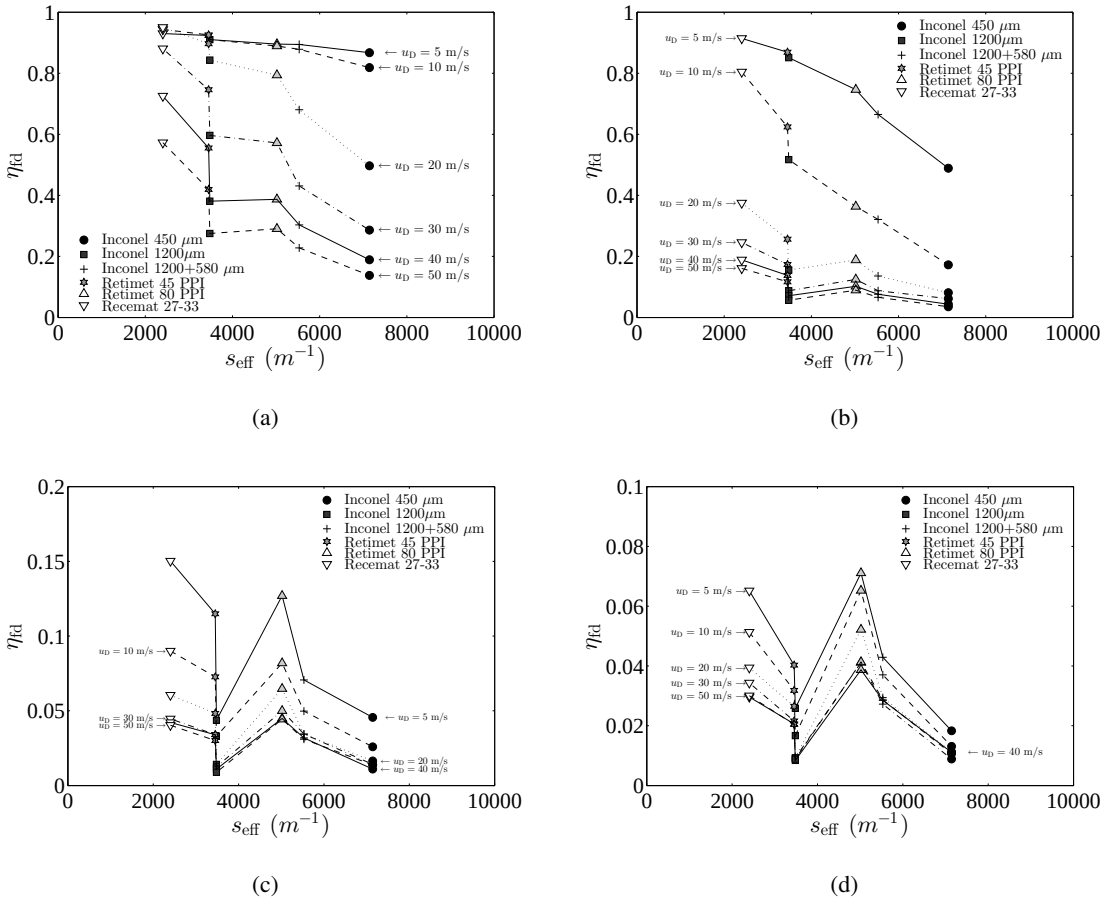

Figure 4.29: Fraction of non-captured droplets computed at the normalized position $z/d_p = 5$ versus the specific surface for four different droplet diameters, (a) 0.5, (b) 1, (c) 3 and (d) 5 µm.

three foam samples. The Retimet 80 PPI showed a particularly low oil capture, even lower than the Recemat capture results for diameters of 3 and 5 µ, which was quite surprising given that the Recemat has a much larger pore size.

It has been shown before that the pressure gradient of the foams is roughly proportional to their specific surface area. Oil capture was also expected to be roughly proportional to the specific surface area, since a larger value of surface area normally implies a greater number of foam solid ligaments per unit volume, therefore increasing the chances of droplet impact. Figure 4.29 shows the fraction of non-captured droplets at $z/d_p = 5$, plotted as a function of the specific surface area, under different flow velocities and for four droplet diameters: 0.5, 1, 3 and 5 µm (from top left, clockwise direction). The fraction of free droplets computed for droplet

diameters of 0.5 and 1 μm showed to be inversely proportional to the surface area. However, the free droplets fraction computed for larger diameters, namely 3 and 5 μm, did not show any clear trend, with the Retimet 80 PPI showing the worst droplet capture relative to its specific surface area. These results seem to imply that the likelihood of a droplet being intercepted by a foam ligament is not only a function of the specific surface area, but also of the particular morphology of the foam solid matrix.

The behaviour of suspended inertial particles in a flow can often be described by the dimensionless Stokes number, which is defined as the ratio of the characteristic particle (or droplet) time to the characteristic time of the flow or obstacle, namely

$$\mathrm{Stk} \equiv \frac{t_d}{t_0} \tag{4.19}$$

where t_d and t_0 are the characteristic time of the droplet and flow respectively. A droplet with a low Stokes number tends to follow the flow streamlines whereas a droplet with a high Stokes number is dominated by inertia and tends to follow its own initial trajectory. For small spherical droplets in an incompressible flow, the Stokes number can be calculated as

$$\mathrm{Stk} = \frac{2\rho_d}{9\rho_f}\left(\frac{d_d}{L}\right)^2 \mathrm{Re} \tag{4.20}$$

with the subscripts d and f denoting the droplet and flow state variables respectively. L is the characteristic length scale of the flow and Re is the flow Reynolds number based on this same length scale. In the context of the present work, the Stokes number can be recast in terms of the appropriate length scales characteristic of the pore-scale flow,

$$\mathrm{Stk} = \frac{2\rho_{\mathrm{oil}}}{9\rho_{\mathrm{air}}}\left(\frac{d_d}{d_p}\right)^2 \mathrm{Re}_p \tag{4.21}$$

where ρ_{oil} and ρ_{air} are the density of the oil and air phase respectively, and d_d is the droplet diameter. Thus, the Stokes number can be plotted as a function of the capture efficiency, which

is defined as

$$\xi = 1 - \eta_{fd} \tag{4.22}$$

where ξ stands for the oil capture efficiency. There are similarities between the oil separation phenomena described by the pore-scale simulations performed here and particle deposition studies carried out on an array of cylinders (Haugen and Kragset, 2010). The oil capture efficiency at $z/d_p = 5$ is plotted in Figure 4.30 as a function of the Stokes number of for all samples simulated, except the Retimet 20 PPI. The Stokes number is taking into account all droplet diameters and flow inlet velocities. The S-shaped capture efficiency curve is typically characteristic of dilute particle flows where the inertial effects are the dominant cause of particle deposition (Konstandopoulos et al., 1993). For Stoke numbers below 0.1, the capture efficiency is quite small and remains rather constant independently of the Stokes number. However, for $0.1 < Stk < 1$, the oil capture efficiency increases dramatically with increasing Stokes number. Stokes number values above 1 are associated with a very high capture efficiency, which remain stable with increasing Stokes numbers.

Results obtained with the Lagragian simulations are able to provide a general picture of oil capture effectiveness of the foam samples investigated. However, one should bear in mind the several limitations of the current modelling methodology. According to Haugen and Kragset (2010), the interception of a particle by a solid body, such as a cylinder for example, can be heavily influenced by the boundary layer characteristics next to the solid surface. Therefore, most studies tend to employ very fine levels of discretization next to the solid surface in order to fully resolve the boundary layer (most numerical particle deposition studies deal with simulating a single or several cylinders at most). Here, even though the mesh was refined up to a point where the cells next to the foam surface are located within the viscous sub-layer ($y^+ < 5$), it remains an open question whether this level of refinement was sufficient to accurately resolve all relevant boundary layer flow features.

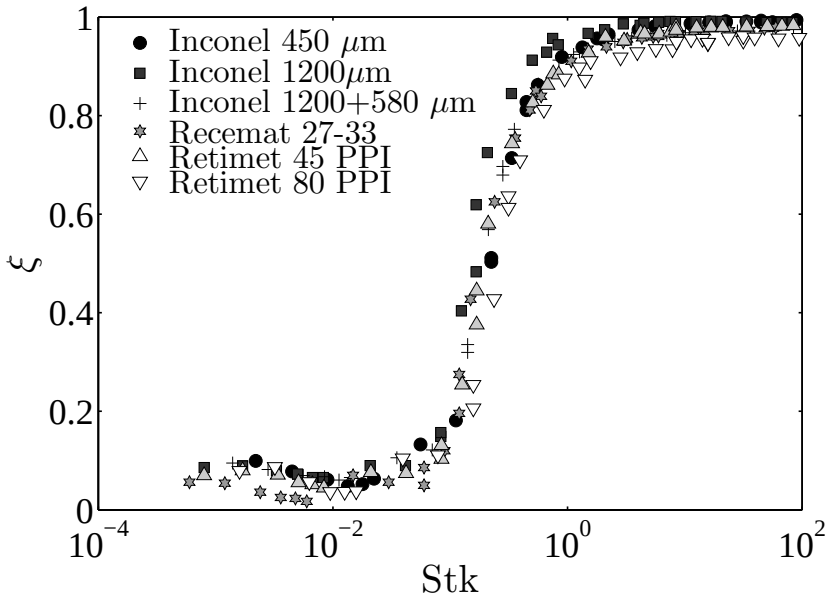

Figure 4.30: Oil droplet capture efficiency as a function of the Stokes number for all foams analysed at the normalized position $z/d_p = 5$ (with excepetion of the Retimet 20 PPI).

Additionally, virtually all phenomena related to droplet dynamics were neglected at the present stage. The oil film formation was not allowed to take place upon droplet impact onto the foam surface. Moreover, no splashing, stripping or rebound of droplets was allowed either. The reason for these simplifications are mainly due to the lack of an appropriate numerical framework for modelling these phenomena. Furthermore, the simplified mathematical models which are available tend to rely heavily on empirical correlations obtained from idealized test cases, carried out in conditions far different from those present here. As stated in the review by Yarin (2006), there is still a lot of improvements yet to be made in order to have reliable and computationally cost effective droplet-impact-related models. Nevertheless, the Lagrangian oil capture approach described here offers a first glimpse on modelling the disperse gas-liquid flow in open-cell metal foams.

4.7 Rotational effects

The open-cell metal foams employed within aero-engine separators are subjected to rotation because they are rigidly attached to the separator's hollow shaft. It was not possible to reproduce these conditions in the airflow pressure gradient measurements, however, rotational effects can be added to the numerical pore-scale modelling approach.

4.7.1 Moving reference frame formulation

Rotating geometries in grid-based numerical simulations can be taken into account by using a moving frame of reference (MRF). For the continuous phase, this results in the addition of two terms in the usual momentum conservation equation

$$\frac{\partial \rho \mathbf{u}'}{\partial t} + \nabla(\rho \mathbf{u}'\mathbf{u}') + 2\rho(\Omega \times \mathbf{u}') + (\Omega \times (\Omega \times \mathbf{x}')) = -\nabla p + \nabla(\overline{\tau}) + \mathbf{F} \tag{4.23}$$

The first addition is a Coriolis term of the form $2\rho(\Omega \times \mathbf{u}')$ where $\mathbf{u}'$ is the velocity vector of the fluid relative to the rotating frame and Ω is the a vector acting along the axis of rotation. The second term is a centrifugal term of the form $(\Omega \times (\Omega \times \mathbf{x}'))$ where $\mathbf{x}'$ is a position vector relative to the rotating reference frame.

For the Lagrangian phase, the additional forces term, $\mathbf{F}$, in Eq. 4.8 can also include forces that arise due to the rotation of the frame of reference. For a rotation defined on the Z axis, for example, the forces acting on the droplets in the Cartesian X and Y directions are given by

$$\left(1 - \frac{\rho}{\rho_d}\right)\omega^2 x + 2\omega\left(u_{d,y} - \frac{\rho}{\rho_d}u_y\right) \tag{4.24}$$

where $u_{d,y}$ and u_y are the droplet and fluid velocity in the Cartesian Y direction, ω is the angular velocity and

$$\left(1 - \frac{\rho}{\rho_d}\right)\omega^2 y + 2\omega\left(u_{d,x} - \frac{\rho}{\rho_d}u_x\right) \tag{4.25}$$

where $u_{d,x}$ and u_x are the droplet and fluid velocity in the Cartesian X direction.

4.7.2 MRF simulations

Only one sample was simulated using the MRF approach, which was the Retimet 45 PPI foam. Based on data obtained from a full aero-engine separator simulation, it was possible to create a computational domain where conditions representative of the ones within a real breather could be reproduced. The metal foam employed in real aero-engine separators has normally the form of an annulus. Based on the annulus dimensions employed in the simulations by Verger and Morvan (2011), the pore-scale computational sample analysed here is constructed as a subset of the full metal foam annulus, located midway between the inner and outer radius of the annulus. Therefore, the pore-scale sample is representative of the conditions that would be found within the interior of a metal foam annulus in a typical aero-engine separator.

Therefore, the computational domain is set as the sector of an annulus, with periodic boundary conditions on the tangential direction. The initial metal foam sample had to be mirrored in order to enable the use of periodic conditions, thus the final sample employed in the simulations is actually two identical samples, as Figure 4.31 illustrates. Figure 4.32 depicts a schematic of the computational domain, showing the location of the periodic boundaries, the flow and rotation directions. Note that the mirroring of the samples introduces some deformations to the foam morphology next to the reflection plane, however this did not significantly change the main morphological parameters such as porosity and specific surface area. The flow solving procedure is identical to the static sample cases.

Two rotational velocities were considered, 2000 and 6000 RPM. The entire domain is set in a moving reference frame with a specified rotational velocity, and the incoming airflow is set in an absolute frame of reference, with an inlet velocity range of 5-50 m/s. The flow is allowed to leave and enter the domain through the periodic boundaries. The pressure gradient is computed in the same way as for the static domain simulations, computing the difference between the

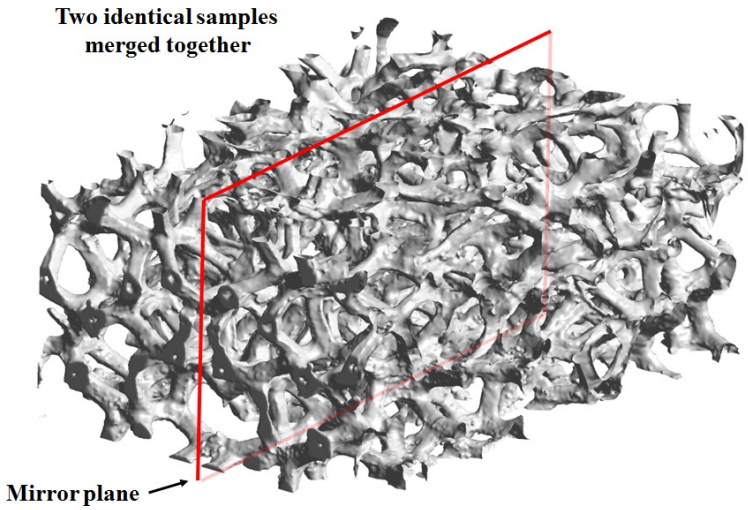

Figure 4.31: Schematic computational foam sample employed for the MRF simulations. Two identical foam samples are merged and mirrored in relation to each other so that periodic boundary conditions can be applied.

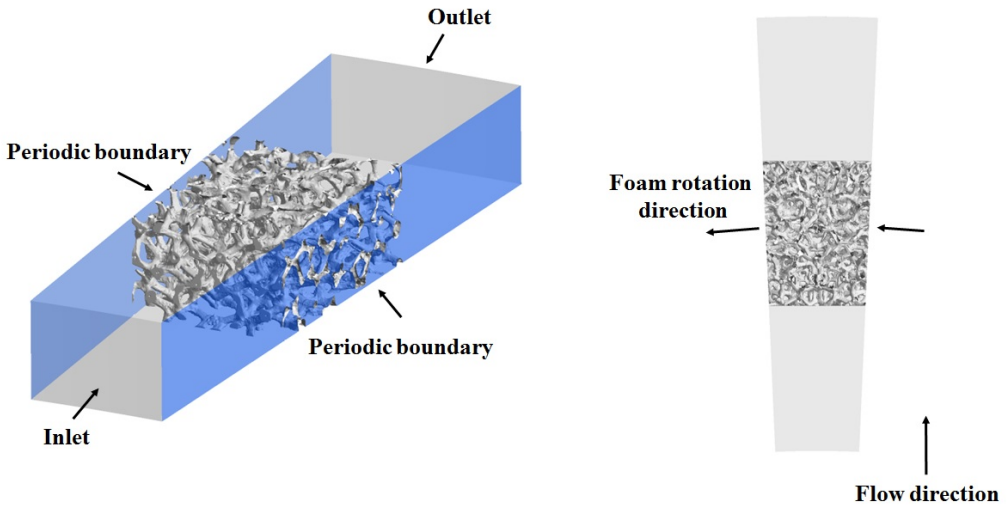

Figure 4.32: Schematic of the MRF computational domain. The walls in blue show the periodic boundaries. The air is injected from the inlet in an absolute frame of reference and the computational domain is set in a moving reference frame with a rotational velocity.

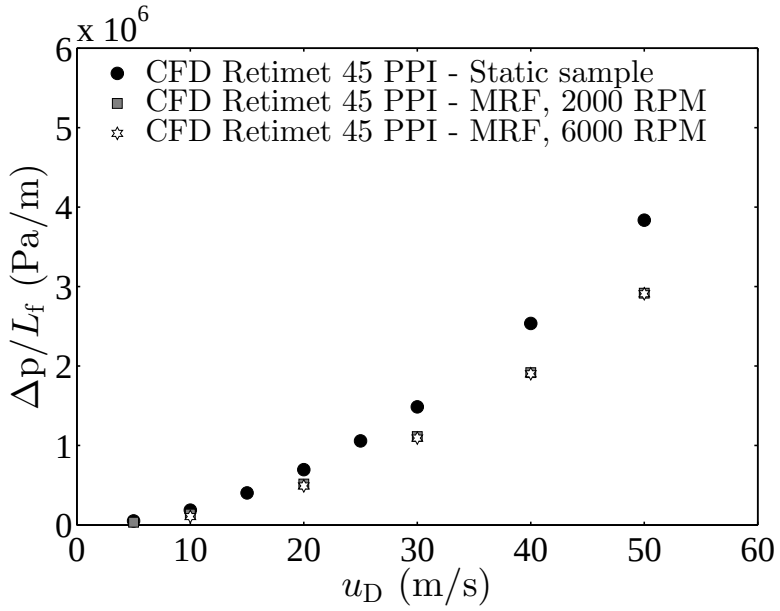

Figure 4.33: Comparison between the simulated pressure gradient for the static Retimet 45 PPI sample, and the MRF Retimet 45 PPI samples at 2000 and 6000 RPM respectively.

area-weighted average static pressure at the inlet and outlet respectively. Figure 4.33 shows a comparison of the pressure gradient curves obtained for the static and MRF Retimet 45 PPI simulations at 2000 and 6000 RPM respectively. The results show the pressure gradient in the inlet/outlet direction seems to be attenuated by the metal foam rotation.

Figure 4.34 shows a comparison between the static pressure contour plots computed for the MRF cases at 2000 and 6000 RPM for an inlet velocity of 20 m/s. Note that the direction of rotation is from right to left in the contour plot. Results do not show a very large difference in overall pressure gradient behaviour along the streamwise length of the foam sample. The largest discrepancies are observed next to the foam entrance and wake respectively.

On the other hand, velocity and vector contour plots obtained for the two rotational velocities investigated show very large differences as Figure 4.35 depicts. Both cases shown are for the same air inlet velocity of 20 m/s. Results clearly show that an increase in the rotational velocity causes a significant change in the direction of the velocity vectors within the pore space, as indicated by the vector arrows. Furthermore, since the contour plot shows the velocity in an

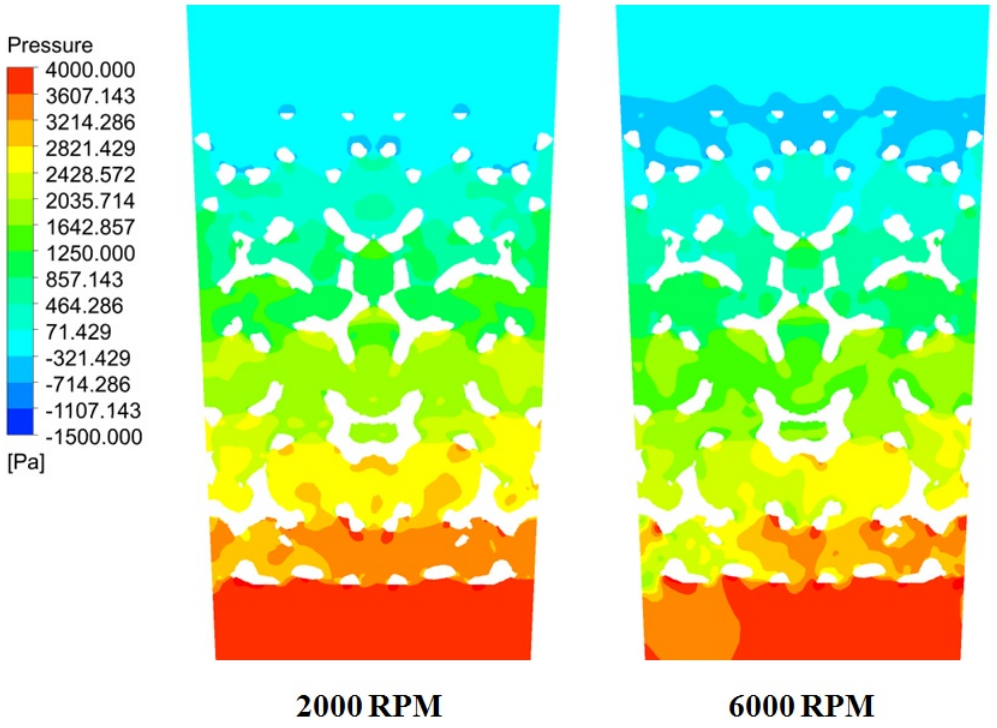

Figure 4.34: Static pressure contour plots for the MRF simulations at 2000 and 6000 RPM respectively, under an air inlet velocity of 20 m/s.

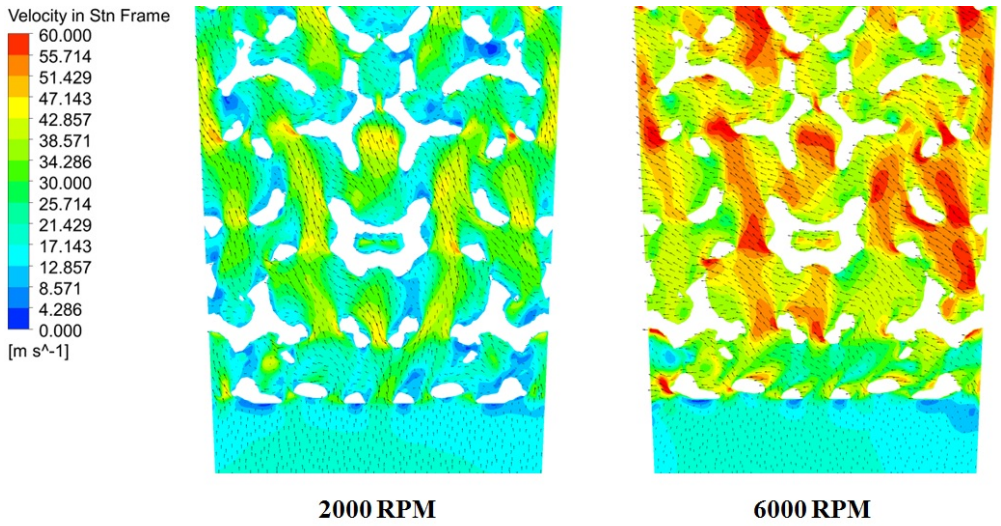

Figure 4.35: Velocity and vector contour plots for the MRF simulations at 2000 and 6000 RPM respectively, under an air inlet velocity of 20 m/s.

absolute frame of reference, higher velocity magnitude values are observed in the interstitial space of the 6000 RPM case.

4.7.3 MRF Lagrangian simulations

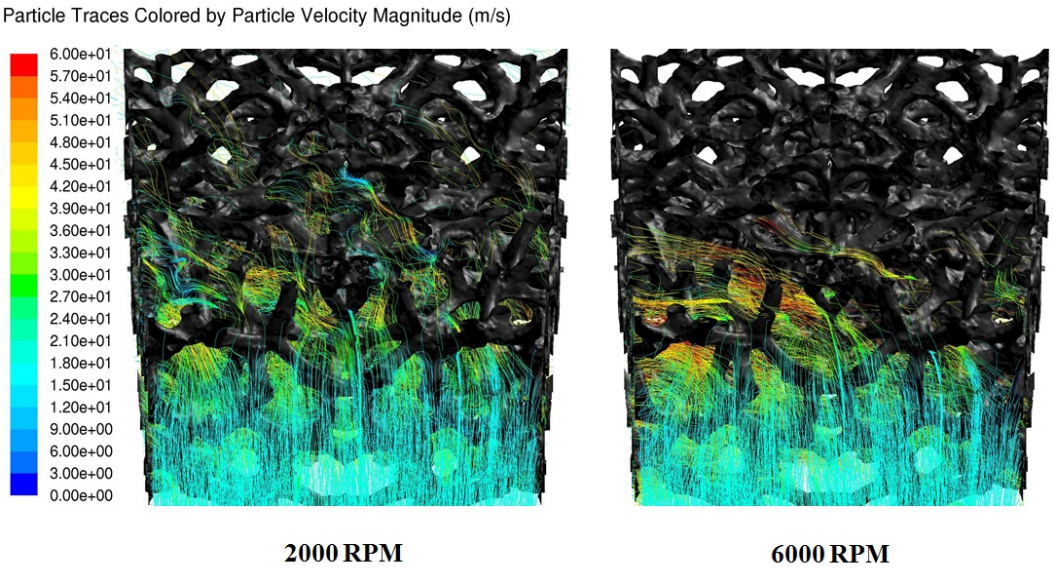

Figure 4.36: Illustration of the simulated 1 µm droplet trajectories across the rotating Retimet 45 PPI using MRF at 2000 and 6000 RPM respectively. The total number of trajectories was reduced for illustration purposes. Rotation direction is from right to left.

Lagrangian oil droplet tracking calculations are carried out using the MRF airflow solutions in the same way as for the static samples. Since the oil capture effectiveness in the simulations increases with an increase in the droplet's inertia, one can expect that higher oil captures would be observed in the MRF cases. When the rotational speed is high relative to the incoming air velocity, the droplet trajectories will be dominated mainly by rotational effects. In those cases, many of the droplets may end up leaving and entering the domain through the periodic boundaries, periodically recirculating through the domain. This will increase their overall path length and consequently, chance of colliding against the foam ligaments. Figure 4.36 depicts the trajectories of 1 µm droplets for the MRF Retimet 45 PPI cases at 2000 and 6000 RPM respectively, at an inlet air velocity of 20 m/s. These results clearly show that the entrainment

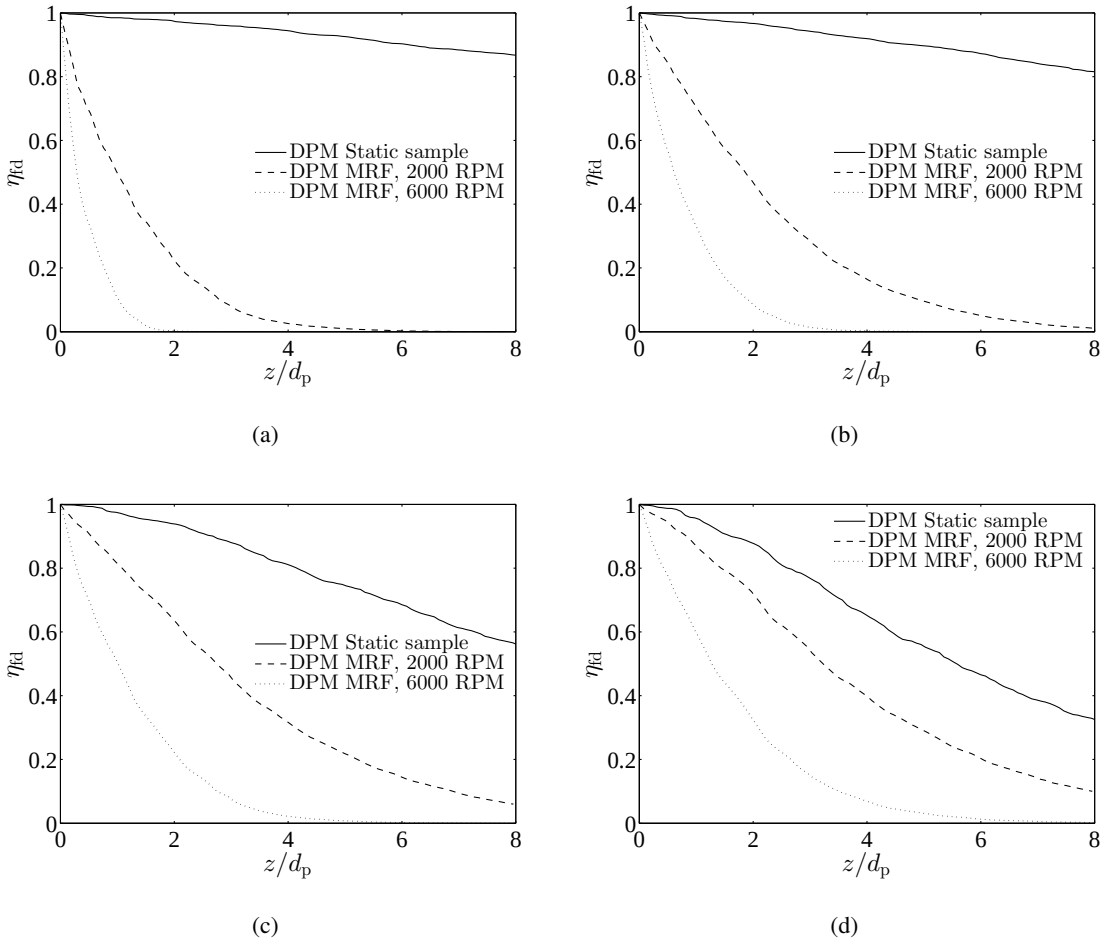

Figure 4.37: Oil capture curves showing the fraction of non-captured droplets versus the pore-size normalized foam streamwise position, for a droplet diameter of 0.5 µm at air inlet velocities of (a) 10, (b) 20, (c) 30 and (d) 40 m/s.

of air caused by the rotation of the foam seems to enhance the likelihood of droplet collision.

The increase in the droplet capture due to rotation is clearly shown in Figure 4.37, which depicts oil capture curves along the sample streamwise length with and without rotation, obtained for a droplet diameter of 0.5 µm. Starting from the top left in the clockwise direction, results are shown for air inlet velocities of 10, 20, 30 and 40 m/s respectively. In the case of a static sample, increasing the inlet air velocity always results in an increase of the droplet capture along the foam. Conversely, for the MRF cases, an increase in the air inlet velocity actually reduces the droplet capture. These results corroborate the arguments stated previously, since an increase

air velocity relative to the rotational speed implies in a smaller chance for the droplets to undergo periodic recirculation, thus decreasing their overall path length and consequently, chance of collision.

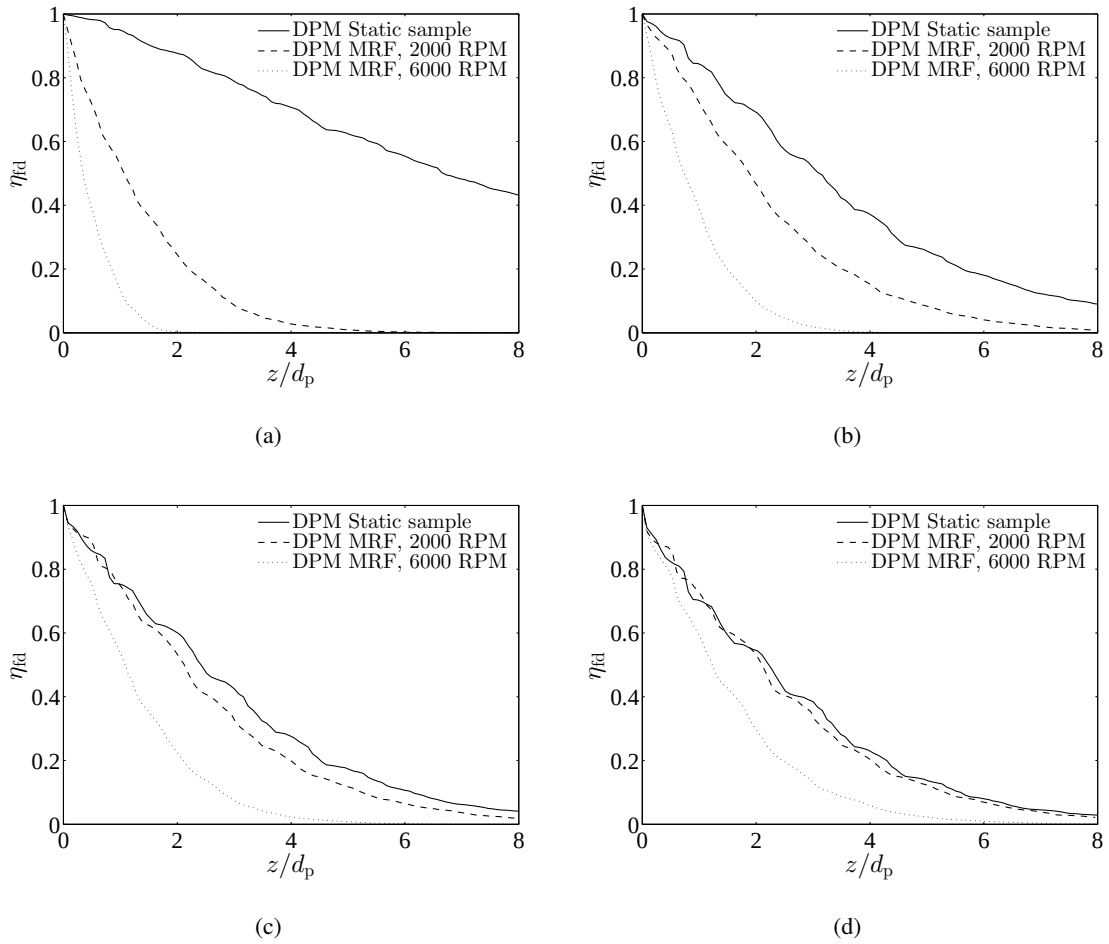

Figure 4.38: Oil capture curves showing the fraction of non-captured droplets versus the pore-size normalized foam streamwise position, for a droplet diameter of 1 μm at air inlet velocities of (a) 10, (b) 20, (c) 30 and (d) 40 m/s.

Figure 4.38 shows exactly the same type of results depicted in Figure 4.37, but for a droplet diameter of 1 μm. Comparison of the oil capture curves between the static and the MRF DPM results at 2000 and 6000 RPM respectively, shows a similar behaviour to the 0.5 μm diameter results. In all cases, the droplets are injected normal to the inlet in an absolute frame of reference. Therefore, due the larger momentum associated with the 1μm droplets, they tend to continue

on their initial trajectory, being less affected by the rotation of the foam. Figure 4.39 further validates this observation, by showing a comparison of the oil capture curves between the static and MRF cases for a droplet diameter of 3 μm.

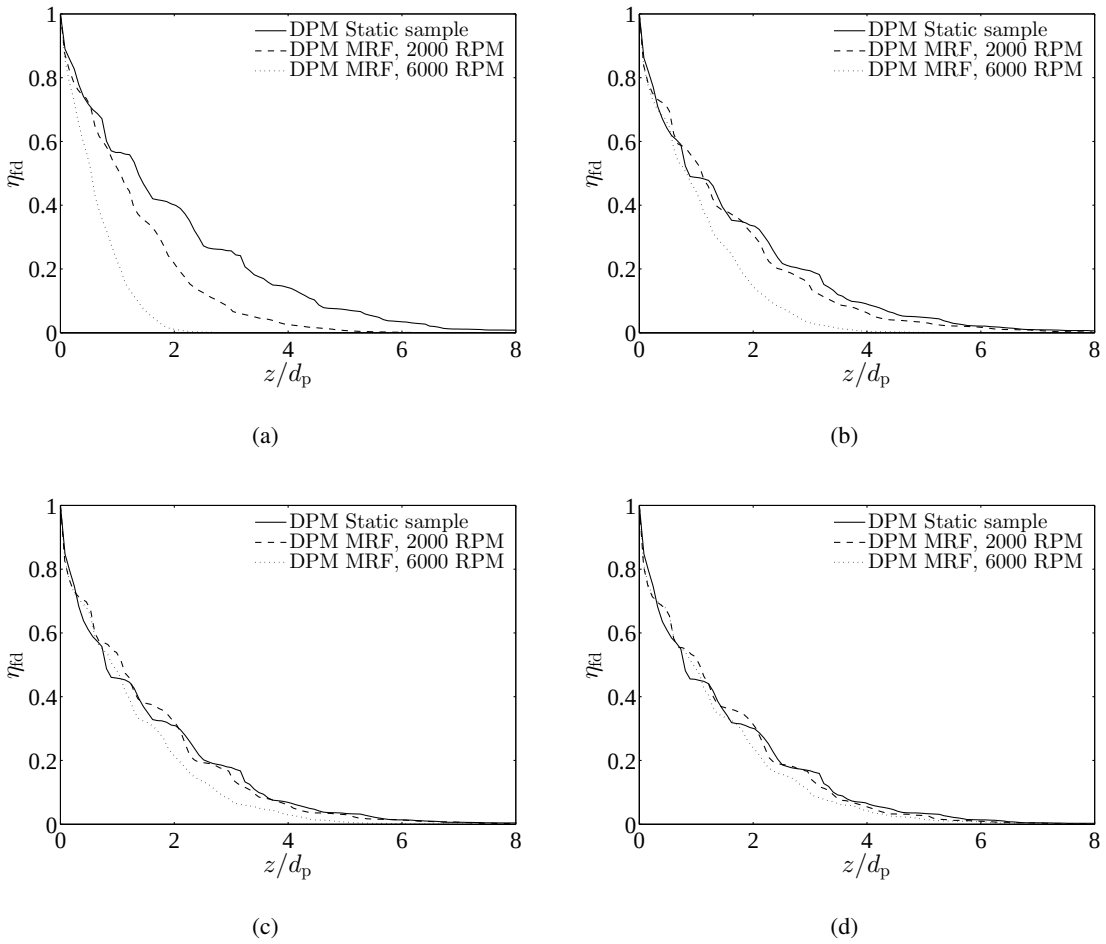

Figure 4.39: Oil capture curves showing the fraction of non-captured droplets versus the pore-size normalized foam length, for a droplet diameter of 3 μm at air inlet velocities of (a) 10, (b) 20, (c) 30 and (d) 40 m/s.

At a first glance, oil capture results using a rotating open-cell metal foam seems to enhance droplet capture, at least qualitatively, according to the oil capture criterion employed here. However, it is important to bear in mind that this behaviour may not be the case in reality, due to the fact that droplet dynamics effects, such as film formation, splashing and stripping for example, may lead to secondary droplet atomization. Nevertheless, the insights obtained with the

current CFD approach may serve as a starting point for future studies that take these additional phenomena into account.

4.8 Macroscopic transferring of pore-scale simulation results

One of the main objectives of the present work is to use a pore-scale simulations to extract information otherwise inaccessible when using macroscopic modelling approaches, or for which there is no experimental data available. The results obtained with the pore-scale simulations should be volume-averaged in a way that they can be employed into a macroscopic flow modelling approach, i.e. a formulation that is able to capture the effects caused by the presence of a porous medium on the two-phase flow but that does not explicitly represent the porous geometry. The transferring of the data gathered by the pore-scale simulations to macroscopic quantities is done for the airflow and Lagrangian tracking calculations respectively.

4.8.1 Transferring of airflow data

A macroscopic porous media flow model essentially incorporates an empirically or numerically determined flow resistance within a region which is defined as ”porous”. Considering the governing equations used to describe ”clear” flows in Section 2.2, the macroscopic porous media model essentially acts as a momentum sink, and is accounted for as a source term in the momentum equations. Therefore, the macroscopic transferring of the airflow data is described here in the context of the formulation employed by the commercial CFD solver used here, namely Ansys Fluent.

The porous media formulation calculates the superficial fluid velocity based on the volumetric flow rate for the porous region, which provides a good approximation of the bulk pressure loss across the medium for highly porous materials. The porous media model adds a momentum source term to the standard fluid flow equations composed of a viscous resistance term and an inertial loss term, such as

$$S_i = -\left(\sum_{j=1}^{3} Q_{ij}\mu u_j + \sum_{j=1}^{3} C_{ij}\frac{1}{2}\rho|u|u_j\right) \tag{4.26}$$

where S_i is the a source term in the i^{th} Cartesian direction in the momentum equations, $|u|$ is the velocity magnitude and Q and C are prescribed matrices that account for the viscous and inertial resistance terms respectively. For flows at very low Re_p, the flow is in the Darcy regime, and the energy dissipation caused by the porous medium is mainly due to viscous losses. However, for higher velocity turbulent flows such as the ones investigated here, an additional inertial loss term is necessary to accurately describe the pressure gradient across the porous material. Therefore, for the case of a homogeneous porous medium, Eq. 4.26 can be simplified to

$$S_i = -\left(\frac{\mu}{K}u_i + C_2\frac{1}{2}\rho|u|u_i\right) \tag{4.27}$$

where K is the permeability and C_2 is the inertial resistance factor. In this case, Q and C are specified as diagonal matrices with $1/K$ and C_2 on the diagonals respectively. It is clear that Eq. 4.27 will introduce a pressure gradient that is a quadratic function of the flow velocity, as in the Forchheimer equation, Eq. 2.44. Therefore, only two input parameters are necessary for the macroscopic porous media model: the permeability, K, and the coefficient C_2, which is related to the Forchheimer coefficient, F, such as $C_2 = 2F$. Values for permeability and Forchheimer coefficient have been computed from the pore-scale simulations, and are listed in Table 4.2. These values are employed in the macroscopic porous media model used here.

It is assumed that the porous medium region has no effect on the turbulence, such that the conservation equations for turbulent quantities are solved as if there was no porous medium present. According to Antohe and Lage (1997), this assumption is reasonable for high porosity media such as the ones analysed here.

4.8.2 Transferring of oil capture data

The macroscopic transferring of the oil capture curves is not as straightforward as for the airflow data, and a certain degree of approximation is inherently necessary. The oil extinction curves obtained by computing the impact streamwise location of each droplet along the entire metal foam length can be used in order to derive a function that relates the droplet diameter, flow velocity and capture effectiveness for a given foam sample. For that purpose, the oil capture can be plotted as a function of the streamwise distance travelled by the droplet inside the foam, z. As shown in Figure 4.27, the oil capture curves have an exponential-like shape, and the data can be fitted using an exponential equation such as

$$\eta_{fd} = \exp^{\beta z} \tag{4.28}$$

where β is the curve fitting coefficient. Figure 4.40 shows an example of the exponential curve fitting, where the fraction of non-captured droplets, η_{fd}, is plotted as a function of the distance travelled by the droplets inside the foam, z. Eq. 4.28 is fitted to two oil capture curves obtained from pore-scale simulations and the square of the correlation coefficient, R^2, is shown for both curves.

Although some small deviations are present, the overall quality of the curve fitting is good, and square of the correlation coefficient was always larger than 0.95. The curve fitting procedure is applied for all the oil capture curves obtained by the Lagrangian simulations for a given foam sample, and a value of the coefficient β is obtained for each curve. The coefficient β is therefore a function of both the droplet diameter and air flow velocity. However, instead of using the droplet diameter and airflow velocity, it is better to use dimensionless quantities. In that sense, β is assumed to be a function of the pore-based Reynolds number, Re_p, and the droplet diameter normalized by the mean pore diameter, d_d/d_p. Thus, β values can subsequently be fitted by a k^{th} order polynomial surface of the form:

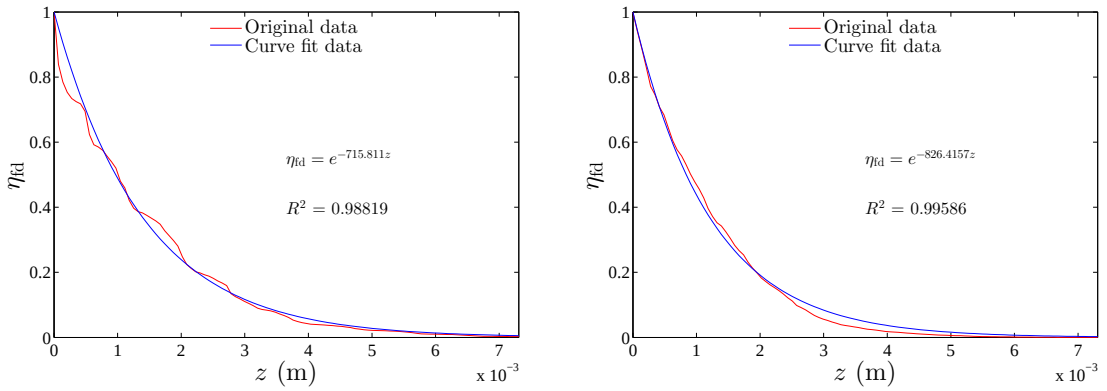

(a) (b)

Figure 4.40: Illustration of two typical oil capture curves, with the fraction of non-captured droplets, η_{fd}, plotted as a function of the distance travelled by the droplets inside the foam, z, for a droplet diameter of (a) 0.5 µm and (b) 3 µm. The curves are fitted using Eq. 4.28 and the square of the correlation coefficient is shown.

$$\beta = a_{0,0} + a_{1,0} * x_1 + a_{0,1} * x_2 + \ldots + a_{1,k-1} * x_1 * x_2^{k-1} + a_{0,k} * x_2^k \tag{4.29}$$

where x_1 and x_2 account for the two independent variables (d_d/d_p and Re_p) and a represents the polynomial coefficients. Figure 4.41 shows the outcome of the surface fitting approach for the oil capture data obtained from the Retimet 45 PPI Lagrangian simulations.

The outcome from the surface fitting approach is a function that relates the fraction of free (non-captured) droplets with the distance travelled within the porous region, the normalized droplet diameter and flow pore-based Reynolds number. Although the overall quality of the surface fitting approach is good, the fitted surface tends to produce negative β values at very low d_d/d_p and Re_p values. In the present context, high β values imply higher chances of a droplet being captured, and $\beta = 0$ is the equivalent of a droplet having 0 % chance of being captured. Therefore, negative β are not physical and should be avoided, or assumed to be equal zero. For the sake of completeness, this undershoot of β values in the surface fitting could not be avoided even when more data points were used (meaning Lagrangian oil capture results

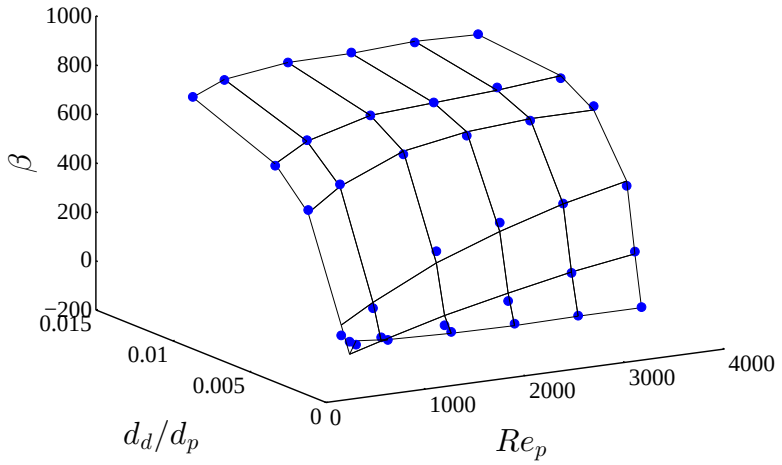

Figure 4.41: Illustration the outcome of the surface fitting approach. Values of β are shown as blue points, and plotted as a function of d_d/d_p and Re_p. The surface is fitted using a 5^{th} order polynomial.

comprising more droplet diameters and flow velocities). Furthermore, changing the order of the surface polynomial did not prevent this undershoot either. Therefore, the condition $\max(\beta, 0)$ was employed for the surface fitting.

An user-defined function (UDF) was written in order to implement this oil capture function in Ansys Fluent 15. At each Lagrangian calculation step, each droplet parcel will have a certain probability of being captured, depending on the distance travelled inside the porous medium, the droplet diameter and its velocity. Therefore, the UDF works by tracking the droplets that are travelling inside the porous region, and randomly terminating their trajectory according to a probability that is computed based on the outcome of the surface fitting approach.

4.8.2.1 Droplet/particle capture UDF

The capture of the droplets as they pass through the porous region is achieved in an analogous way to the modelling of radioactive decay. Here, rather considering the probability that a nuclei will decay in a given time, we have the probability, $P(z)$, that a droplet can travel some distance,

z, through the porous medium without it being captured

$$P(z) = \exp(-\beta z), \tag{4.30}$$

where β is the equivalent of the reciprocal of the decay constant in radioactive decay. So, when $z = 0$, it is certain to not have been captured, as $z \to \infty$, then it is certain to have been captured.

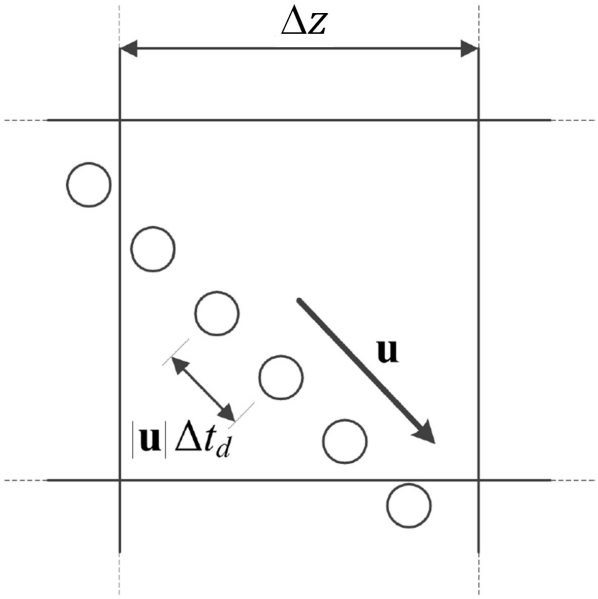

Figure 4.42: Schematic of the transit of a droplet through a mesh cell in Fluent.

In Fluent, each particle that is being tracked as part of the DPM steps forward in space in a number of increments, governed by the particle timestep Δt_d. This is not to be confused with the flow timestep, which can be completely different. Depending on the mode of operation, Fluent works out the size of the particle timestep based on the velocity in, $\mathbf{u}$, and size of, Δz, the cell which the particle is in (Figure 4.42). Fluent tries to ensure that the particle will take n steps through the cell, where n is typically 5.

As the droplet/particle moves through the cell, the UDF that was written for the purpose, calculates the distance the particle moves in a timestep, $\mathbf{u}\Delta t_d$. A random number generator then produces a number, λ_{01}, between 0 and 1. If $\lambda_{01} < \beta \mathbf{u} \Delta t_d$, then the droplet is deemed to have been captured and the mass of the droplet is stored in a user-defined memory (UDM), which keeps a tally of the mass of droplet(s) captured in that mesh cell. When captured, the

droplet is removed from the droplets being tracked and ceases to exist. Rather than explicitly calculate $\mathbf{u}\Delta t_d$, the UDF finds the difference between the droplet's coordinates from the previous and current particle timestep, leaving the calculation of these positions to the particle tracking algorithm.

To calculate β at each particle timestep, the pore-based Reynolds number, Re_p, and the normalised droplet diameter, d_d/d_p, are calculated and β is found from Eq. 4.29.

The key aspect of this approach is that it is stochastic and treats every particle timestep as distinct and independent. There is no cumulative effect implicit in this method, the droplet is unaware that it may have travelled some distance through the porous medium already. In many ways, it mimics the real experience of the droplet, where at each instant there is a chance that it may encounter a filament inside the metal foam, something that is not influenced from whence it came. Details of the UDF code are shown in Appendix D.

4.8.3 Validation of the enhanced macroscopic porous model

A simple test case was devised in order to validate the enhanced macroscopic porous model described here. The validation is done by comparing the results of the macroscopic model simulations against pore-scale results. Thus, a computational domain with the same dimensions as the pore-scale domain employed for the Retimet 45 PPI simulations is created. Figure 4.43 illustrates the computational domain of the macroscopic model validation case. The dimensions are exactly the same as for the square channel domain employed in the Retimet 45 PPI pore-scale simulations. The main difference is that instead of explicitly representing the metal foam, a porous region is defined instead. A hexahedral mesh was employed with a total mesh count of 10,000 cells. For comparison purposes, the pore-scale domain for the Retimet 45 PPI had 4.72×10^6 mesh cells.

The boundary conditions are exactly the same as the ones used in the pore-scale simulations, except for the porous region. Viscous and inertial resistance coefficients were defined for the

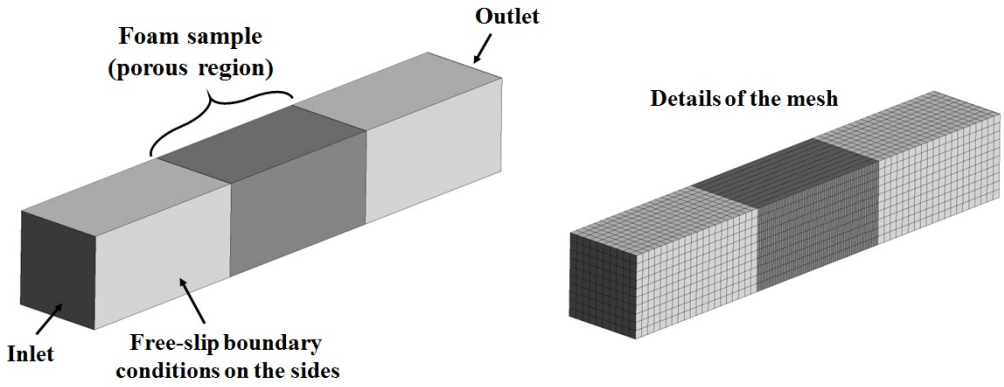

Figure 4.43: Illustration the computational domain used for validation of the macroscopic porous media model. Domain dimensions are identical to the pore-scale square channel domain employed for the Retimet 45 PPI simulations. A porous region is defined instead of explicitly representing the Retimet 45 PPI porous geometry.

porous region using the values of permeability and Forchheimer coefficient computed from the pore-scale simulations results for the Retimet 45 PPI. Simulations are carried out for incompressible steady state airflow using the RNG k-ε turbulence model, under a velocity range of $u_D = 5 - 50$ m/s.

Similarly to the pore-scale simulations, the pressure gradient is calculated across the porous region. Figure 4.44 shows a comparison between the pressure gradient curves obtained by the pore-scale and macroscopic model simulations respectively, showing excellent agreement. Moreover, Figure 4.45 depicts the static pressure contour plots for both approaches, showing the pressure gradient behaviour along the foam region. In the case of the pore-scale simulations, a complex pressure distribution is seem due to the complex foam geometry, whereas a linear pressure gradient is observed for the macroscopic case. However, it has been shown in Section 4.3.1, that taking the area-weighted averaged pressure profile in multiple cross-sections perpendicular to the flow, yields an apparent linear pressure gradient profile for the pore-scale results. Thus, the excellent agreement between both approaches shows that the macroscopic model is able to accurately reproduce the pressure gradient along the foam samples.

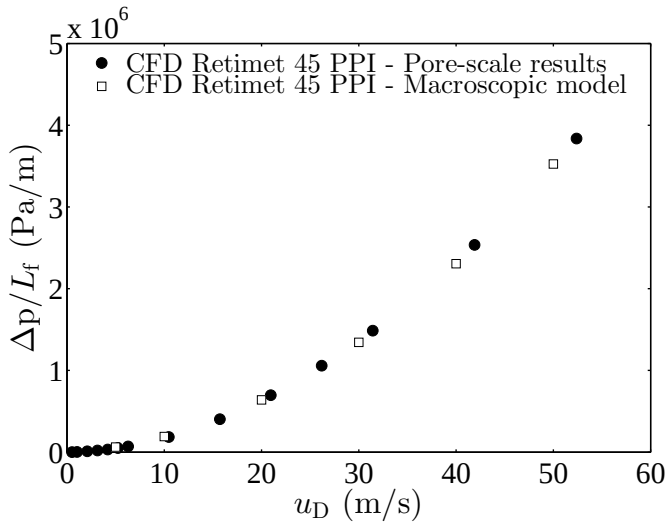

Figure 4.44: Comparison of the pressure gradient curves obtained by the pore-scale and macroscopic model simulations for the Retimet 45 PPI foam.

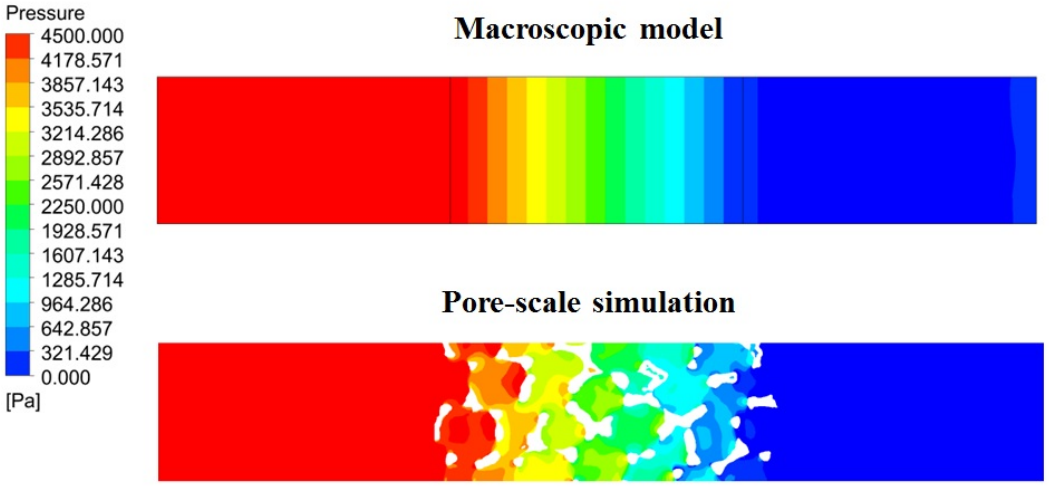

Figure 4.45: Comparison of the static pressure contour plots obtained by the pore-scale and macroscopic model simulations for the Retimet 45 PPI foam, at $u_D = 20$ m/s.

Lagrangian oil droplet tracking calculations are performed using the same settings as the ones used for the pore-scale simulations. For that purpose, the droplets are injected in a plane located halfway between the inlet and porous region entrance. A UDF is employed in order to randomly terminate the droplet trajectories according to a probability computed from the surface polynomial equation obtained from the pore-scale oil capture results. Therefore, for validation purposes, oil capture curves can be extracted in exactly the same way as for the pore-scale

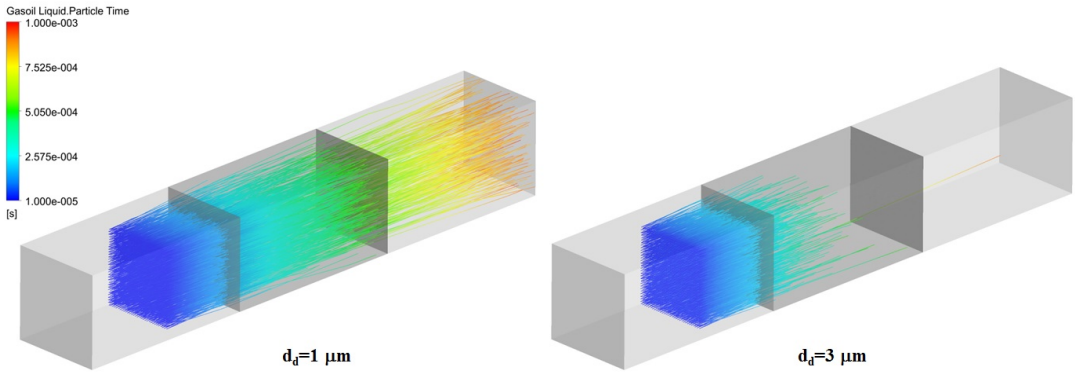

Figure 4.46: Droplet trajectories through the macroscopic Retimet 45 PPI foam model for an inlet velocity of 20 m/s and two uniform droplet diameters: 1 and 3 µm. The number of trajectories was reduced for illustration purposes.

simulations. The termination of droplet trajectories due to the macroscopic oil capture model is clearly seem in Figure 4.46, which shows a the trajectories across the macroscopic Retimet 45 PPI foam model at an inlet velocity of 20 m/s and two uniform droplet diameters: 1 and 3 µm. In the same sense as for the pore-scale Lagrangian simulations, as the droplet diameter increases, so does the probability of it being captured, or in the context of the UDF, having its trajectory terminated.

In order to perform a meaningful comparison between the oil capture results obtained for the pore-scale and macroscopic simulations, the fraction of free droplets for both approaches is computed at the normalized position $z/d_p = 5$, and plotted together in Figure 4.47 for four different droplet diameters, 0.5, 1, 3 and 5 µm, at varying flow velocities. The results obtained with the macroscopic oil extinction model showed an overall good agreement with the pore-scale results. Larger deviations from the pore-scale results are observed for a droplet diameter of 0.5 µm, at lower flow velocities. This was expected, as the surface fitting procedure described previously produces negative β values within a small region which is representation of small droplet sizes and low flow velocities. It is important to mention that in the UDF, negative β were not allowed and considered to be zero instead.

Figure 4.48 depicts the oil capture curves computed from the pore-scale and macroscopic

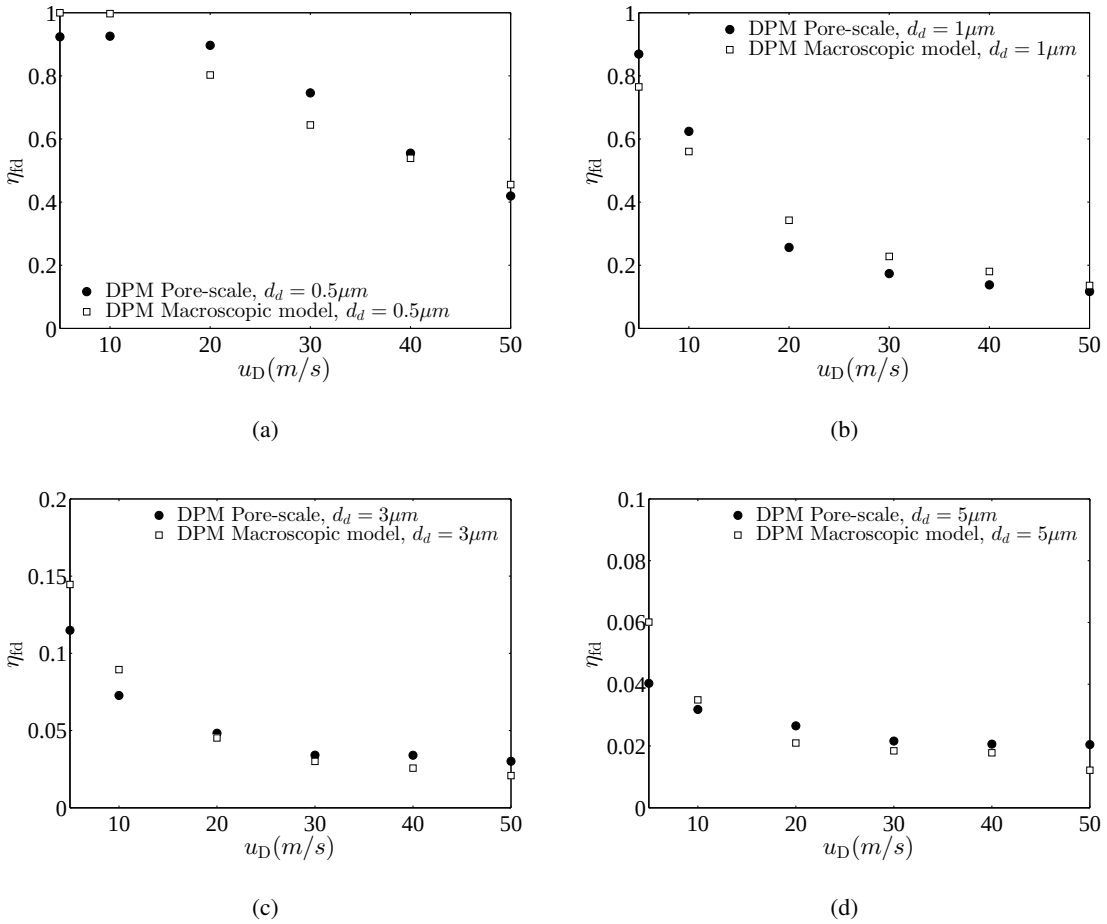

Figure 4.47: Comparison between the results obtained by the pore-scale and macroscopic model Lagrangian calculations showing the fraction of non-captured droplets computed at the normalized position $z/d_p = 5$ versus the Darcian velocity for four different droplet diameters, (a) 0.5, (b) 1, (c) 3 and (d) 5 µm.

simulations respectively. The results show the fraction of free droplets as a function of the normalized streamwise foam length at a flow velocity of 20 m/s, for four droplet diameters, 0.5, 1, 3 and 5 µm. Again, worst agreement between both approaches happens for the smallest droplets sizes, and is specially troublesome for the 0.5 µm diameter.

The transferred results obtained for the other foams showed very similar trends. The surface fitting approach employed here seems to have a reduced accuracy for the oil capture results obtained at low flow velocities and for smaller droplet diameters. Nevertheless, the main objective

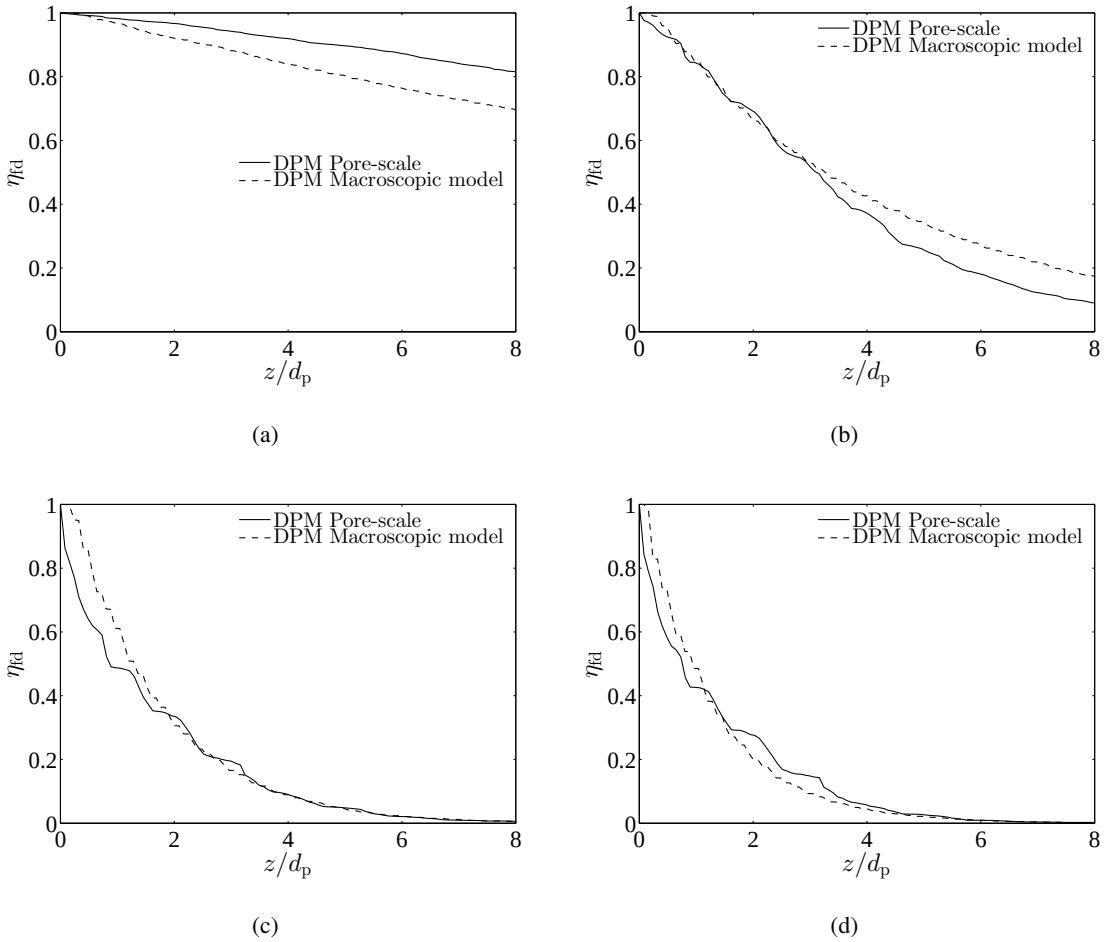

Figure 4.48: Comparison between the results obtained by the pore-scale and macroscopic model Lagrangian calculations showing the oil capture curves computed from the pore-scale and macroscopic model calculations respectively. Results are shown for four droplet diameters, (a) 0.5, (b) 1, (c) 3 and (d) 5 µm.

of the present work is to provide a qualitative evaluation of the oil capture effectiveness in several commercial open-cell metal foams. Given the fact that the pore-scale Lagrangian oil capture results already take into account a certain degree of uncertainty, it is reasonable to say that the macroscopic oil capture model described here still provides a good qualitative agreement of the droplet extinction rates throughout the foam samples. Furthermore, the enhanced macroscopic model can be easily implemented in a commercial CFD solver, with very low associated computational costs.

4.9 Summary

This chapter described the application of a pore-scale modelling methodology to solve single and two-phase flow across several commercial open-cell metal foams. The pore-scale computational domain consisted of a rectangular channel with free-slip enclosing walls. The simulations were run at the HPC facility in the university, using 24 to 32 processor cores in parallel, depending on the availability. Converged steady state solutions took an average of 0.5-2 hours to be reached. The airflow simulations were able to reproduce well the experimental pressure gradient curves for the samples analysed. Some relatively large discrepancies were observed between experimental and numerical values of permeability and Forchheimer coefficient for some samples, which indicate a high sensitivity of these parameters to small deviations on pressure gradient values. Interestingly, the work of Ranut et al. (2014) highlighted that this level of discrepancy is rather commonly found in similar studies, even showing that two different experiments performed for the same metal foam can yield distinct values of permeability and Forchheimer coefficient. There are several possible factors that can influence the pressure gradient behaviour in open-cell metal foams, such as wall effects, entrance/exit effects, time-dependent flow features, fluid compressibility and anisotropy of the foam structure.

These additional effects were numerically investigated here. A number of separate test cases and computational domains were devised in order to do so. Walls effects were analysed by simulating airflow through a cylindrical-like domain. Results showed that the pressure gradient across the foam can be strongly affected by wall effects if the cylinder radius relative to the mean pore size is small. Since the radius of the samples employed in the pressure gradient experiments was large relative to the pore size (for all samples), the use of a rectangular channel showed to be more appropriate for the purpose of validation against experimental measurements.

Size-related effects on the pressure gradient have been observed experimentally in a number of studies in the literature. The pore-scale numerical simulations performed here were able to re-

produce size-related effects on the pressure gradient by solving the airflow in samples of varying streamwise thickness. Simulated pressure gradient results showed that the critical streamwise thickness for the sample investigated lies between 25 to 50 pore sizes, a value that agrees well with literature results (Dukhan and Patel, 2010). This also highlights the importance of the use of computational domains which have a similar streamwise thickness to the experimental samples for validation purposes.

Unsteady flow simulations were carried out to investigate time-dependent flow features and whether they affect the overall pressure gradient across the samples. Simulation results showed the presence of a certain level of unsteadiness in the flow, by monitoring the streamwise velocity component in several points in the wake of the foam sample. However, a comparison between the pressure gradient obtained by the steady state and time-averaged unsteady simulations showed a negligible difference between both approaches. Given the fact that the unsteady simulations are roughly one order of magnitude more expensive to compute, their use is therefore not justified in the context of the present work.

Fluid compressibility effects can become significant when Mach number values higher than 0.3 are reached within the pore space. Such conditions have been observed at high pore-based Reynolds numbers ($\mathrm{Re}_p > 2000$), as shown by simulations assuming the air as an ideal gas. Moreover, a comparison between incompressible and compressible simulations showed that the pressure gradient results obtained by both approaches start to diverge from each other at high flow velocities. Assumption of fluid compressibility has also shown to affect permeability and Forchheimer coefficient values, showing better agreement between experimental and computational Forchheimer coefficient values. On the other hand, a greater discrepancy between permeability results was observed.

As shown in Ranut et al. (2014), the shape of the pores may be elongated along one particular direction due to the foam manufacturing process and changing the orientation of the sample against the flow direction may cause a deviation of up to 20 % on the pressure gradient. The

anisotropy on the foam structure was investigated numerically, and results have shown that there is a certain degree of anisotropy in the solid matrix of the samples analysed here. Variation of the spatial alignment of the foam sample with the flow direction has shown that the pressure gradient results can have deviations up of to 20 % relative to the mean pressure gradient, similarly to results obtained in Ranut et al. (2014).

Finally, artificially varying the porosity of a given foam sample has been shown to strongly affect the pressure gradient across the foam. Changes in porosity will consequently have an effect on permeability and Forchheimer coefficient values. Therefore, an accurate description of the pore-scale geometry is essential in order to obtain accurate flow results. In summary, the numerical modelling framework described here can be used to compute the transport properties of single phase flow in open-cell metal foams with a reasonable level of accuracy.

The dispersed oil phase flow was simulated using a Lagrangian tracking approach. One-way coupling was assumed given the low mass fraction of oil within aero-engine separators and all droplet calculations were performed in steady state. Converged airflow pore-scale solutions were employed as the base flow for the Lagrangian tracking approach. A simplified oil capture criterion was employed which assumed the droplet to be extinct when colliding against the foam solid ligaments. Note however that this approach is neglecting complex droplet dynamics phenomena such as splashing, stripping and film formation, mainly because of the lack of computationally-efficient models capable of modelling accurately such phenomena.

Nevertheless, the Lagrangian tracking calculations were able to provide a good qualitative evaluation of the droplet capture effectiveness in the samples analysed. The droplet's inertia is apparently the determining factor in the oil capture given the criterion employed here. Increasing the droplet momentum enhances its probability of deviating from its initial trajectory and intercepting the foam solid structure. Therefore, the oil capture effectiveness will vary according to the flow velocity and droplet size. Sub-micron droplets were shown to be the most problematic, and presented a low chance of being captured whilst travelling inside the foams.

Increasing flow velocity was shown to increase the probability of droplet capture. Based on the results shown here, it is reasonable to say that escaped sub-micron droplets are the most likely cause of breather smoke.

The rotation of the metal foams was simulated by using a MRF approach, with the purpose of reproducing conditions similar to the ones found in aero-engine separators. Airflow results showed the pressure gradient in the streamwise direction to be weakly affected by the rotation of the foam, and rotational effects seemed to attenuate the streamwise pressure gradient. Oil capture results obtained by means of Lagrangian tracking calculations showed that the rotation of the foam essentially increases the likelihood of droplet collision against the foam solid ligaments.

Finally, a methodology for transferring the pore-scale results into a macroscopic formulation is presented. The effect of the foam sample in the airflow is quite straightforward to represent macroscopically, mainly requiring the use of a momentum source term which accounts for the pressure gradient imposed by the presence of the foam sample. Macroscopic transferring of the pore-scale oil capture results was more laborious, and required a certain degree of approximation. Nevertheless, the oil capture curves computed across the foam streamwise position within the foam can be fitted by an exponential-like equation. Subsequently, the exponential coefficients can be fitted by a polynomial surface, which yields a statistical function that relates the probability of capture with varying flow velocity and droplet size. This function was implemented in a CFD solver by means of a user-defined function. Validation results for the macroscopic porous model showed good overall agreement against pore-scale results. Furthermore, to the knowledge of the author, the modelling methodology described in this chapter is the first ever attempt to model the oil capture within open-cell metal foams employed in aero-engine separators. Ultimately, the goal of this project is to employ an enhanced macroscopic porous model in simulations of a full aero-engine separator.

Chapter 5

Application to an aero-engine separator

A general description of the functioning of aero-engine separators was provided in Chapter 1 along with a comment on the issues related to unwanted emissions of oil and formation of *breather smoke*. The use of CFD to simulate the two-phase flow within aero-engine separators can provide essential information regarding the flow behaviour which would be otherwise inaccessible experimentally. Normally, aero-engine separators make use of a porous material in order to increase the oil capture effectiveness. Open-cell metal foams are usually employed for this task due to their high surface area to unit volume and low associated pressure drop. The modelling of the two-phase flow through this type of porous material is one of the largest gaps yet to be filled within the current modelling framework applied to aero-engine separators.

This chapter describes the CFD simulations of two-phase flow in a full aero-engine separator. Oil capture and pressure gradient results obtained from pore-scale simulations are transferred to a macroscopic porous media model and applied to the full separator simulations. The main objectives consist of obtaining good quantitative agreement for air flow and at least qualitative agreement for oil separation from the simulations against experimental results. The aero-engine separator design is a reproduction of the experimental air/oil separator test rig located at the Karlsruhe Institute of Technology (KIT). Experimental measurements for the pressure drop and oil separation were conducted by KIT and are employed for validation of the simulations. Since the experimental studies performed by KIT are not yet published in the open literature, a

brief description of the experimental procedure is provided for completeness.

5.1 Separator design and experimental apparatus

The aero-engine separator investigated here is based on an industrial design and is a reproduction of the modular oil separation test rig at KIT. Figure 5.1a illustrates the main components of the separator, with the light and dark grey parts representing the static and rotating parts respectively. The rotor is attached to a rotating hollow shaft, and has a compartment which can contain an open-cell metal foam or similar porous material. This assembly (rotor + porous medium) is commonly referred to as the *breather*. The cylindrical static chamber has an inner diameter of 300 mm and fully encloses the breather. There are two plates that protrude inside the chamber throughout the circumference. Six tangential inlet pipes with a diameter of 13 mm each are distributed around the chamber circumference as shown in Figure5.1b. Three scavenge ports with a diameter of 11 mm are located at the bottom of the separator.

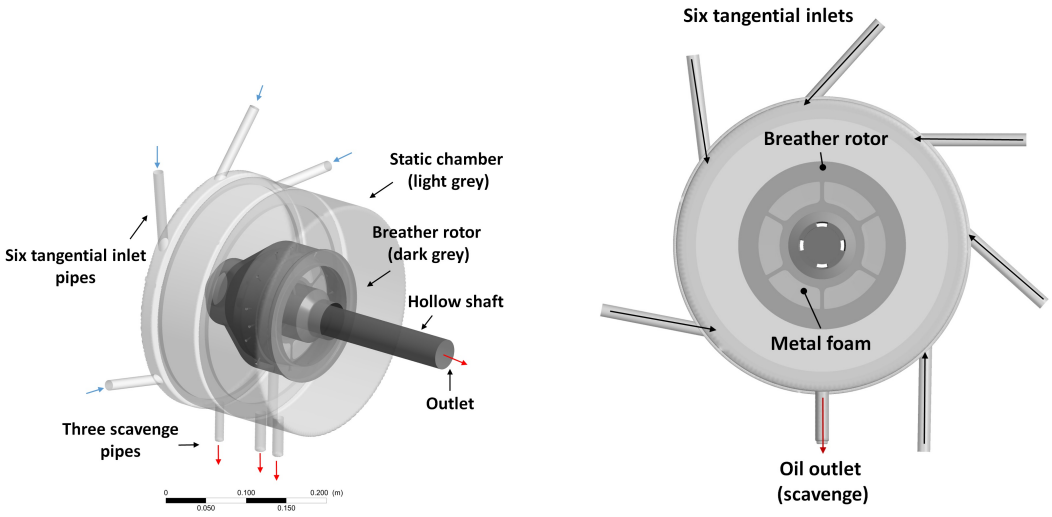

(a) (b)

Figure 5.1: (a) 3-D model of the separator indicating the inlets, outlets and most relevant parts and a (b) frontal view of the separator on a cut-plane through the inlet pipes.

The air/oil mixture enters the separator through the six tangential inlets, which creates a pre-

swirl in the flow even when the breather is not rotating. This inlet configuration has the purpose of increasing the oil separation through centrifugal effects. The rotating airflow undergoes a 180° turn in order to enter the breather and pass through the metal foam compartment. The flow takes a subsequent 180° turn in order to leave the metal foam compartment and flow through the hollow shaft towards the separator outlet. This sequence of turns has the intent of increasing the overall path length of the flow and enhancing oil separation. Figure 5.2a presents a schematic of the separator highlighting the main components and airflow path. Additionally, it shows the approximate locations of the pressure transducers used in the pressure drop measurements.

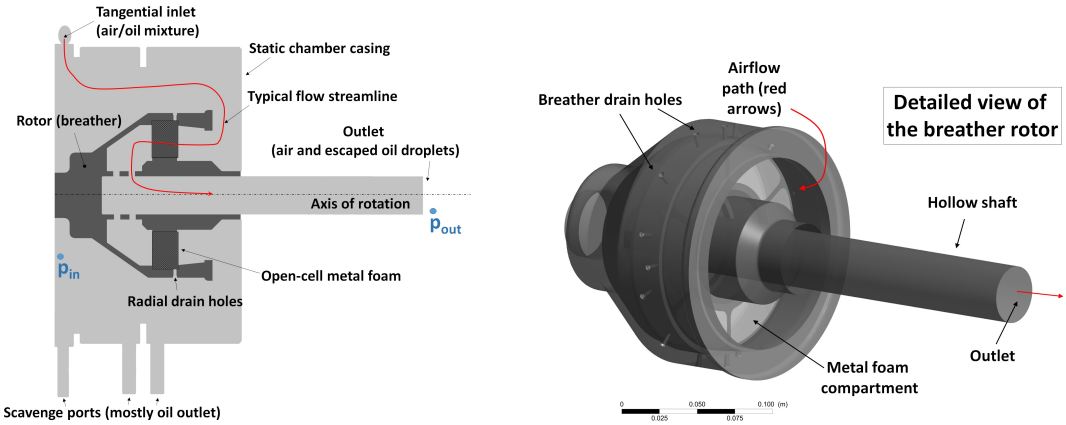

(a) (b)

Figure 5.2: (a) Cut-plane schematic of the separator, showing the approximate locations of the pressure transducers; (b) Detailed 3-D view of the rotor (breather) and its components.

The rotating breather has an outer diameter of 164 mm and is rigidly attached to a hollow shaft which is driven by an electric motor. The breather has a central compartment with the format of an annulus, and can be fitted with an open-cell metal foam. Incoming oil is supposed to coalesce and accumulate over the metal foam and be directed radially outwards due to centrifugal effects. Sixteen radial drain holes are present onto the breather outer wall in order to allow collected oil to flow back into the main chamber. Figure 5.2b provides a detailed view of the rotating breather highlighting its main components.

The incoming oil is essentially a dilute flow with the oil in the form of droplets. Primary

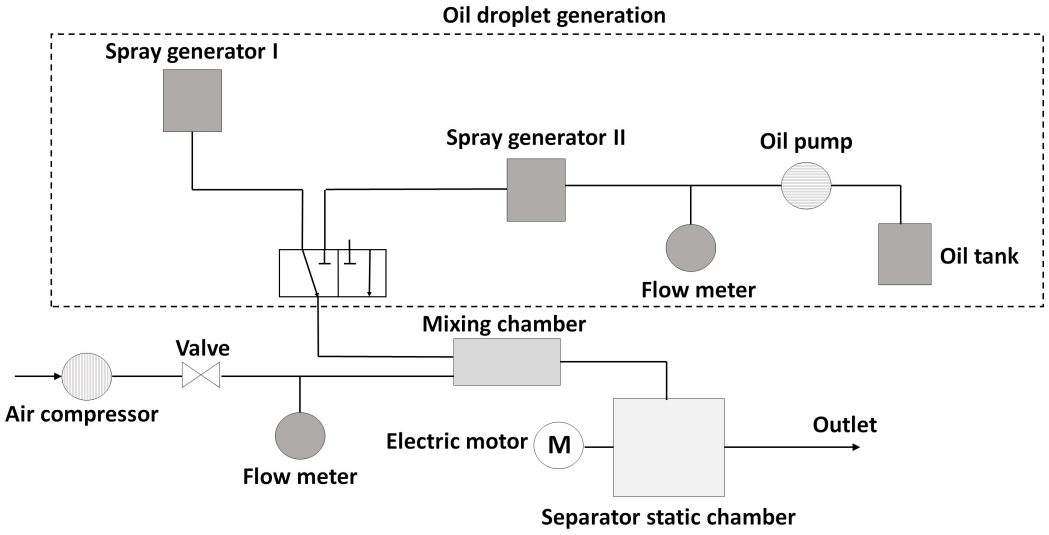

Figure 5.3: Schematic of the experimental test rig at KIT.

oil separation occurs by means of centrifugal effects induced by the swirling flow, which direct the largest droplets towards the static chamber outer wall, where an oil film is generally formed. The oil film tends to flow, under gravity, towards the scavenge ports where it is subsequently collected into closed containers. Smaller droplets will follow the airflow through the breather, where secondary separation takes place inside the metal foam as described in the previous paragraph.

5.1.1 Experimental procedure

A simplified schematic of the experimental test rig at KIT is depicted in Figure 5.3. The hollow shaft is driven by an electric motor capable of rotational speeds of up to 7,000 RPM. The test rig is supplied with compressed air up to 10 bar at ambient temperature, and mass flow rates ranging from 10 to 100 g/s. A hot film probe is employed to measure the air mass flow with an accuracy of $\pm 3\%$. The inlet air pressure is controlled using a valve, whilst the pressure at the outlet of the test rig is ambient at all conditions tested.

Two types of spray generators are used in order to represent the dilute oil flow conditions characteristic of aero-engine separators. Each spray generator produces a distinct droplet size

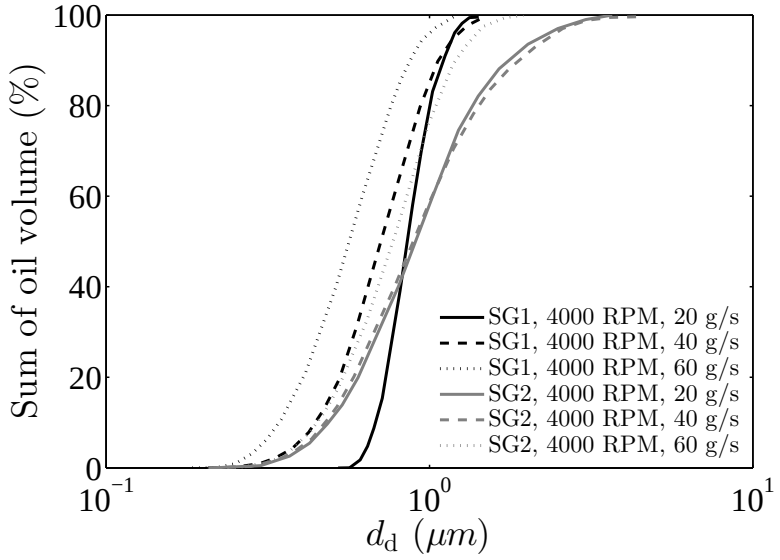

Figure 5.4: Droplet diameter distributions for both spray generators at 4,000 RPM and varying air mass flow rates.

distribution, which is characterized at the inlet of the separator by the using a laser diffraction method. The oil flow from the spray generator is mixed with the air flow inside a mixing chamber located prior to the separator. The first spray generator (SG1) produces droplets with a maximum diameter of 2 µm and an oil flow rate of 0.04 litres per hour. The second spray generator (SG2) produces droplets with a diameter of up to 10 µm and oil flow rates between 0.7 to 1.8 litres per hour, depending on the air mass flow rate. The incoming oil mass is measured by weighting the oil from the first spray generator (SG1) before and after each test run. An oval wheel counter with an accuracy of $\pm 1\%$ is employed to measure the oil flow rate from the second spray generator (SG2). Figure 5.4 depicts the measured droplet distributions produced by both spray generators at 4,000 RPM for varying air mass flow rates.

The air-oil mixture enters the static chamber evenly distributed through the six inlet pipes. Three breather configurations were investigated in the experiments, one without a metal foam, and two using the Retimet 45 and 80 PPI metal foams respectively. The separated oil which leaves the separator through the three scavenge ports and is collected in containers closed to the atmosphere, which are later weighted using a pair of scales with an accuracy of ± 1 mg

and ± 100 mg receptively. The separation efficiency is measured assuming a stationary system by dividing the mass of collected oil in the containers by the total mass of oil injected. In order to ensure that a stationary state has been reached, a lead time of 30 minutes was allowed prior to the measurements. For measurements using the SG1, one hour of experiment time was required to produce a sufficient amount of separated oil with a reasonable accuracy. 30 minutes of experiment time proved sufficient for the SG2, and the measurement uncertainty was determined to be $\pm 2\%$.

The pressure drop across the separator was measured as well, using two pressure transducers as shown in Figure 5.2a, where p_{in} and p_{out} denote the inlet and outlet pressure measurement locations. The pressure drop is computed by subtracting the inlet and outlet pressure, $\Delta p = p_{\text{in}} - p_{\text{out}}$. Both pressures were recorded several times during the entire test duration and averaged, in order to account for any transient effects.

Both oil separation efficiency and pressure drop were investigated for all three breather configurations, under varying air mass flow rates and shaft rotational speeds. The air mass flow rate was varied from 10 to 100 g/s and the rotational speed was varied from 0 to 6,000 RPM.

5.1.2 Experimental oil separation results

The oil separation results are reported here in terms of the percentage of the oil volume that has escaped (not separated) the separator. These results can be used for comparison and validation against the CFD simulations. Table 5.1 summarizes the experimental oil separation results. The experiments have showed that when the SG1 spray generator was used, it resulted in a higher volume of escaped oil, which was expected since the SG1 injects very small droplets. This trend is experienced for both configurations without foam and with the Retimet 80 PPI. Oil separation results obtained with the Retimet 80 PPI showed better oil capture efficiency when compared to the cases without foam, for both SG1 and SG2.

The air mass flow has a stronger impact on the oil separation than the breather rotational

Table 5.1: Summary of oil separation experimental results.

Escaped oil (% total volume of oil injected)

	Without foam			Retimet 80 PPI		
SG1	20 g/s	40 g/s	100 g/s	20 g/s	40 g/s	100 g/s
0 RPM	98	90	97	-	83	-
2,000 RPM	92	85	96	82	-	89
4,000 RPM	89	81	94	-	73	-
6,000 RPM	95	89	95	48	-	97
SG2	20 g/s	40 g/s	100 g/s	20 g/s	40 g/s	100 g/s
0 RPM	-	52	-	-	60	-
2,000 RPM	16	-	81	35	-	93
4,000 RPM	-	48	-	-	50	-
6,000 RPM	44	-	77	18	-	92

speed. For the cases without foam, increasing the air mass flow generally worsened the oil separation, especially for the SG2 spray generator. A similar trend was observed when the Retimet 80 PPI was employed. An increase in the breather rotational speed showed some improvement of the oil capture up to 4,000 RPM for the SG1. Further increasing the rotational speed impacted negatively the oil separation.

Even though an increase in the air mass flow rate will also increase the droplet momentum, it may also cause a reduction in the droplet diameter, by promoting break-up and secondary atomization. In addition to that, there might be oil film formation on the separator walls, which can eventually detach and separate at sharp corners, promoting re-entrainment of droplets into the main flow. Although the analysis of the experimental oil separation results point out the importance of droplet re-atomization and re-entrainment, these effects could not be evaluated with the current experimental apparatus.

5.2 CFD methodology

5.2.1 Computational domain

The computational geometry was generated from CAD files of the actual static chamber and breather employed in the test rig. Some minor simplifications were performed on the geometry, such as the removal of all bolts and screws, but the emphasis was on keeping the maximum amount of detail. Therefore, the computational domain is essentially the 3-D model depicted in Figure 5.1a. Due to the complexity of the geometry, the mesh generation involved the creation of an unstructured tetrahedral grid and later conversion to a polyhedral mesh, similar to the mesh generation employed for the pore-scale simulations. The reasons for that are basically the same, to obtain a good quality mesh with a reasonable total mesh count. Grid-refinement was applied next to areas of high curvature and narrow gaps. A prismatic inflation layer was employed next to the walls to ensure good resolution of the flow boundary layer.

Table 5.2: Grid independence study mesh cell count.

Mesh	Cell count	Type of refinement/coarsening
Coarse	1,544,066	global, $\times 1.32$
Reference	2,474,905	-
Fine	3,285,247	global, $\times 0.63$

A mesh independence study was carried out in order to rule out numerical errors in the flow solution. Three meshes with different levels of refinement were built as shown in Table 5.2. Steady state flow simulations are carried out for each mesh, using the two-equation RNG k-ε turbulence model, at 4,000 RPM and 50 g/s of airflow. The porous medium is not considered in the simulations. An integral convergence criterion is the overall pressure drop within the separator. Figure 5.5 shows pressure drop values obtained for mesh. Results show a significant difference between pressure drop values obtained with the *coarse* mesh and the other two.

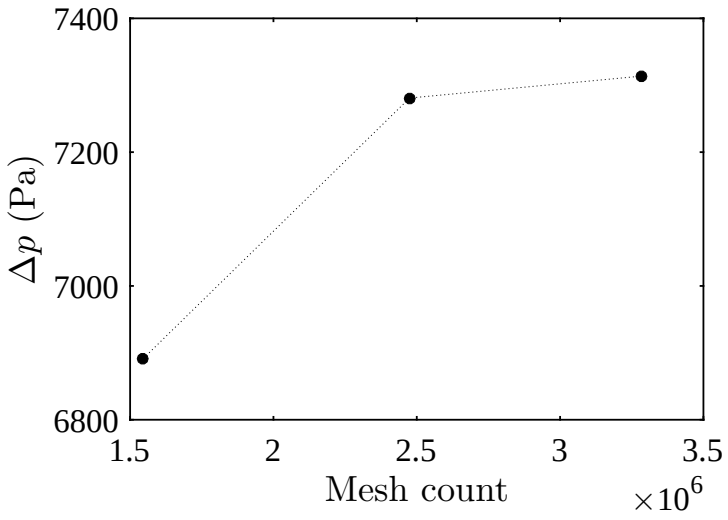

Figure 5.5: Overall separator pressure drop versus mesh count, for the three different meshes.

Conversely, the discrepancy between the *reference* and *fine* meshes is almost negligible.

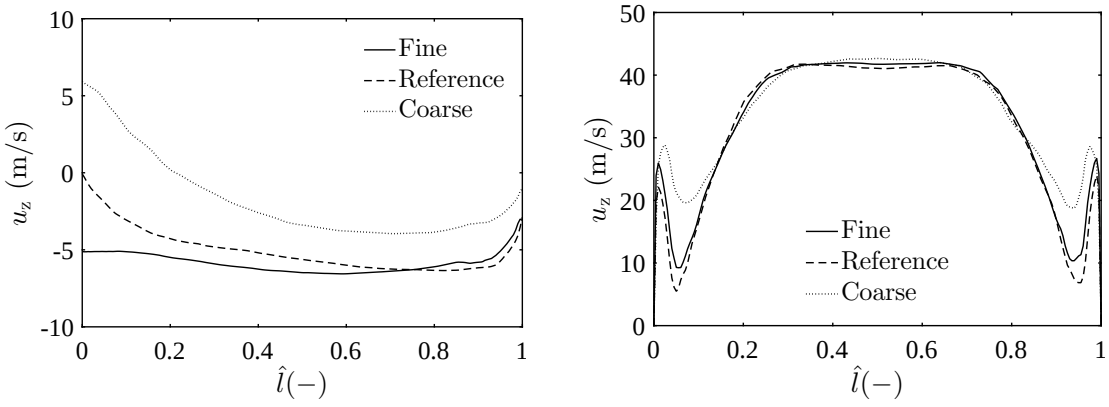

Figure 5.6: Axial velocity, u_z, profile versus the normalized line length at lines located (a) at the rotor entrance and (b) inside the hollow shaft. Exact line locations are shown in Appendix C, Figure C.1, lines 2 and 4.

A more detailed investigation is done by analysing individual velocity profiles within the separator. Figure 5.6 shows the axial velocity profiles obtained at two lines located in sensitive areas within the separator. The profiles depicted in Figure 5.6a are located at next to the rotor entrance, whereas the profiles shown in Figure 5.6b are located inside the hollow shaft. Exact line locations are depicted in Appendix C, Figure C.1, namely lines 2 and 4. The results show

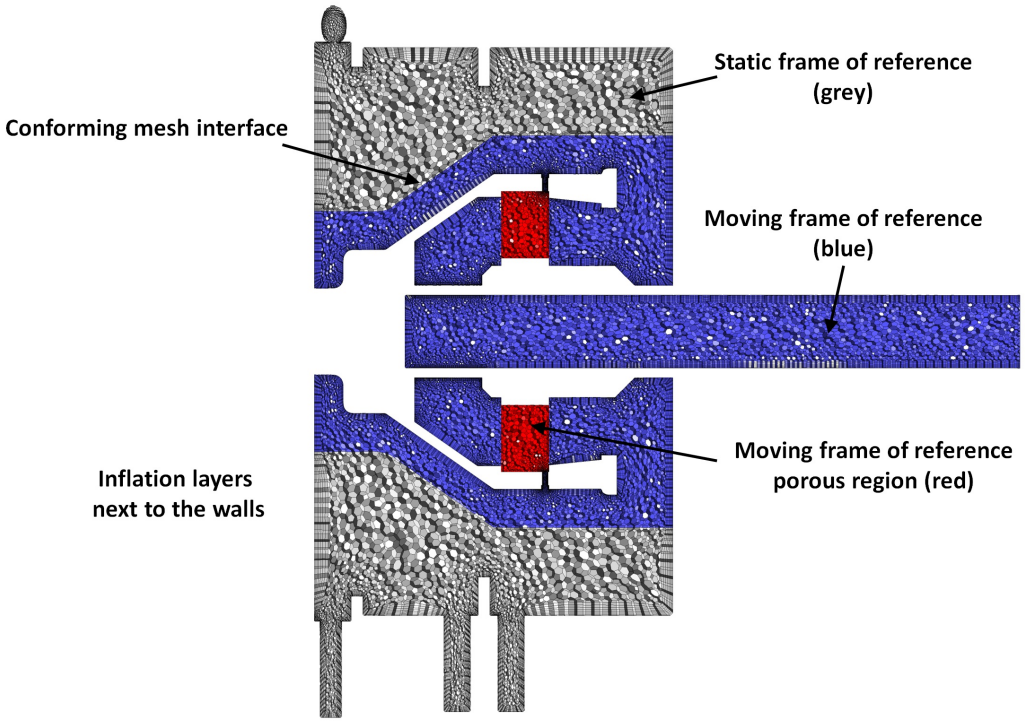

Figure 5.7: Cut-plane of the polyhedral mesh and the different fluid zones defined.

a significant difference between the axial velocity profiles obtained with the *coarse* mesh and the other two. Although there is some discrepancy between the *reference* and *fine* meshes, it does not seem to justify the extra computational effort needed for the *fine* mesh. Therefore, it is concluded that a grid with 2.4×10^6 polyhedral cells is sufficient to ensure mesh independence and minimize numerical errors. Additionally, Table 5.3 shows the average y^+ values with the reference mesh at the rotor and static chamber surfaces, for two operational conditions, 0 RPM with 20 g/s of airflow and 6,000 RPM with 100 g/s of airflow. This range of y^+ values will require a near wall treatment capable of dealing with values located at the three distinct boundary layer regions, the viscous, buffer and logarithmic layer.

One of the aims here is to improve the current modelling methodology employed for aero-engine separators. Previous studies have often made use of a *moving wall* approach in order to simulate the rotation of the shaft and breather parts. A moving wall approach works by imposing a rotational (or translational) speed about a specified axis (or direction). This approach is not

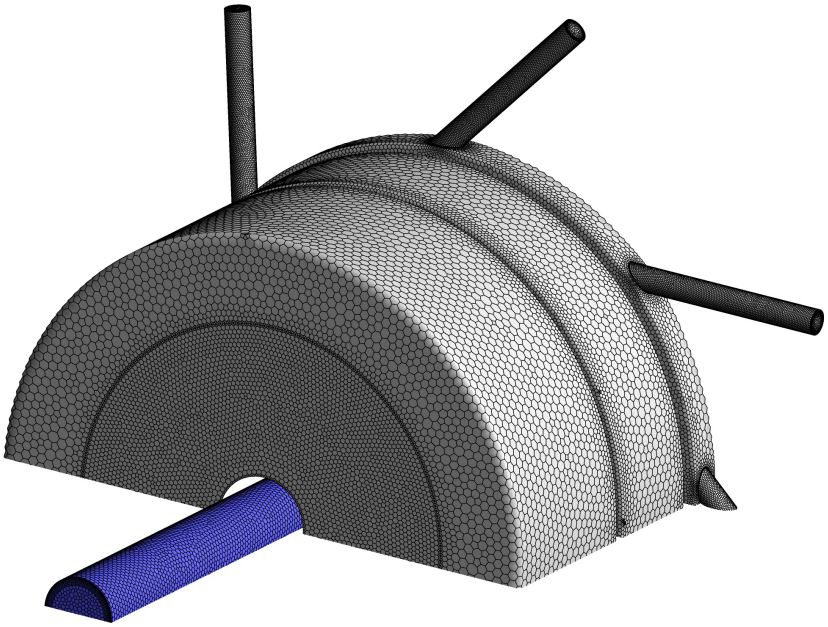

(a)

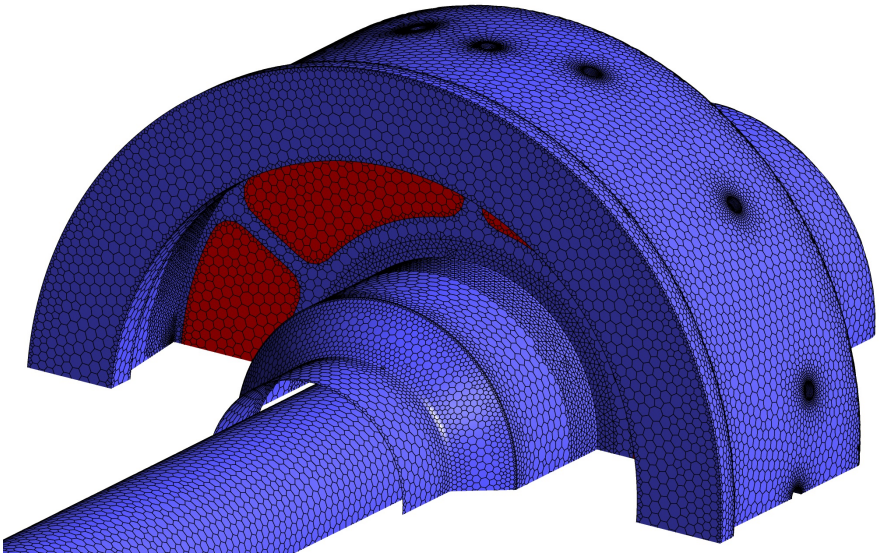

(b)

Figure 5.8: (a) View of the computational mesh of the static chamber, inlet pipes and hollow shaft; (b) Detailed view of the breather mesh. Grey, blue and red regions denote the static, moving and porous zones.

Table 5.3: Average y^+ values at the rotor and static chamber.

Location	0 RPM 20 g/s	6,000 RPM 100 g/s
Rotor, avg. y^+	9.7	11.3
Static chamber, avg. y^+	11.6	29.7

suitable if the wall motion with respect to the adjacent fluid region has a component that is normal to the wall itself. For such problems a moving reference frame approach can be better suited.

Figure 5.7 depicts a cut-plane of the mesh, highlighting its most relevant features. The fluid region was divided into three distinct fluid zones in order to enable the use of multiple reference frames (MRF) to account for rotation of the breather. In Figure 5.7, the grey mesh depicts the fluid region modelled in an absolute frame of reference. The blue mesh illustrates the fluid region modelled in a moving frame of reference (with respect to the absolute one). A fully conformal interface was created halfway between the static chamber and the rotor, connecting both the static and MRF fluid regions. Lastly, the red mesh illustrates the porous medium (metal foam) region, which is also modelled in a MRF. The porous region parameters are obtained from the pore-scale simulations. Figure 5.8 provides a detailed view of the computational mesh of the static chamber and breather. The quasi-symmetry of the separator geometry favours the use of MRF, and some studies have shown that MRF tends to be more accurate than moving wall approaches for rotating machinery problems Liu and Hill (2000); Cheah et al. (2007).

5.2.2 Airflow modelling

An Eulerian-Lagrangian approach is employed in order to model the two-phase flow within the separator. The flow governing equations are the essentially the same as the ones employed in the pore-scale simulations, described in Section 2.2. Since the Mach number is expected to exceed 0.3 at high mass flow conditions, compressibility effects are considered, and air is modelled as

an ideal gas. Two turbulence models are evaluated, the two-equation RNG k-ε, which assumes an isotropic turbulence and the RSM, which solves each component of the Reynolds stresses, thus solving a total of seven equations. An enhanced wall treatment approach is employed for both models (ANSYS, 2013), since it is capable of dealing with y^+ values such as the ones reported in Table 5.3.

The porous medium is modelled as a separate MRF fluid zone, using the enhanced macroscopic porous media model described in Section 4.8. The viscous and inertial resistance coefficients are computed from the pore-scale simulation results performed on the Retimet 45 and 80 PPI foams respectively. As shown previously, the entire computational domain was divided into static and moving frames of reference zones. Therefore, rotation of the breather is taken into account by imposing a tangential velocity component about the axial direction in the MRF zones.

The commercial finite volume solver Ansys Fluent 15 (ANSYS, 2013), was employed to solve the governing equations and turbulence closure models. The SIMPLE algorithm was used for pressure-velocity coupling. Both steady state and transient simulations were performed. A conformal mesh interface was employed between static and moving frames of reference zones. A second-order upwind scheme was employed for spatial discretization. For transient calculations, time was discretized using a second-order scheme. The linearised equations were solved using algebraic multi-grid acceleration. A non-dimensional convergence criterion of 10^{-5} was set for the scaled residuals together with monitoring of selected field-variables inside the separator to ensure that the solution has become stationary.

Figure 5.9 depicts typical convergence plots of selected field-variables computed from a steady-state simulation. The rotor moment coefficient, C_m, provides a good measure of convergence for such type of flow. The total moment vector on the rotor is computed by summing the cross products of the pressure and viscous force vectors, and dividing by $\frac{1}{2}\rho u^2 AL$, where u, A and L are the reference velocity, area and length respectively. Figure 5.9a shows that the rotor

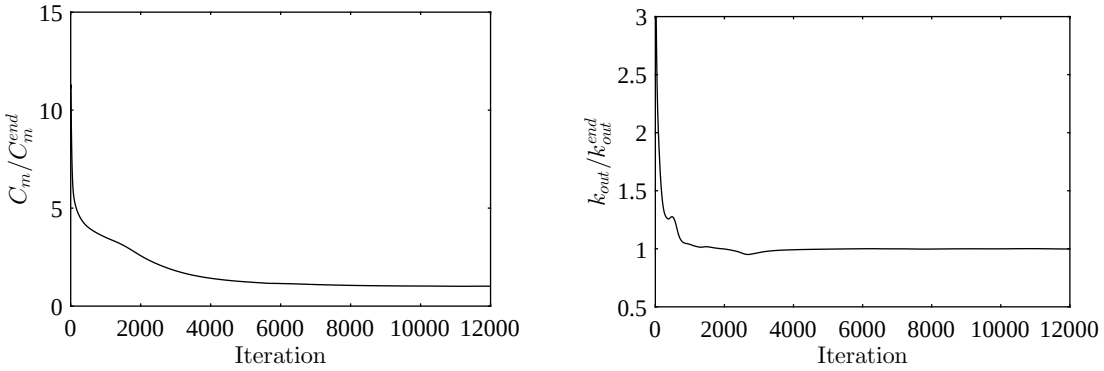

(a) (b)

Figure 5.9: Convergence of the (a) rotor moment coefficient and (b) average turbulent kinetic energy at the separator outlet. Both variables are normalized by the their value at the last iteration.

moment coefficient starts to stabilize after approximately 8,000 iterations. Figure 5.9b shows the turbulent kinetic energy convergence, which starts to stabilize earlier, at approximately 4,000 iterations. The solutions is given as converged when at least both variables have stabilized around a mean value.

5.2.3 Dispersed oil phase modelling

The dispersed oil phase was modelled using a Lagrangian particle tracking approach, with the formulation already described in Section 4.6.1. The oil volume fraction is quite small ($<1\%$), even when at the highest flow rate from the spray generators (SG2, 1.8 litres/h), and lowest air mass flow rate. The maximum droplet size analysed here is 10 μm. The assumptions for the oil phase are essentially the same as the ones taken for the pore-scale Lagrangian calculations. Thus, it is reasonable to assume that the oil phase is sufficiently disperse such that droplet-droplet interactions can be neglected, and that the droplets are perfectly spherical. The incoming location of the droplets is averaged over the whole inlet area, with a direction normal to the inlet surface. Droplets are injected at the same speed as the air.

The Lagrangian calculations are divided into two categories: steady-state and transient.

Steady state calculations were one-way coupled and considered turbulent dispersion by means of a stochastic random walk model. Droplet trajectories are assumed to terminate once the they impact against a wall (no rebounding, or splashing). However, in reality it is likely that an oil film forms over the chamber walls. The film may also detach at sharp edges promoting re-atomization. These phenomena are extremely complex and very difficult to model. Here, the feasibility of capturing some degree of film formation and re-atomization is investigated by means of a Lagrangian thin film approach. When the film model is employed, droplet calculations are transient and two-way coupled (which is a requirement of the film model). When the droplets impact against a wall, four outcomes are possible: stick, spread, rebound, or splash, based on the impact energy. Furthermore, the film is allowed to detach at sharp edges. It is important to be aware that the film model was developed based on simple idealized cases, and its correlations may not be entirely valid for the conditions simulated here. Gravitational acceleration was taken into account and is aligned with the scavenge pipes (normal to the scavenge outlet).

5.2.4 Oil film modelling

A film is defined as a layer of liquid partially bounded by a solid phase, with a distinct interface between the liquid and another fluid, usually a gas. Generally, the thickness of the film is orders of magnitude smaller than its size in other dimensions. The oil film inside aero-engine separators is normally assumed to be thin, in a way that the velocity field is approximately planar, with the velocity component normal to the solid surface being negligible compared to the components parallel to it.

The liquid film model employed here uses a Lagrangian formulation, which is based on the work of O'Rourke and Amsden (1996). This model allows for a single droplet parcel to impinge upon a boundary surface and form a thin film. Therefore, the assumption is that the film thickness is less than 500 μm at least, so that a linear velocity profile can be assumed. The

film model can be subdivided into four subtopics: droplet interaction with a wall boundary, tracking of the impinged droplets on surfaces, computation of film variables and coupling with the gas phase.

There are essentially four possible outcomes after a droplet impact on a surface: stick, rebound, spread or splash. The criterion by which the outcomes are partitioned is based on the impact energy and boiling temperature of the liquid. This wall interaction model is based on the work of Stanton and Rutland (1996); O'Rourke and Amsden (2000). The impact energy is a dimensionless parameter defined as

$$E^2 = \frac{\rho_l u_r^2 d_d}{\sigma} \left(\frac{1}{\min(h_0/d_d, 1) + \delta_{bl}/d_d} \right) \tag{5.1}$$

where ρ_l is the liquid density, u_r is the relative velocity of the droplet to the wall, such as $u_r^2 = (u_d - u_w)^2$, with u_w as the velocity at the wall, d_d is the droplet diameter, h_0 is the film height and σ is the surface tension. δ_{bl} is a boundary layer thickness defined as

$$\delta_{bl} = \frac{d_d}{\sqrt{Re_l}} \tag{5.2}$$

where Re_l is defined as $Re_l = \rho_l u_r d_d / \mu$.

Therefore, the choice of droplet impact outcome is based on the value of E. The sticking outcome is applied when the dimensionless energy is less than 16, then the droplet velocity is set equal to the wall velocity. The rebound outcome only takes place when the wall temperature is higher than the boiling temperature of the liquid, however that does not happen under the operational conditions considered here. When the dimensionless energy is $16 < E < 57.7$, the impact outcome is the spreading regime. The initial direction and velocity of the droplet are computed using a wall-jet model as described in (ANSYS, 2013), where the probability of a droplet having a particular direction along the surface is given by an analogy of an inviscid liquid jet and an empirically defined radial dependence for calculation of the momentum flux.

Finally, when the dimensionless energy is above 57.7, splashing occurs. The number of

splashed droplet parcels is a user defined parameter between three and ten. The properties (diameter, velocity and direction) of the splashed particles are randomly sampled from experimentally obtained distribution functions. The detailed formulation of the splashing algorithm is beyond the scope of the current thesis and can be found in (ANSYS, 2013; Stanton and Rutland, 1996). It is important to bear in mind that all the droplet-wall interaction phenomena mentioned above are extremely complex in nature, and the current model aims to provide an approximation of what would happen.

Except for the rebound regime, all the other droplet outcomes imply the formation of a thin layer of liquid film on the wall. The thin film model is a particle-based approach, and the momentum equation for a Lagrangian film parcel is given by

$$\rho h \frac{d\mathbf{u_d}}{dt} = \tau_g \mathbf{t} + \tau_\mathbf{w} + \mathbf{F} + \rho_l h(\mathbf{g} - \alpha_\mathbf{w}) \tag{5.3}$$

where $\mathbf{u_d}$ is the film parcel velocity, τ_g is the magnitude of the shear stress of the gas flow in the surface of the film, $\mathbf{t}$ is the unit vector in the direction of the film surface velocity, τ_w is the stress the wall exerts on the film, $\mathbf{F}$ is the force necessary to keep the film on the surface, h is the film height at the parcel location and $\rho_l h(\mathbf{g} - \alpha_\mathbf{w})$ is a body force term.

The wall stress is defined as

$$\tau_\mathbf{w} = -2\frac{\mu_l}{h}(\mathbf{u_d} - \mathbf{u_w}) \tag{5.4}$$

where μ_l is the liquid film viscosity and $\mathbf{u_w}$ is the wall velocity.

No mass or energy transfer are considered at the moment since the flow is expected to remain close to ambient temperature.

5.2.5 Boundary conditions

The simulations comprised the operational configurations investigated experimentally. Three breather configurations were investigated: without the metal foam and with the Retimet 45

and 80 PPI foams respectively. Four shaft rotational speeds were considered for each breather configuration: 0, 2,000, 4,000 and 6,000 RPM and five different air mass flow rates: 20, 40, 60, 80 and 100 g/s, were considered for each shaft speed. This gives a total of 60 distinct cases. The inlet conditions were set at ambient temperature (300 K), and temperature variations within the separator are only due to air compressibility effects.

It is worth noting however, that the operational conditions simulated here are representative of the experimental conditions investigated at the KIT test rig, and some of those conditions would never happen in practice, within a real engine. Nevertheless, previous studies on real engines have shown worst oil separation effectiveness to take place at lower rotational and airflow rates (ground idle regime). For comparison purposes, typical real engine conditions at the ground idle regime would comprise a rotational speed of $\sim$ 5,000 RPM and airflow rates of 20 to 40 g/s.

A mass-flow inlet condition is defined at the inlets, such that the total air mass flow is distributed evenly through the six inlets. A zero gauge pressure is set at the outlet, assuming a radial equilibrium pressure distribution, which is a close approximation to actual experimentally measured values at the outlet. No air is allowed to leave the domain through the scavenges, which is in accordance to experimental conditions where closed containers were attached to the scavenge pipes. A no-slip condition is applied at the walls, which all have a zero velocity relative to the adjacent fluid region. An exception is a portion of the static chamber wall which is adjacent to the MRF region, and is defined as a moving wall with zero velocity in the absolute frame of reference. Table 5.4 shows the boundary conditions for the incoming air flow, rotational speeds and the porous medium parameters for the three breather configurations

Boundary conditions for the incoming oil are based on the information extracted from the two spray generators employed in the KIT test rig. In the experiments, oil flow rate and mean droplet size vary slightly with the air mass flow and separator rotational speed. In order to simplify the computational boundary conditions, oil injection parameters are held constant, re-

Table 5.4: Modelling boundary conditions showing the inlet air mass flow rates, rotational speeds and breather porous medium parameters investigated in the simulations.

Boundary condition		Value	
Inlet mass flow (g/s)		20, 40, 60, 80, 100	
MRF rotational speed (RPM)		0, 2,000, 4,000, 6,000	
Outlet pressure (Pa)		0 (gauge)	
Porous medium parameters	without foam	Retimet 45 PPI	Retimet 80 PPI
$1/K \times 10^8$ (m^{-2})	-	3.47	3.75
C_2 (m^{-1})	-	2099.71	2397.71
Porosity	-	0.83	0.88

gardless of air mass flow or rotational speed. The simulations assume that the oil is injected at maximum oil flow rates, using droplet diameter distributions calculated at those conditions. A Rosin-Rammler size distribution was fitted to the data from the two spray generators, using 10 distinct droplet diameters. Velocity of incoming oil is assumed to be the same as air with a direction normal to the inlet surface. Oil material properties are those of gasoil-liquid, $C_{16}H_{29}$. Table 5.5 summarizes the oil injection properties used in the simulations.

The oil flow characteristics investigated by KIT and here are not necessarily representative of real engine conditions. Since the focus of the present study is on the separation effectiveness of the smallest droplets, much lower oil flow rates are considered here. For comparison purposes, at the ground idle regime, the oil flow rate within real engines ranges from 50 to 100 g/s typically.

5.3 Airflow simulations

Two turbulence models were evaluated here, the RNG k-ε and RSM. The simulations which employed the RSM started from a converged steady state solution obtained using the RNG k-ε

Table 5.5: Oil boundary conditions used in the simulations

Spray generator:	SG1	SG2
Mean droplet size (µm)	0.8	1
Minimum droplet size (µm)	0.2	0.2
Maximum droplet size (µm)	2	6
Spread factor	3.5	3
Number of diameters	10	10
Oil volumetric flow (l/h)	0.04	1.8
Oil mass flow (g/s)	9.22×10^{-3}	0.415
Injection velocity	Same as air	Same as air

model. Fluid compressibility and rotation of the frame of reference were included right from the beginning of the calculations. The solver under-relaxation factors had to be reduced from its default values in order to ensure a stable and converged solution, especially when using the RSM. The simulations were run using the university's HPC facility, employing normally 24 to 32 Intel Harpertown 3 GHz cores. Typically, a converged steady state solution required several hours of computing time.

5.3.1 Pressure drop results

The pressure drop is an important parameter for aero-engine separators, since it affects the secondary airflow system and overall engine efficiency. The approximate locations of the pressure transducers employed in the experimental measurements performed by the KIT are illustrated in Figure 5.2a. In the computational model, the inlet pressure is computed as the volume-average static pressure in a small spherical volume around the actual experimental measurement location. The outlet pressure is taken as zero (gauge), which is a close approximation to the experimental conditions. The experimental pressure drop values are used for validation of the

numerical approach. Results presented in this section are concerned with steady state air flow simulations.

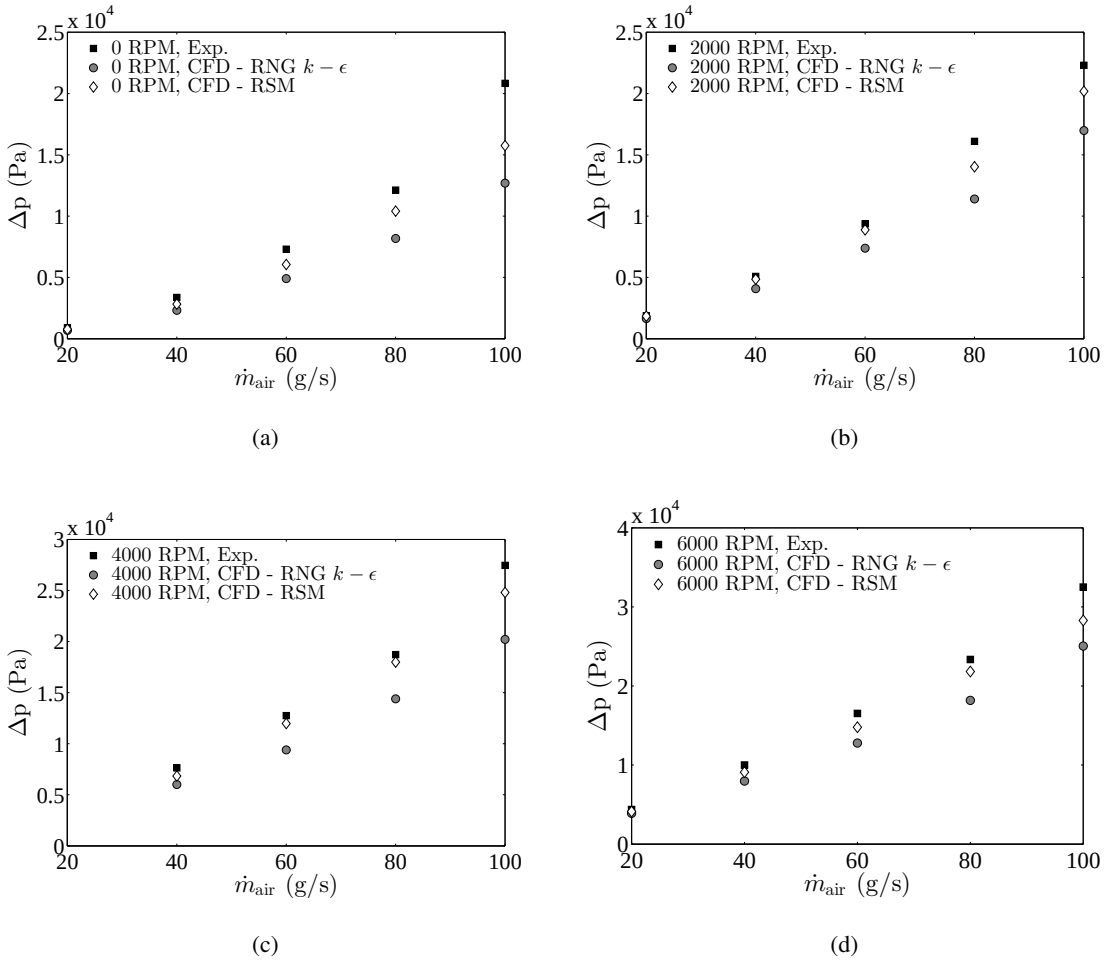

Figure 5.10: Comparison between experimental and simulation pressure drop results employing the RNG k-ε and RSM turbulence models, with the Retimet 80 PPI foam. The pressure drop is plotted as a function of the inlet air mass flow, for rotational speeds of (a) 0 RPM, (b) 2,000 RPM, (c) 4,000 RPM and (d) 6,000 RPM.

Figure 5.10 shows a comparison between experimental and simulated pressure drop results using the RNG k-ε and RSM turbulence models, with the configuration using the Retimet 80 PPI foam. Note that a description of the theoretical differences between both models is complex and beyond the scope here. The swirling character of the flow within the separator is inherently three-dimensional and turbulence is expected to be strongly anisotropic. It has been reported

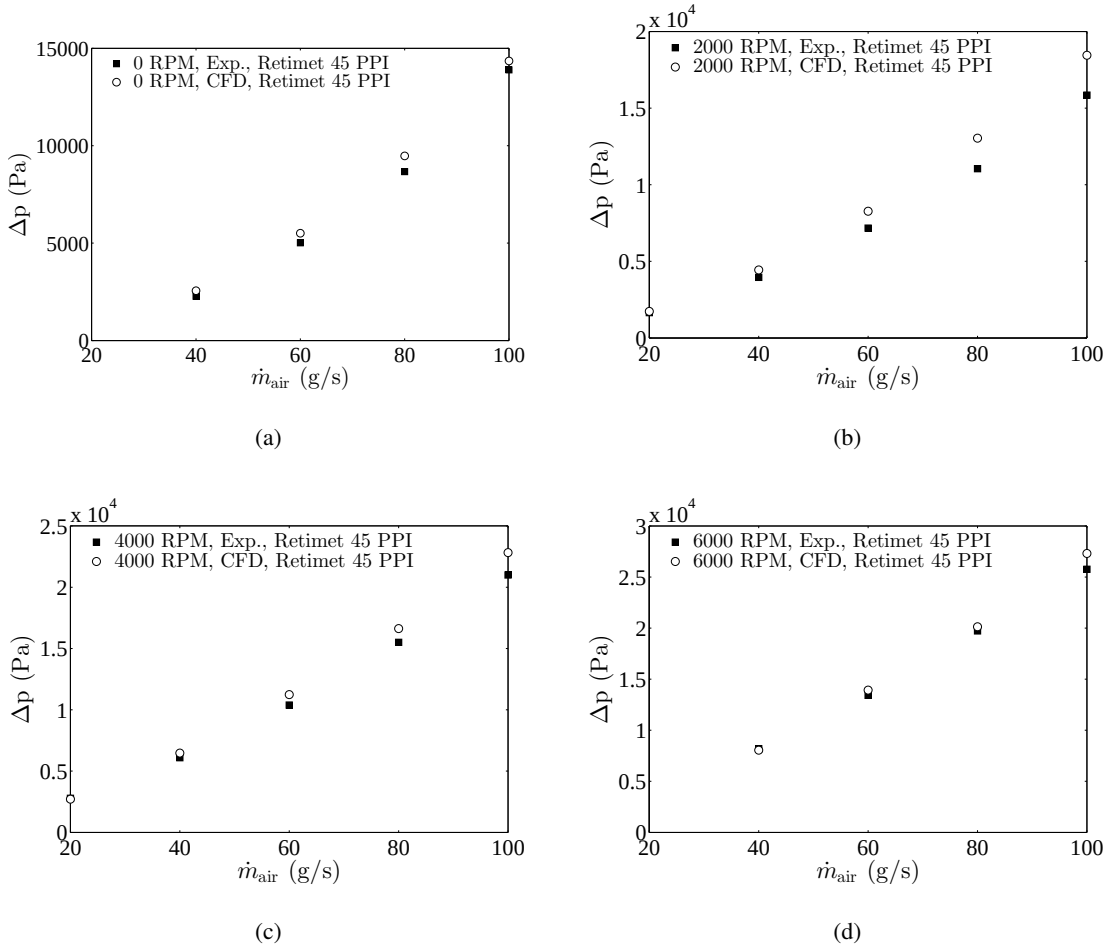

Figure 5.11: Comparison between experimental and simulation pressure drop results employing the RSM, with the Retimet 45 PPI foam. The pressure drop is plotted as a function of the inlet air mass flow, for rotational speeds of (a) 0 RPM, (b) 2,000 RPM, (c) 4,000 RPM and (d) 6,000 RPM.

that two-equation turbulence models are ill-suited for such cases Slack et al. (2000); Wang et al. (2006); Gronald and Derksen (2011), due to the assumption of isotropic turbulence. Results obtained with the simulations here are in line with this observation, with the RSM showing better agreement against the experimental data. The average normalized root-mean-square (NRMS) deviations for the pressure drop using the RNG k-ε and RSM turbulence models are 23.52 % and 9.92 % respectively. The NRMS deviation calculation uses the experimental data as the reference. From this point forwards, the results shown were obtained with the RSM.

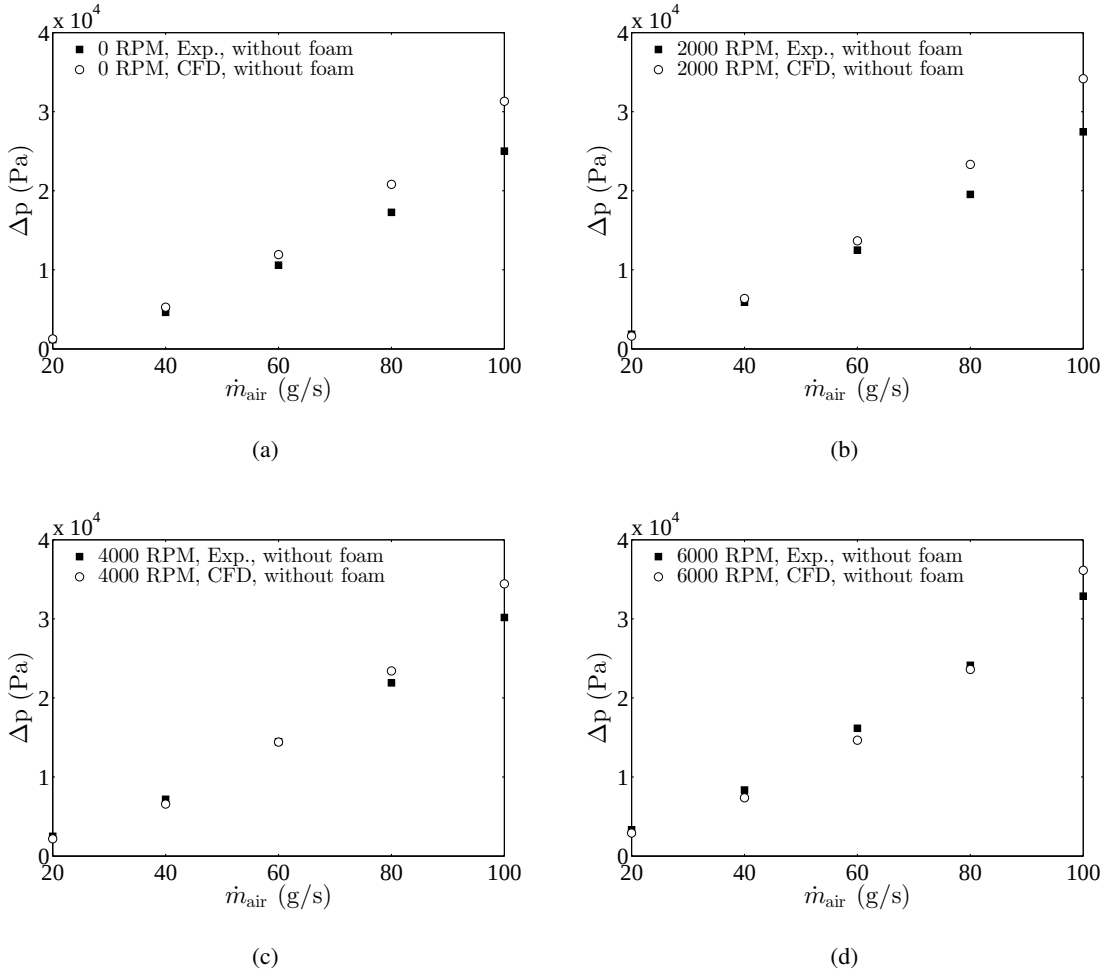

Figure 5.12: Comparison between experimental and simulation pressure drop results employing the RSM, without using a foam. The pressure drop is plotted as a function of the inlet air mass flow, for rotational speeds of (a) 0 RPM, (b) 2,000 RPM, (c) 4,000 RPM and (d) 6,000 RPM.

Figures 5.11 and 5.12 show a comparison between the experimental and simulated pressure drop results obtained with the Retimet 45 PPI foam and without a foam respectively. Table 5.6 shows the NRSM deviation between the experimental and simulated pressure drop results for each rotational speed and breather configuration. It seems a better agreement is observed for higher rotational speeds. The average NRMS deviations for the results without a metal foam and with the Retimet 45 PPI were 11.97 % and 7.86 % respectively. Pressure drop values obtained with both Retimet foams showed to be very similar, with the Retimet 80 PPI causing a slightly higher pressure drop, as expected. The main difference between the two foams is the pore

size, with the Retimet 80 PI having a smaller pore size. This difference is reflected as different viscous and inertial coefficients in the macroscopic porous medium model.

Increasing air mass flow has a stronger effect on the pressure drop than increasing rotational speed. For the case without metal foam, doubling the air mass flow rate from 40 to 80 g/s increases the pressure drop by 220 to 290 %, depending on the shaft speed, with a more significant pressure drop increase at lower rotational speeds. On the other hand, doubling the shaft speed from 2,000 to 4,000 RPM increases the pressure drop by only 8.7 % on average, depending on the air mass flow. At 20 g/s, the magnitude of this increase is approximately 30 %, however at 100 g/s the increase is lower than 1 %. This shows that the pre-swirl generated by the six inlets has a dominant effect on the flow and pressure drop for the cases without foam.

Results obtained with the Retimet foams presented a slightly different flow behaviour. Increasing air flow still has a stronger effect on the pressure drop than increasing rotational speed, however not as significant as for the cases without foam. Doubling the air mass flow rate from 40 to 80 g/s increases the pressure drop by 140 to 270 %, depending on shaft speed. However, doubling the rotational speed from 2,000 to 4,000 RPM increases the pressure drop by 37 % on average. As in the cases without metal foam, at 20 g/s the pressure drop increase caused by increasing shaft speed is more significant than at higher air mass flow rates. The discrepancy between cases with and without metal foam can be attributed to the damping effect caused by the metal foam on the flow pre-swirl.

The cases without metal foam showed a higher pressure drop than the cases with the Retimet foams, a trend in agreement with the experiments. This is explained by the reduction in the flow tangential velocity as it passes through the metal foam, before being re-accelerated by the rotor as it leaves the foam region. Conversely, if no metal foam is present, there is no obstruction to the flow swirl and higher tangential velocities are achieved. More details about the main flow characteristics are provided in the following section. Furthermore, Appendix C depicts the normalized tangential and axial velocity profiles taken at five different locations inside the

Table 5.6: Average NRSM deviation between experiments and simulations for each rotational speed.

	Average NRSM deviation (%)		
Rotational speed (RPM)	without foam	Retimet 45 PPI	Retimet 80 PPI
0	15.83	7.56	17.05
2000	14.53	13.33	6.73
4000	8.43	6.56	6.93
6000	9.07	3.99	8.98
Mean	11.97	7.86	9.92

separator, at all rotational speeds for the configurations without foam and with the Retimet 80 PPI.

5.3.2 Main flow characteristics

There are several effects which contribute to the pressure drop within the separator. Four main effects can be identified: losses due to wall friction, the pressure loss due to the presence of the metal foam, vortex losses due to the swirling flow, and the rotation of the breather casing, which affects the angular momentum of the flow. It is easier to understand the flow behaviour by analysing the cases with zero breather rotational speed. Very similar results were obtained with both Retimet foams, therefore the following analysis will show the results for the Retimet 80 PPI only.

Figure 5.13 shows pressure contour plots at 0 RPM and 20 g/s of airflow, for the cases without a foam and the Retimet 80 PPI respectively. The pressure distribution across the separator varies mainly with the radial direction. For the case with the Retimet 80 PPI, the presence of the foam also affects the pressure distribution within the separator, especially downstream of the foam region. However, the results clearly show that the pressure distribution within the sep-

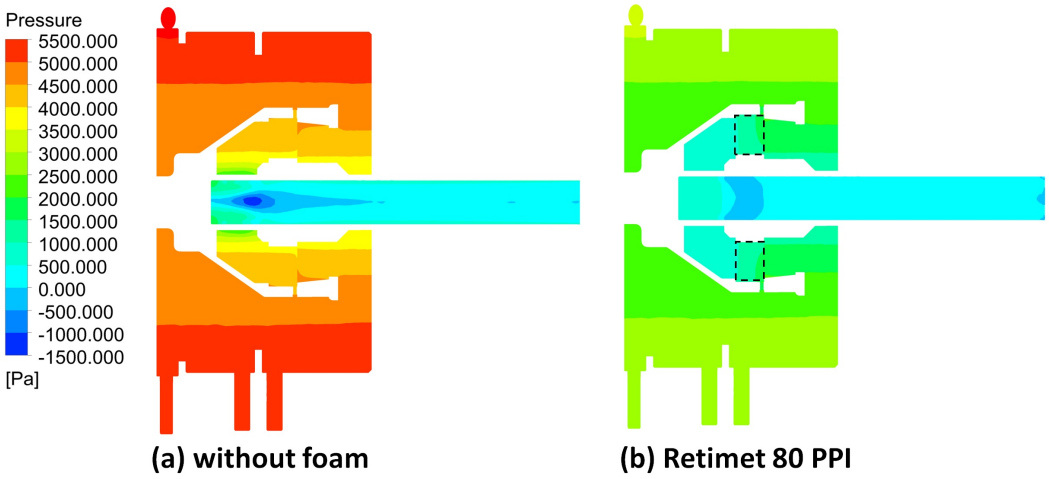

Figure 5.13: Pressure contour plot without a foam and with the Retimet 80 PPI, at 0 RPM and 40 g/s of air mass flow. The region within the dashed lines denotes the metal foam location.

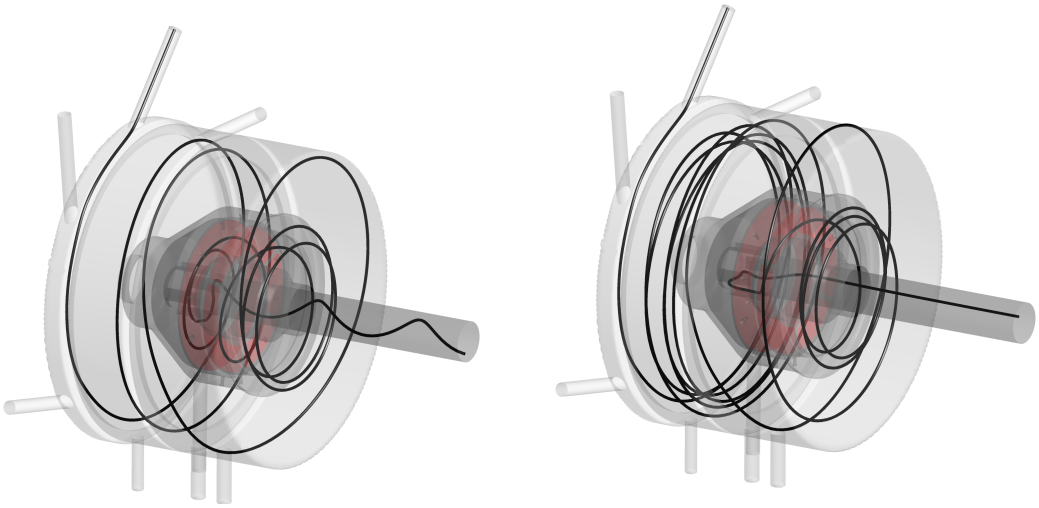

(a) (b)

Figure 5.14: Illustration of an arbitrary streamline for a case without rotation of the breather. (a) without foam and (b) with the Retimet 80 PPI. The red surface highlights the location of the metal foam.

arator is dominated mainly by centrifugal effects and the pressure drop is higher in the cases without a metal foam. This trend persisted when the rotational speed was above zero as well.

The flow pre-swirl is generated by the six tangential inlets, and when the metal foam is present, the pre-swirl tends to be damped. Figure 5.14 clearly illustrates this effect by showing

two flow streamlines, one for the case without foam and the other with the Retimet 80 PPI, both at 0 RPM. The flow pattern upstream the metal foam is practically identical for both cases. It is clear that in the case with the Retimet 80 PPI, the pre-swirl generated by the inlets is almost completely damped by the metal foam, whereas in the case without a foam, the swirl continues downstream of the foam region into the hollow shaft.

Further investigation of the numerical results showed the axial velocity to be weakly affected by the presence of the metal foam, thus being very similar for both configurations. This suggests that the pressure within the separator is mainly governed by the flow tangential velocity, v_t. Distinct differences in the tangential velocity profile are observed between the cases with and without metal foam. Figure 5.15 depicts contour plots of the normalized tangential velocity both without and with the Retimet 80 PPI at 0 RPM. The tangential velocity is normalized by the inlet tangential velocity, computed next to the inlet pipes exit, $v_t/v_{t,0}$, which is located at the outer radius of the chamber, r_0. Additionally, an arbitrary streamline is shown and divided into representative sections to help better understand the flow characteristics and the tangential velocity radial profile.

Considering the case with zero rotational speed, from points 1 to 2 along the streamline depicted in Figure 5.15, there is a sudden reduction in the tangential velocity due to the widening of the incoming jet from the inlet pipes. After entering the main chamber, the flow starts a helical path and is re-accelerated up to the region next to the second protruding plate on the outer wall. From there to point 2, the tangential velocity is gradually reduced due to an increase in the cross-section. From points 2 to $2'$, since the angular momentum is conserved, there is an increase in the tangential velocity when the air flow radially inwards. From points $2'$ to 3, the radius and tangential velocity remains practically constant. The flow behaviour is almost identical for both cases without and with a foam from point 1 to 3. Downstream of point 3, the tangential velocity profile is dependent on the breather configuration (with or without metal foam). For the case with a metal foam, from point 3 to $3'$, the tangential velocity is reduced to zero, and remains

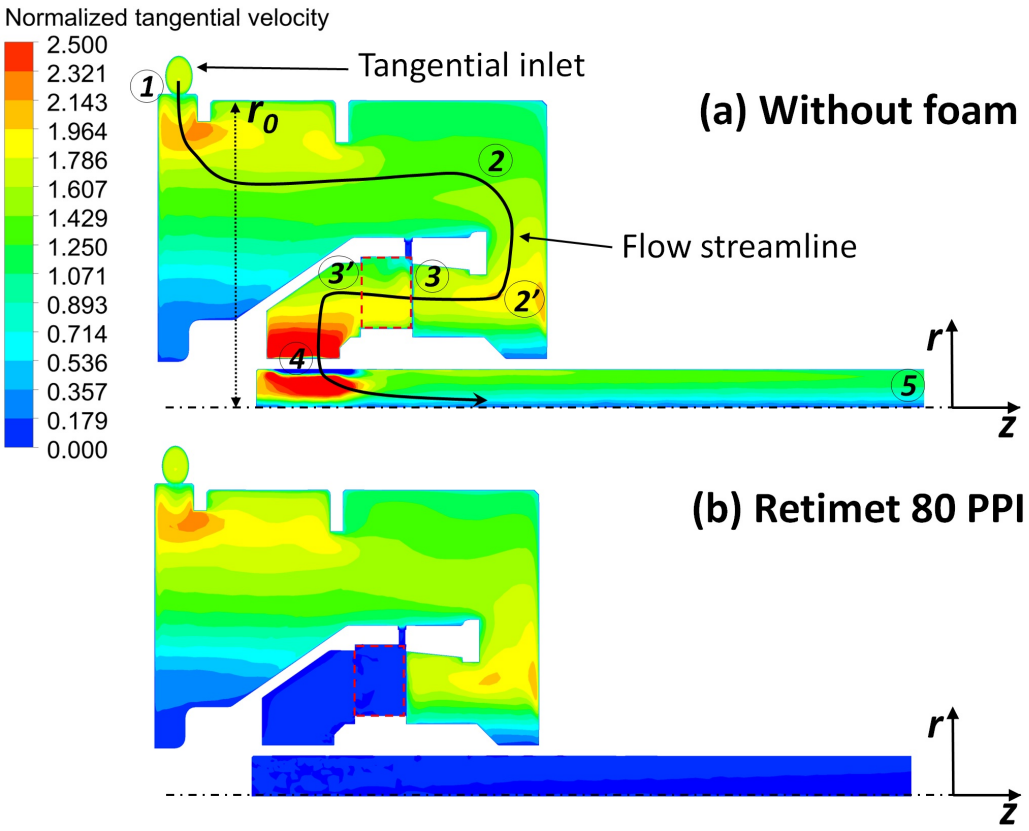

Figure 5.15: Contour plot of the normalized tangential velocity, $v_t/v_{t,0}$, without a foam and with the Retimet 80 PPI, at 0 RPM. r_0 denotes the outer radius of the main chamber, and v_t is normalized by the value of v_t at the inlets (r_0). The numbers are used to divide the typical streamline into representative sections with distinct flow behaviour. The red dashed lines denote the metal foam region.

close to zero until point 5, located next to the outlet. The pressure drop within the foam region becomes mainly a function of the axial velocity and the porous medium viscous and inertial resistances.

For the case without a foam, the radius and tangential speed remain roughly constant from points 3 to 3′. However, from points 3′ to 4, the tangential velocity is increased up to its maximum value, due to conservation of angular momentum, and the streamline goes into the hollow shaft towards the outlet. From points 4 to 5 there is a sudden reduction in the tangential velocity right next to point 4 and then it stabilizes until the outlet. The flow in this case, consists of

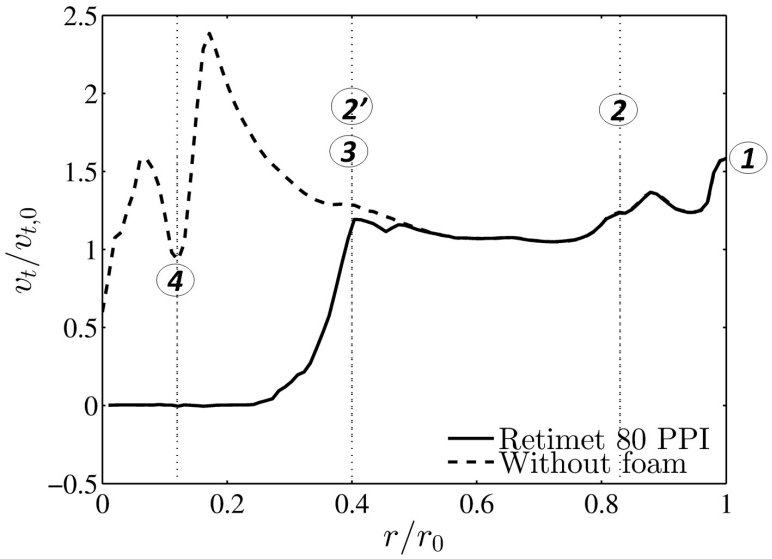

Figure 5.16: Normalized tangential velocity, $v_t/v_{t,0}$, plotted as a function of the normalized radius, r/r_0, for the cases with zero rotational speed, both without and with the Retimet 80 PPI foam. This data is an average over 1,000 streamlines.

mainly two vortices, one in the main chamber, and the other inside the breather.

Figure 5.16 adds credibility to these observations, showing the normalized tangential velocity radial profile without and with the Retimet 80 PPI foam respectively. The radial position is normalized by the outer chamber radius, r_0. The profile was computed by taking the average normalized tangential velocity radial profile over 1,000 flow streamlines. Figure 5.16 also depicts the estimated locations of points 1 to 5 as a function of the normalized radius. The normalized tangential velocity profile for both cases is practically identical up until the metal foam entrance. As mentioned before, the presence of the foam reduces the tangential velocity to zero, and remains at that level until the outlet of the separator. When no foam is present, the tangential velocity continues to increase until it reaches a maximum next to the entrance of the hollow shaft.

The flow behaviour changes significantly when considering the rotation of the breather. Figure 5.17 depicts the pressure and normalized tangential velocity contour plots at 4,000 RPM for the cases without foam and with the Retimet 80 PPI respectively. Similarly to the case

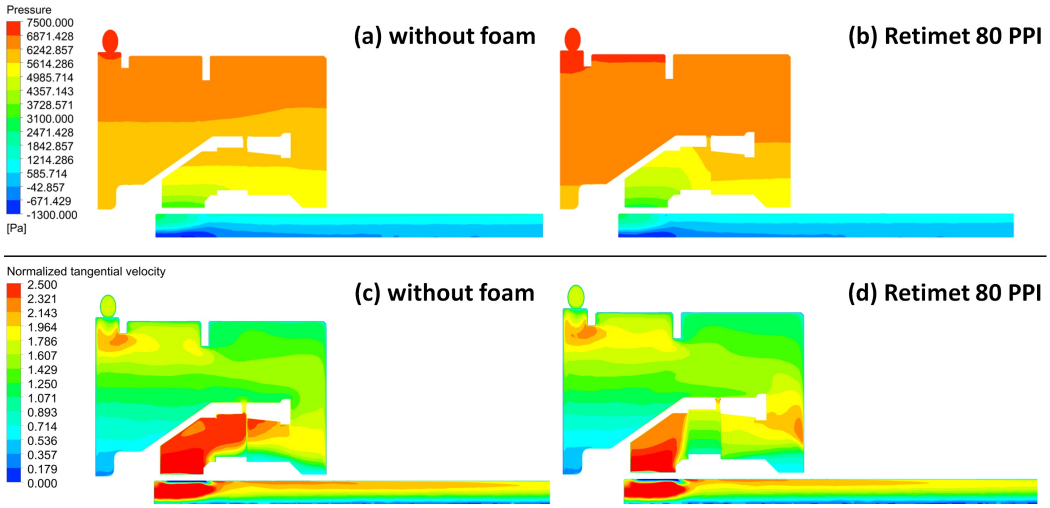

Figure 5.17: Pressure contour plots at 4000 RPM for the cases (a) without foam and (b) with the Retimet 80 PPI. Normalized tangential velocity contour plots at 4000 RPM or the cases (c) without foam and (d) with the Retimet 80 PPI.

without rotation, the flow behaviour prior to the metal foam region is quite similar for both cases. However, at the metal foam region, the pressure drop varies mainly with the radial position, whereas in the case with the Retimet 80 PPI, the pressure drop varies with both radial and axial directions. The main difference when compared with the cases with zero rotational speed is in the region downstream the foam region. Since the foam is rotating as well, it does not completely damp the tangential velocity to zero, instead, it causes only a moderate reduction. Figure 5.18 depicts the normalized tangential velocity radial profile at 4,000 RPM without and with the metal foam. It clearly shows the damping on the tangential velocity caused by the presence of the metal foam. However, downstream the foam, the flow is re-accelerated again and the profiles computed for both configurations are very similar.

Both cases at 0 and 4000 RPM analysed in this section were concerned with an air mass flow rate of 40 g/s. For comparison purposes, at 0 RPM, the case without foam has a pressure drop 46.54 % higher than the case with the Retimet 80 PPI. In contrast, at 4,000 RPM, the case without foam shows a pressure drop 3.84 % lower than the case with the Retimet 80 PPI. Both comparisons considered the case without foam as the reference.

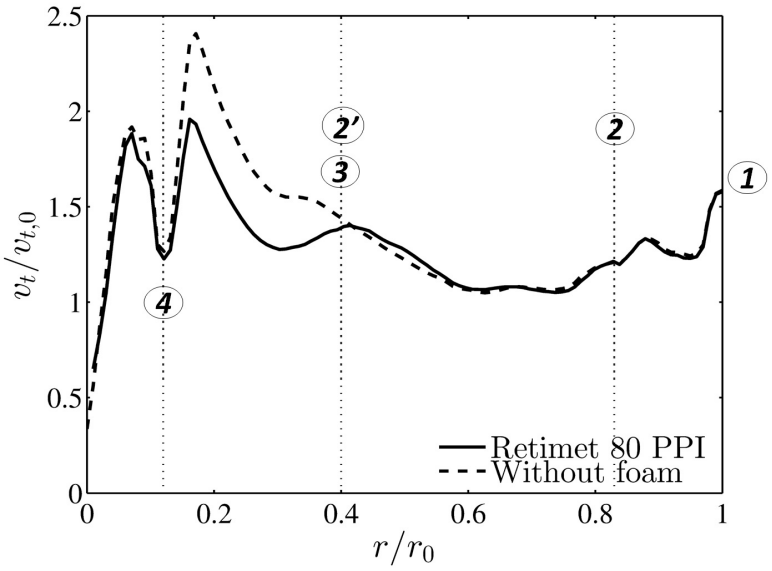

Figure 5.18: Normalized tangential velocity, $v_t/v_{t,0}$, plotted as a function of the normalized radius, r/r_0, for the cases with zero rotational speed, both without and with the Retimet 80 PPI foam. This data is an average over 1,000 streamlines.

Another interesting flow feature was observed for all cases, which might affect the oil separation effectiveness. In theory, any amount of oil which is accumulated within the metal foam is supposed to flow radially outwards back into the main chamber through the 16 drain holes present in the breather casing. Airflow results show that the flow is entering the drain holes from the main chamber instead of the opposite, as illustrated by the vector plots in Figure 5.19. The pressure on the main chamber is higher than the pressure within the metal foam region, and that holds at practically all operational conditions. It is possible that in reality, when enough oil is accumulated within the foam, centripetal forces acting on the oil will dominate shear and overcome this adverse pressure gradient. However, the design of the rotor could be improved for these two effects to add to each other.

The vector plots also point out another possible problem, which is the cross-flow right next to the drain holes exit. If in reality the oil manages to exit the metal foam through these drain holes, the presence of this cross-flow can possibly re-atomize or breakup the droplets, thus generating smaller droplets which are more difficult to separate.

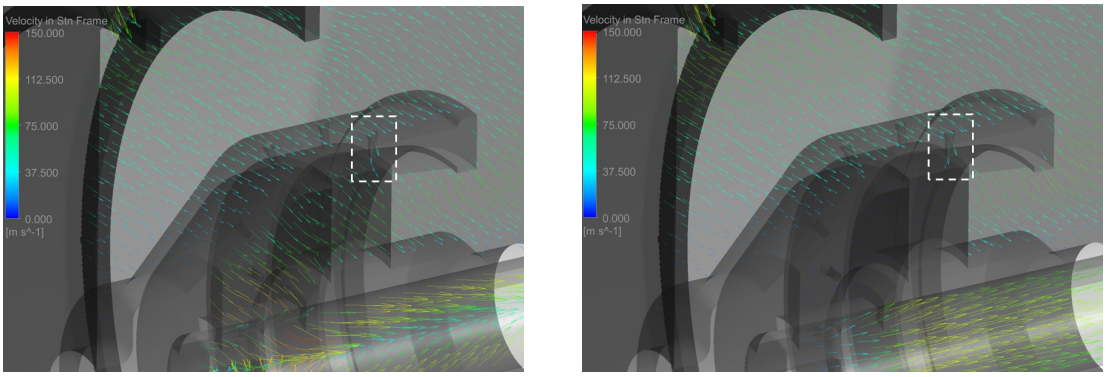

(a) (b)

Figure 5.19: Velocity vectors at 0 RPM and 100 g/s of air mass flow for the cases (a) without foam and (b) with the Retimet 80 PPI. The dashed lines highlight the region next to the drain holes.

5.3.3 Transient flow simulations

It is common for complex swirling flows such as the ones investigated here to have an unsteady behaviour. Transient vortex motion, oscillating flow features and secondary flow effects are common features. In order to assess the significance of time-dependent effects, a series of transient calculations were performed starting from steady state solutions and the pressure drop was monitored at each time step. Due to the longer run times required, transient simulations were run for a few selected operational conditions due to time constraints. The simulations were run such that the average flow Courant number (Eq. 4.6) remained close to unity.

Figure 5.20 shows the relative of pressure drop deviation between steady state and transient calculations, for the configuration using the Retimet 80 PPI at several selected operational conditions. It takes roughly 0.2 to 0.5 seconds of flow time in order to achieve a stationary or oscillating periodic behaviour, depending on the rotational speed and air mass flow. The relative difference between steady state pressure drop values and the time-averaged solution after the flow becomes steady ranged from 3 %, to 10 %, with lower shaft speeds showing larger discrepancies. Pressure drop results obtained from steady state simulations generally under-predicted

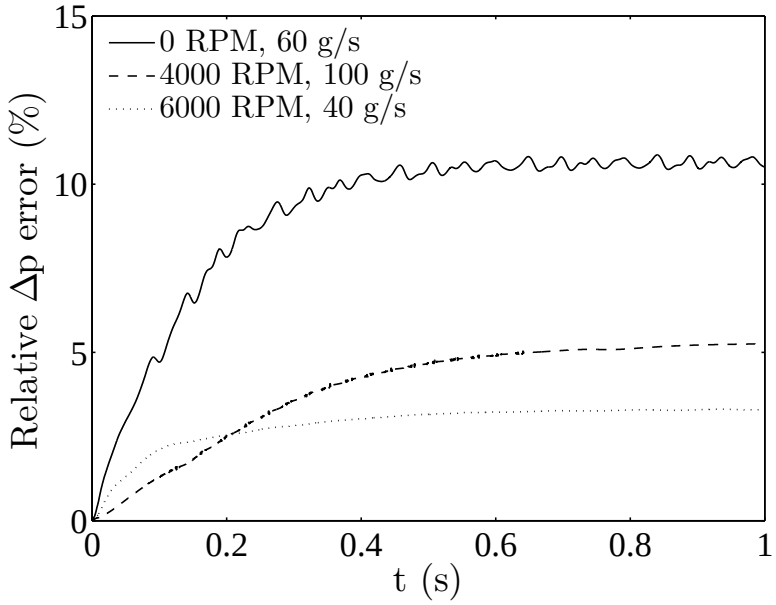

Figure 5.20: Development of the relative pressure drop deviation between the steady state solution ($t = 0$) and the transient simulation for multiple operational conditions.

the experimental values. Without exception, the time-averaged pressure drop from transient simulations showed better agreement with the experimental data, as shown in Table 5.7. As the results do not indicate any periodic or oscillating flow pattern, it appears that the transient simulations simply improve the convergence of steady state solutions. The main flow characteristics of the time-averaged solutions remained practically identical to the steady state solutions.

Table 5.7: Comparison between the time-averaged and steady state normalized RSM pressure drop deviation results.

Case	Steady state Δp NRMS (%)	Time-averaged Δp NRMS (%)
0 RPM, 60 g/s	17.08	8.29
4,000 RPM, 100 g/s	9.68	4.92
6,000 RPM, 40 g/s	6.06	6.02

5.4 Eulerian-Lagrangian air-oil simulations

The oil phase Lagrangian simulations are divided into two categories: steady-state one-way coupled and transient two-way coupled with a Lagrangian thin film model. The oil injection properties used for the simulations are depicted in Table 5.5. The macroscopic oil extinction model described in Section 4.8 is employed for the cases with the Retimet foams. However, the present modelling methodology still has one major limitation, since it neglects the accumulation of oil within the metal foams. Consequently, no oil leaves the porous zone through the drain holes in the simulations.

Experimental oil separation data was available for all three breather configurations, for both droplet generators, at air mass flow rates of 20, 40 and 100 g/s and rotational speeds of 0, 2,000, 4,000 and 6,000 RPM. No experimental data regarding velocity, size and concentration of droplets at the outlet of the separator was available.

5.4.1 Steady state Lagrangian results

A total of 15,000 droplet parcel injections (each parcel is representative of a large number of actual droplets) were employed for each simulation, which produced results that were independent of the number of parcel injections. This section is concerned with steady-state one-way coupled Lagrangian simulations, i.e. the droplets do not have any effect on the airflow. The Lagrangian particle tracking calculations were run within the converged steady state solutions for airflow. Since the flow conditions here are quite similar to the ones employed for the pore-scale simulations, most of the assumptions and simplifications described in Section 4.6.3 are also valid here. Furthermore, similar to the pore-scale Lagrangian simulations, the droplet trajectories are terminated if they impact against the separator walls. Therefore, the oil capture effectiveness in this section is defined as the difference between the total number of parcels injected and the number of parcels that impacted against the walls, and the remainder is defined as the escaped droplets. Turbulent dispersion was taken into account using the DRW model. Since the steady

state Lagrangian calculations are neglecting significant flow aspects such as the interaction with the continuous phase and oil film formation, their use is mainly to provide qualitative oil separation results. The likelihood of droplet capture will be governed by the droplet's inertia. Thus, droplets with more inertia will have a higher probability of impacting against the separator walls.

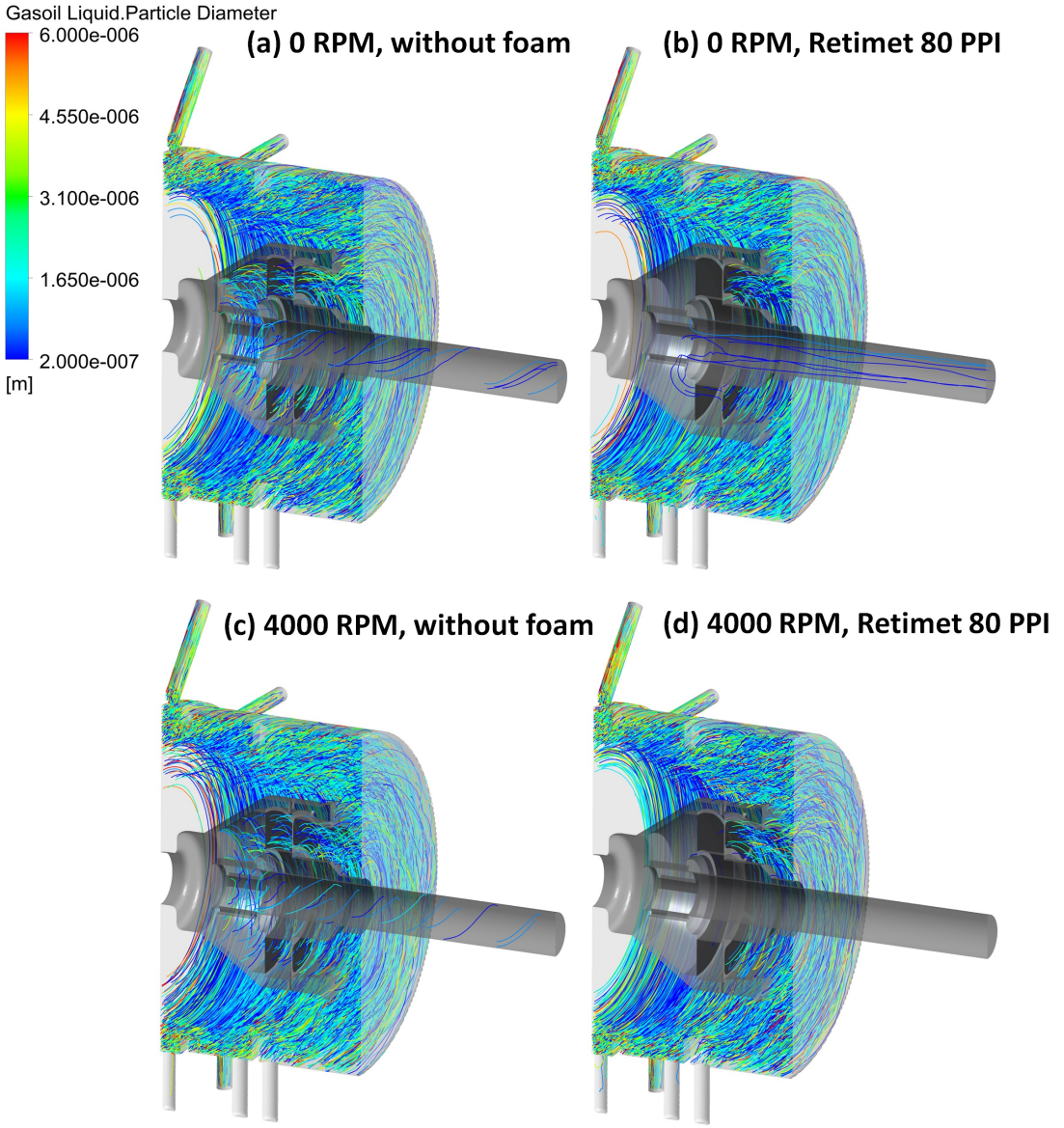

Figure 5.21: Lagragian droplet trajectories at an air mass flow rate of 40 g/s using the SG2 droplet diameter distribution and:(a) 0 RPM without foam, (b) 0 RPM with the Retimet 80 PPI, (c) 4,000 RPM without foam, and (d) 4,000 RPM with the Retimet 80 PPI. The number of droplet tracks was reduced for illustration purposes.

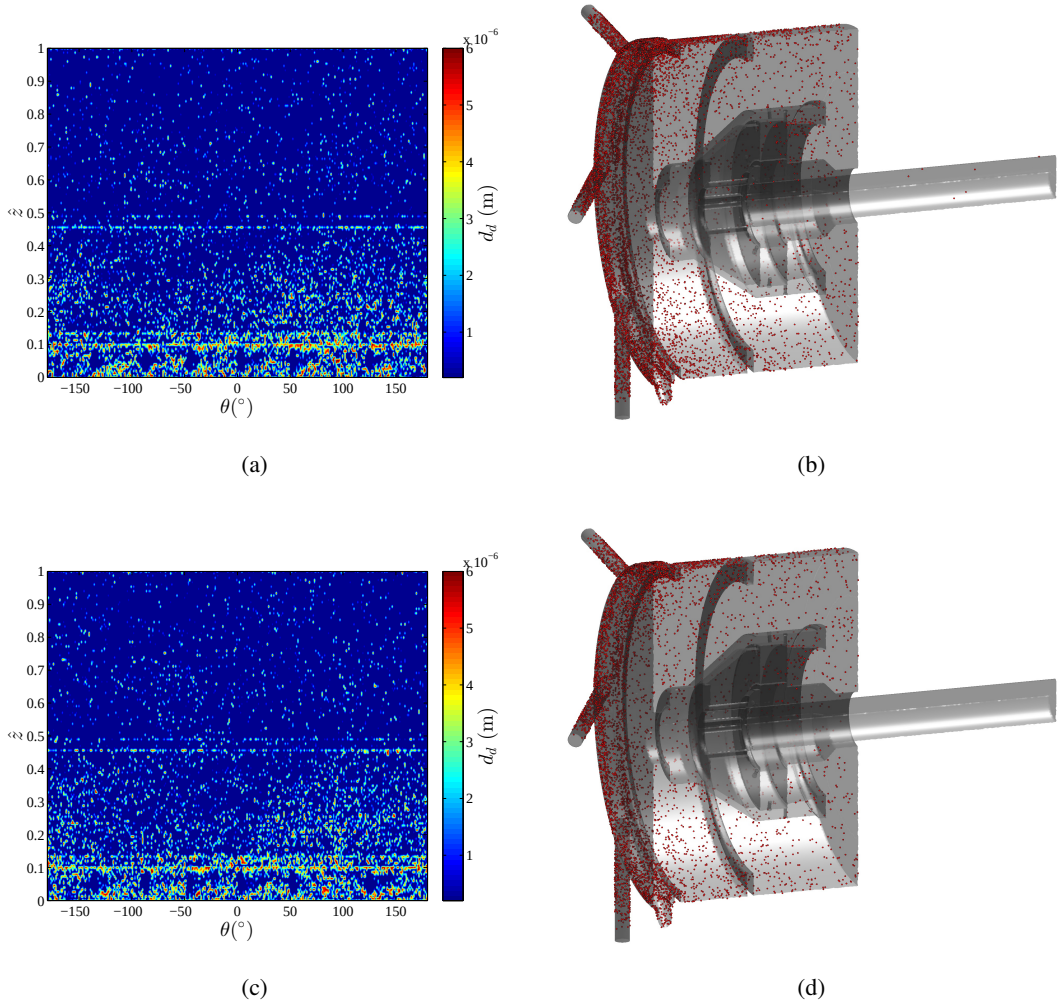

Figure 5.22: Simulated 2-D projection of impact locations on the outer wall and the 3-D impact locations for: (a,b) 0 RPM and (c,d) 4,000 RPM, all for an air mass flow rate of 40 g/s, with the Retimet 80 PPI and the SG2 size distribution.

Generally, the droplet trajectories were very similar regardless of the operational condition. Figure 5.21 shows the droplet trajectories coloured by diameter at four different operational conditions: (a) 0 RPM without foam, (b) 0 RPM with the Retimet 80 PPI, (c) 4,000 RPM without foam, and (d) 4,000 RPM with the Retimet 80 PPI, all for an air mass flow rate of 40 g/s and the SG2 (larger droplets) spray generator. Clearly, in all cases only the smallest droplets are able to pass through the breather and escape. Furthermore, a comparison between the two cases at 4,000 RPM without and with the Retimet 80 PPI clearly show the oil capture effect induced

by the foam using the macroscopic porous medium model.

Results obtained when using the SG1 droplet diameter distribution showed very similar behaviour, but a larger number (roughly twice) of droplets are able to pass through the breather and escape. This was largely expected since the SG1 droplets are significantly smaller compared to the SG2. A common feature observed in both the SG1 and SG2 droplet size distributions was the large number of droplets that impacted against the chamber outer walls, especially within the region between the inlets and the two protruding plates. Figure 5.22 depicts 2-D projections of the impact locations on the chamber outer wall as well as the 3-D impact locations, for 0 and 4,000 RPM at an air mass flow rate of 40 m/s, with the Retimet 80 PPI foam. These results show a large number of droplets colliding against the walls in the region between the inlets and the first protruding plate. The number of impacted droplets decreases along the axial direction towards the breather entrance. The droplet deposition pattern showed to be similar for both 0 and 4,000 RPM conditions. This makes sense, giving the fact that the airflow within the chamber is dominated by the pre-swirl generated from the inlets, and is weakly affected by the rotational speed of the breather.

Tables 5.8 and 5.9 summarize the droplet fates obtained with the steady state Lagrangian simulations, without and with the Retimet 80 PPI foam. Results are averaged for the three air mass flow rates simulated (20,40 and 100 g/s) at each breather rotational speed. Since the intent is to qualitatively evaluate the oil separation, the results show the average droplet fates by number, instead of by mass. Results obtained with the Retimet 45 PPI foam are very similar to the ones with the Retimet 80 PPI, and not shown here for the sake of brevity.

Results showed a very high oil capture, which is not in agreement with experimental results, and indicate the apparent inability of reproducing the oil separation phenomena with steady state one-way coupled Lagrangian simulations. The escaped oil (by number) is $< 1\%$ for all cases simulated, and it would be even smaller if converted to the percentage of oil volume, since the escaped droplets are mainly very small. This contrasts greatly with the experimental results

Table 5.8: Summary of steady state Lagrangian simulations for the case without a foam.

Average droplet fates (% of total number of droplets)				
SG1	0 RPM	2,000 RPM	4,000 RPM	6,000 RPM
Impacted the walls	99.42	99.67	99.82	99.89
Escaped	0.57	0.33	0.18	0.093
Captured by the foam	-	-	-	-
d_c (μm)	2	2	2	2
$\bar{d}_{\text{out}}$ (μm)	0.94	0.95	0.94	0.92
SG2	0 RPM	2000 RPM	4000 RPM	6000 RPM
Impacted the walls	99.79	99.86	99.92	99.94
Escaped	0.20	0.14	0.076	0.058
Captured by the foam	-	-	-	-
d_c (μm)	5.36	5.14	5.36	5.14
$\bar{d}_{\text{out}}$ (μm)	1.32	1.36	1.40	1.34

depicted in Table 5.1, which shows much higher values for the escaped oil.

The number of escaped droplets reduced with increased shaft speed, air flow and mean droplet size. Even if results are not quantitatively similar, they provide a good idea of the overall droplet trajectories and can be used in order to compute the critical diameter, d_c, defined as the largest droplet diameter at the metal foam entrance and the average droplet diameter at the exit of the metal foam region, defined as $\bar{d}_{\text{out}}$.

It is interesting to note that the results show that when the separator does not have a foam, a higher number of droplets impact against the walls, compared to the cases with the Retimet 80 PPI. This is explained by the fact that higher tangential velocities are achieved within the separator when the foam is not employed. Since the likelihood of wall impact is proportional to the droplet inertia, higher tangential velocities enhance primary oil capture (capture due to centrifugal effects). The number of escaped droplets (droplets that have reached the outlet) was

Table 5.9: Summary of steady state Lagrangian simulations for the case with the Retimet 80 PPI

Average droplet fates (% of total number of droplets)				
SG1	0 RPM	2,000 RPM	4,000 RPM	6,000 RPM
Impacted the walls	97.54	96.28	97.00	97.01
Escaped	0.851	0.207	0.002	0.000
Captured by the foam	1.604	3.518	2.996	2.991
d_c (µm)	2	2	2	2
$\bar{d}_{\text{out}}$ (µm)	0.57	0.23	0.2	0
SG2	0 RPM	2,000 RPM	4,000 RPM	6,000 RPM
Impacted the walls	98.74	98.38	98.62	98.57
Escaped	0.304	0.180	0.007	0.000
Captured by the foam	0.951	1.440	1.373	1.429
d_c (µm)	4.71	4.71	5.57	4.71
$\bar{d}_{\text{out}}$ (µm)	0.41	0.2	0.2	0

very small ($< 1\%$) for all cases, and decreased with increased shaft speed, for both without and Retimet 80 PPI configurations.

Analysis of d_c and $\bar{d}_{\text{out}}$ showed that for the SG1 diameter distribution, d_c remain at 2 µm for all cases, regardless of the operational condition or the presence of the foam. When the SG2 diameter distribution is employed, the cases with the metal foam showed a slightly lower d_c value when compared with the cases without foam. Moreover, d_c seems to be independent of the shaft rotational speed.

The average droplet diameter at the exit of the metal foam region, $\bar{d}_{\text{out}}$, was generally lower than the critical diameter, even for the cases without the presence of the foam. This is explained by the fact that when the foam is not present, the droplets continue to follow their helical path through the breather, increasing their overall path length and consequently, chance of hitting the casing walls. For the cases without foam, when the SG1 diameter distribution was employed,

the droplet at the exit of the foam compartment is roughly half the diameter at the entrance, whereas when the SG2 was employed, it was approximately four times smaller.

The results with the Retimet 80 PPI showed a smaller number of droplets captured by impacting against the chamber walls (primary separation), compared to the cases without foam. However, the droplet capture induced by the foam compensates for the higher number of droplets passing through the breather, and overall separation efficiency is slightly improved when the Retimet 80 PPI is employed. Better capture efficiency was observed with increasing the shaft speed. Furthermore, $\bar{d}_{\text{out}}$ is significantly smaller compared to the results obtained without a foam.

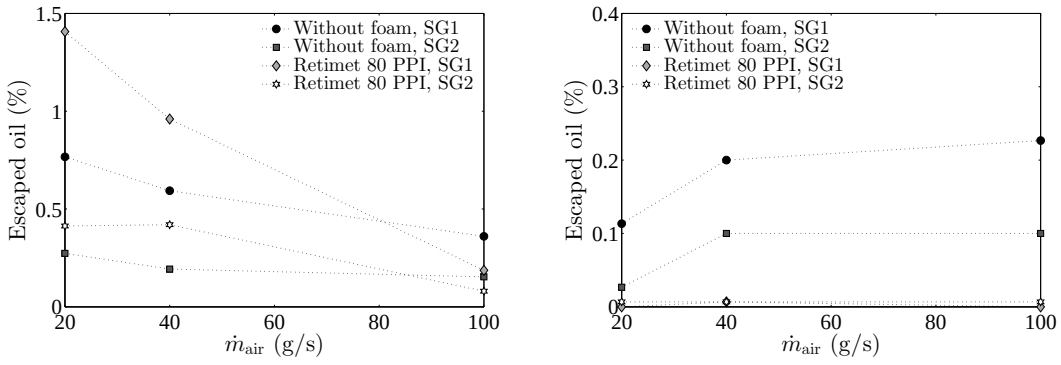

Figure 5.23: Percentage of escaped oil droplets as a function of the air mass flow rate for (a) 0 RPM and (b) 4,000 RPM.

Figure 5.23 shows the percentage of escaped oil droplets as a function of the air mass flow rate for 0 and 4,000 RPM respectively. The results obtained with the Lagrangian simulations do not show any quantitative agreement against the experiments, which is not surprising, since potentially important physical phenomena related to droplet dynamics have been neglected. However, the overall separation trends can be analysed qualitatively. The percentage of escaped oil decreased for both cases without foam and with the Retimet 80 PPI, when the rotational speed was increased from 0 to 4,000 RPM. Experiments also showed a similar trend. At 0

Table 5.10: Average droplet residence time (s) at the metal foam entrance.

	Without foam			Retimet 80 PPI		
SG1	20 g/s	40 g/s	100 g/s	20 g/s	40 g/s	100 g/s
0 RPM	0.393	0.199	0.097	0.397	0.190	0.086
2,000 RPM	0.375	0.182	0.093	0.379	0.186	0.106
4,000 RPM	0.317	0.193	0.091	0.361	0.191	0.089
6,000 RPM	0.339	0.203	0.090	0.339	0.189	0.083
SG2	20 g/s	40 g/s	100 g/s	20 g/s	40 g/s	100 g/s
0 RPM	0.395	0.191	0.090	0.386	0.215	0.081
2,000 RPM	0.393	0.185	0.093	0.347	0.182	0.108
4,000 RPM	0.286	0.195	0.094	0.343	0.179	0.086
6,000 RPM	0.0349	0.192	0.091	0.325	0.191	0.087

RPM, increasing the air mass flow worsened oil separation, also in agreement with the trends observed experimentally. However, at 4,000 RPM, simulation results showed better oil capture with higher air mass flow rates, not in agreement with the experiments. This may be explained by the fact that in reality, when the breather is rotating, the oil that is accumulated within the foam can flow back into the main chamber via the 16 drain holes in the breather casing. As the oil is re-entrained into the main flow, it is likely that smaller droplets will be formed, negatively affecting the oil separation efficiency. This effect is not captured in the simulations.

Table 5.10 lists the average droplet residence time at the entrance of the metal foam region, without and with the Retimet 80 PPI foam. The average droplet residence time at the entrance of the metal foam compartment is weakly affected by the breather rotational speed. When the air mass flow is low (20 g/s), the droplet residence time reduces when the rotational speed is increased. However, for higher air mass flow rates this behaviour does not hold, and no clear trend is observed. On the other hand, the residence time is strongly affected by the air mass flow,

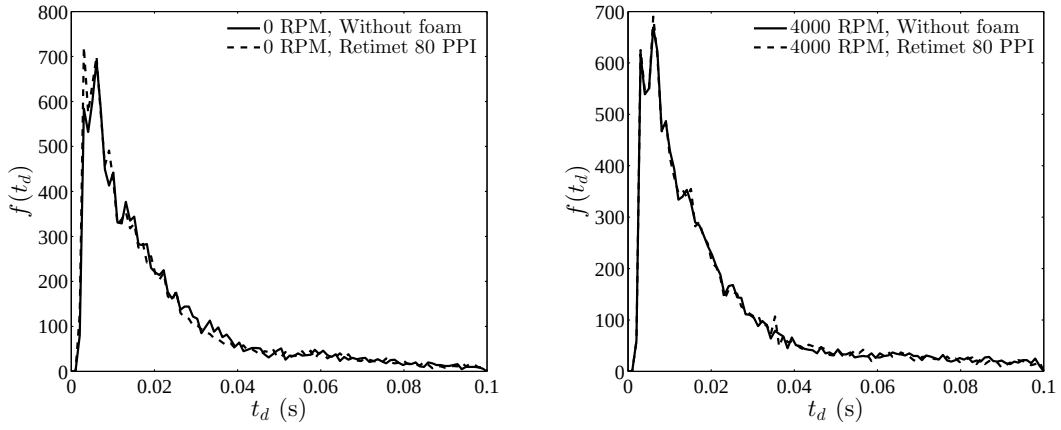

(a) (b)

Figure 5.24: Droplet wall impact time distributions for: (a) 0 RPM and (b) 4,000 RPM using the SG2 diameter distribution for a fixed air mass flow rate of 40 g/s.

being significantly reduced when the mass flow is increased. Apparently, the droplet diameter distribution (SG1 or SG2) does not really affect the mean droplet residence time at the foam entrance. Furthermore, the cases without foam showed almost no difference when compared with the cases with the Retimet 80 PPI, which is explained by the airflow prior to the foam entrance being very similar for both configurations.

Figure 5.24 depicts the wall impact time distributions, i.e. the time at which the droplets collided against a wall surface, at 0 and 4,000 RPM using the SG2 diameter distribution, under a fixed air mass flow rate of 40 g/s. Results show the droplet impact time distribution to be very similar regardless of the operational condition or the presence of the foam. Furthermore, it also shows the majority of wall impacts happened early after the droplets are injected. This shows agreement with the results depicted in Figure 5.22, where most of the droplet impact locations take place next to the inlet region. Figure 5.25 shows the mean impact time as a function of the breather rotational speed. The droplets tend to have a higher residence time within the separator when the SG1 diameter distribution (smaller droplets) is employed. The time taken to impact against a wall surface seems to increase, when the rotational speed is increased from 2,000 to

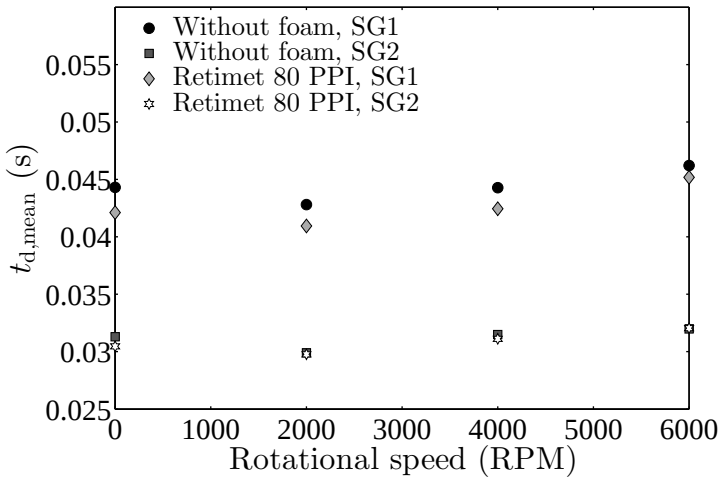

Figure 5.25: Mean wall impact time as a function of the breather rotational speed without a foam and with the Retimet 80 PPI, and both SG1 and SG2 droplet diameter distributions.

4,000 RPM. Results at 0 RPM show a slight increase of the droplet impact time when compared with the results at 2,000 RPM. Table 5.11 shows the mean, median and mode impact time for the cases investigated. The mean droplet impact time is approximately one fifth of the average time needed for the droplet to reach the metal foam entrance.

Table 5.11: Mean, median and mode wall impact time (averaged at all rotational speeds).

Case	no foam, SG1	no foam, SG2	Retimet 80 PPI, SG1	Retimet 80 PPI, SG2
$t_{\mathrm{d,mean}}$ (s)	0.044	0.031	0.042	0.030
$t_{\mathrm{d,median}}$ (s)	0.021	0.016	0.021	0.015
$t_{\mathrm{d,mode}}$ (s)	0.011	0.012	0.013	0.011

Sub-micron droplets are the most problematic in terms of capture effectiveness since they mainly follow the air path without hitting any surface. Thus, worst droplet capture results were obtained when the SG1 diameter distribution was used. Essentially, based on the simplified oil capture criterion employed here, results show that better droplet capture is achieved at higher rotational speeds and moderate air mass flow rates. The droplet residence time seem to increase with increasing the breather rotational speed. It is important to notice however that the pore-

scale oil capture function used here does not let oil to accumulate inside the metal foam, a limitation that seem to greatly affect the overall separation results.

5.4.2 Transient Lagrangian results

The transient Lagrangian simulations were carried out at just one operational condition, 4,000 RPM at 40 g/s of air flow, using the Retimet 80 PPI and SG2 droplet size distribution. The Lagrangian thin film model was employed and the simulations were carried out two-way coupled. The starting point of the simulation was the converged steady state solution obtained at the same operational condition. At the time of writing, 5.60 seconds of real flow time have been simulated. However, this amount of time was not enough in order for the two-phase flow to reach a steady state flow pattern.

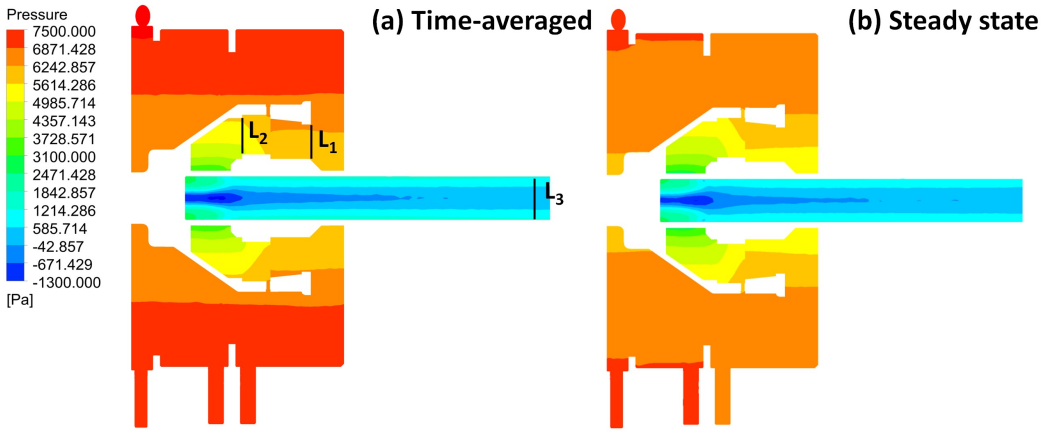

Figure 5.26: Comparison between the time-averaged two-way coupled and steady state solutions showing the pressure contour plot. Lines L_1, L_2 and L_3 depict the location where the velocity profiles where computed.

Nevertheless, the following analysis will take into account the time-averaged results obtained so far. Since the simulations were performed two-way coupled, the effect of the droplets on the gas phase has to be evaluated. Figure 5.26 shows a comparison between the pressure contour plots obtained for the time-averaged two-way coupled and steady state one-way coupled simulations. Time-averaged results show higher pressure values on the main chamber. The

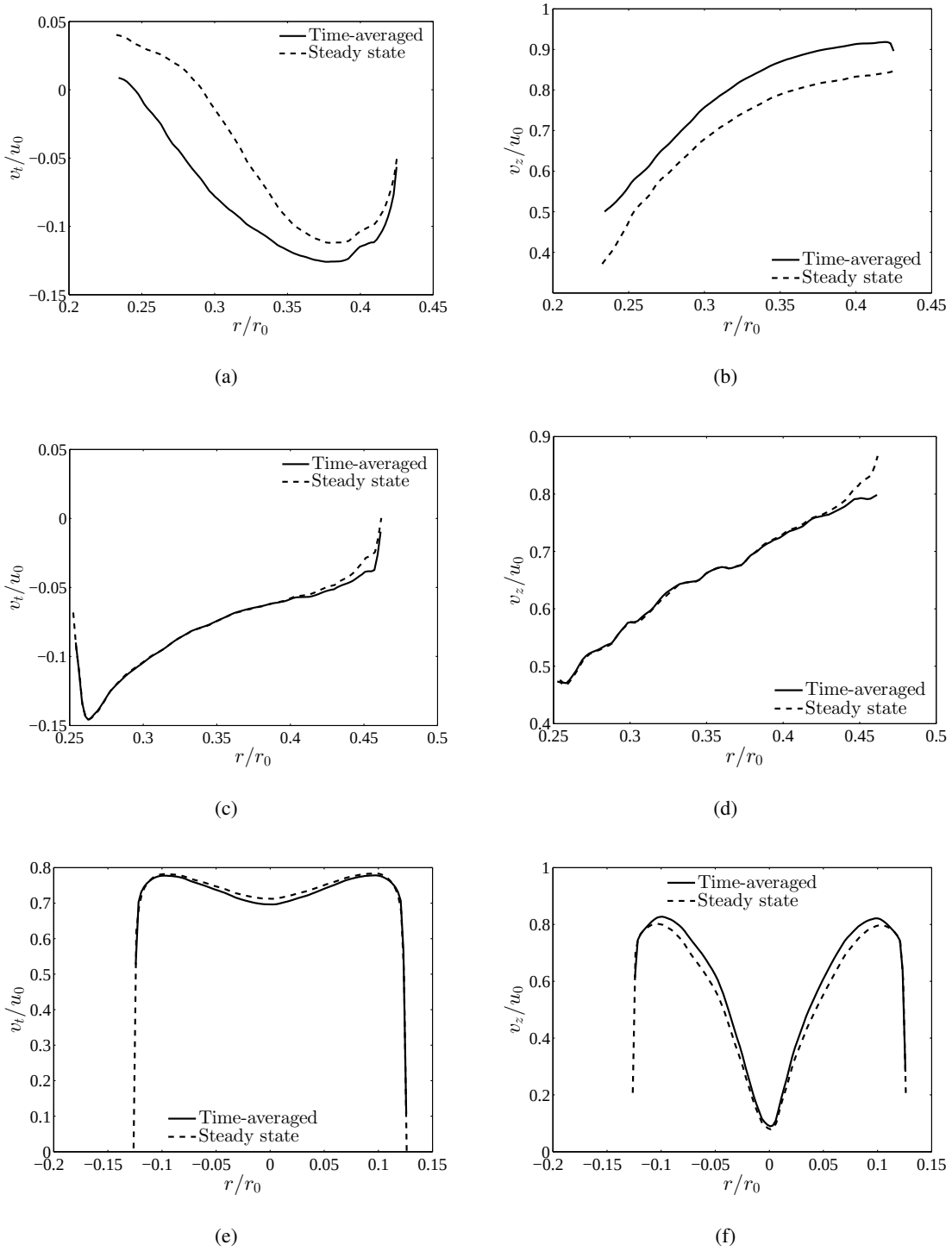

Figure 5.27: Comparison of the time-averaged and steady state tangential and axial velocity radial profiles at lines L_1, L_2 and L_3. Normalized (a,c,e) tangential and (b,d,f) axial velocity radial profiles on lines L_1, L_2 and L_3 respectively. Results are normalized by the chamber outer radius (r_0) and superficial inlet velocity (u_0).

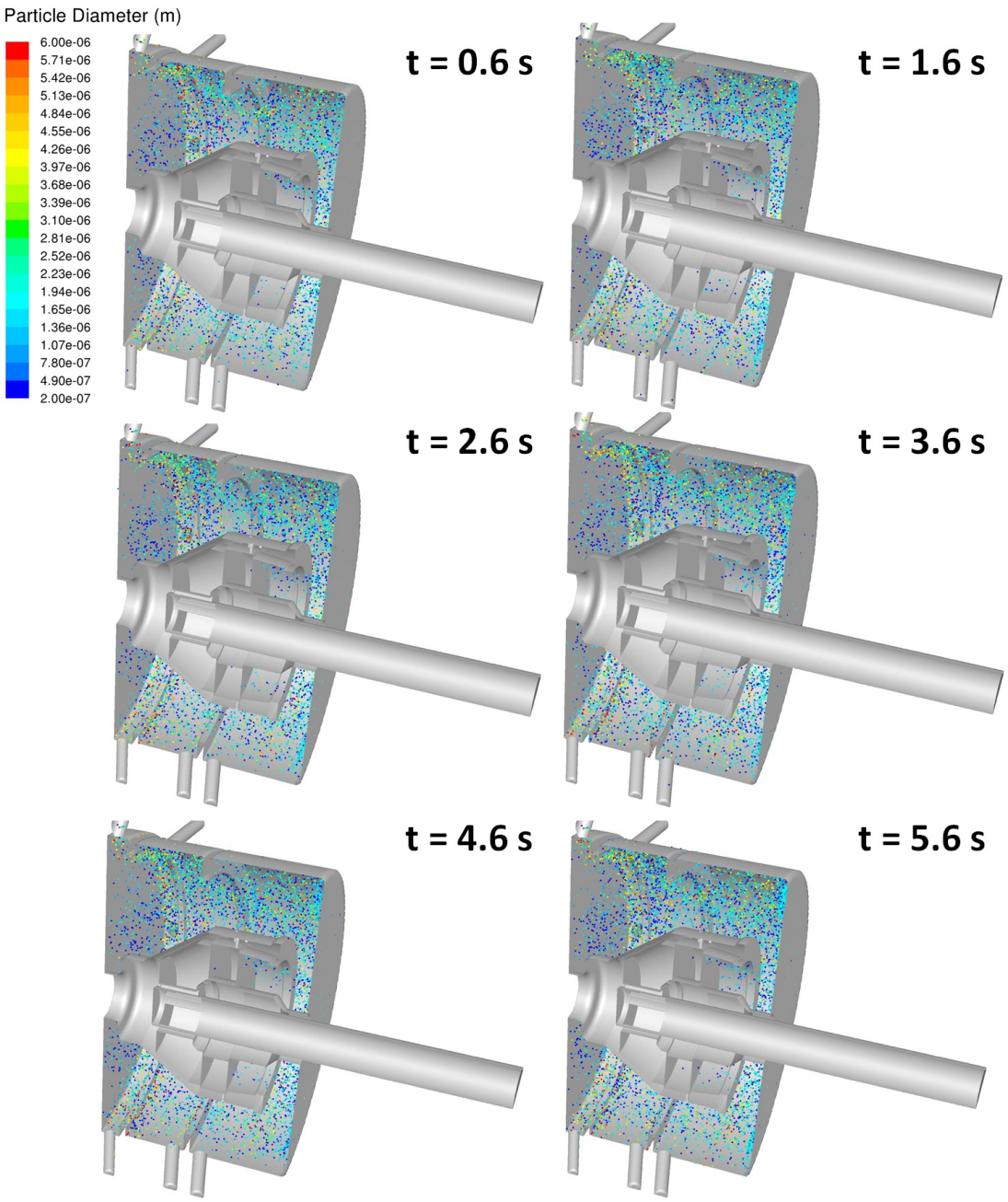

Figure 5.28: Snapshots of the instantaneous droplet positions showing the time evolution of the droplets within the separator. Lagrangian droplets at the wall (film) are neglected and only free-stream droplets are depicted. The total number of droplets was reduced by a factor of 3 for illustration purposes.

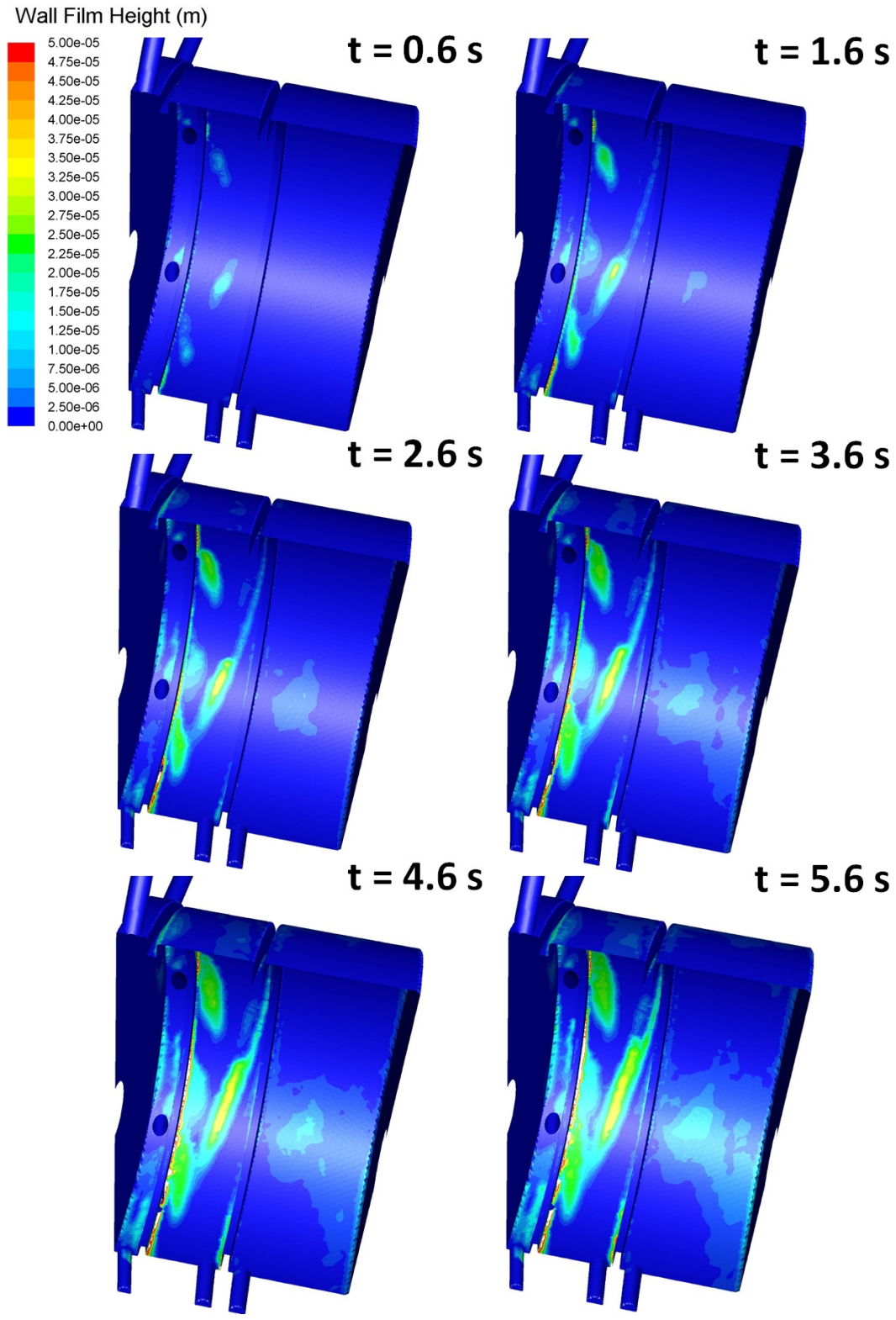

Figure 5.29: Snapshots of the Lagrangian wall film showing the time evolution of the film thickness within the separator.

tangential and axial velocity profiles were extracted at three locations depicted in Figure 5.26, namely the lines L_1, L_2 and L_3. A comparison of the normalized tangential and axial velocity radial profiles computed from the time-averaged and steady state solutions at lines L_1, L_2 and L_3 is depicted in Figure 5.27.

The time-averaged and steady state solutions show practically identical results for lines L_2 and L_3, which are located immediately downstream the metal foam and next to the outlet in the hollow shaft. On the other hand, the time-averaged solution showed smaller tangential velocity values upstream the metal foam, showing a certain damping effect on the rotational velocity components. Conversely, the axial velocity upstream the metal foam is accelerated by the presence of the droplets. One explanation for the almost identical results obtained downstream of the metal foam region is that not many droplets were able to pass through the foam region during the amount of flow time simulated ($t = 5.6$ seconds). Therefore, the flow downstream the foam remains mostly unaffected by the droplets.

Figure 5.28 depicts several snapshots of the instantaneous free-stream droplet positions within the separator. The great majority of the free-stream droplets has a diameter smaller than 2 μm, with the droplets next to the metal foam entrance being mostly sub-micron in size. The results clearly show that even after 5.6 seconds of flow time not many droplets are able to pass through the metal foam region. Hence, a longer simulation time is necessary in order for the flow to approach a steady state.

Figure 5.29 shows the snapshots of the Lagrangian wall film, illustrating the time evolution of the film thickness. The film formed at the outer chamber walls due to the droplet impacts is mostly quite thin, with a thickness of the order of tens of microns, and is concentrated mostly in the area between the two protruding plates. Analysis of the film velocity magnitude showed it to be very low (< 0.1 m/s) compared to the gas phase velocity.

Figure 5.30 depicts the evolution of the mass fraction of oil film within the separator. The film mass fraction is apparently converging around values above ~ 0.9. As a comparison, steady

state DPM results for the same operational condition showed a mass fraction of $\simeq 0.97$ for the droplets that impacted the separator walls. However, a longer simulated flow time is needed for a more definite answer. Figure 5.30 also shows the evolution of the average diameter of a film droplet normalized by the mean injection diameter. Results show that the droplets collected on the film are almost four times larger than the mean droplet diameter.

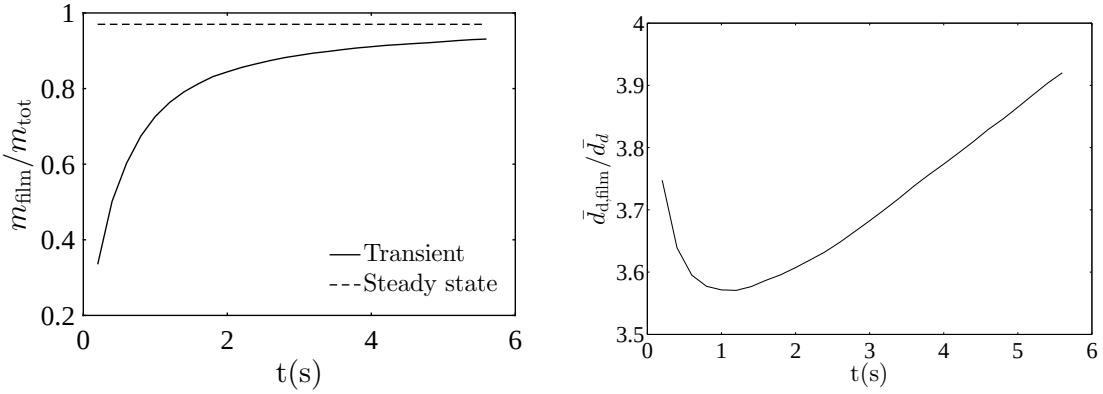

(a) (b)

Figure 5.30: (a) Evolution of the mass fraction of oil film within the separator, where m_{film} is the total oil film mass, m_{oil} is the total mass of oil and t is the flow time. Steady state value is plotted for comparison. (b) Evolution of the mean diameter of the Lagrangian film parcel normalized by the mean injection diameter.

It was not possible to identify which droplets, if any, were generated due to splashing and/or film detachment, since this information was not readily available in the CFD solution. Any comparison of oil capture effectiveness against experiments is meaningless at the present stage, since the flow has not achieved a steady state. As a feasibility study, the oil separation simulations presented here show that the complexity of the two-phase flow separation phenomena poses a significant challenge in the development of a modelling framework capable of capturing the oil separation phenomena accurately, even when using state-of-the-art modelling approaches. However, results presented here provide substantial information and show important improvements when compared with past similar studies.

5.5 Summary

One of the main objectives of this work was to apply the pore-scale results into a macroscopic porous media model to be used in a full aero-engine separator simulation, with the intent of better capturing the oil separation phenomena. Additionally, performing accurate CFD simulations of a full aero-engine separator is another objective in itself. This chapter described the development, application and improvement of the current modelling methodology employed for aero-engine air-oil separators.

Two-phase flow inside a typical separator design was simulated using an Eulerian-Lagrangian approach. The separator design and geometry investigated here are based on the experimental oil separation rig located at the KIT. Experimental pressure drop and oil separation effectiveness supplied by KIT are employed for validation of the numerical approach. The overall separator pressure drop was the parameter employed for validation of the single-phase simulations.

Airflow simulations were performed in steady state, with air assumed to behave as an ideal gas, and inlet conditions set at ambient pressure and temperature. Three breather configurations were analysed: without a foam and with the Retimet 45 and 80 PPI respectively. Two turbulence models were investigated, namely the RNG k-ε and the RSM. Comparison between experimental measurements and numerical pressure drop results showed the RSM to obtain a better agreement. Simulation results showed an average normalized RMS deviation ranging from 7.8 to 12 % (with the experimental data as the reference), depending on the breather configuration. The pressure drop was higher when no metal foam was employed, a fact that was also observed experimentally. Such increase was attributed to the damping effect that the metal foam caused to the flow pre-swirl, thus lowering the tangential velocity when compared to cases without foam. Transient simulations showed an improved convergence when compared to steady state solutions, and time-averaged pressure drop results presented better agreement with measurements. However, only a few selected cases were able to be run due to time constraints.

Lagrangian droplet tracking calculations are performed for the configuration without foam and for the Retimet 80 PPI, which employed the macroscopic oil capture approach described in Section 4.8. Lagrangian simulations were performed primarily in steady state and one-way coupled, and secondly, as transient two-way coupled. Steady state simulations assumed the trajectories to be terminated at a wall impact, and results showed that a very large number of droplets impact against the walls regardless of the operational condition. The oil capture in these cases (likelihood of wall collision) were shown to be weakly affected by the breather rotational speed and strongly affected by the inlet air mass flow rate. Results obtained for the configuration without foam showed a higher number of wall impacts when compared with the Retimet 80 PPI cases. However, the overall separation efficiency obtained with the Retimet 80 PPI cases was slightly better, due to the capture of droplets within the metal foam region (by the macroscopic porous medium model). The critical droplet diameter (at the metal foam entrance) was between 4 and 5 μm for the SG2 and 2 μm for the SG1. The oil capture function developed here provides a good agreement for primary droplet deposition on surfaces. However, at the moment it cannot take into account the effects of oil accumulation on the metal foam ligaments, which probably presents a major limitation and might greatly affect oil separation results. Comparison with experimental oil separation data showed a poor quantitative agreement, with simulation results showing much higher oil capture.

Transient simulations proved to be very time consuming but is a more realistic approach that extends the possible fates of a droplet impact. Results from the transient simulations show the majority of the oil droplets to impact against the outer chamber wall and form a film, presenting some qualitative agreement with steady-state Lagrangian solutions. At the time of writing, 5.6 seconds of flow time was simulated, which was not enough for the droplets to reach a steady state regime. Thus, a very small number of droplets are seen passing through the metal foam and exiting the separator, a fact that does not agree with experimental observations. Droplet-droplet collisions and droplet breakup were not considered here, but could be subject of future work.

The modelling framework currently described should not be seen as a definite answer but as an improvement upon the current state-of-the-art, and provides important lessons for future similar studies on aero-engine separators.

Chapter 6

Conclusions and recommendations

The research described in this thesis was targeted towards the ultimate goal of improving the current modelling framework for simulating aero-engine separators. The present investigation was divided in two distinct parts. The first was focused on bridging one of the biggest gaps in the current framework, which is the modelling of two-phase flow across open-cell metal foams within aero-engine separators. The second part was aimed at the application of the knowledge gained from the two-phase flow investigations across open-cell metal foams, into a simulation of a full aero-engine separator. The relevant conclusions of both parts are summarized in the following sections, along with possibilities and recommendations for future work.

6.1 Pore-scale modelling approach

A tomography-based pore-scale modelling approach was employed in order to obtain accurate representations of the flow across open-cell metal foams. Tomography scans and pressure drop measurements data were supplied by a separate research group within the university, with details of the experiments described in (Oun and Kennedy, 2014). A total of seven distinct commercial open-cell metal foam samples were analysed here.

6.1.1 Morphological characterization

An in-house Matlab code was developed to perform the volume renderings and a series of morphological characterization routines directly on the tomographic datasets. Measurements have shown the foam samples to be highly porous, with a porosity ranging from 0.82 to 0.89. Results

were compared against experimental MIP porosimetry measurements, showing good agreement. Pore and strut size distributions were computed on all the tomographic datasets, and the mean pore and strut size were determined. The mean pore diameter varied from approximately 0.4 to 2.25 mm, whereas the mean strut size varied from roughly 0.1 to 0.3 mm. Computations of the specific surface area per unit volume showed it to be inversely proportional to the pore size. The minimum REV size was computed, and results showed convergence of porosity values when a cubic volume with an edge length above $\sim 2d_p$ was employed.

Additionally, a combination of Euclidean and watershed transforms was used to segment the pore space of the foams into distinct cells. Each cell is basically a polyhedron, and analysis of the mean cell width in each Cartesian direction can indicate whether the foam is anisotropic or not. Measurements revealed a certain degree of anisotropy in all samples, with the cells being slightly elongated in one or more spatial directions.

At the time of writing of this thesis, the literature database of tomography-based morphological measurements applied to open-cell metal foams was quite scarce, and the present work contributes to the area by further expanding this database. Although the morphological characterization routines were focused solely on open-cell metal foams, the methods presented here are generally applicable to all types of cellular solids.

6.1.2 Pore-scale airflow simulations

The aim of the present work was to use standard CFD techniques to simulate the two-phase flow within open-cell metal foams. Thus, the modelling methodology was developed with the intent of working with commercial finite volume solvers. The foam geometry was directly generated from the tomography datasets using the in-house volume rendering routine, and exported to a mesh generation software.

The computational domains were designed in such a way to be representative of the conditions present at the experimental measurements, which were used for validation of the numerical

approach. A rectangular domain with free-slip enclosing walls was chosen for validation against experiments. The streamwise length of the computational samples was kept as similar as possible to the experimental ones. Simulations were run in steady state, considering incompressible air as a fluid, and solved using the commercial solver Ansys Fluent 15. Simulations were run at the HPC facility in the university, using 24 to 32 processor cores in parallel, depending on the availability. Converged steady state solutions had an average run time of 0.5 to 2 hours.

The validation parameter was the foam pressure gradient, defined as the pressure drop normalized by the sample streamwise length. The incompressible steady state airflow solutions achieved an overall good agreement to the experimental measurements. It is assumed that the pressure gradient is a quadratic function of the Darcian velocity. The permeability and Forchheimer coefficient were computed performing a least squares curve fitting on the pressure gradient curves. The square of correlation coefficient (R^2) was above 0.99 for all cases. Some large discrepancies were observed between experimental and simulated permeability values. It is important to note that the permeability term accounts for viscous losses, which are predominant in low velocity flow regimes, e.g. creeping flow. However, since the flow regimes analysed here are well above the Darcy regime (low velocity), inertial effects are likely to be dominant. Consequently, the Forchheimer coefficient, which accounts for these inertial effects will be the dominant parameter. This assumption was confirmed by performing the pressure gradient curve fittings assuming the permeability to be equal to zero. Thus, results show that the quadratic term by itself seems to be sufficient to describe the pressure gradient of the foam samples under the flow conditions analysed here.

An additional set of simulations was performed with the intent of isolating and analysing particular effects which may affect the pressure gradient in open-cell metal foams. Simulations with samples of varying streamwise length showed that there is a critical length for which the pressure gradient is no longer affected if the length is increased. Transient flow simulations showed the presence of unsteady periodic flow features, however, time-averaged pressure gra-

dient results were almost identical to the steady state solutions.

Simulations assuming the air to be an ideal gas were performed to investigate possible fluid compressibility effects. Results have shown that fluid compressibility becomes significant when Mach number values above 0.3 are reached within the pore space. Another set of simulations was carried out on cubical samples, varying the flow direction in all three Cartesian directions. Since a certain level of anisotropy was found in the foam samples, it was necessary to test if the pressure gradient could be affected by the spatial alignment of the flow. Simulation results showed the pressure gradient to be significantly affected by the variation of the flow spatial alignment, with deviations up to 20 % on the pressure gradient. Finally, simulations involving a sample with artificially varying porosity were performed. Pressure gradient results were also strongly affected by a variation in the porosity values.

The pore-scale modelling approach developed and applied here was able to obtain a good representation of the airflow within several commercial open-cell metal foams. The results obtained for a comprehensive number of metal foam samples and analysis of additional effects presented here provide a substantial contribution to the area. Furthermore, most studies published in the literature deal with low velocity fluid regimes. Here, the investigated conditions have ventured deep into the fully turbulent regime, which is an important contribution as well. It is worth mentioning that this pore-scale approach could be expanded in order to take into account heat and mass transfer. In summary, the numerical modelling framework described here can be used to compute the transport properties of single phase flow in open-cell metal foams within a reasonable level of accuracy.

6.1.3 Pore-scale Lagrangian simulations

An Eulerian-Lagrangian approach was employed to model the disperse flow of oil droplets within open-cell metal foams. Therefore, the characterization of the two-phase flow is basically a two-stage process. Firstly, for any given foam sample, a converged steady state solution

(or solutions, for different flow velocities) for the airflow must be obtained. Secondly, a Lagrangian particle tracking approach is employed to compute a representative number of droplet trajectories within the converged airflow solution.

In order to qualitatively evaluate the oil separation effectiveness of the foam samples, a simplified oil capture criterion was assumed. Droplet trajectories were terminated upon impact against the foam solid ligaments, with no rebound allowed. This droplet capture criterion makes the droplet's inertia the determinant factor influencing oil capture, since higher inertia implies a greater degree of deviation from its initial trajectory. The current approach enables the qualitative characterization of the primary droplet deposition behaviour across all the foam samples. Droplets with a diameter from 0.1 to 10 μm were considered. Lagrangian simulations results showed that better oil capture is achieved at higher flow velocities (higher droplet inertia). However, sub-micron droplets are hardly affected by the presence of the foam, and tend to follow the air path. Oil capture curves were obtained for each foam sample, relating the fraction of free (non-captured) droplets with their streamwise position inside the foam. Therefore, an oil capture curve is computed for each flow velocity, each droplet diameter and each foam sample. However, the current modelling approach for the oil phase is neglecting complex droplet dynamics phenomena, e.g. splashing, stripping, film formation or re-atomization.

Lastly, the foam rotation experienced under conditions present within aero-engine separators was accounted for using a MRF approach. Airflow pressure gradient in the streamwise direction seems to be weakly affected by the rotation of the foam. On the other hand, Lagrangian calculations showed an overall increase in the oil capture when compared to static sample results. This fact was attributed to an increase of the droplet's inertia and overall path length caused by the rotation of the foam, consequently increasing the likelihood of droplet collision.

6.1.4 Macroscopic transferring of pore-scale results

A method to transfer the pore-scale results into a macroscopic porous medium model was presented. The pressure gradient induced by the foam can be correctly represented as a momentum sink in the *clear* flow governing equations. Thus, instead of explicitly defining the porous medium geometry, a porous region is defined instead, which assumes the pressure gradient to be a quadratic function of the superficial flow velocity. Therefore, this approach only requires the values of linear and quadratic coefficients for the pressure gradient function, which are directly related to the permeability and Forchheimer coefficient, that have been computed from the experiments and simulations.

Transferring of the droplet capture results made use of an approach analogous to the modelling of radiative decay. For that purpose, the oil capture curves obtained from the Lagrangian simulations were used to derive a function that computed the probability of a droplet being captured after having travelled a certain distance within the foam sample. This is implemented in Ansys Fluent 15 by means of an UDF.

Validation results using the macroscopic porous medium model showed very good agreement with the pore-scale simulations. The mesh count for the enhanced macroscopic model case is approximately 500 times lower than the actual pore-scale computational domain. The information gained from the pore-scale simulations can be employed to derive a macroscopic porous medium model capable of reproducing the essentially the same results, utilizing a fraction of the computational power necessary for a pore-scale calculation.

6.2 Aero-engine separator simulations

The improvement of the current modelling framework applied to aero-engine separators was another main objective of this work. The enhanced macroscopic porous medium model was applied in a full separator CFD simulation. The geometry and design of the aero-engine separator

investigated here were based on the experimental oil separation test rig at the KIT. Pressure drop and oil separation measurements were used for validation of the CFD approach.

A representative range of operational conditions was investigated along with different breather configurations such as without foam, and with two Retimet foams of different grades. Airflow simulation results were able to predict the overall pressure drop within a reasonable degree of accuracy, showing deviations of 7.8 to 12 % (with the experimental data as the reference), depending on the breather configuration. Further analysis of the airflow characteristics showed that the pressure distribution within the separator is dominated by the centrifugal effects. Higher pressure drop results were recorded for the cases without a foam, which can be explained by the damping effect that the foam has on the flow swirl.

The oil phase was modelled using a Lagrangian approach similar to the pore-scale simulations, which was further subdivided in two categories: steady state one-way coupled and transient two-way coupled. The one-way coupled Lagrangian calculations assumed the droplet trajectories to terminate once they collided against a wall. Hence, the oil capture effectiveness was defined based on the number of collided droplets relative to the total number of droplets injected. Results have shown a very high oil capture regardless of the operational condition. The great majority of droplets ($> 95\%$) end up colliding against the static chamber outer walls, and a very small number is seem following the air path towards the breather and foam region. These results do not agree with experimental observations, which showed generally a much higher amount of escaped oil. However, the one-way coupled simulations did not take into account the possibility of droplet re-atomization or film formation. In reality, it is likely that the oil forms a film onto the chamber walls, which can separate and detach at sharp edges, and splash upon droplet impact. Moreover, the current enhanced oil capture model employed for the foams do not take into account the possibility of oil accumulation within the foam.

Transient two-way coupled Lagrangian simulations were also performed including the modelling of oil film formation on the walls. Only one operational condition was investigated and

the simulations required long run times. At the time of writing of this thesis, a steady state flow still had not been reached for the two-phase flow. However, the monitoring of the oil film mass fraction shows an apparent convergence around values above ~ 0.9, which has some qualitative agreement with the steady state simulations. However, meaningful oil separation results comparisons against experimental data can only be made when the flow reaches a steady state.

Nevertheless, the two-phase flow results obtained with both steady state and transient Lagrangian approaches provided substantial information regarding the overall state of the droplets within the separator under various operational conditions. Results obtained so far seem to indicate that the current modelling methodology still requires further improvement in order to obtain accurate oil separation results. As has been stated previously, it seems that droplet reatomization might play an important role in the two-phase flow phenomena within aero-engine separators. Furthermore, droplet breakup may also be important and could be considered in future studies.

Even though the modelling methodology employed here was not able to obtain a quantitative agreement of the oil separation, the information extracted from the simulations performed in this work make a significant contribution to the area. This study is one of the very few which have presented validation of the airflow against experiments. Additionally, the Lagrangian simulations have comprised a large number of distinct operational conditions and breather configurations. Finally, this study was the first to compute droplet trajectories past the metal foam entrance, and should be seen as a first step on modelling of the gas-liquid flow through open-cell metal foams.

6.3 Recommendations

A number of different routes could be taken to improve the research described here. One obvious necessary step is the development of an experimental apparatus able to isolate and quantify the oil capture on open-cell metal foams. For that purpose, a relatively simple experiment

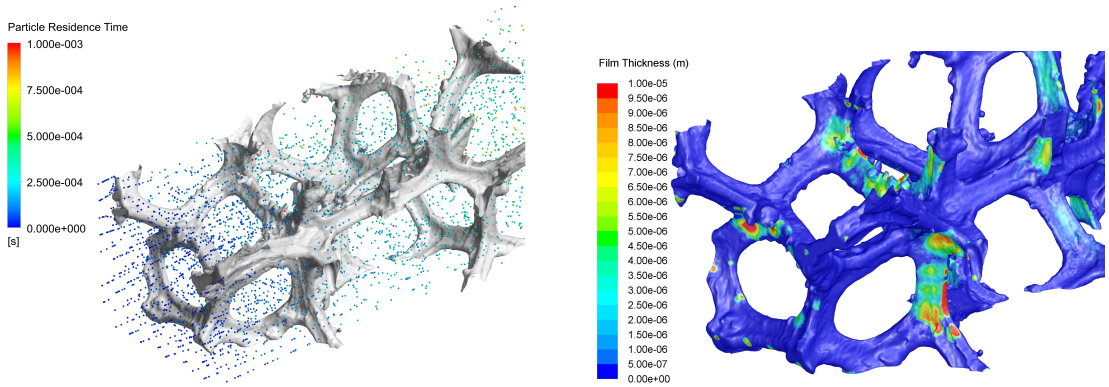

(a) (b)

Figure 6.1: (a) Snapshot of instantaneous droplet positions across the Retimet 20 PPI foam. (b) Contour of the film thickness on the surface of the foam ligaments.

could be designed in such a way to firstly, perform pressure gradient measurements across the foam samples. Secondly, a suitable liquid droplet generator should be devised in order to inject droplets with a pre-defined diameter distribution into the airflow. Additionally, it would be very helpful to measure the droplet diameter distribution and oil volume downstream of the foam sample.

6.3.1 Pore-scale thin film modelling

The pore-scale modelling approach can be further expanded to incorporate the formation of oil film on the surface of the foam solid ligaments. A thin film model could be employed, such as the one described in Section 5.2.4. Thus, different outcomes could be assumed upon droplet impact, such as collection and film formation, splashing or rebound. An example of such type of simulation is illustrated in Figure 6.1. In that case, a transient Lagrangian tracking approach was employed in conjunction with a thin film model. The foam sample is the Retimet 20 PPI, and the starting point for the simulation is a converged steady state airflow solution. The results clearly show the formation of thin film (< 10 μm) patches on the surface of the foam.

Obviously, this type of simulation can become very time consuming because of the transient treatment and the necessity of achieving a stable steady state. On the other hand, the use of a

thin film approach seems suitable, since it is expected for the liquid film to be quite thin compared to the pore-size. It is also much less computationally intensive than an interface-resolving approach such as VOF for example, since it computes essentially a depth-averaged version of the governing equations. Nevertheless, one of the greatest challenges related to developing such approach is the difficulty in gathering relevant validation data, since this would require a detailed knowledge of the liquid film behaviour on the surface of a given metal foam sample.

6.3.2 Modelling of open-cell foam structures

One of the most time consuming parts of the current work was to obtain the tomographic scans of the foam samples and perform the subsequent volume rendering procedure. One possible way of overcoming such difficulty is to construct the geometry using an open-cell foam model, such as the one proposed in the work of Lautensack et al. (2008). Their method makes use of random Laguerre tessellations (weighted versions of the well-known Voronoi tessellations), to model the structure of open-cell foams.

The foam geometry generation process is illustrated in Figure 6.2, and is being currently developed by the author. It starts with the generation of a dense packing of spheres, which must have a diameter (or diameter distribution) equivalent to the intended pore diameter (or distribution) of the modelled foam structure. The dense packing of spheres can be accomplished by making use the open-source software Large-scale Atomic/Molecular Massively Parallel Simulator (LAMMPS) (Plimpton, 1995), developed by the Sandia National Laboratories. The packing is generated by employing the discrete element method (DEM) to pour spheres inside a container, simulating the action of gravity and contact forces, letting them settle into a stable configuration, which is shown at the leftmost part of Figure 6.2.

The next step consists in computing the Laguerre tessellation on the generated packing of spheres. This can be carried out by using another open source software, namely the Voro++ (Rycroft, 2009), which is essentially a library of various tessellation functions that can be di-

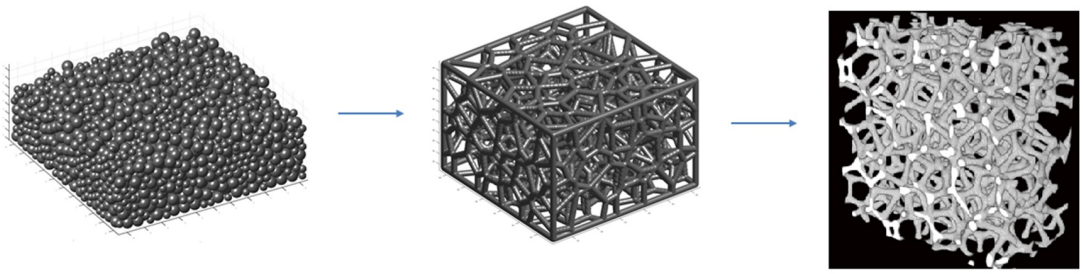

Figure 6.2: Schematic of the foam geometry generations process. Generation of dense packing of spheres (left); computation of the Laguerre tessellation on the packing of spheres (centre) and application of an adaptive dilation algorithm to the tessellation edge system (right).

rectly applied to the DEM output file generated by LAMMPS. Voro++ generates a file which contains all the coordinates of the Laguerre tessellation edge system.

The tessellation edge coordinates must then be converted to a binary 3-D image for further processing, see centre of Figure 6.2. Finally, an adaptive image dilation algorithm is applied to the edge system in the binary image, to generate the foam strut system (right of Figure 6.2). The dilation algorithm can be fully customizable so that the generated struts can have a realistic shape representative of real foam structures. Validation of this foam geometry generation methodology can be done by performing morphological measurements on the generated foam and comparing against the measurements performed on tomographic datasets of real foam samples. A successful development of such approach could save a significant amount of time in the geometry generation process of pore-scale computational domains. Additionally, the computer-generated samples could have arbitrary pore and strut sizes, which could enable a parametric study analysing the influence of several morphological parameters on the foam transport properties.

References

Akolkar, A. and Petrasch, J. (2012). Tomography-based characterization and optimization of fluid flow through porous media. *Transport in porous media*, 95(3):535–550.

Al-Kharusi, A. S. and Blunt, M. J. (2007). Network extraction from sandstone and carbonate pore space images. *Journal of Petroleum Science and Engineering*, 56(4):219–231.

Al-Raoush, R. and Willson, C. (2005). Extraction of physically realistic pore network properties from three-dimensional synchrotron x-ray microtomography images of unconsolidated porous media systems. *Journal of Hydrology*, 300(1):44–64.

Alazmi, B. and Vafai, K. (2000). Analysis of variants within the porous media transport models. *Journal of Heat Transfer*, 122(2):303–326.

Amiri, A. and Vafai, K. (1994). Analysis of dispersion effects and non-thermal equilibrium, non-darcian, variable porosity incompressible flow through porous media. *International Journal of Heat and Mass Transfer*, 37(6):939–954.

ANSYS (2013). *Fluent 15 Theory Guide, 2013*.

Antohe, B. and Lage, J. (1997). A general two-equation macroscopic turbulence model for incompressible flow in porous media. *International Journal of Heat and Mass Transfer*, 40(13):3013–3024.

Bakke, S., Øren, P.-E., et al. (1997). 3-d pore-scale modelling of sandstones and flow simulations in the pore networks. *Spe Journal*, 2(02):136–149.

Banhart, J. (2001). Manufacture, characterisation and application of cellular metals and metal foams. *Progress in materials Science*, 46(6):559–632.

Baril, E., Mostafid, A., Lefebvre, L.-P., and Medraj, M. (2008). Experimental demonstration of entrance/exit effects on the permeability measurements of porous materials. *Advanced Engineering Materials*, 10(9):889–894.

Bear, J. (2013). *Dynamics of fluids in porous media*. Courier Corporation.

Bear, J. and Corapcioglu, M. Y. (2012). *Fundamentals of transport phenomena in porous media*, volume 82. Springer Science & Business Media.

Bhattacharya, A., Calmidi, V., and Mahajan, R. (2002). Thermophysical properties of high porosity metal foams. *International Journal of Heat and Mass Transfer*, 45(5):1017–1031.

Blunt, M. J. (2001). Flow in porous mediapore-network models and multiphase flow. *Current opinion in colloid & interface science*, 6(3):197–207.

Blunt, M. J., Bijeljic, B., Dong, H., Gharbi, O., Iglauer, S., Mostaghimi, P., Paluszny, A., and Pentland, C. (2013). Pore-scale imaging and modelling. *Advances in Water Resources*, 51:197–216.

Blunt, M. J., Jackson, M. D., Piri, M., and Valvatne, P. H. (2002). Detailed physics, predictive capabilities and macroscopic consequences for pore-network models of multiphase flow. *Advances in Water Resources*, 25(8):1069–1089.

Bodla, K. K., Murthy, J. Y., and Garimella, S. V. (2010). Microtomography-based simulation of transport through open-cell metal foams. *Numerical Heat Transfer, Part A: Applications*, 58(7):527–544.

Boek, E. S. and Venturoli, M. (2010). Lattice-boltzmann studies of fluid flow in porous media with realistic rock geometries. *Computers & Mathematics with Applications*, 59(7):2305–2314.

Boomsma, K., Poulikakos, D., and Ventikos, Y. (2003). Simulations of flow through open cell metal foams using an idealized periodic cell structure. *International Journal of Fluid and Heat Flow*, 24:825–834.

Brinkman, H. (1949). A calculation of the viscous force exerted by a flowing fluid on a dense swarm of particles. *Applied Scientific Research*, 1(1):27–34.

Brunauer, S., Emmett, P. H., and Teller, E. (1938). Adsorption of gases in multimolecular layers. *Journal of the American Chemical Society*, 60(2):309–319.

Cheah, K., Lee, T., Winoto, S., and Zhao, Z. (2007). Numerical flow simulation in a centrifugal pump at design and off-design conditions. *International Journal of Rotating Machinery*, 2007.

Chew, J. W. (1996). Analysis of the oil film on the inside surface of an aero-engine bearing chamber housing. In *ASME 1996 International Gas Turbine and Aeroengine Congress and Exhibition*, pages V001T01A082–V001T01A082. American Society of Mechanical Engineers.

Darcy, H. (1856). *Les fontaines publiques de la ville de Dijon: exposition et application...* Victor Dalmont.

De Lemos, M. J. (2012). *Turbulence in porous media: modeling and applications*. Elsevier.

Dems, P., Eastwick, C., and Morvan, H. P. (2009). Cfd study of the two-phase oil/air flow in a breather system. Technical report, Nottingham Rolls-Royce University Technology Centre in Gas Turbine.

do Carmo, M. P. (1976). *Differential geometry of curves and surfaces*, volume 2. Prentice-Hall Englewood Cliffs.

Du Plessis, J. P. and Diedericks, G. P. (1997). Pore-scale modelling of interstitial transport phenomena. *INTERNATIONAL SERIES ON ADVANCES IN FLUID MECHANICS*, 13:61–104.

Du Plessis, P., Montillet, A., Comiti, J., and Legrand, J. (1994). Pressure drop prediction for flow through high porosity metallic foams. *Chemical Engineering Science*, 49(21):3545–3553.

Dukhan, N. and Ali, M. (2012a). Effect of confining wall on properties of gas flow through metal foam: an experimental study. *Transport in porous media*, 91(1):225–237.

Dukhan, N. and Ali, M. (2012b). Strong wall and transverse size effects on pressure drop of flow through open-cell metal foam. *International Journal of Thermal Sciences*, 57:85–91.

Dukhan, N., Bağcı, Ö., and Özdemir, M. (2014). Metal foam hydrodynamics: Flow regimes from pre-darcy to turbulent. *International Journal of Heat and Mass Transfer*, 77:114–123.

Dukhan, N. and Patel, K. P. (2010). Entrance and exit effects for fluid flow in metal foam. In *Porous media and its applications in science, engineering and industry: 3rd International Conference*, volume 1254, pages 299–304. AIP Publishing.

Dupuit, A. J. E. J. (1863). *Études théoriques et pratiques sur la mouvement des eaux dans les canaux découverts et à travers les terrains perméables: avec des considérations relatives au régime des*

grandes eaux, au débouché à leur donner, et à la marche des alluvions dans les rivières à fond mobile. Dunod.

Eastwick, C., Simmons, K., Wang, Y., and Hibberd, S. (2006). Study of aero-engine oil-air separators. *Proceedings of the Institution of Mechanical Engineers, Part A: Journal of Power and Energy*, 220(7):707–717.

Eaton, J. K. (2009). Two-way coupled turbulence simulations of gas-particle flows using point-particle tracking. *International Journal of Multiphase Flow*, 35(9):792–800.

Edouard, D., Lacroix, M., Huu, C. P., and Luck, F. (2008). Pressure drop modeling on solid foam: State-of-the art correlation. *Chemical Engineering Journal*, 144(2):299–311.

Elghobashi, S. (1994). On predicting particle-laden turbulent flows. *Applied Scientific Research*, 52(4):309–329.

Ergun, S. (1952). Fluid flow through packed columns. *Chemical engineering progress*, 48.

Ettrich, J. (2014). *Fluid flow and heat transfer in cellular solids*, volume 39. KIT Scientific Publishing.

Farrall, M., Hibberd, S., and Simmons, K. (2001). Computational modelling of two-phase air/oil flow within an aero-engine bearing chamber. *ROLLS ROYCE PLC-REPORT-PNR*.

Fatt, I. et al. (1956). The network model of porous media. *Petroleum Transactions*, 207.

Forchheimer, P. (1901). Wasserbewegung durch boden. *Z. Ver. Deutsch. Ing*, 45(1782):1788.

Glahn, A., Kurreck, M., Willmann, M., and Wittig, S. (1995). Feasibility study on oil droplet flow investigations inside aero engine bearing chambers: Pdpa techniques in combination with numerical approaches. In *ASME 1995 International Gas Turbine and Aeroengine Congress and Exposition*, pages V001T01A024–V001T01A024. American Society of Mechanical Engineers.

Glahn, A. and Wittig, S. (1996). Two-phase air/oil flow in aero engine bearing chambers: characterization of oil film flows. *Journal of engineering for gas turbines and power*, 118(3):578–583.

Glahn, A. and Wittig, S. (1999). Two-phase air/oil flow in aero-engine bearing chambers–assessment of an analytical prediction method for the internal wall heat transfer. *International Journal of Rotating Machinery*, 5(3):155–165.

Gostick, J. T. (2013). Random pore network modeling of fibrous pemfc gas diffusion media using voronoi and delaunay tessellations. *Journal of The Electrochemical Society*, 160(8):F731–F743.

Gronald, G. and Derksen, J. (2011). Simulating turbulent swirling flow in a gas cyclone: a comparison of various modeling approaches. *Powder technology*, 205(1):160–171.

Habisreuther, P., Djordjevic, N., and Zarzalis, N. (2009). Statistical distribution of residence time and tortuosity of flow through open-cell foams. *Chemical Engineering Science*, 64(23):4943–4954.

Hargather, M. J. and Thole, K. A. (2013). Characterization of flow through porous metals. In *ASME Turbo Expo 2013: Turbine Technical Conference and Exposition*, pages V03CT14A016–V03CT14A016. American Society of Mechanical Engineers.

Harting, J., Chin, J., Venturoli, M., and Coveney, P. V. (2005). Large-scale lattice boltzmann simulations of complex fluids: advances through the advent of computational grids. *Philosophical Transactions of the Royal Society of London A: Mathematical, Physical and Engineering Sciences*, 363(1833):1895–1915.

Haugen, N. E. L. and Kragset, S. (2010). Particle impaction on a cylinder in a crossflow as function of stokes and reynolds numbers. *Journal of Fluid Mechanics*, 661:239–261.

Haussener, S., Coray, P., LipiĹ, W., Wyss, P., Steinfeld, A., et al. (2010). Tomography-based heat and mass transfer characterization of reticulate porous ceramics for high-temperature processing. *Journal of Heat Transfer*, 132(2):023305.

Hirt, C. W. and Nichols, B. D. (1981). Volume of fluid (vof) method for the dynamics of free boundaries. *Journal of computational physics*, 39(1):201–225.

Hoogerbrugge, P. and Koelman, J. (1992). Simulating microscopic hydrodynamic phenomena with dissipative particle dynamics. *EPL (Europhysics Letters)*, 19(3):155.

Hossain, M., Hibberd, S., and Simmons, K. (2000). Cfd study of the two-phase oil/air flow in a breather system. Technical report, Nottingham Brite Euram II INTRANS.

Hutter, C., Zenklusen, A., Kuhn, S., and Rudolf von Rohr, P. (2011). Large eddy simulation of flow through a streamwise-periodic structure. *Chemical Engineering Science*, 66(3):519–529.

Iaccarino, G., Ooi, A., Durbin, P., and Behnia, M. (2003). Reynolds averaged simulation of unsteady separated flow. *International Journal of Heat and Fluid Flow*, 24(2):147–156.

Kader, B. (1981). Temperature and concentration profiles in fully turbulent boundary layers. *International Journal of Heat and Mass Transfer*, 24(9):1541–1544.

Klingsporn, M. (2004). Advanced transmission and oil system concepts for modern aero-engines. In *ASME Turbo Expo 2004: Power for Land, Sea, and Air*, pages 391–398. American Society of Mechanical Engineers.

Knudsen, M. (1950). *The kinetic theory of gases: some modern aspects*. Metheun & Company.

Konstandopoulos, A. G., Labowsky, M. J., and Rosner, D. E. (1993). Inertial deposition of particles from potential flows past cylinder arrays. *Journal of aerosol science*, 24(4):471–483.

Kopanidis, A., Theodorakakos, A., Gavaises, E., and Bouris, D. (2010). 3d numerical simulation of flow and conjugate heat transfer through a pore scale model of high porosity open cell metal foam. *International Journal of Heat and Mass Transfer*, 53(11):2539–2550.

Koplik, J., Banavar, J. R., and Willemsen, J. F. (1988). Molecular dynamics of poiseuille flow and moving contact lines. *Physical review letters*, 60(13):1282.

Kraynik, A. and Reinelt, D. (1999). Foam microrheology: from honeycombs to random foams. In *15th Annual Meeting Polymer Processing Sosiety*.

Krishnan, S., Murthy, J. Y., and Garimella, S. V. (2006). Direct simulation of transport in open-cell metal foam. *Journal of heat transfer*, 128(8):793–799.

Kulick, J. D., Fessler, J. R., and Eaton, J. K. (1994). Particle response and turbulence modification in fully developed channel flow. *Journal of Fluid Mechanics*, 277:109–134.

Lacroix, M., Nguyen, P., Schweich, D., Huu, C. P., Savin-Poncet, S., and Edouard, D. (2007). Pressure drop measurements and modeling on sic foams. *Chemical engineering science*, 62(12):3259–3267.

Launder, B. E. and Spalding, D. (1974). The numerical computation of turbulent flows. *Computer methods in applied mechanics and engineering*, 3(2):269–289.

Lautensack, C., Giertzsch, M., Godehardt, M., and Schladitz, K. (2008). Modelling a ceramic foam using locally adaptable morphology. *Journal of microscopy*, 230(3):396–404.

Lee, J., Sung, N., Cho, G., and Oh, K. (2010). Performance of radial-type metal foam diesel particulate filters. *International Journal of Automotive Technology*, 11(3):307–316.

Liu, J., Wu, W., Chiu, W., and Hsieh, W. (2006). Measurement and correlation of friction characteristic of flow through foam matrixes. *Experimental thermal and fluid science*, 30(4):329–336.

Liu, M. and Liu, G. (2010). Smoothed particle hydrodynamics (sph): an overview and recent developments. *Archives of computational methods in engineering*, 17(1):25–76.

Liu, Z. and Hill, D. L. (2000). Issues surrounding multiple frames of reference models for turbo compressor applications.

Lorensen, W. E. and Cline, H. E. (1987). Marching cubes: A high resolution 3d surface construction algorithm. In *ACM siggraph computer graphics*, volume 21, pages 163–169. ACM.

Magnico, P. (2009). Analysis of permeability and effective viscosity by cfd on isotropic and anisotropic metallic foams. *Chemical Engineering Science*, 64(16):3564–3575.

Maire, E., Colombo, P., Adrien, J., Babout, L., and Biasetto, L. (2007). Characterization of the morphology of cellular ceramics by 3d image processing of x-ray tomography. *Journal of the European Ceramic Society*, 27(4):1973–1981.

Malevanets, A. and Kapral, R. (1999). Mesoscopic model for solvent dynamics. *The Journal of chemical physics*, 110(17):8605–8613.

Maurer Jr, C. R., Qi, R., and Raghavan, V. (2003). A linear time algorithm for computing exact euclidean distance transforms of binary images in arbitrary dimensions. *Pattern Analysis and Machine Intelligence, IEEE Transactions on*, 25(2):265–270.

Meakin, P. and Tartakovsky, A. M. (2009). Modeling and simulation of pore-scale multiphase fluid flow and reactive transport in fractured and porous media. *Reviews of Geophysics*, 47(3).

Medraj, M., Baril, E., Loya, V., and Lefebvre, L.-P. (2007). The effect of microstructure on the permeability of metallic foams. *Journal of materials science*, 42(12):4372–4383.

Menter, F. R. (1994). Two-equation eddy-viscosity turbulence models for engineering applications. *AIAA journal*, 32(8):1598–1605.

Meyer, F. (1994). Topographic distance and watershed lines. *Signal processing*, 38(1):113–125.

Montminy, M. D., Tannenbaum, A. R., and Macosko, C. W. (2004). The 3d structure of real polymer foams. *Journal of colloid and interface science*, 280(1):202–211.

Morsi, S. and Alexander, A. (1972). An investigation of particle trajectories in two-phase flow systems. *Journal of Fluid Mechanics*, 55(02):193–208.

Mukherjee, P. P., Kang, Q., and Wang, C.-Y. (2011). Pore-scale modeling of two-phase transport in polymer electrolyte fuel cellsprogress and perspective. *Energy & Environmental Science*, 4(2):346–369.

Nakayama, A. and Kuwahara, F. (1999). A macroscopic turbulence model for flow in a porous medium. *Journal of fluids engineering*, 121(2):427–433.

Øren, P.-E. and Bakke, S. (2003). Reconstruction of berea sandstone and pore-scale modelling of wettability effects. *Journal of Petroleum Science and Engineering*, 39(3):177–199.

O'Rourke, P. and Amsden, A. (1996). A particle numerical model for wall film dynamics in port-injected engines. Technical report, SAE Technical Paper.

O'Rourke, P. J. and Amsden, A. (2000). A spray/wall interaction submodel for the kiva-3 wall film model. Technical report, SAE Technical Paper.

Otsu, N. (1975). A threshold selection method from gray-level histograms. *Automatica*, 11(285-296):23–27.

Oun, H. and Kennedy, A. (2014). Experimental investigation of pressure-drop characteristics across multi-layer porous metal structures. *Journal of Porous Materials*, 21(6):1133–1141.

Oun, H. and Kennedy, A. (2015). Tailoring the pressure-drop in multi-layered open-cell porous inconel structures. *Journal of Porous Materials*, 22(6):1627–1633.

Patankar, S. V. and Spalding, D. B. (1972). A calculation procedure for heat, mass and momentum transfer in three-dimensional parabolic flows. *International journal of heat and mass transfer*, 15(10):1787–1806.

Pedras, M. H. and de Lemos, M. J. (2001). Macroscopic turbulence modeling for incompressible flow through undeformable porous media. *International Journal of Heat and Mass Transfer*, 44(6):1081–1093.

Petrasch, J., Meier, F., Friess, H., and Steinfeld, A. (2008a). Tomography based determination of permeability, durpuit-forchheimer coefficient, and interfacial heat transfer coefficient in reticulate porous ceramics. *International Journal of Fluid and Heat Flow*, 29:315–326.

Petrasch, J., Wyss, P., Stämpfli, R., and Steinfeld, A. (2008b). Tomography-based multiscale analyses of the 3d geometrical morphology of reticulated porous ceramics. *Journal of the American Ceramic Society*, 91(8):2659–2665.

Petrasch, J., Wyss, P., and Steinfeld, A. (2007). Tomography-based monte carlo determination of radiative properties of reticulate porous ceramics. *Journal of Quantitative Spectroscopy and Radiative Transfer*, 105(2):180–197.

Phillips, A. (2003). *Two-phase flow in rapidly rotating porous media*. PhD thesis, University of Nottingham.

Pierre, S. (1999). Morphological image analysis: Principles and applications.

Płaczek, M., Dyga, R., and Witczak, S. (2012). Experimental investigation of void fraction in horizontal air-water flow through fecraly foam. *Procedia Engineering*, 42:690–703.

Plimpton, S. (1995). Fast parallel algorithms for short-range molecular dynamics. *Journal of computational physics*, 117(1):1–19.

Pomeau, B. H. Y. and Frisch, U. (1986). Lattice-gas automata for the navier-stokes equation. *Phys. Rev. Lett*, 56(14):1505.

Raeini, A. Q., Blunt, M. J., and Bijeljic, B. (2012). Modelling two-phase flow in porous media at the pore scale using the volume-of-fluid method. *Journal of Computational Physics*, 231(17):5653–5668.

Ranut, P., Nobile, E., and Mancini, L. (2014). High resolution microtomography-based cfd simulation of flow and heat transfer in aluminum metal foams. *Applied Thermal Engineering*, 69(1):230–240.

Rycroft, C. (2009). Voro++: A three-dimensional voronoi cell library in c++. *Lawrence Berkeley National Laboratory*.

Schladitz, K., Redenbach, C., Sych, T., and Godehardt, M. (2008). *Microstructural characterisation of open foams using 3d images*. Fraunhofer-Institut für Techno-und Wirtschaftsmathematik, Fraunhofer (ITWM).

Sheppard, A. P., Sok, R. M., and Averdunk, H. (2004). Techniques for image enhancement and segmentation of tomographic images of porous materials. *Physica A: Statistical mechanics and its applications*, 339(1):145–151.

Shih, T.-H., Liou, W., Shabbir, A., Yang, Z., and Zhu, J. (1994). A new k-epsilon eddy viscosity model for high reynolds number turbulent flows: Model development and validation.

Slack, M., Prasad, R., Bakker, A., and Boysan, F. (2000). Advances in cyclone modelling using unstructured grids. *Chemical Engineering Research and Design*, 78(8):1098–1104.

Speziale, C. G. (1990). Analytical methods for the development of reynolds stress closures in turbulence. Technical report, DTIC Document.

Stanton, D. W. and Rutland, C. J. (1996). Modeling fuel film formation and wall interaction in diesel engines. Technical report, SAE Technical Paper.

Tennekes, H. and Lumley, J. L. (1972). *A first course in turbulence*. MIT press.

Teruel, F. E. et al. (2009). A new turbulence model for porous media flows. part i: Constitutive equations and model closure. *International Journal of Heat and Mass Transfer*, 52(19):4264–4272.

Thompson, K. E. (2002). Pore-scale modeling of fluid transport in disordered fibrous materials. *American Institute of Chemical Engineers. AIChE Journal*, 48(7):1369.

Thomson, W. (1887). Lxiii. on the division of space with minimum partitional area. *The London, Edinburgh, and Dublin Philosophical Magazine and Journal of Science*, 24(151):503–514.

Topin, F., Bonnet, J.-P., Madani, B., and Tadrist, L. (2006). Experimental analysis of multiphase flow in metallic foam: flow laws, heat transfer and convective boiling. *Advanced Engineering Materials*, 8(9):890–899.

Vafai, K. (1984). Convective flow and heat transfer in variable-porosity media. *Journal of Fluid Mechanics*, 147:233–259.

Vafai, K. and Tien, C. (1981). Boundary and inertia effects on flow and heat transfer in porous media. *International Journal of Heat and Mass Transfer*, 24(2):195–203.

Verger, P. and Morvan, H. P. (2011). Trent 1000 breather cfd project. Technical report, Nottingham Rolls-Royce University Technology Centre in Gas Turbine.

Versteeg, H. K. and Malalasekera, W. (2007). *An introduction to computational fluid dynamics: the finite volume method*. Pearson Education.

Vicente, J., Topin, F., and Daurelle, J.-V. (2006). Open celled material structural properties measurement: from morphology to transport properties. *Materials transactions*, 47(9):2195–2202.

Walther, G., Klöden, B., Büttner, T., Weissgärber, T., Kieback, B., Böhm, A., Naumann, D., Saberi, S., and Timberg, L. (2008). A new class of high temperature and corrosion resistant nickel-based open-cell foams. *Advanced Engineering Materials*, 10(9):803–811.

Wang, B., Xu, D., Chu, K., and Yu, A. (2006). Numerical study of gas–solid flow in a cyclone separator. *Applied Mathematical Modelling*, 30(11):1326–1342.

Wang, Y., Hibberd, S., Simmons, K., Eastwick, C., and Care, I. (2001). Application of cfd to modelling two-phase flow in a high-speed aero-engine transmission chamber. In *ASME Fluids Engineering Division Summer Meeting, New Orleans, LA, May*, pages 249–254.

Weaire, D. and Phelan, R. (1994). A counter-example to kelvin's conjecture on minimal surfaces. *Philosophical Magazine Letters*, 69(2):107–110.

Whitaker, S. (1986). Flow in porous media i: A theoretical derivation of darcy's law. *Transport in porous media*, 1(1):3–25.

Whitaker, S. (1998). *The method of volume averaging*, volume 13. Springer Science & Business Media.

Wilcox, D. C. et al. (1998). *Turbulence modeling for CFD*, volume 2. DCW industries La Canada, CA.

Willenborg, K., Klingsporn, M., Tebby, S., Ratcliffe, T., Gorse, P., Dullenkopf, K., and Wittig, S. (2008). Experimental analysis of air/ oil separator performance. *Journal of Engineering for Gas Turbines and Power*, 130(6):062503.

Wittig, S., Glahn, A., and Himmelsbach, J. (1993). Influence of high rotational speeds on heat transfer and oil film thickness in aero engine bearing chambers. In *ASME 1993 International Gas Turbine and Aeroengine Congress and Exposition*, pages V03AT15A060–V03AT15A060. American Society of Mechanical Engineers.

Wolfshtein, M. (1969). The velocity and temperature distribution in one-dimensional flow with turbulence augmentation and pressure gradient. *International Journal of Heat and Mass Transfer*, 12(3):301–318.

Yakhot, V., Orszag, S., Thangam, S., Gatski, T., and Speziale, C. (1992). Development of turbulence models for shear flows by a double expansion technique. *Physics of Fluids A: Fluid Dynamics (1989-1993)*, 4(7):1510–1520.

Yarin, A. (2006). Drop impact dynamics: splashing, spreading, receding, bouncing. *Annu. Rev. Fluid Mech.*, 38:159–192.

Appendices

Appendix A

Morphological measurements

A.1 Pore size distributions

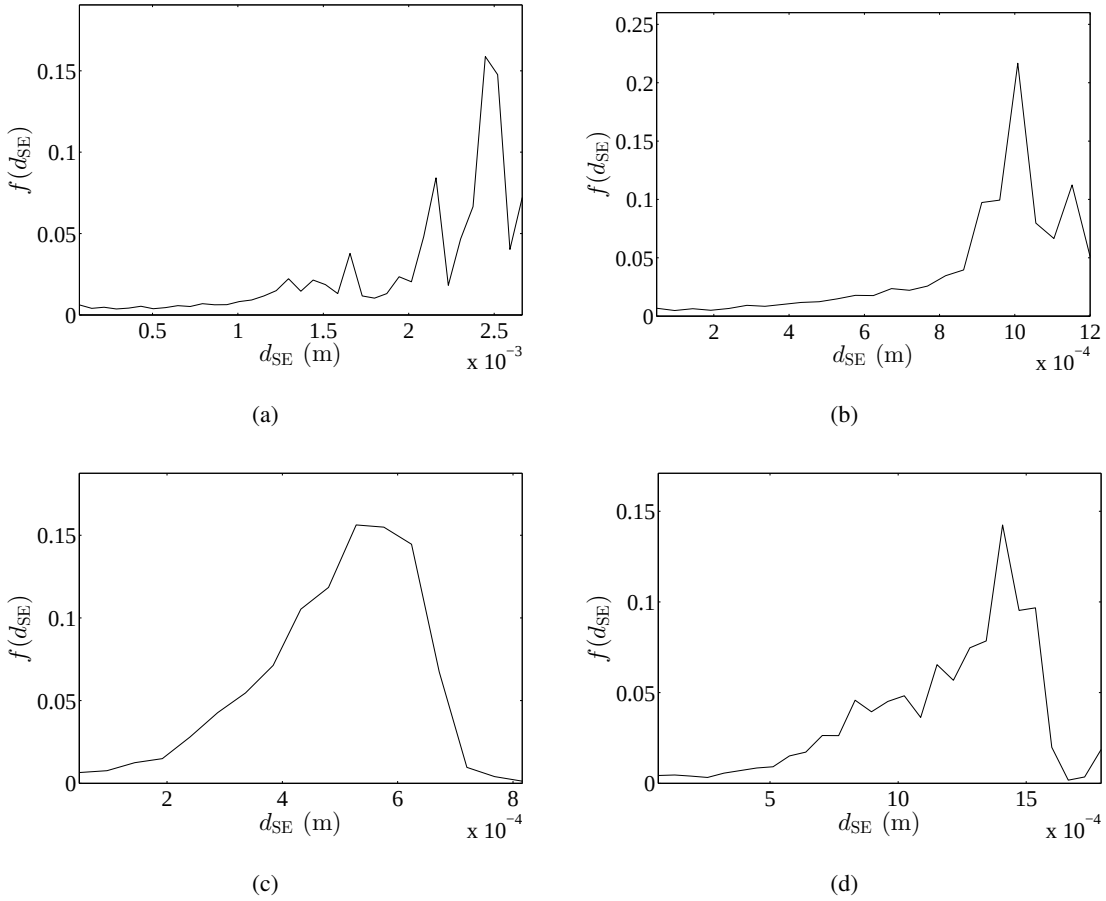

Figure A.1: Pore size distributions computed using the opening size distributions for the (a) Retimet 20 PPI, (b) Retimet 45 PPI, (c) Retimet 80 PPI, (d) Inconel 1200+580 μm and (e) Recemat.

A.2 Strut size distributions

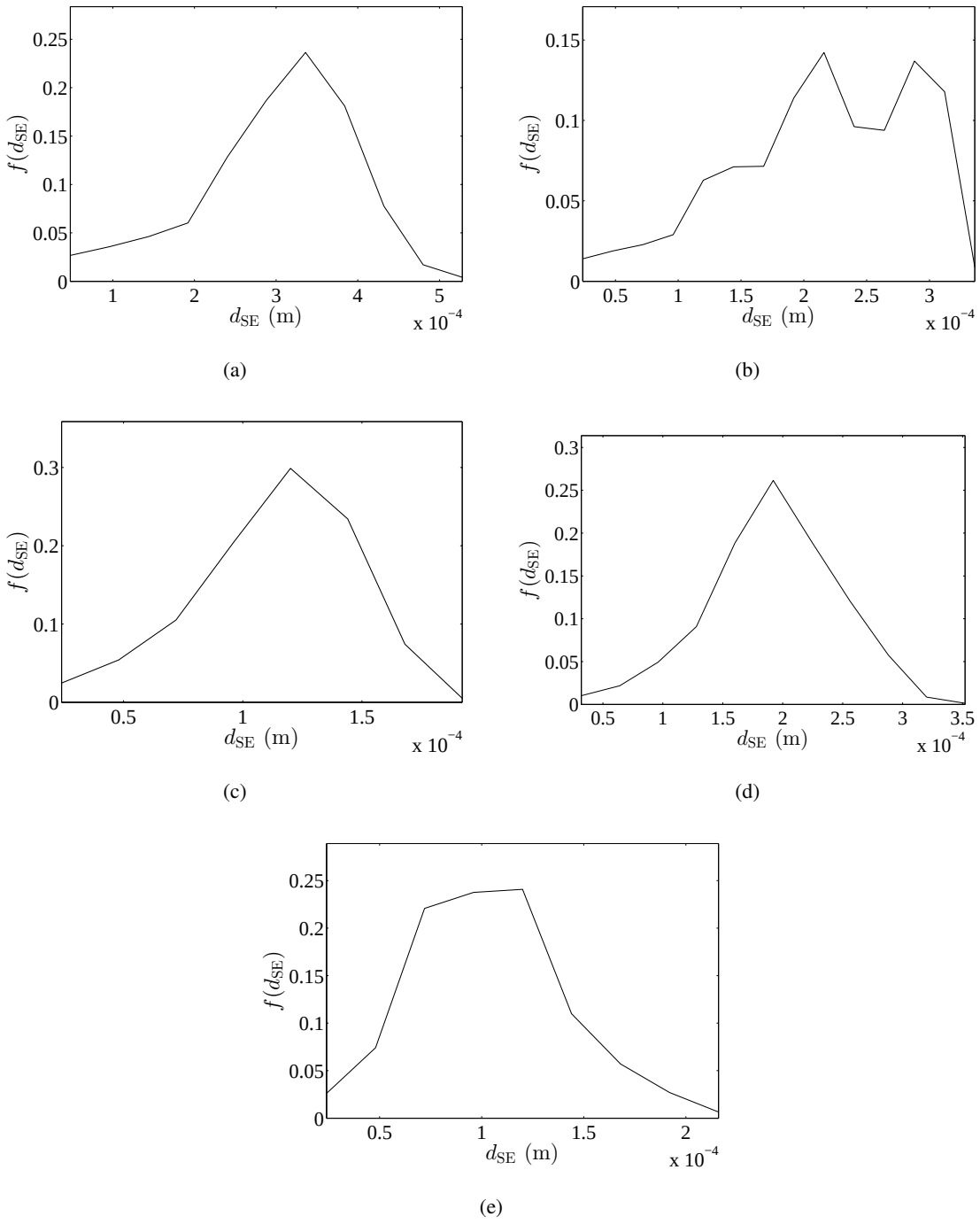

Figure A.2: Strut size distributions computed using the opening size distributions for the (a) Retimet 20 PPI, (b) Retimet 45 PPI, (c) Retimet 80 PPI, (d) Recemat and (e) Inconel 1200+580 µm.

A.3 Minimum geometrical representative volume

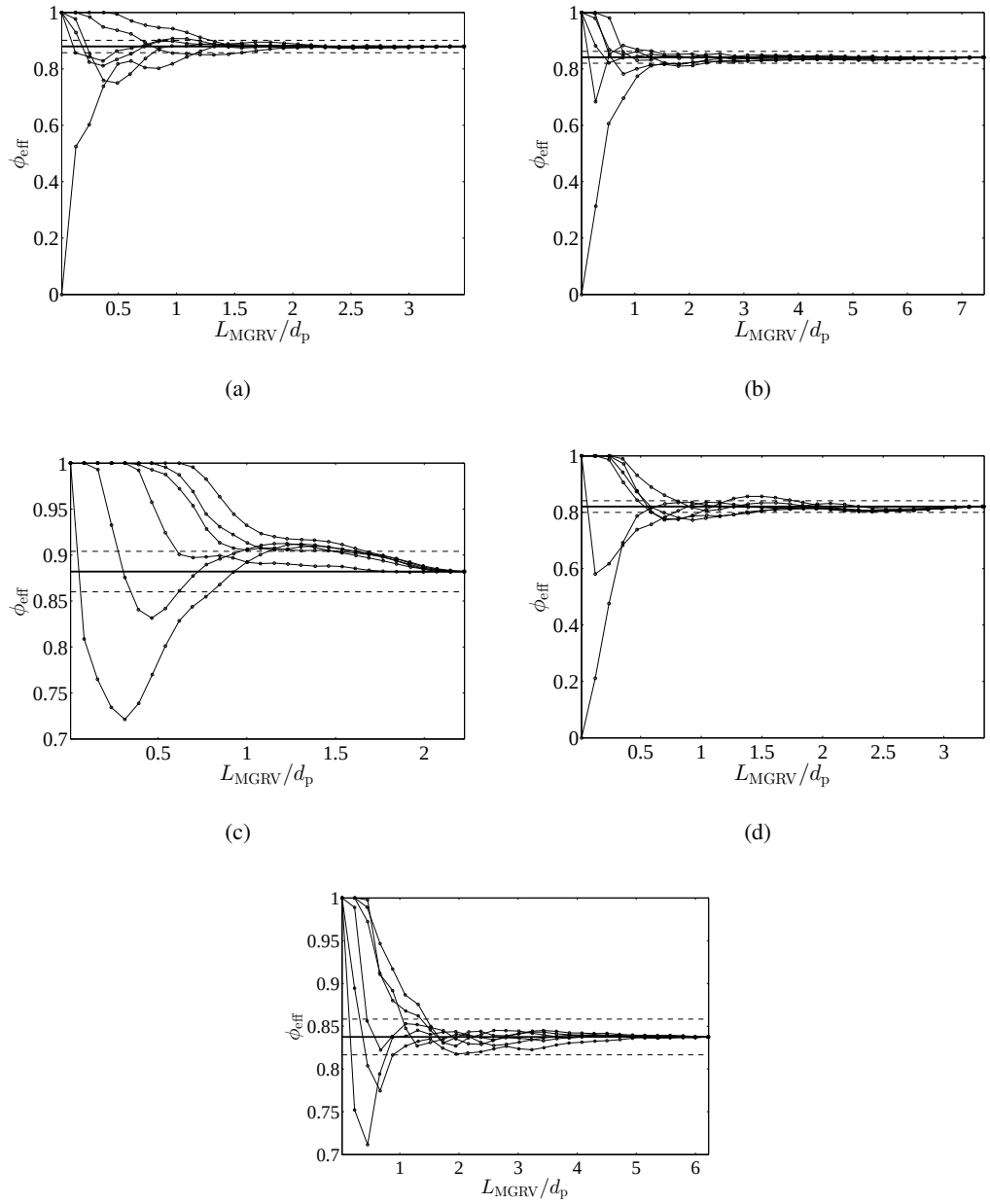

Figure A.3: Effective porosity as function of the normalized sampling cubic edge L_{MGRV}/d_p for the (a) Inconel 1200 µm, (b) Inconel 1200+580 µm, (c) Retimet 20 PPI, (d) Retimet 45 PPI and (e) Retimet 80 PPI. The dashed horizontal lines denote the ± 0.025 bands. Six random starting points are used.

Appendix B

Lagrangian oil capture curves

Figure B.1 shows a schematic of the droplet capture approach and its relation to the oil capture curves. The final streamwise locations of all droplets is recorded, and the oil capture curve is basically a histogram that relates the proportion of free (non-captured) droplets at a particular streamwise position along the foam sample. The streamwise position, defined as z, is subsequently normalized by the mean pore size, d_p, of the particular foam which is being analysed. This section shows the capture curves computed for all foam samples investigated. Furthermore, it also shows the oil capture curves computed for the rotating MRF cases at 2000 and 6000 RPM respectively. Only the Retimet 45 PPI foam was simulated using the MRF approach.

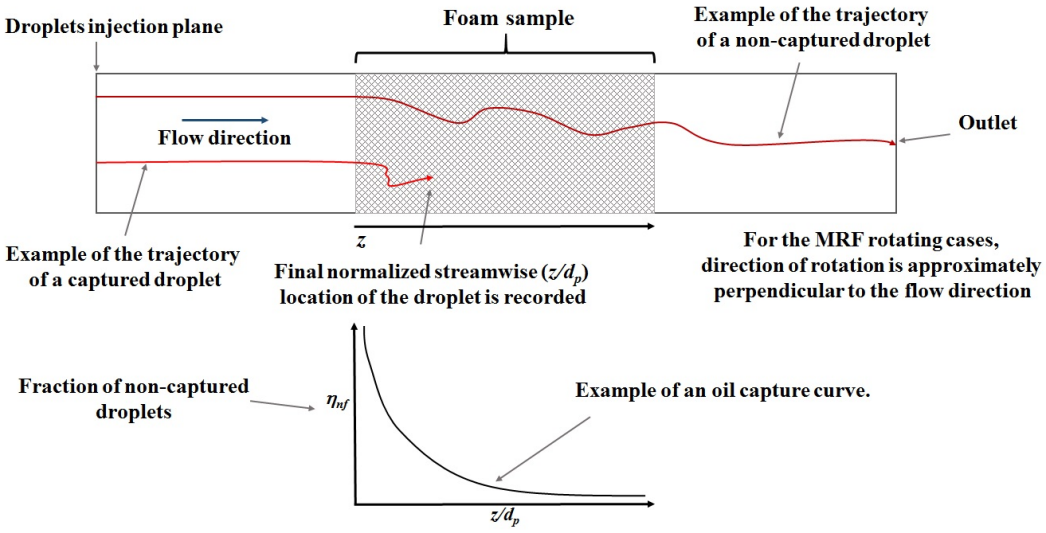

Figure B.1: Schematic of the Lagrangian droplet capture approach and its relation to the oil capture curves based on the normalized streamwise position.

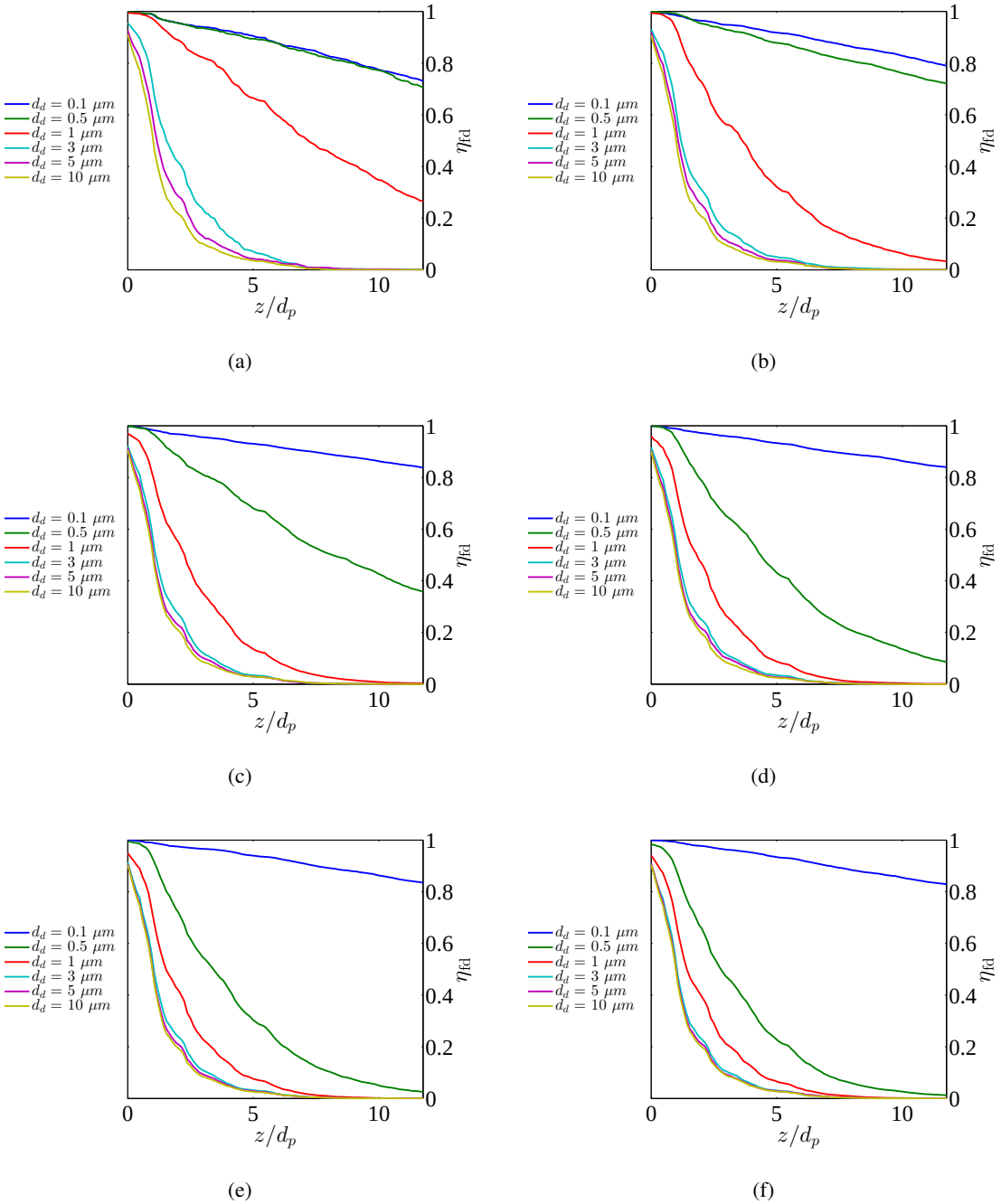

Figure B.2: Lagrangian simulations results showing oil capture curves for the Inconel 1200+580 µm foam, for six different droplet diameters. Results are shown for six Darcian velocities: (a) 5, (b) 10, (c) 20, (d) 30, (e) 40 and (f) 50 m/s.

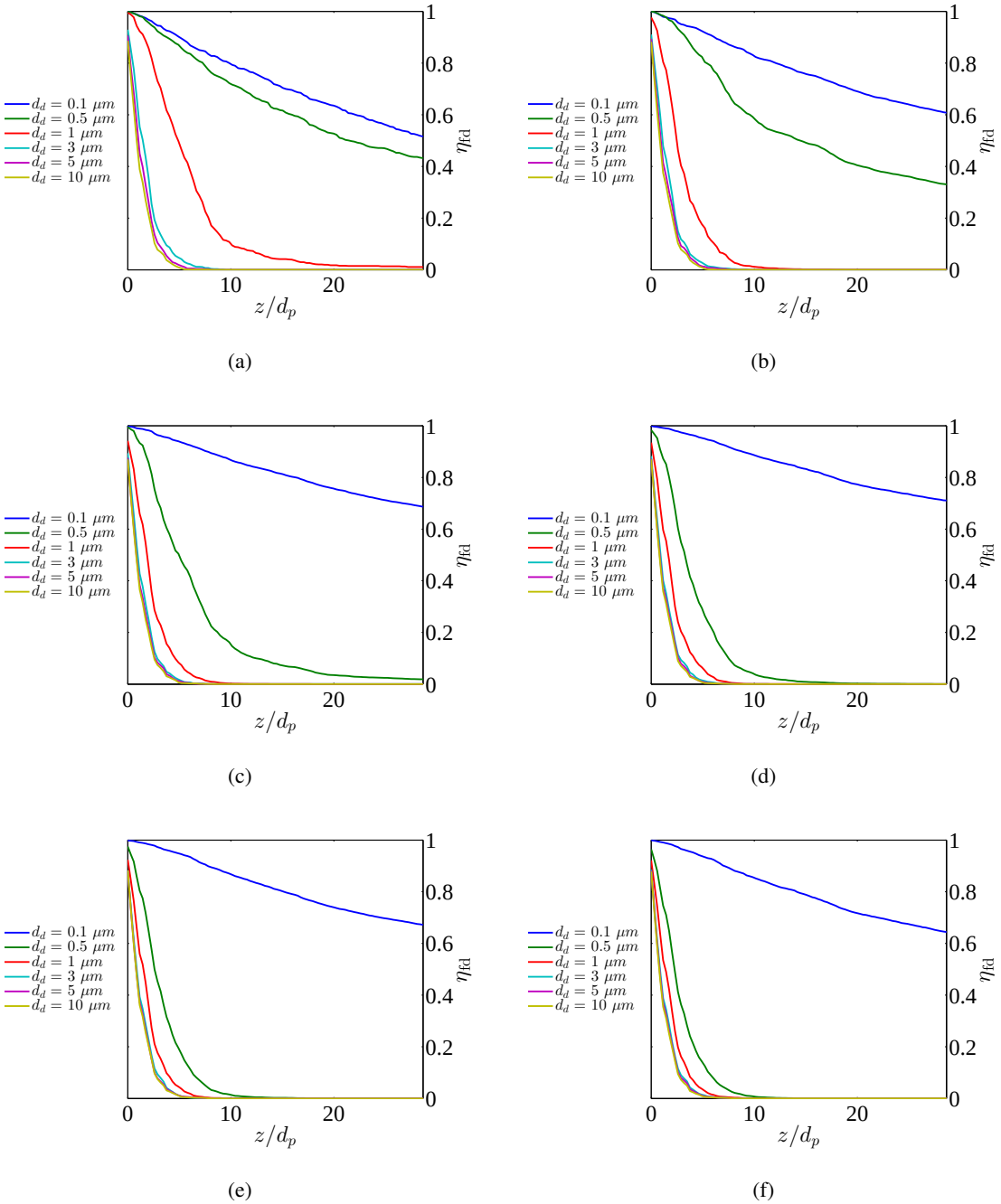

Figure B.3: Lagrangian simulations results showing oil capture curves for the Inconel 450 µm foam, for six different droplet diameters. Results are shown for six Darcian velocities: (a) 5, (b) 10, (c) 20, (d) 30, (e) 40 and (f) 50 m/s.

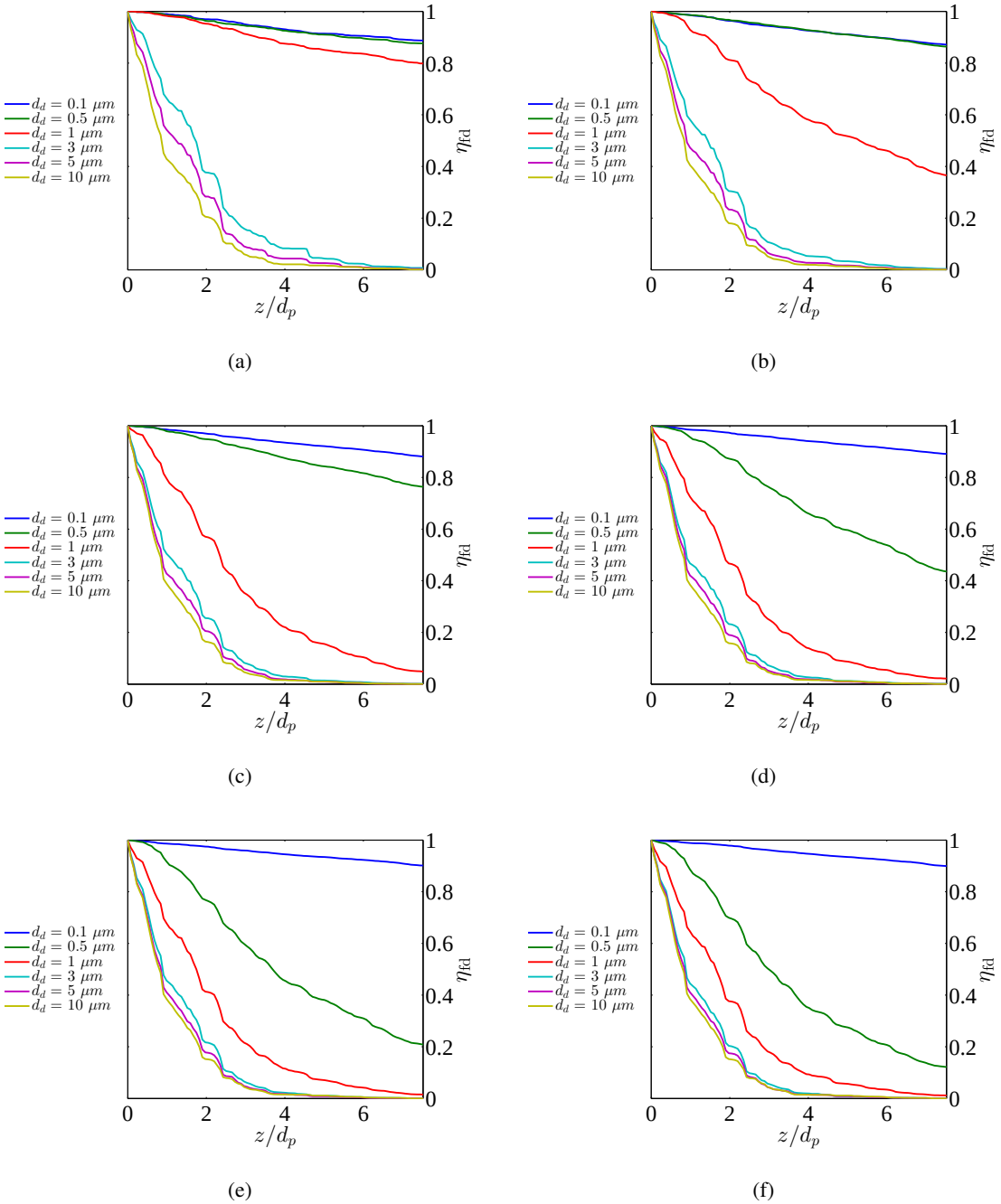

Figure B.4: Lagrangian simulations results showing oil capture curves for the Inconel 1200 µm foam, for six different droplet diameters. Results are shown for six Darcian velocities: (a) 5, (b) 10, (c) 20, (d) 30, (e) 40 and (f) 50 m/s.

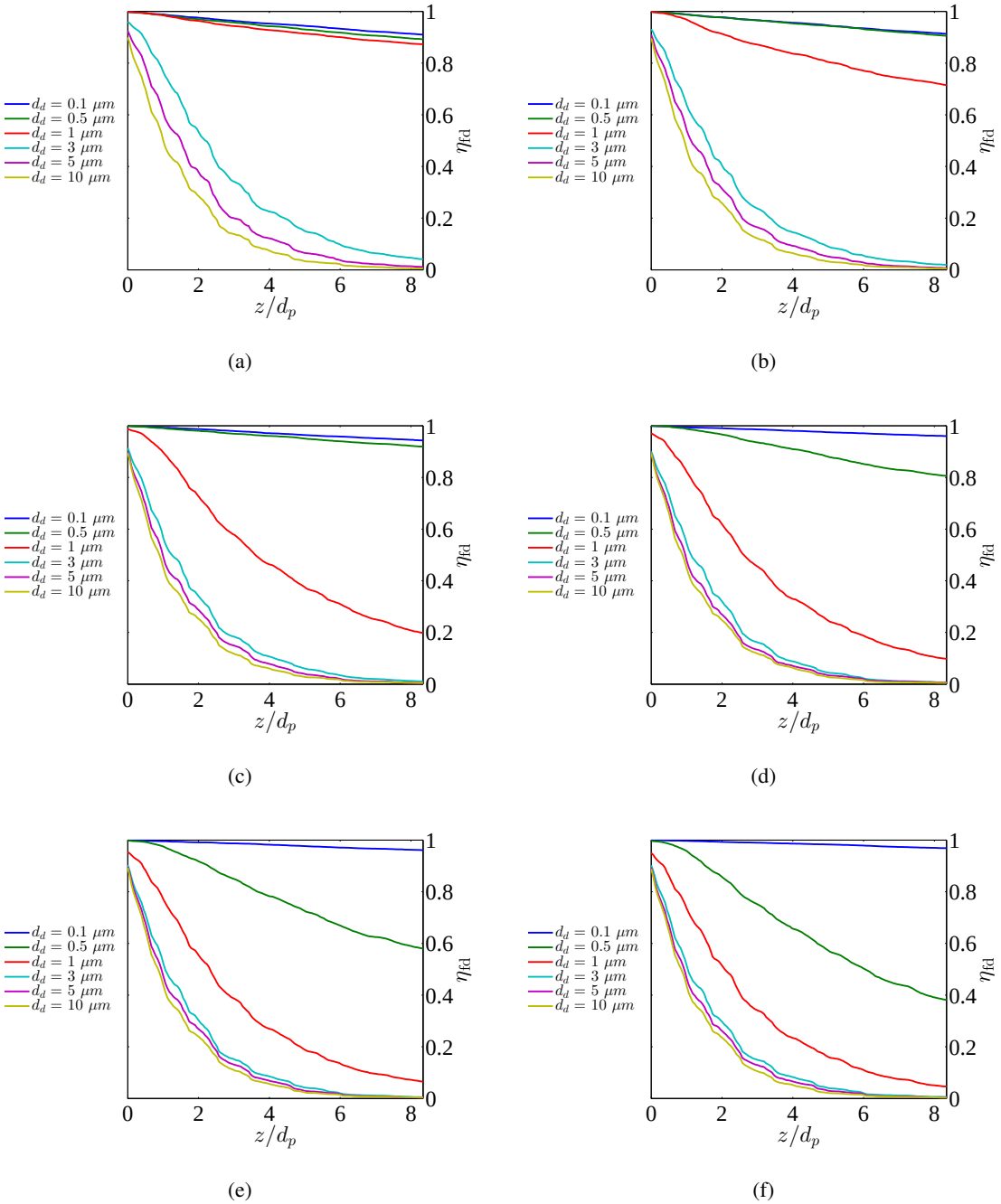

Figure B.5: Lagrangian simulations results showing oil capture curves for the Recemat foam, for six different droplet diameters. Results are shown for six Darcian velocities: (a) 5, (b) 10, (c) 20, (d) 30, (e) 40 and (f) 50 m/s.

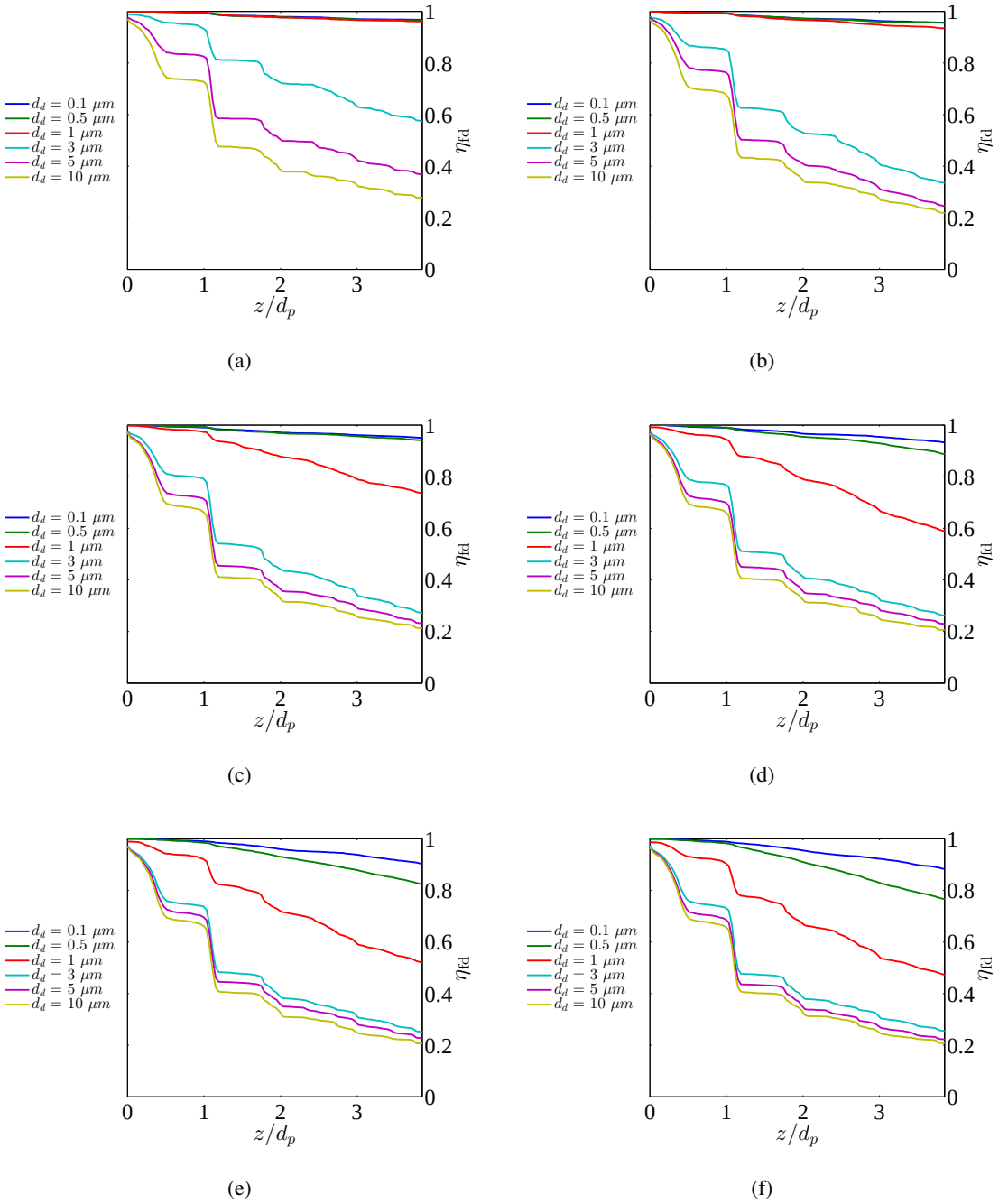

Figure B.6: Lagrangian simulations results showing oil capture curves for the Retimet 20 PPI foam, for six different droplet diameters. Results are shown for six Darcian velocities: (a) 5, (b) 10, (c) 20, (d) 30, (e) 40 and (f) 50 m/s.

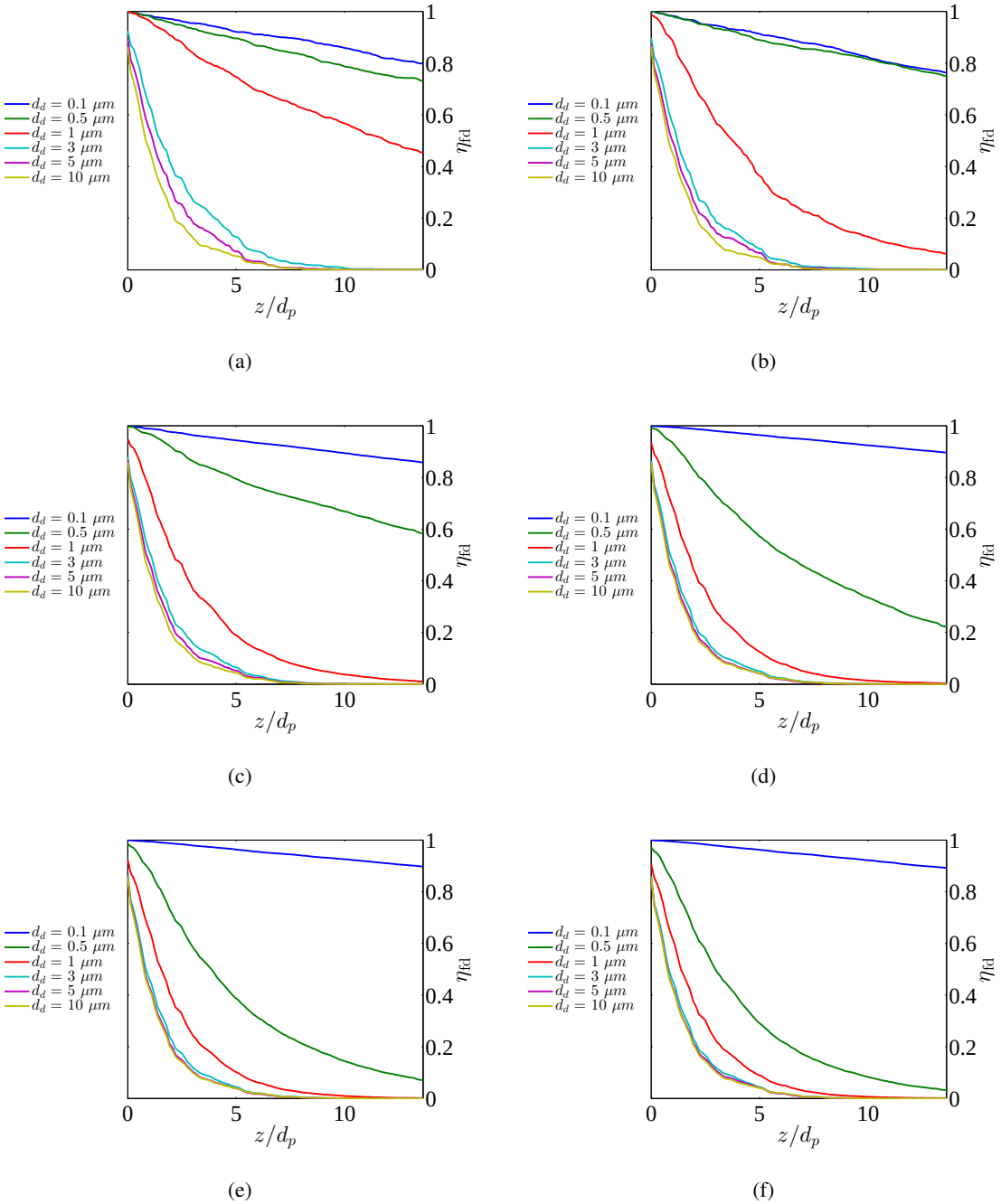

Figure B.7: Lagrangian simulations results showing oil capture curves for the Retimet 80 PPI foam, for six different droplet diameters. Results are shown for six Darcian velocities: (a) 5, (b) 10, (c) 20, (d) 30, (e) 40 and (f) 50 m/s.

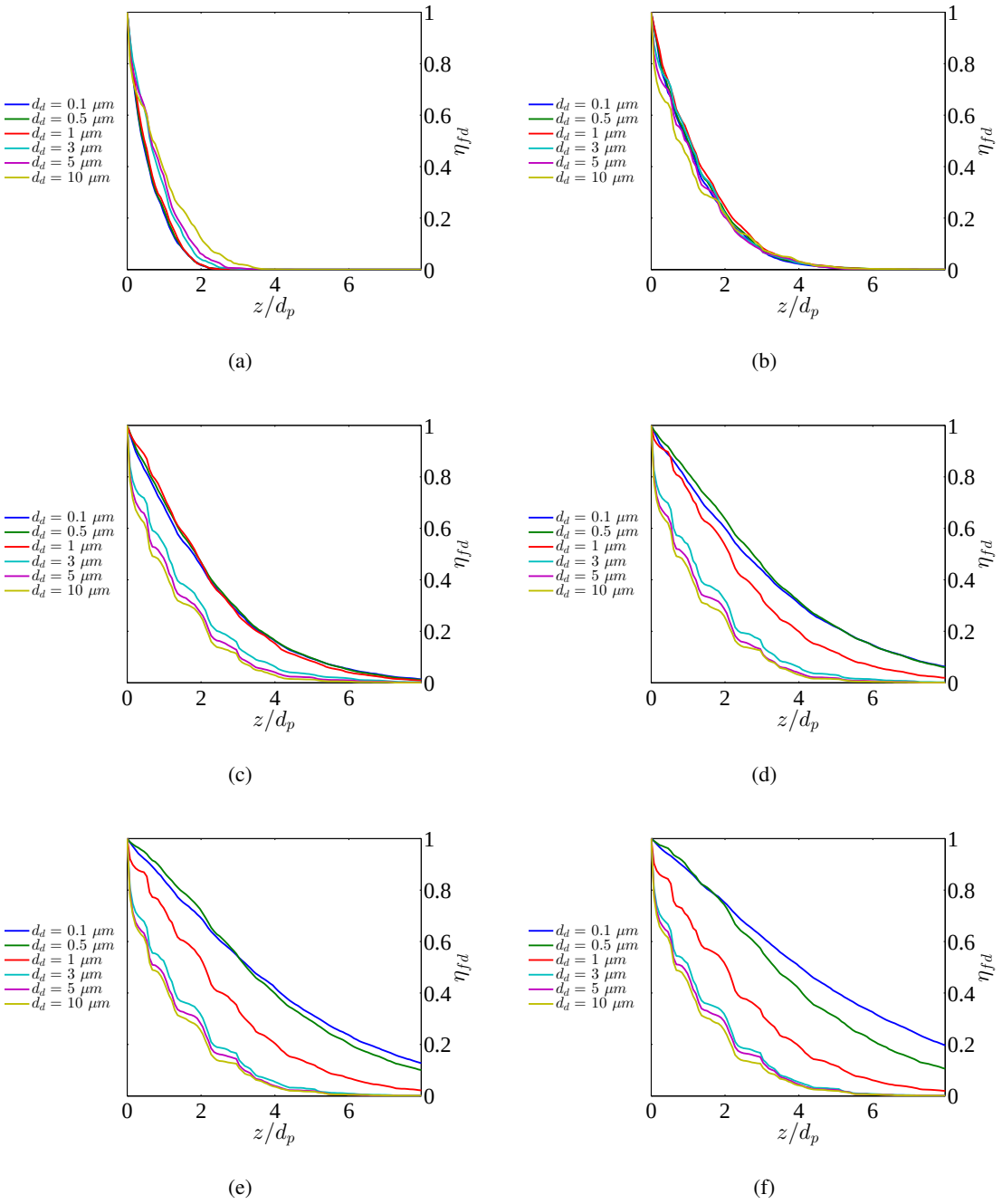

Figure B.8: MRF Lagrangian simulations results at 2000 RPM showing oil capture curves for the Retimet 45 PPI foam, for six different droplet diameters. Results are shown for six Darcian velocities: (a) 5, (b) 10, (c) 20, (d) 30, (e) 40 and (f) 50 m/s.

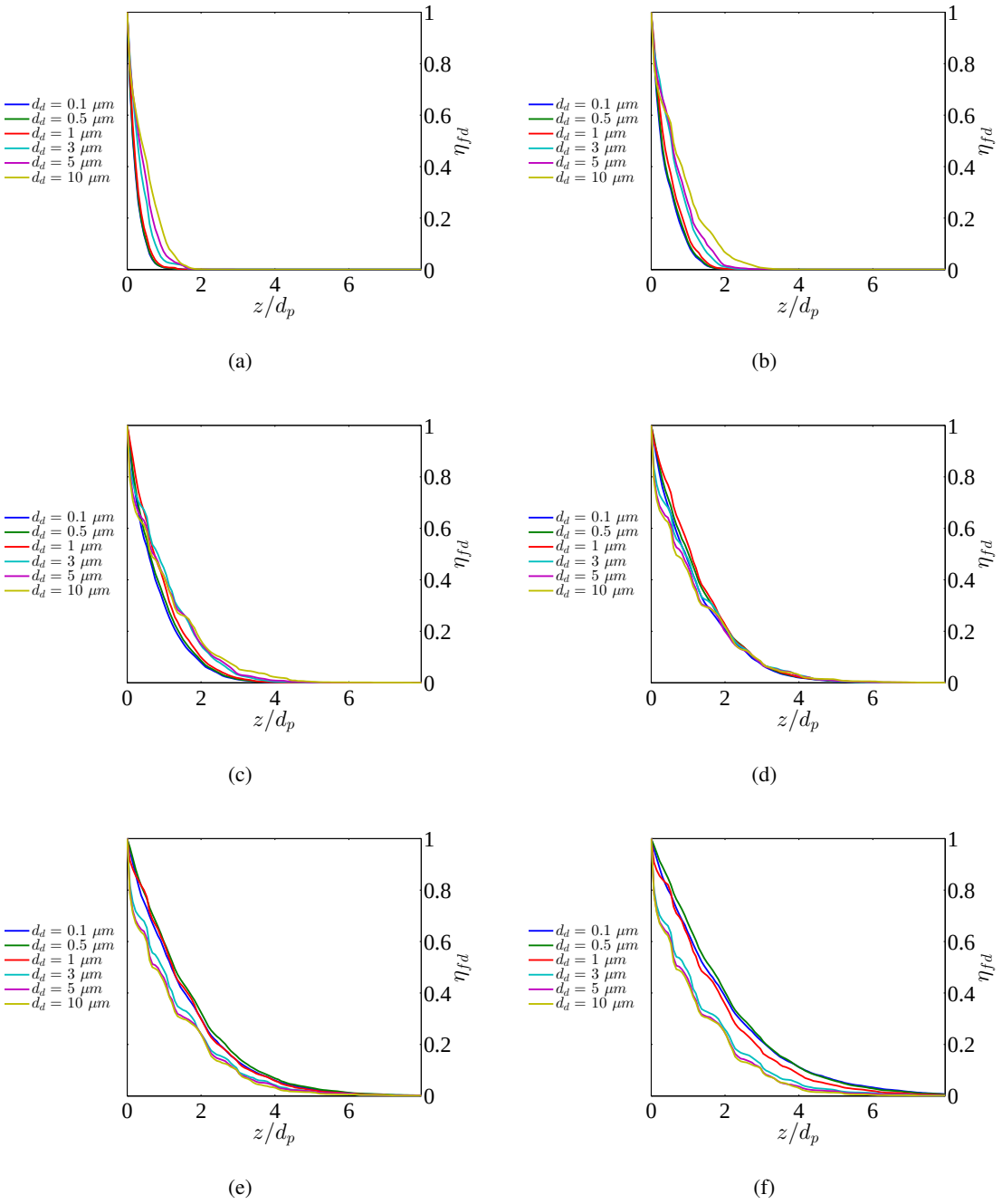

Figure B.9: MRF Lagrangian simulations results at 6000 RPM showing oil capture curves for the Retimet 45 PPI foam, for six different droplet diameters. Results are shown for six Darcian velocities: (a) 5, (b) 10, (c) 20, (d) 30, (e) 40 and (f) 50 m/s.

Appendix C

Velocity profiles within the separator

This section depicts the normalized axial and tangential velocity radial profiles taken at five different locations inside the simulated aero-engine separator, at all rotational speeds investigated. Axial and tangential velocity are normalized by the average velocity magnitude at the inlets, defined as u_0. Figure C.1 illustrates the location of the five lines where the radial profiles were computed. Line L_1 is located at the same axial position as the entrance of the rotor, starting from the outer radius of the rotor and finishing on the chamber outer radius, defined as r_0. Line L_2 is at the same axial position as L_1, but starts from the outer rotor radius and finished at the hollow shaft. Line L_3 is located at the exit of the foam region. Line L_4 is located inside the hollow shaft, next to the slots leading from the foam exit to the hollow shaft. Lastly, line L_5 is located at one shaft diameter away from the outlet.

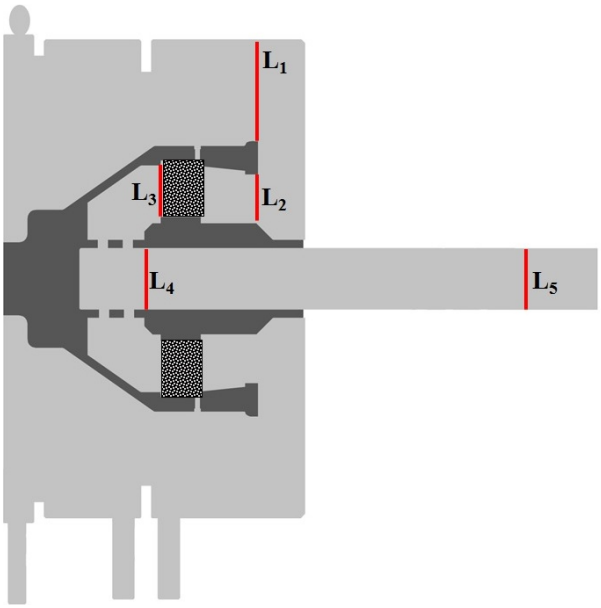

Figure C.1: Location of the five lines where the normalized axial and tangential velocity radial profiles were computed.

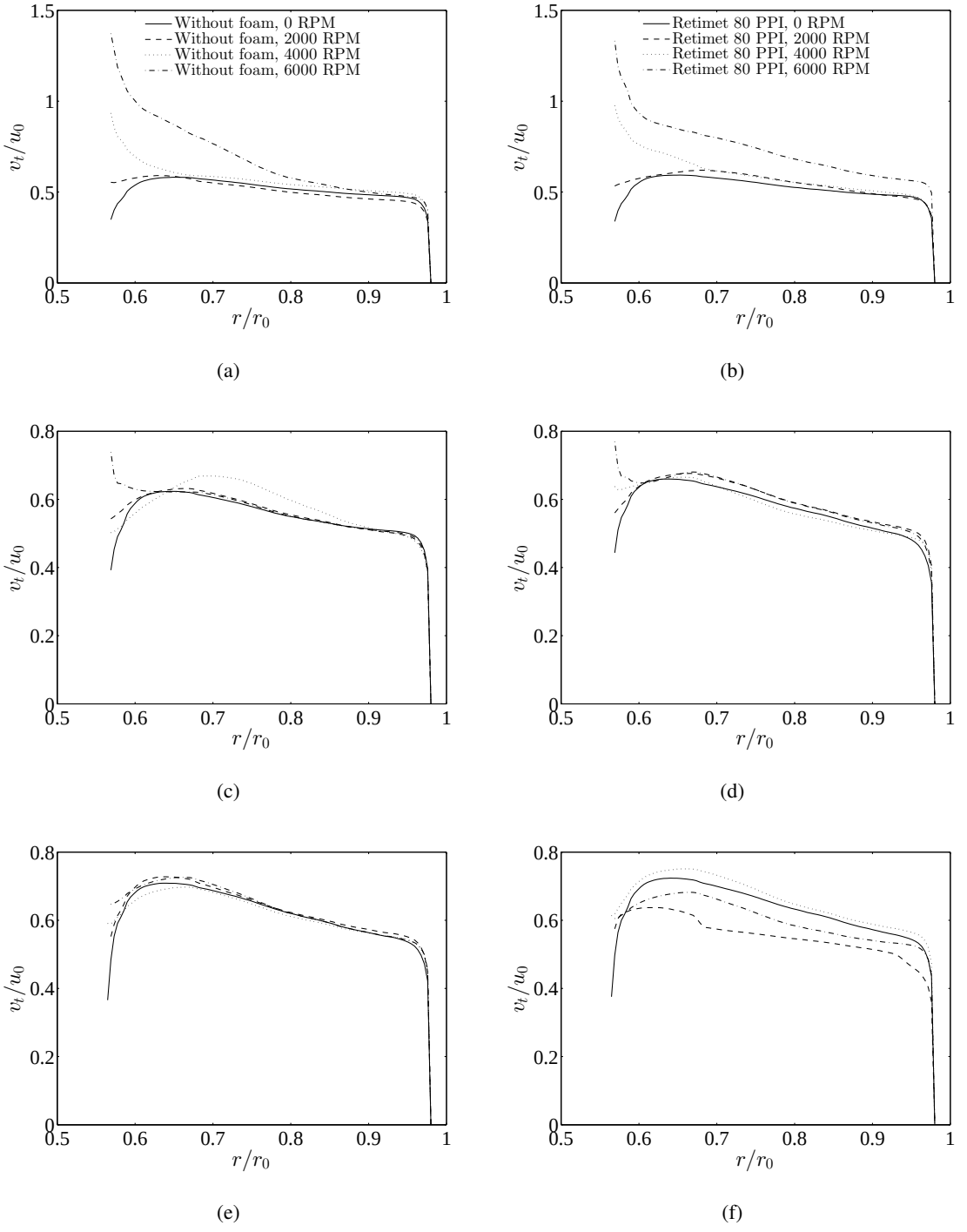

Figure C.2: Normalized tangential velocity at line L_1 for the cases without foam and with the Retimet 80 PPI. Left column comprises the results obtained without foam. Right column comprises the results obtained with the Retimet 80 PPI. (a,b) 20 g/s, (c,d) 40 g/s, and (e,f) 100 g/s of airflow.

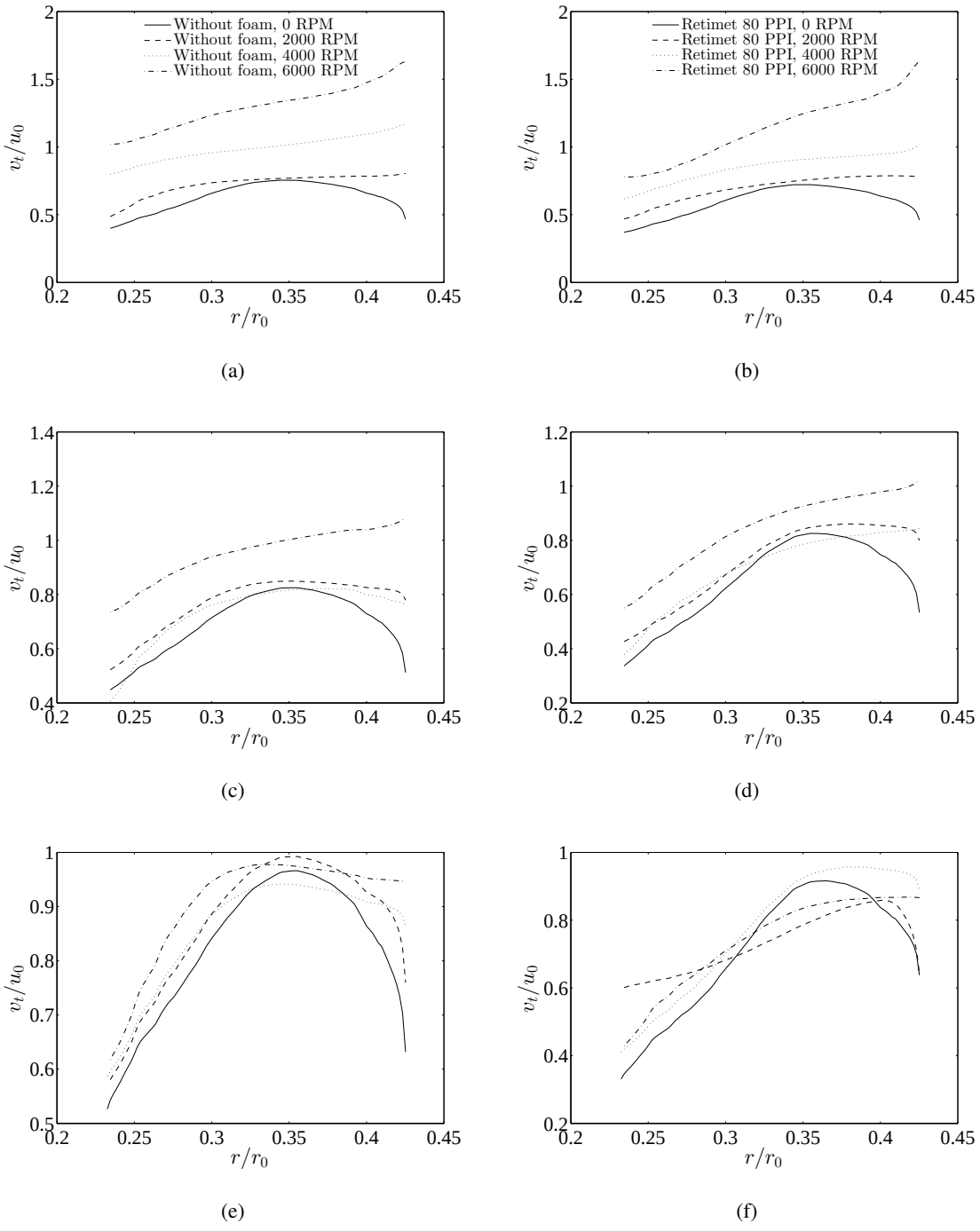

Figure C.3: Normalized tangential velocity at line L_2 for the cases without foam and with the Retimet 80 PPI. Left column comprises the results obtained without foam. Right column comprises the results obtained with the Retimet 80 PPI. (a,b) 20 g/s, (c,d) 40 g/s, and (e,f) 100 g/s of airflow.

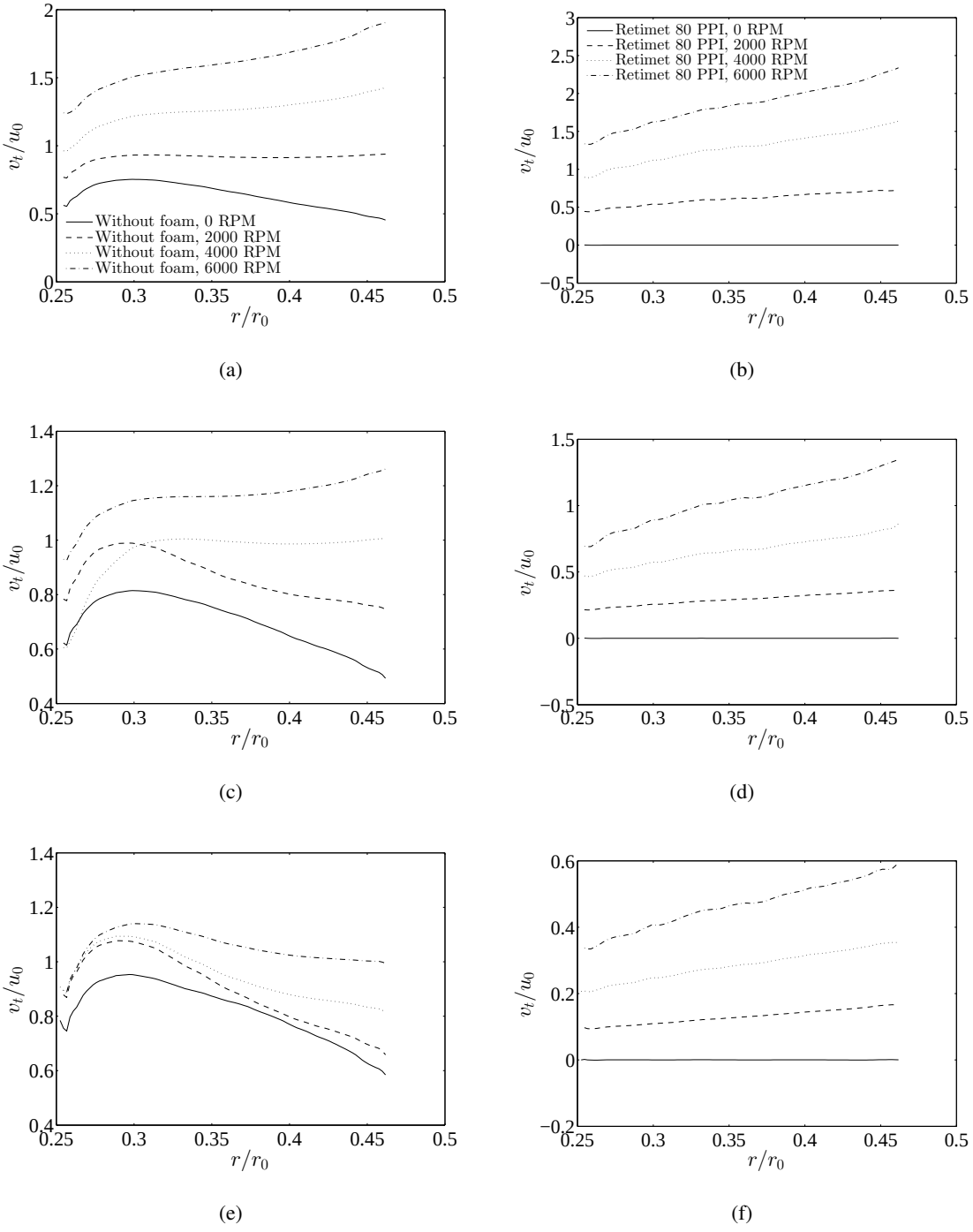

Figure C.4: Normalized tangential velocity at line L_3 for the cases without foam and with the Retimet 80 PPI. Left column comprises the results obtained without foam. Right column comprises the results obtained with the Retimet 80 PPI. (a,b) 20 g/s, (c,d) 40 g/s, and (e,f) 100 g/s of airflow.

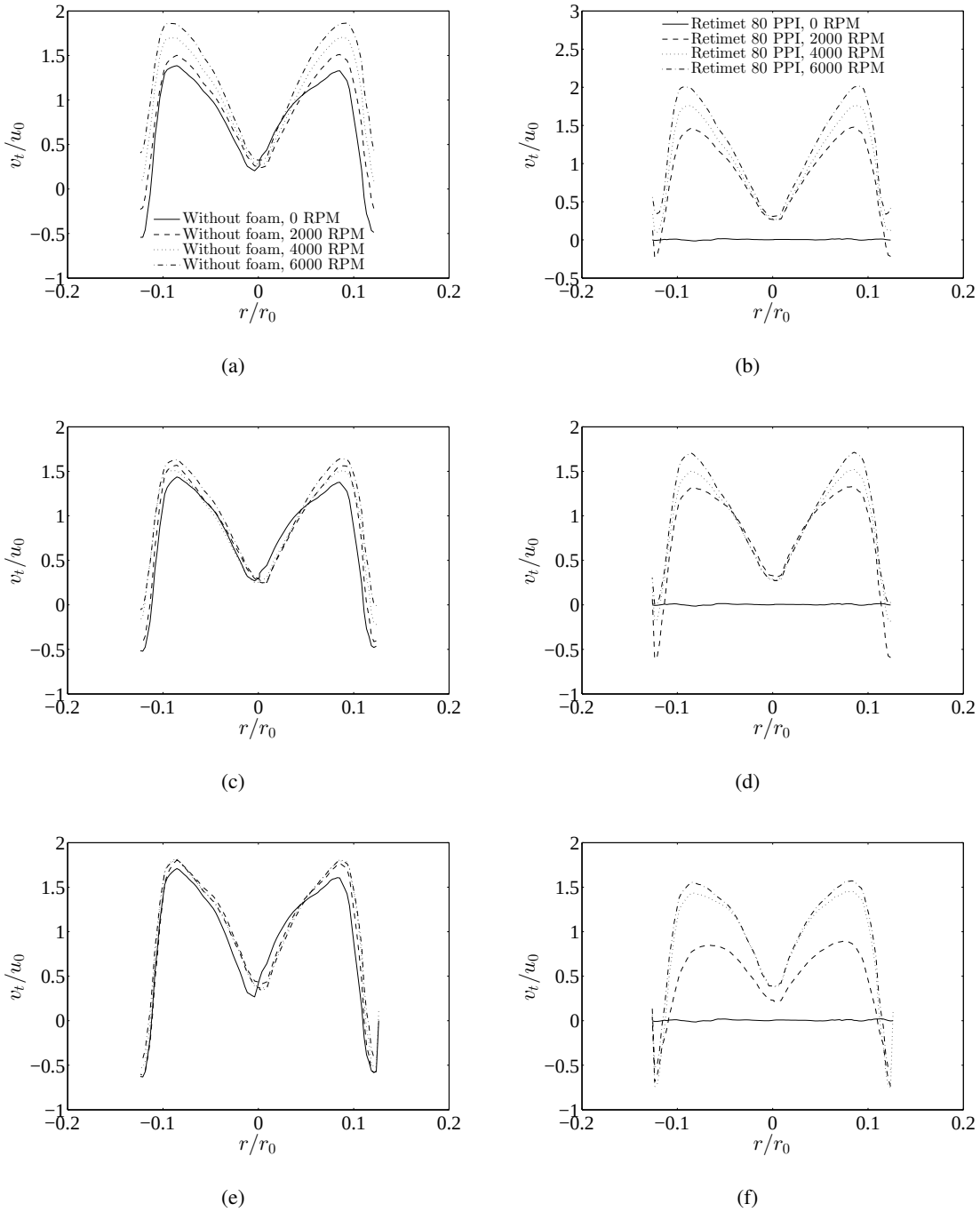

Figure C.5: Normalized tangential velocity at line L_4 for the cases without foam and with the Retimet 80 PPI. Left column comprises the results obtained without foam. Right column comprises the results obtained with the Retimet 80 PPI. (a,b) 20 g/s, (c,d) 40 g/s, and (e,f) 100 g/s of airflow.

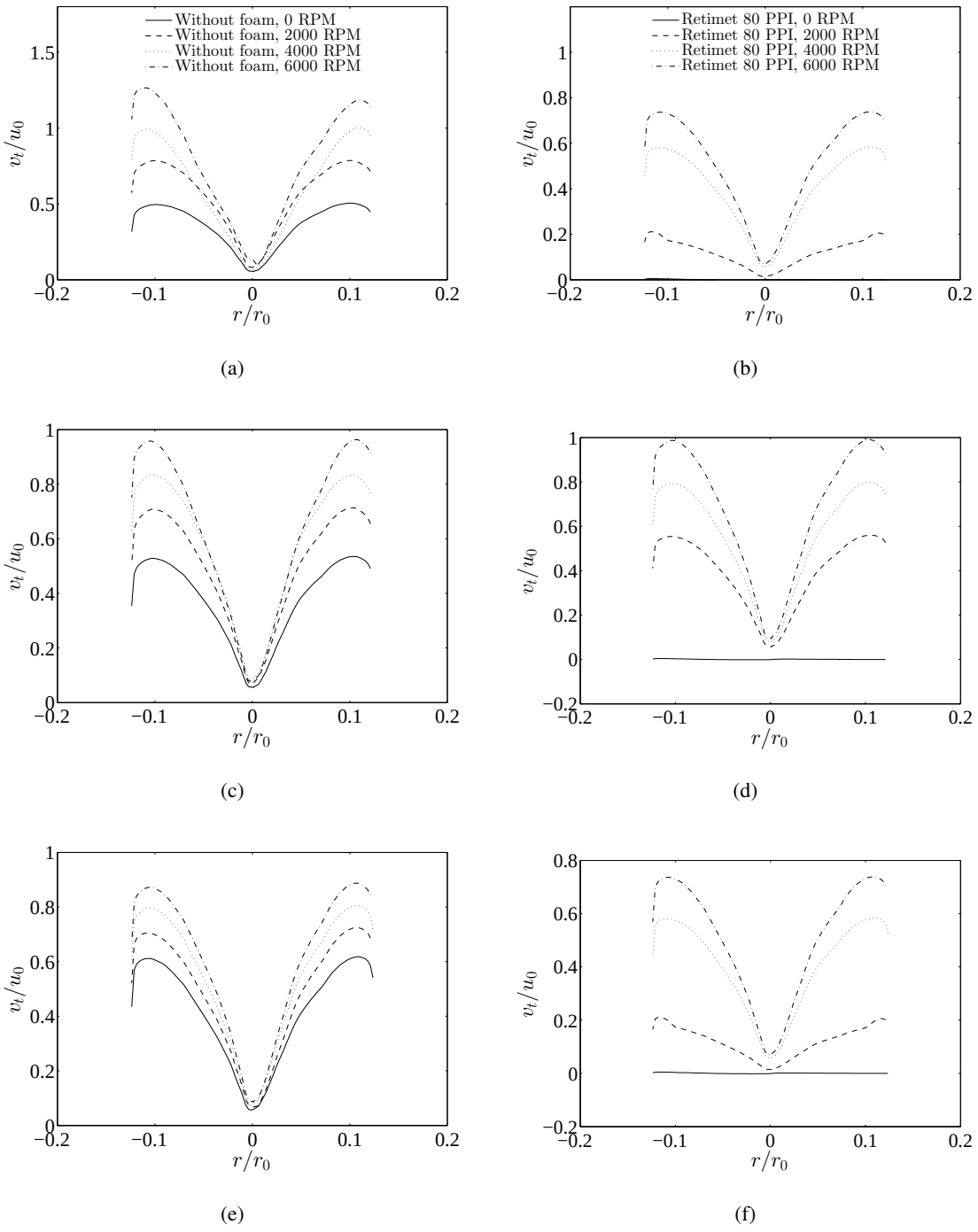

Figure C.6: Normalized tangential velocity at line L_5 for the cases without foam and with the Retimet 80 PPI. Left column comprises the results obtained without foam. Right column comprises the results obtained with the Retimet 80 PPI. (a,b) 20 g/s, (c,d) 40 g/s, and (e,f) 100 g/s of airflow.

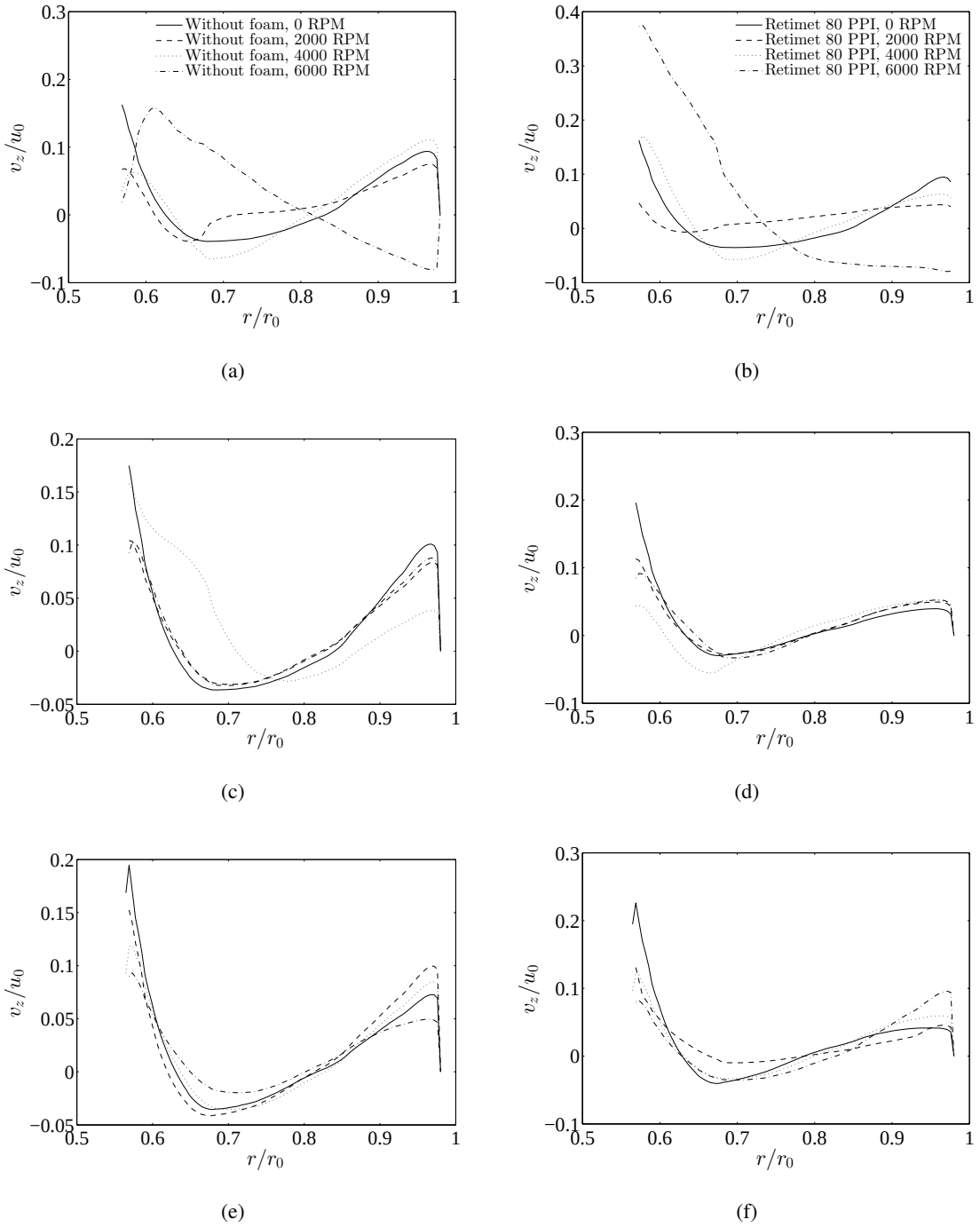

Figure C.7: Normalized axial velocity at line L_1 for the cases without foam and with the Retimet 80 PPI. Left column comprises the results obtained without foam. Right column comprises the results obtained with the Retimet 80 PPI. (a,b) 20 g/s, (c,d) 40 g/s, and (e,f) 100 g/s of airflow.

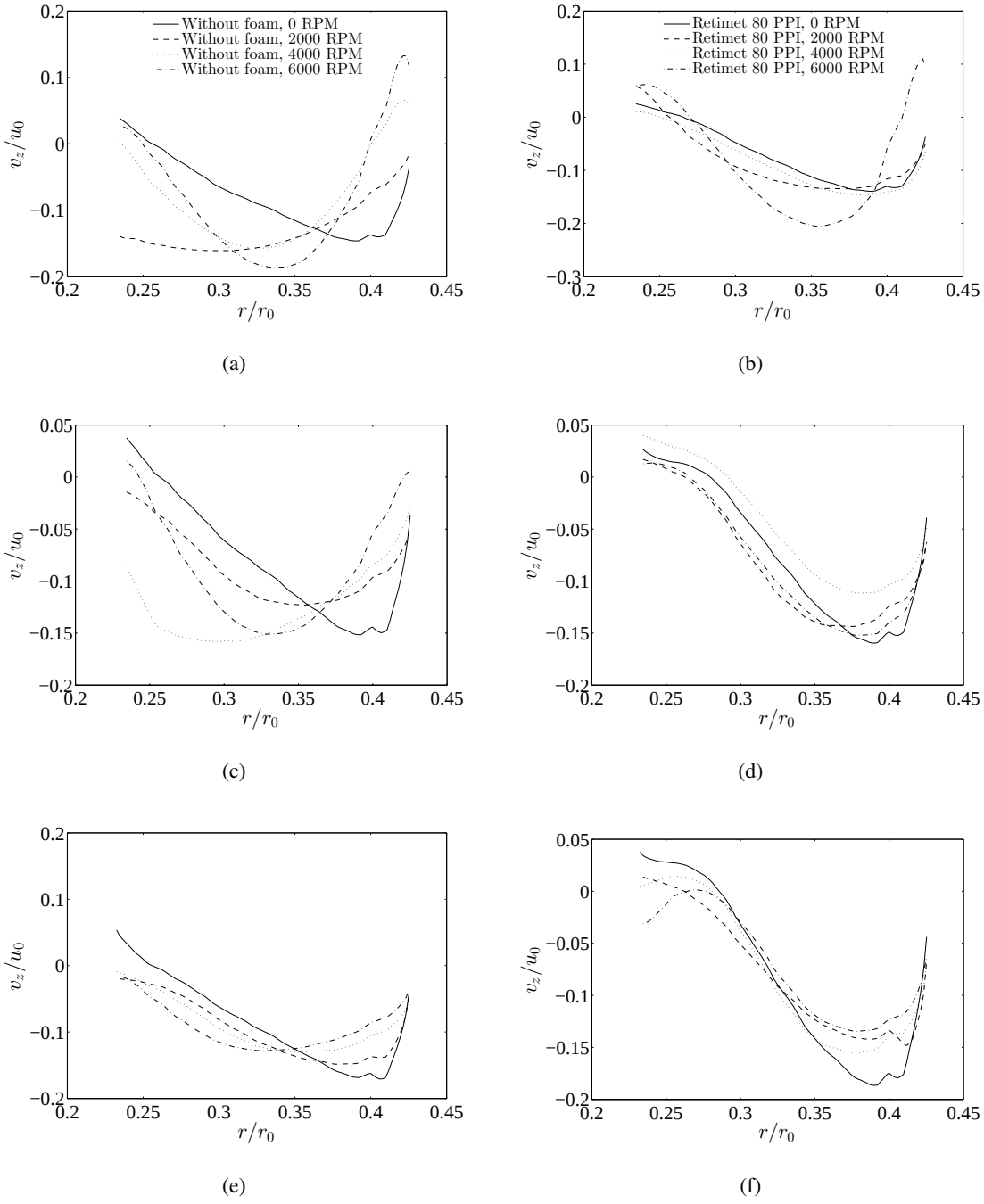

Figure C.8: Normalized axial velocity at line L_2 for the cases without foam and with the Retimet 80 PPI. Left column comprises the results obtained without foam. Right column comprises the results obtained with the Retimet 80 PPI. (a,b) 20 g/s, (c,d) 40 g/s, and (e,f) 100 g/s of airflow.

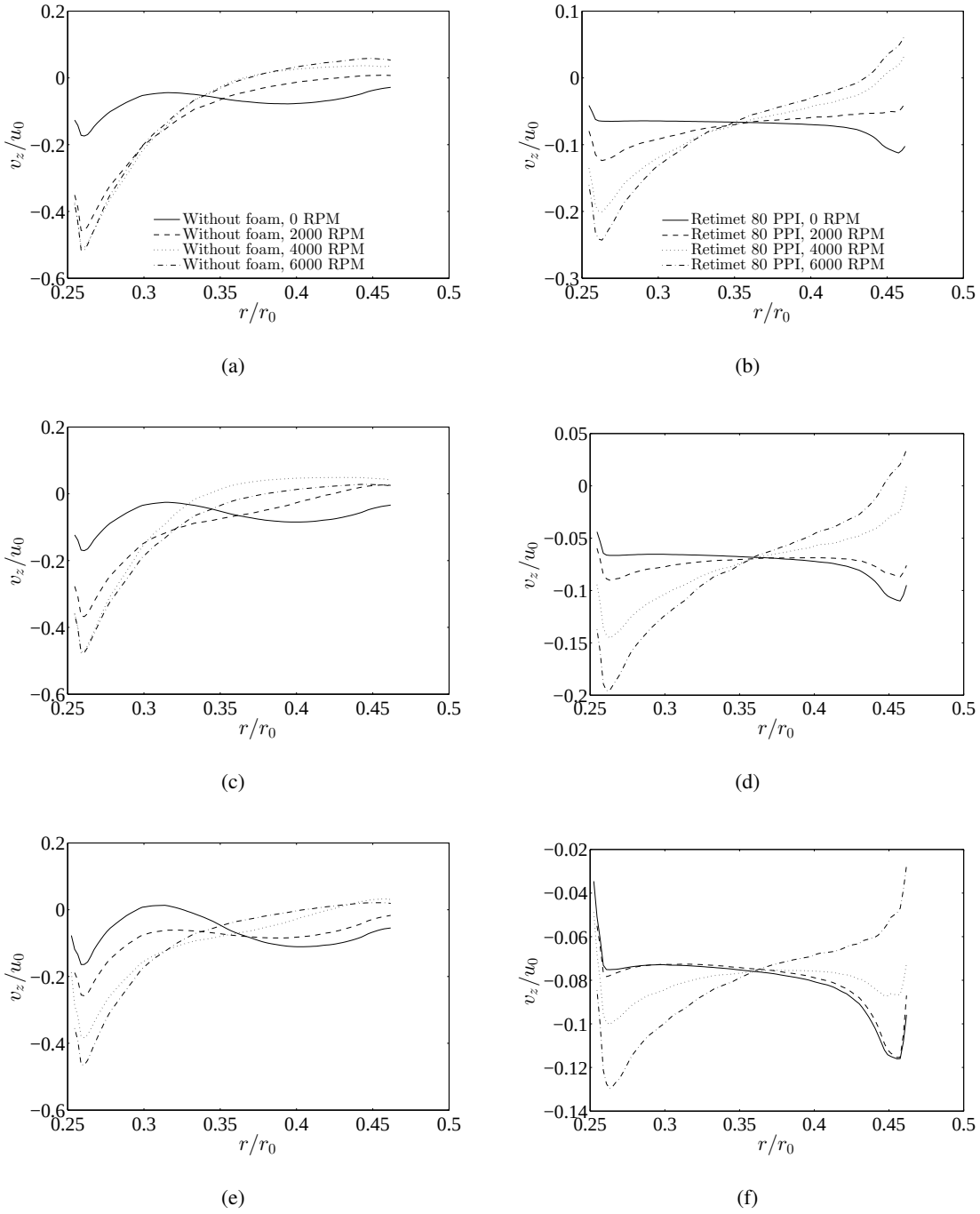

Figure C.9: Normalized axial velocity at line L_3 for the cases without foam and with the Retimet 80 PPI. Left column comprises the results obtained without foam. Right column comprises the results obtained with the Retimet 80 PPI. (a,b) 20 g/s, (c,d) 40 g/s, and (e,f) 100 g/s of airflow.

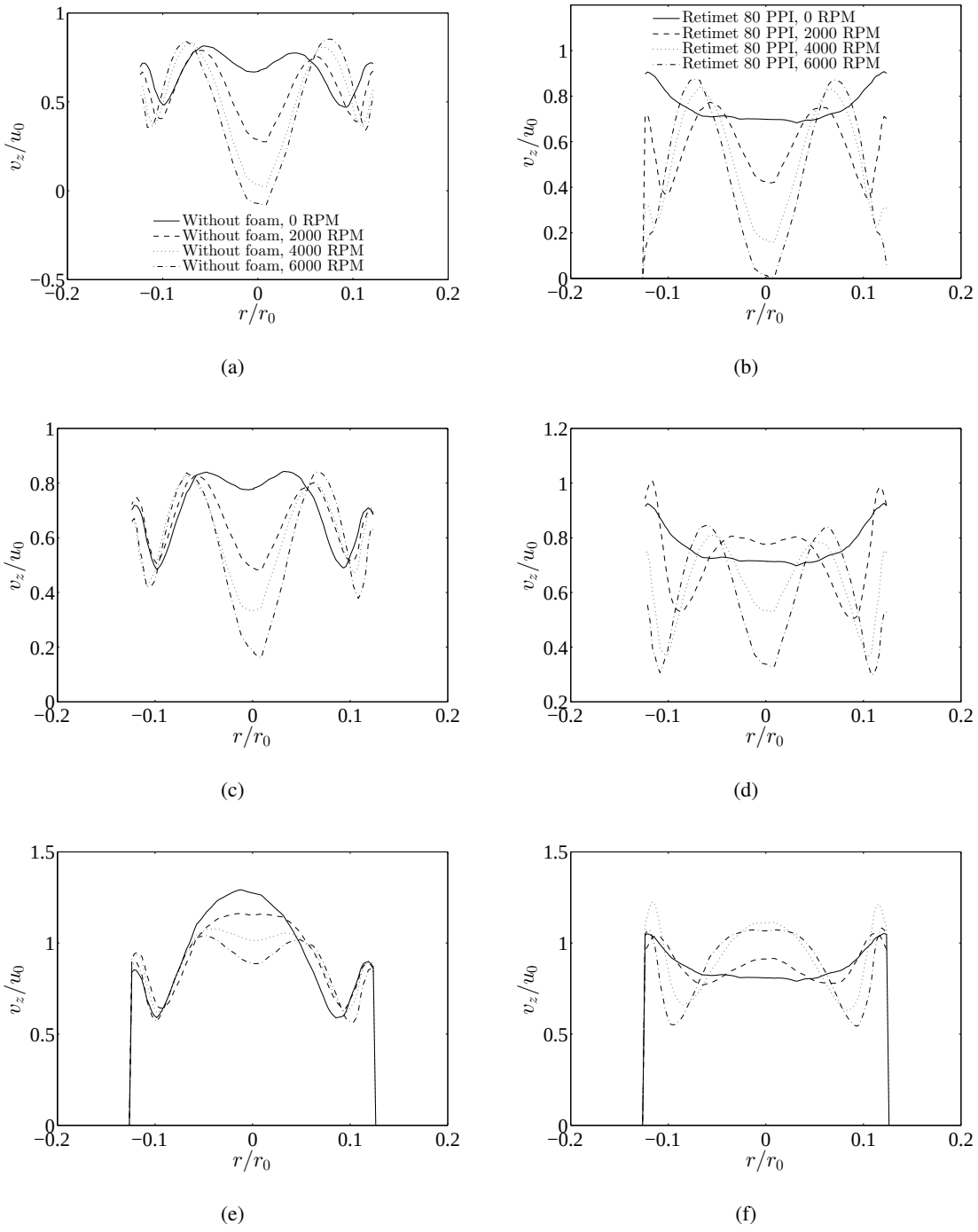

Figure C.10: Normalized axial velocity at line L_4 for the cases without foam and with the Retimet 80 PPI. Left column comprises the results obtained without foam. Right column comprises the results obtained with the Retimet 80 PPI. (a,b) 20 g/s, (c,d) 40 g/s, and (e,f) 100 g/s of airflow.

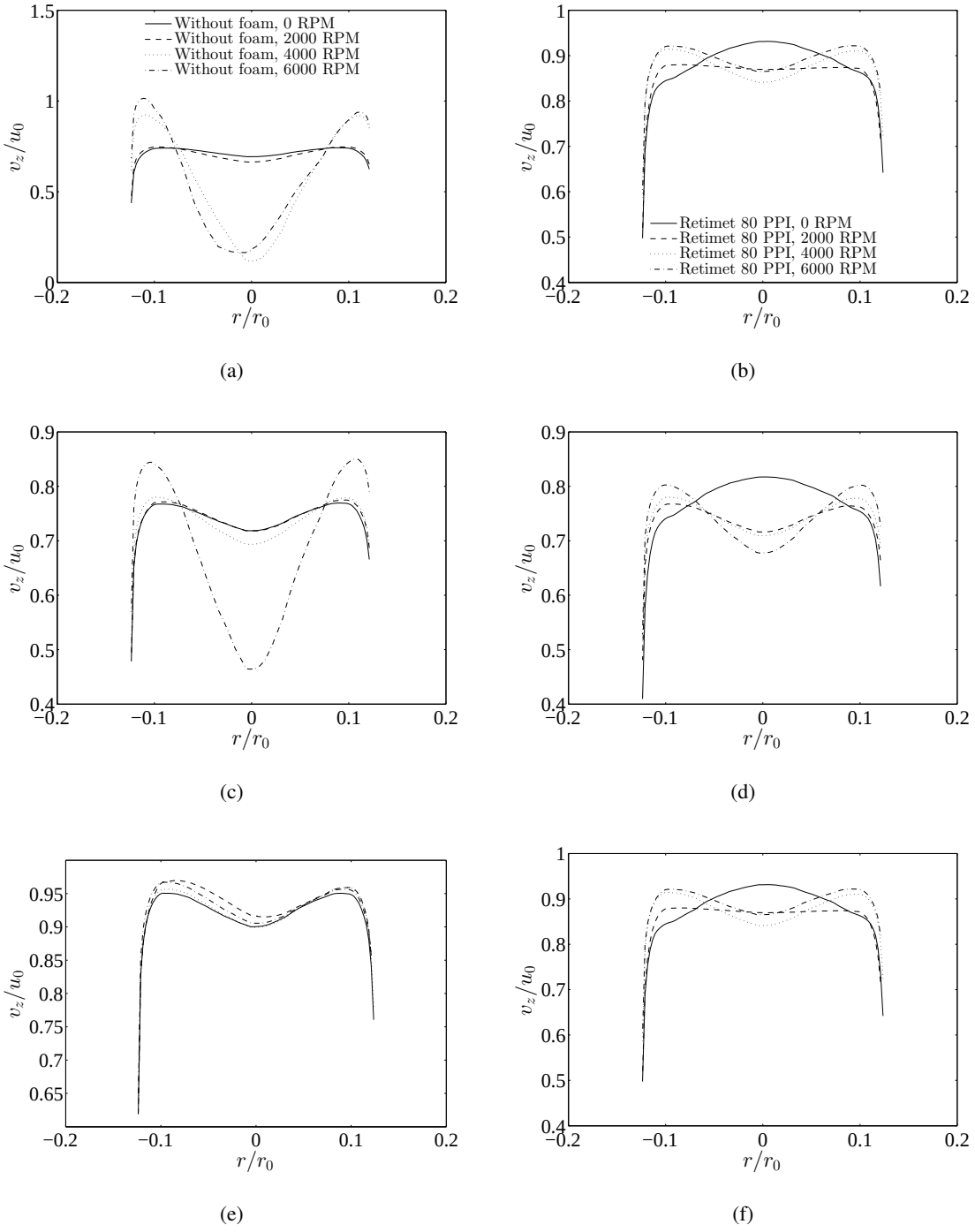

Figure C.11: Normalized axial velocity at line L_5 for the cases without foam and with the Retimet 80 PPI. Left column comprises the results obtained without foam. Right column comprises the results obtained with the Retimet 80 PPI. (a,b) 20 g/s, (c,d) 40 g/s, and (e,f) 100 g/s of airflow.

Appendix D

Oil capture UDF code

The following example employed the coefficients obtained for the Retimet 80 PPI foam.

```
/************************************************************
* UDF to randomly kill particles in a porous medium          *
************************************************************/

#include "udf.h"     /* Header file inlcuded for the UDF to work */
#include <stdlib.h>  /* Header needed for the random number */

#define POROUS_ID  14  /* The porous cell zone ID (from the Fluent interface */
#define UDM_PMASS  0   /* UDM index for the dumped mass */

#define DPORE      9.183e-04 /* Mean pore diameter (m) */

static Thread *pt;     /* The porous cell zone thread pointer */

/* Function to return the value of beta, based on local flow velocity and
particle diameter */
real calcBeta(real Re1, real dStar1)
{
real lCoeff[21] =
{
5.47488604307871e-15,
-6.45168581635287e-10,
-4.55045689799892e-11,
-0.000767425343220316,
```

```
1.50402849140321e-05,

1.34075011367275e-07,

-515.107764713126,

13.8122887176922,

-0.115365435005229,

-0.000150598708144689,

-753841366.115888,

17686444.6594384,

-145801.645594743,

511.296301104271,

-0.00861825839122889,

-1.75927425074776e+15,

38061832057970.1,

-269525279945.642,

761721876.832481,

-689134.389332830,

100.262611788739

};


real Re2, Re3, Re4, Re5, dStar2, dStar3, dStar4, dStar5;


Re2 = Re1*Re1;

Re3 = Re2*Re1;

Re4 = Re3*Re1;

Re5 = Re4*Re1;

dStar2 = dStar1*dStar1;

dStar3 = dStar2*dStar1;

dStar4 = dStar3*dStar1;

dStar5 = dStar4*dStar1;


/* Return the value of beta */

return (
```

```
lCoeff[0]*Re5
+ lCoeff[1]*Re4*dStar1
+ lCoeff[2]*Re4
+ lCoeff[3]*Re3*dStar2
+ lCoeff[4]*Re3*dStar1
+ lCoeff[5]*Re3
+ lCoeff[6]*Re2*dStar3
+ lCoeff[7]*Re2*dStar2
+ lCoeff[8]*Re2*dStar1
+ lCoeff[9]*Re2
+ lCoeff[10]*Re1*dStar4
+ lCoeff[11]*Re1*dStar3
+ lCoeff[12]*Re1*dStar2
+ lCoeff[13]*Re1*dStar1
+ lCoeff[14]*Re1
+ lCoeff[15]*dStar5
+ lCoeff[16]*dStar4
+ lCoeff[17]*dStar3
+ lCoeff[18]*dStar2
+ lCoeff[19]*dStar1
+ lCoeff[20]
);
}

DEFINE_ON_DEMAND(captureSetup)
{
Domain *domain = Get_Domain(1);  /* Get the pointer to the domain */
Thread *ct;
cell_t c;

/* Lookup the thread pointer for the porous cell zone */
Message("Looking up the thread pointer for zone %2d...",POROUS_ID);
```

```
pt = Lookup_Thread(domain, POROUS_ID);
Message("done.\n");

/* Initialise the random number generator */
Message("Initialising the random number generator...");
srand(time(0));
Message("done.\n");

/* Allocate memory for the particle scalars that will hold the coordinates
from the previous timestep, if not already done */
if (NULLP(user_particle_vars))
{
Message("Allocating memory for particle scalars...");
Init_User_Particle_Vars();
Message("done.\n");
}

/* Zeroise the user-defined memory location that stores mass */
Message("Zeroing the user-defined memory location...");
thread_loop_c(ct, domain)
{
begin_c_loop(c,ct)
{
C_UDMI(c,ct,UDM_PMASS) = 0.0;
}
end_c_loop(c,ct);
}
Message("done.\n");
}

DEFINE_DPM_SCALAR_UPDATE(captureInPorous,c,ct,initialize,p)
{
```

```
/* On the first call, set up the user scalar which will hold the particle's

previous coordinates */

if (initialize)

{

P_USER_REAL(p,0) = P_POS(p)[0];

P_USER_REAL(p,1) = P_POS(p)[1];

P_USER_REAL(p,2) = P_POS(p)[2];

}

else

{

/* Is the particle in the porous cell zone? */

if ( ct == pt )

{

/* Generate a random number between 0 and 1 */

real r01 = rand()/((real)RAND_MAX);


/* Calculate the distance moved by the particle

in the last timestep */

real dx = P_POS(p)[0]-P_USER_REAL(p,0);

real dy = P_POS(p)[1]-P_USER_REAL(p,1);

real dz = P_POS(p)[2]-P_USER_REAL(p,2);

real ds = sqrt(dx*dx+dy*dy+dz*dz);


real uMag = sqrt( C_U(c,ct)*C_U(c,ct)

+ C_V(c,ct)*C_V(c,ct)

+ C_W(c,ct)*C_W(c,ct) );


real Re = C_R(c,ct)*uMag*DPORE/C_MU_L(c,ct);


real dStar = P_DIAM(p)/DPORE;


/* Remove the particle if the random number is less than
```

```
the scaled distance

Message("%15.4e%15.4e%15.4e%15.4e%15.4e \n",

Re, dStar, calcBeta( Re, dStar), r01, ds); */


if ( r01 < ds*calcBeta( Re, dStar ) )

{

/* Dump the mass of the particle into the

User-Defined Memory for this cell */

C_UDMI(c,ct,UDM_PMASS) += P_MASS(p);


/* This line kills the particle */

MARK_PARTICLE(p, P_FL_REMOVED);

}

}


/* Update the particle scalars for the next

time the particle is moved */

P_USER_REAL(p,0) = P_POS(p)[0];

P_USER_REAL(p,1) = P_POS(p)[1];

P_USER_REAL(p,2) = P_POS(p)[2];

}

}
```